Displacement and Damage Monitoring for Masonry Buildings Subjected to Ground Movements Induced by Underground Construction



Yiyan Liu

Exeter College

University of Oxford

A thesis submitted for the degree of

Doctor of Philosophy

Trinity 2023

To Autumn

Abstract

Monitoring displacements and damage in masonry buildings subjected to ground movements due to nearby underground construction poses significant challenges. Existing monitoring techniques provide limited displacement data and employ simple models, such as equivalent beam models, to estimate damage. This thesis develops alternative monitoring techniques offering robust displacement monitoring and interpretation as well as direct crack detection and quantification.

To collect the required measurements for algorithm development, a large-scale test campaign is initially conducted. This campaign involves three half-scale brick masonry building models, subjected to induced settlement with varying opening configurations, floor structures, and weight arrangements. Digital Image Correlation (DIC) is utilised to monitor building displacements and damage, with laser scans executed pre- and post-test.

This study initially assesses the ability of widely-adopted equivalent beam models to locate and quantify damage in the test building models. To do this, the equivalent beam models utilise the DIC measurement data to infer crack widths and locations. Comparisons between the inferred and observed damage indicate that equivalent beam models underestimate crack widths and cannot accurately locate cracks.

Subsequently, this research proposes an alternative formulation termed the Equivalent Frame Approach (EFA), which discretises the building façade into individual structural components. Synthetic validations through linear and non-linear Finite Element (FE) analyses show that the EFA approach captures the deformation kinematics. Using DIC displacement data from the experiments, it is demonstrated that EFA can accurately locate cracks and quantify crack widths up to moderate damage.

To provide more easily obtainable displacement data for EFA analyses, a new point cloud monitoring technique is developed. The resulting Point Cloud-based Equivalent Frame Approach (PC-EFA) matches distinctive masonry surface features from pre- and post- test point clouds and filters the noisy displacement fields using appropriate kinematic functions. In addition, a Point Cloud-based Crack Detector and Quantifier (PC-Cr) approach is developed to offer direct damage detection and quantification from a kinematic perspective. Both techniques are applied and validated using the laser scan and DIC data from the test campaign. The results demonstrate the potential of PC-EFA and PC-Cr to offer reliable and robust displacement and damage monitoring for masonry buildings.

Acknowledgement

The research described in this thesis was carried out at Oxford during the period between October 2019 and September 2023, and was made possible by the full financial support of the Engineering and Physical Sciences Research Council (EPSRC) and Arup through an iCASE studentship.

I am particularly indebted to my academic supervisors, Professor Sinan Acikgoz and Professor Harvey Burd. Their invaluable guidance and mentorship throughout the course of this research have been indispensable to my academic growth. I am also grateful to my industrial supervisors, Ben Gilson and Michael Devriendt from Arup, for their sustained interest, guidance, and invaluable advice. I wish to acknowledge with thanks the assistance and support received from Professor Korhan Dalgic and Burcu Gulen in the collection of research data. Their contributions have been instrumental in the completion of this research.

I would like to express my gratitude to my former colleagues John Lamont, Chris Burgess, Collin Warren, Jonathan Gammon, Felicity Sims, and Sarah Trinder at Halcrow, Jacobs, and High Speed Two Limited. They first piqued my interest in data analysis and computational thinking. Their trust and the opportunities they provided allowed me to hone my skills and interests, which have been invaluable in the pursuit of this research.

I would also like to extend heartfelt gratitude to all my friends, both here at Oxford and elsewhere, who have been pillars of support through difficult moments.

My heartfelt thanks are extended to my parents, Jenny Jinxiu Yan and Dan Liu, and my grandmother, Chuanfang Zeng. Their unwavering support and love have been a constant source of strength throughout this journey.

Last but certainly not least, I would like to pay tribute to my late grandfather, Tianyou Liu, who has been an inspiration throughout my life. I know you would be proud of me.

Contents

ABSTRACT ..... **I**

ACKNOWLEDGEMENT ..... **III**

CONTENTS ..... **IV**

1. INTRODUCTION **1**

1.1. BACKGROUND 1
1.2. RESEARCH OBJECTIVES 4
1.3. THESIS OUTLINE 5

2. LITERATURE REVIEW **7**

2.1. MONITORING OF MASONRY ASSETS SUBJECTED TO SETTLEMENT INDUCED BY UNDERGROUND CONSTRUCTION: CURRENT PRACTICE AND RELATED RESEARCH 7
2.1.1. Displacement monitoring *7*
2.1.2. Strain and crack monitoring *9*
2.1.3. Monitoring data interpretation and management *12*
2.2. IMAGED-BASED STRUCTURAL MONITORING 15
2.2.1. Displacement monitoring *16*
2.2.2. Strain and crack monitoring *20*
2.3. POINT CLOUD-BASED STRUCTURAL MONITORING 24
2.3.1. Displacement monitoring *25*
2.3.2. Strain and crack monitoring *29*
2.4. CONCLUSION 32

3. INTRODUCTION TO LARGE-SCALE BUILDING SETTLEMENT TEST **34**

3.1. PURPOSE 34
3.2. BUILDING MODELS 35
3.3. TEST PROCEDURE 36
3.4. INSTRUMENTATION DETAILS 37
3.4.1. 2D DIC system *38*
3.4.2. Terrestrial laser scan system *40*
3.5. EXPORT AND VALIDATION OF DIC DISPLACEMENT DATA 41
3.5.1. Export of displacement data from video files *41*
3.5.2. Evaluation of out-of-plane displacements *42*
3.5.3. Assessment of DIC in-plane measurement errors *43*
3.5.4. Cross-validation with FBG and LVDT *44*
3.5.5. Validation of virtual LVDT results *46*
3.6. DAMAGE ASSESSMENT OF BUILDING MODELS 52
3.7. THE ROLE OF THE AUTHOR OF THIS THESIS IN THE TEST CAMPAIGN 54
3.8. CONCLUSION 55

4. ESTIMATION OF BUILDING DAMAGE USING EQUIVALENT BEAM IDEALISATION **56**

4.1. PURPOSE 56
4.2. METHODOLOGY 56
4.2.1. Distortion measures *57*
4.2.2. Strain estimation *58*
4.2.3. Tensile strain and damage correlation *61*

4.3. PERFORMANCE EVALUATION OF EQUIVALENT BEAM MODELS 61
4.3.1. 3O-RF *61*
4.3.2. 3O-JF-W1 ..... *64*
4.3.3. 50O-RF-W1 ..... *66*
4.4. OVERALL PERFORMANCE OF THE EQUIVALENT BEAM MODELS 67
4.5. CONCLUSION 70

5. EQUIVALENT FRAME APPROACH 71

5.1. PURPOSE 71
5.2. PROPOSED METHODOLOGY 71
5.2.1. Façade discretisation *71*
5.2.2. Strain estimation *72*
5.3. VALIDATION USING 3D FINITE ELEMENT MODELS 74
5.3.1. Validation of EFA with synthetic data from linear FE analysis *75*
5.3.2. Validation of EFA with synthetic data from nonlinear FE analysis *83*
5.4. APPLICATION TO THE LARGE-SCALE BUILDING SETTLEMENT TEST 87
5.4.1. Sample strain calculation *87*
5.4.2. Tensile strain – damage correlation *88*
5.4.3. Crack size – tensile strain maps *91*
5.5. CONCLUSION 95

6. INTRODUCTION TO POINT CLOUD-BASED EQUIVALENT FRAME APPROACH (PC-EFA) AND VALIDATION USING SYNTHETIC DATASET 98

6.1. PURPOSE 98
6.2. METHODOLOGY 98
6.2.1. Point cloud collection *100*
6.2.2. Point cloud preprocessing *101*
6.2.3. Feature calculation and matching *104*
6.2.4. Displacement filtering *113*
6.2.5. Strain analysis and damage screening *123*
6.3. VALIDATION WITH SYNTHETIC DATA FROM FE MODEL 128
6.3.1. Sample validation of a pier *129*
6.3.2. Validation with synthetic data from linear FE analysis *137*
6.3.3. Validation with synthetic data from nonlinear FE analysis *142*
6.4. CONCLUSION 145

7. APPLICATION OF POINT CLOUD-BASED EQUIVALENT FRAME APPROACH (PC-EFA) TO THE LARGE-SCALE BUILDING SETTLEMENT TEST 148

7.1. PURPOSE 148
7.2. APPLICATION TO THE LARGE-SCALE BUILDING SETTLEMENT TEST 148
7.2.1. Overview *148*
7.2.2. Point cloud pre-processing *149*
7.2.3. Feature calculation and matching *151*
7.2.4. Displacement filtering *157*
7.3. RESULTS AND DISCUSSION 167
7.3.1. Overview *167*
7.3.2. 3O-RF-W3 ..... *168*
7.3.3. 3O-RF-W1 ..... *172*
7.3.4. 3O-JF-W1 ..... *174*

7.4. CONCLUSION 177
8. POINT CLOUD-BASED CRACK DETECTION AND CRACK MEASUREMENTS 179
8.1. PURPOSE 179
8.2. METHODOLOGY 180
8.2.1. Overview 180
8.2.2. Rolling window initialisation and displacement filtering 182
8.2.3. Feature clustering and crack identification 184
8.2.4. Crack measurement 195
8.2.5. Post-processing 199
8.3. MINIMUM DETECTABLE CRACK WIDTH 202
8.4. APPLICATION TO THE LARGE-SCALE BUILDING SETTLEMENT TEST 205
8.4.1. Overview 205
8.4.3. Feature clustering and crack identification 206
8.4.4. Crack measurement 208
8.4.5. Post-processing 208
8.5. RESULTS AND DISCUSSION 209
8.5.1. 3O-RF-W3 209
8.5.2. 3O-JF-W1 218
8.6. CONCLUSION 227
9. CONCLUSIONS AND FUTURE RESEARCH 229
9.1. CONCLUSIONS 229
9.2. FUTURE RESEARCH 234
9.2.1. Additional field applications and validations 234
9.2.2. Process optimisation for PC-EFA and PC-Cr 235
9.2.3. Extension of building material adaptivity for PC-EFA and PC-Cr 235
9.2.4. Enhancement in handling complex cracking with PC-Cr 236
10. REFERENCES 237

1. Introduction

1.1. Background

With the continuing trend of urbanisation and the consequent constraints on surface area, the utilisation of underground space has emerged as a popular option for urban development. A 2019 market survey by the International Tunnelling Association (ITA) highlighted this trend, reporting an average construction of 500 km of metro tunnels globally each year (ITA-AITES, 2019). In the UK, significant infrastructure projects like Crossrail, High Speed Two, and Thames Tideway have necessitated extensive tunnelling and excavation, particularly in urban settings. However, such utilisation of underground spaces, especially in soft ground conditions, invariably induces ground movements during construction and in the post-construction phases. These movements pose notable risks to adjacent structures, making the impact on nearby buildings a critical consideration in urban tunnelling projects (Mair, 1998). Given these risks, the implementation of meticulous and robust monitoring and surveying schemes for masonry buildings during urban underground construction is essential.

Before construction, potential building damage is typically assigned to one of six categories following a three-phase assessment described by Mair et al. (1996). Crossrail and High Speed Two mandate all buildings in 'moderate' risk category and above to be monitored from one year prior to construction until the settlement has ceased (Crossrail Limited, 2008; High Speed Two Limited, 2017). For Crossrail alone, according to Lazarus and Jung (2018), there were approximately 4000 buildings along the route, including 300 listed buildings. It is therefore not surprising to see more than £60 million was spent on Crossrail for instrumentation and monitoring (VINCI Construction, 2014).

Masonry buildings are particularly vulnerable to damage caused by ground movement due to the low tensile strength of the material (Boscardin and Cording, 1989). Cracks and other damages often appear on the masonry assets due to the settlement, leading to aesthetic and structural degradation. The 2008 English House Survey report indicates that 95% of dwellings are of traditional masonry (Department for Communities and Local Government, 2010). Given the UK's longstanding tradition of masonry use and the cultural significance of many historic buildings, monitoring of masonry buildings subjected to settlement is a key priority for underground construction.

While cracks in masonry buildings can be directly monitored in terms of their width—e.g. by installing tell-tale monitoring gauges or employing the 'three-screws' method (BRE, 1989)—such monitoring is typically reserved for selected buildings due to its intrusive and labour-intensive nature. Monitoring of this sort involves detailed condition surveys, installation of crack gauges or screws at observed or expected crack locations, repeated inspections for new cracks, and manual measurements of cracks. Instead, building response is primarily monitored by total station surveying and precise levelling (Burland et al., 2001). The potential damage to a building is typically screened using maximum settlement and/or tilt. Meanwhile, the severity of cracks is often 'interpreted' using the equivalent beam approach, in which the building is idealised as an equivalent Timoshenko Beam. In this model, monitored displacement data of the building are used to estimate the maximum tensile strain developed in the idealised beam, which is then interpreted in terms of crack width through pre-established correlations. However, this form of representation and quantification often results in limited reliability in the estimated damage (Acikgoz et al., 2022).

On the other hand, advancements in technology have enabled various computer vision techniques, utilising both digital image and point cloud methods, to increasingly facilitate

tasks such as change detection and object recognition in numerous applications in our daily lives. Digital images and point clouds can be readily obtained using digital cameras and laser scanners; they contain rich texture and geometric information about the entire object being imaged or scanned. In many instances, these two forms of data are already being collected routinely for construction projects for diverse purposes, including condition surveys and construction documentation and archiving. Given that the data are readily available and considering the successful applications of relevant computer vision techniques in different domains, numerous attempts have been made to model displacement and damage monitoring within the field of surface asset monitoring as classic change detection and recognition tasks (Acikgoz et al., 2017; Fan et al., 2020; Mohan and Poobal, 2018; Mukupa et al., 2017; Zou et al., 2019). However, deploying such paradigms on masonry assets, especially those impacted by settlements induced by underground construction, introduces additional challenges.

Firstly, the displacements imposed on buildings due to settlement generally have a small magnitude. Change detection paradigms that excel in scenes involving large displacement may not suffice to identify the small relative distortion of a building's structural component. Secondly, damage—specifically, cracks in masonry assets—can manifest in various forms. Visually, cracks can resemble shadows due to the rough surfaces of masonry, leading to potential misidentification. Additionally, the visual quantification of crack width is subject to similar issues; variations in lighting conditions can alter the appearance of cracks, making them seem wider or narrower.

Overall, the monitoring of masonry buildings affected by underground construction profoundly influences mitigation and construction activities. With the evolving standards on asset protection, traditional building monitoring approaches, which primarily employ displacement monitoring at isolated points, are facing considerable limitations on their

reliability and accuracy for building damage assessment. While computer vision techniques hold promising prospects as potential solutions for both displacement and damage monitoring, they also introduce additional challenges. This research aims to address these challenges in a systematic manner.

1.2. Research objectives

The first objective of this research is to conduct a comprehensive appraisal of the performance of widely adopted equivalent beam models in assessing damage to masonry buildings subjected to settlement. This appraisal utilises rich and accurate monitoring data collected from representative physical testing.

In addition, this research aims to develop innovative non-contact displacement monitoring and damage detection/quantification methods for masonry assets experiencing ground movement. These methods apply computer vision techniques and utilise accessible tools in less controlled environments. Specifically, the developed solutions do not require specialised hardware or adhere to stringent monitoring conditions. The monitoring data are attainable through standard practices, employing commercial laser scanners and/or consumer-grade digital cameras. These methods provide high-resolution 3D details about the asset—information not available through traditional monitoring techniques—while also delivering accurate measurement results. These results can be directly incorporated into established assessment and decision-making procedures. Upon development, in addition to synthetic validation using simulated datasets, these methods are subjected to rigorous validation utilising experimental data collected from physical testing, benchmarked against dense and accurate monitoring data from alternate sources.

1.3. Thesis outline

In Chapter 2, the current practice of masonry asset monitoring during underground construction is reviewed via an extensive analysis of industry standards, specifications, guidance documents, and research papers. The emphasis is on state-of-the-art computer vision techniques for (a) displacement monitoring and (b) crack monitoring in a broader structural monitoring context. This review highlights the significance of this research and pinpoints potential techniques that can be employed to achieve the research objectives.

Chapter 3 presents a recent large-scale building settlement test campaign in which three half-scale building models were subjected to induced settlement. This chapter describes the test design, setup, and implementation, and it outlines the instrumentation and monitoring results of the building models. It also includes a validation of the displacement data obtained through Digital Image Correlation (DIC).

Chapter 4 delivers a comprehensive review of widely used equivalent beam models and evaluates their efficacy in assessing damage to masonry assets using the DIC data collected from the settlement test campaign. The collected DIC data facilitates a valuable direct comparison between the actual observed damage and the damage category indicated by equivalent beam models. This review highlights the limitations of the current models and reveals the reasons for these limitations.

Reflecting on the identified limitations, Chapter 5 explores an equivalent frame idealisation of buildings. This type of idealisation is commonly used to formulate computationally efficient numerical models of masonry structures, but it has not been employed in the context of monitoring. In the proposed Equivalent Frame Approach (EFA), where a building is discretised into piers, spandrels and connectors, beam kinematic assumptions are applied at the pier/spandrel level rather than for the entire building façade. By employing a series of

statistical measures, an in-depth validation of this idealisation is initially conducted using both linear and nonlinear finite element models. Subsequently, the proposed EFA is assessed with DIC data collected from the test campaign.

The adoption of EFA for damage assessment would require a larger number of displacement measurement points than currently adopted in practice. Building on the concept of EFA, Chapter 6 proposes a monitoring approach that leverages the high-resolution 3D geometric information contained in point cloud data, termed the 'Point Cloud-based Equivalent Frame Approach' (PC-EFA). Within PC-EFA, errors inherent in point cloud-derived displacement data are managed through iterative filtering and fitting. The proposed method is then validated using synthetic data obtained from FE analysis, with added noise to simulate the error profiles of displacement data from point cloud feature matching. The method is capable of deriving reliable EFA model parameters, even in challenging noise environments. Chapter 7 continues the validation by applying the proposed PC-EFA to point cloud data collected from four different tests in the settlement test campaign.

Results from Chapter 7 show that the continuum model (i.e. the beam model) utilised in PC-EFA can only approximate the kinematics of a damaged structural component to a certain extent. As damage progresses, these models begin to lack consistency in indicating damage severity and location. To address these limitations, Chapter 8 proposes a crack detector and quantifier, termed PC-Cr. The proposed PC-Cr employs a newly formulated crack model, termed 'segmented rigid-body crack model', to quantify cracks from a kinematic perspective. After establishing theoretical minimum detectable crack widths, the effectiveness of the proposed PC-Cr method is validated using point cloud data obtained during the settlement test campaign, benchmarked against crack observations and measurements from DIC.

Chapter 9 consolidates the key findings and contributions of this research and proposes avenues for future work.

2. Literature review

This review begins by establishing the current practice and state of the art research related to displacements and damage monitoring in masonry buildings subjected to settlements. This is achieved through an extensive analysis of existing industry standards, specifications, guidance documents, and research articles. Subsequently, the review critically examines and discusses image and point cloud-based computer vision techniques within the broader context of structural health monitoring.

2.1. Monitoring of masonry assets subjected to settlement induced by underground construction: Current practice and related research

2.1.1. Displacement monitoring

The response of buildings subjected to settlement is primarily monitored in practice through total station surveying and/or precise levelling (Burland et al., 2001; Crossrail Limited, 2008; High Speed Two Limited, 2017). These survey methods determine the position of reference points on buildings. The key difference between total station surveying and precise levelling is that the former provides 3D coordinates of points, whereas the latter only determines elevation. Depending on the specific surveying method employed, reference points on buildings are typically 3D reflective prisms, precise levelling points, or Building Research Establishment (BRE) sockets. Survey results are then referenced to project or national benchmarks to establish the true coordinates (elevations) of these reference points. As a project progresses, displacements of each individual reference point are determined by subtracting the pre-construction baseline from the current coordinates (elevations). According to Burland et al. (2001) and the Tunnel Lining Design Guide published by the British Tunnelling Society (2004), the practical accuracy of total stations and precise levels can be as high as 0.5mm to 1mm.

However, both total station surveying and precise levelling require the installation of reference points on the façade of the concerned building. Such installations are intrusive and may not always be permitted or preferred, leading to a limited number of reference points available on an individual building level. For instance, Crossrail typically employed three points on each building (Crossrail Limited, 2008). An example of installed prisms on a masonry building is shown in Figure 2.1. It is worth noting that even for large projects, dedicated building surveying is typically reserved for selected buildings. For instance, for Crossrail, this was limited to protected properties, defined as buildings expected to incur damage categories exceeding 'moderate' (Crossrail Limited, 2008).



Figure 2.1; A typical building monitoring setup involves installing a 3D reflective prism and surveying the position of the installed prism. The figures used here are courtesy of terrainsurveys.co.uk, Google Street View, and Leica Geosystems.

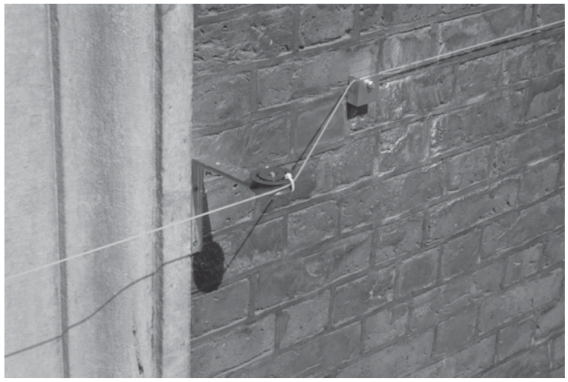
In academic research, satellite-based levelling techniques have also been explored as an alternative method for assessing building displacements. These techniques, including Differential Global Position Satellite (DGPS) and Interferometric Synthetic-Aperture Radar (InSAR), were traditionally used for long-term monitoring of 'regional' surface movements (British Tunnelling Society, 2004). Although Synthetic-Aperture Radar provides images over extensive areas, accurate metric differential measurements using InSAR were not

possible until high-resolution SAR data became available recently. By selecting a motionless reference point in the InSAR image, the projection of the relative displacement of a point on the structure of interest can be measured along the satellite line of sight (Giardina et al., 2019). However, interpreting 1D measurements in the context of tunnelling-induced movements requires a priori assumptions. For example, some studies assume that buildings only experience settlements (e.g. Giardina et al., 2019), which can lead to erroneous interpretations. Furthermore, due to the limited positioning accuracy of the radar scatterers, even Multi-Temporal InSAR (MT-InSAR) is not sufficient for reliable displacement monitoring (Hu et al., 2019). Additionally, the long acquisition time of satellite images makes satellite-based levelling techniques unsuitable for monitoring rapid ground movement during construction (Marti et al., 2017).

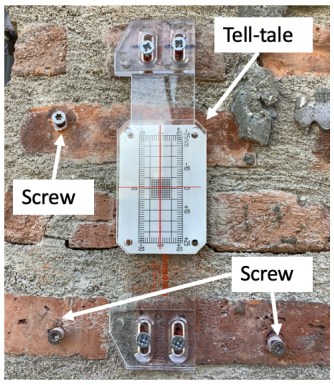
2.1.2. Strain and crack monitoring

In practice, large scale direct monitoring of strain and crack on buildings subjected to settlement are uncommon. As reported in case studies from the construction of the Jubilee Line Extension (Burland et al., 2001), such monitoring is often reserved for a few selected properties or are commissioned by research projects. For example, optical fibre sensors (e.g. Fibre Bragg Grating (FBG) sensors, see example application in Figure 2.2a), due to their accuracy, reliability in strain measurement (with an accuracy of approximately 1με as reported by Chen et al., 2011), and compact size, have gained significant attention in the civil engineering industry. Various successful field applications of optical fibre sensors for strain measurements in the context of structural health monitoring have been reported (Ye et al., 2014). Numerous research papers using strain measurement from optical strain sensors for crack detection have been published (e.g. Barrias et al., 2016; Glisic and Inaudi, 2012; Habel and Krebber, 2011), with some recent works attempting to quantify crack movements (e.g. Berrocal et al., 2020; Rodríguez et al., 2015). However, field applications on masonry

buildings subjected to tunnel-induced settlement are limited (e.g. Acikgoz et al., 2022) because optical strain sensors measure axial strain only along a predefined direction, whereas damage may occur in any direction. Moreover, interpreting the strain results obtained from optical sensors can be challenging in the absence of contextual displacement information, such as overall building displacements.



(a)



(b)



(c)



(d)

Figure 2.2; (a) A section of Fibre Optical Bragg (FBG) cable installed on the south façade of St Mary Abchurch (reproduced from Acikgoz et al., 2022); (b) A tell-tale installed traversing an observed crack on a masonry building model. Additional screws are installed for the implementation of the 'three-screw' method; c) Demec strain gauge. Image courtesy of Accolade Measurement (https://accolademeasure.co.uk); (d) Crack ruler measuring the width of an observed crack. Original photo courtesy of Korhan Denzi and Burcu Gulen.

On the other hand, traditional crack monitoring involves the use of tell-tale crack gauges (Figure 2.2b), the 'three-screws' method (Figure 2.2b) or crack gauge rulers (Figure 2.2d) (BRE, 1989). Although tell-tale gauges are relatively straightforward to install, they are intrusive, which may make them less preferred for aesthetic or operational reasons. This intrusive nature also restricts their use to pre-existing cracks or selected locations where

cracks are anticipated. Moreover, tell-tale gauges often fail due to anchorage slip and are susceptible to vandalism. The tell-tale measurements of crack movements are obtained by technicians reading the scale manually. Their accuracy largely depends on the experience of the technician. Frequent readings make the data acquisition process labour-intensive and susceptible to human errors. Conversely, the 'three-screws' method involves drilling and installing screws on either side of the crack. The distances between a pair of screws are measured using a calliper to assess the displacement of the wall on one side of the crack relative to the other. Although the 'three-screws' method is less prone to vandalism and more accurate than the tell-tale method, it is similarly restricted to selected pre-existing cracks or anticipated crack locations because of the need for screw installation and manual measurements.

For the Jubilee Line Extension (JLE) project, a research team opted to use DEmountable MEChanical (Demec) strain gauges (Figure 2.2c) for crack monitoring. Compared to the 'three-screws' method and tell-tale gauges, Demec gauges offer limited ranges but higher resolution and accuracy (British Tunnelling Society, 2004). The project demonstrated that these gauges could serve as a reliable and relatively cost-effective technique for measuring relative movements across existing cracks (Burland et al., 2001). However, like the 'three-screws' method, the installation of Demec studs is required, and readings must be taken manually. Additionally, the market also offers various other kinds of crack metres, such as potentiometers and vibrating wire strain gauges. Nonetheless, these all necessitate permanent intrusive installations, which may not be feasible in many circumstances.

As illustrated in Figure 2.2d, crack widths can also be quantified using crack gauge rulers. At a specific point along the crack, the width is assessed by aligning the graduations on the ruler with the visible crack opening. Although this method seems straightforward, the accuracy of the measurements predominantly depends on the technicians' capability to

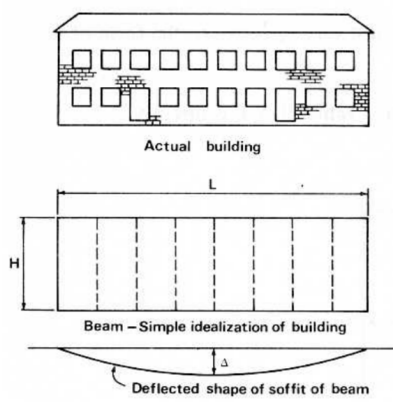
accurately interpret what constitutes a crack opening—particularly when considering uneven crack edges—and their proficiency in aligning the graduations accurately. Similar to other crack measurement methods, when repeated readings are required at multiple locations, the process becomes labour-intensive. Furthermore, the crack ruler can only quantify the crack's opening by its width but not the horizontal movement along the crack (crack slip).

2.1.3. Monitoring data interpretation and management

In underground construction, monitoring surface assets forms part of the settlement control and asset management strategy (British Tunnelling Society, 2011). The collected data are used to assess the impact of the settlement, verify design parameters and models, and guide construction control. The monitoring results are often used as the performance indicator of assets in response to the ground movement. It is a common practice for the main contractor to operate a 'traffic light' system enabling appropriate actions to be undertaken when 'trigger values' are exceeded (Crossrail Limited, 2008; High Speed Two Limited, 2017). Such systems often form the bedrock of the contractor's risk management strategy; therefore, the reliability and timeliness of the monitoring data are of great importance.

The performance assessment of masonry assets subject to settlement induced by underground construction typically necessitates both displacement and crack monitoring. Before the appearance of observable cracks, data from displacement monitoring provide insightful information on the structural response. Conversely, crack monitoring offers a more direct and quantifiable indication of the overall condition. However, due to its laborious and intrusive nature, direct monitoring of cracks in buildings is often impractical, particularly on a large scale. Instead, discrete building displacement data, collected through total station surveying and precise levelling, are processed using an engineering model to

estimate the distribution of tensile strain in the building. In the absence of adequate building displacement data, adjacent ground levelling data are sometimes used to infer building displacements. Subsequently, empirical correlations between the estimated maximum tensile strain and notional damage categories are employed to classify the building damage.



(a)

Damage category	Normal degree of severity	Description of typical damage	Approximate crack width (mm)	Range of maximum tensile strains (ε^{t}_{max})
0	Negligible	Hairline cracks	< 0.1	0 – 0.05
1	Very slight	Fine cracks easily treated during normal redecoration. Perhaps	0.1 - 1	0.05 – 0.075
2	Slight	Cracks easily filled.	1 - 5	0.075 – 0.15
3	Moderate	Cracks may require cutting out and patching.	5 – 15 or severe > 3	0.15 – 0.3
4	Severe	Extensive repair involving removal and replacement of sections of walls.	15 – 25 also depends on numbers of cracks	>0.3
5	Very severe	Major repair required involving partial or complete re-construction.	>25 depends on numbers of cracks	-

(b)

Figure 2.3; (a) Illustration of the equivalent beam approach where a building is idealised as a beam with dimensions: length (*L)* and height (H), experiencing a maximum deflection, Δ. The figure is reproduced from Burland and Wroth (1974); (b) Classification for masonry building damage (based on the work of Burland and Wroth, 1974 and Boscardin and Cording, 1989)

The method of interpreting building displacements and assessing building damage varies from practice to practice, and quite often, such interpretation is only undertaken when certain trigger values (e.g. maximum settlement) are exceeded (Devriendt, 2012). In the preliminary stages of pre-construction building damage assessment, damage is typically evaluated using an equivalent beam model based on predicted greenfield settlements (Crossrail Limited, 2008; High Speed Two Limited, 2017). For subsequent monitoring, continuing with this method for damage assessment has the added benefit of validating predictions. To employ the equivalent beam method, first, building displacement measurements are converted into a distortion measure, 'deflection ratio' (defined as Δ/L in Figure 2.3a). Second, distortion measures are used to estimate strains, using a beam idealisation. Finally, maximum tensile strains in the equivalent beam model are associated to a damage category, using established strain-damage correlations (see Figure 2.3b). This approach, however, does not consider the influence of important building characteristics, such as façade openings (e.g. windows and

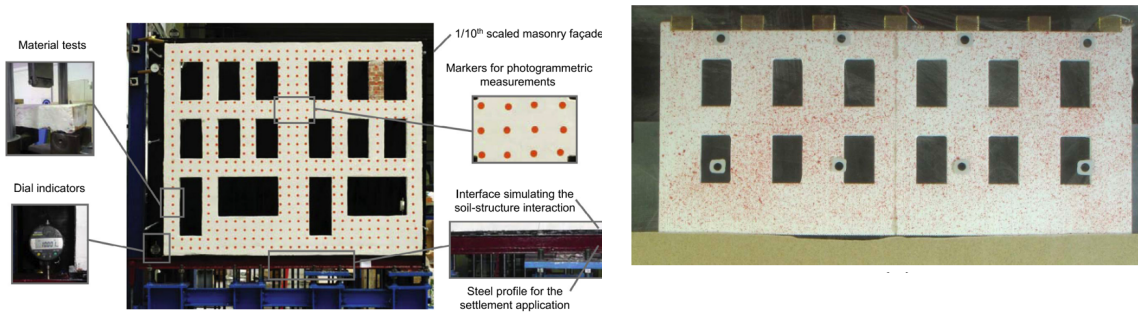
doors) and floor structures (e.g. slabs). To account for these aspects, alternative equivalent beam formulations (e.g. Son and Cording, 2005; Finno et al., 2005) have been proposed.

It is evident that the effectiveness of the equivalent method in indicating building damage depends on several factors, including (a) the quality and spatial resolution of the building displacement data; (b) the extent to which the equivalent beam model can describe the building response; and (c) the reliability of the established strain-damage correlation.

While the displacement data from total station surveying and precise levelling are, in general, of high accuracy (with a point accuracy of 0.5mm to 1mm), their spatial resolution is extremely sparse. For example, on Crossrail, the number of available monitoring points on buildings is often limited to 3. Moreover, the widely adopted strain–damage correlation, as depicted in Figure 2.3b, is of a semi-empirical nature. Specifically, the lower bound of the 'slight' damage category, established by Burland and Wroth (1974), is based on the tensile strain causing visible cracking in walls and panels as observed during various masonry laboratory tests. The walls and panels tested varied in size, and one dataset concerning the testing of multiple 12 ft by 4 ft (3.66 m by 1.22 m) masonry walls was reported by Burhouse (1969). It is also important to note that the tensile strains related to visible cracking, as reported in Burland and Wroth (1974), show considerable scatter. Beyond this bound (the lower bound of the 'slight' damage category), the strain and damage correlations proposed by Boscardin and Cording (1989) are largely empirical. While these correlations align well with earlier angular distortion criteria derived for frame buildings presented in Skempton and MacDonald (1956), this observed agreement likely indicates that the associated strain values presented in Figure 2.3b incorporate a 'length' measure relative to building size.

Furthermore, experimental evaluations of the robustness of existing damage estimation approaches are limited. Giardina et al. (2012) and Laefer et al. (2011) investigated the displacement and damage pattern of masonry buildings subjected to excavation using a 1/10

scale masonry model (see Figure 2.4a for the model used in Giardina et al., 2012); however, these studies were limited to one specific type of building structure. Ritter et al. (2020) analysed the angular distortion and damage in six 3D-printed building specimens with varying building openings and tunnel eccentricity in a geotechnical centrifuge. The small length scale of these tests (1/75) (see Figure 2.4b) makes it challenging to evaluate currently used damage estimation techniques which relate crack width observations to strain estimates.



(a) (b)

Figure 2.4; (a) A 1/10 scale masonry model, as used in Giardina et al. (2012). Reproduced from Giardina et al. (2012); (b) A 1/75 scale 3D-printed building specimen, as used in Test A in Ritter et al. (2020). Reproduced from Ritter et al. (2020).

Overall, as reviewed above, for underground construction projects in urban environments, direct strain and crack monitoring on affected buildings are limited due to substantial installation requirements and the laborious nature of these tasks. In current practice, assessing damage to individual buildings often relies on interpreting building displacement data. However, given the limited spatial resolution of such data, coupled with uncertainties associated with the widely adopted equivalent beam model and the related strain-damage criteria, accurate damage assessment for buildings subjected to settlement becomes a particularly challenging task.

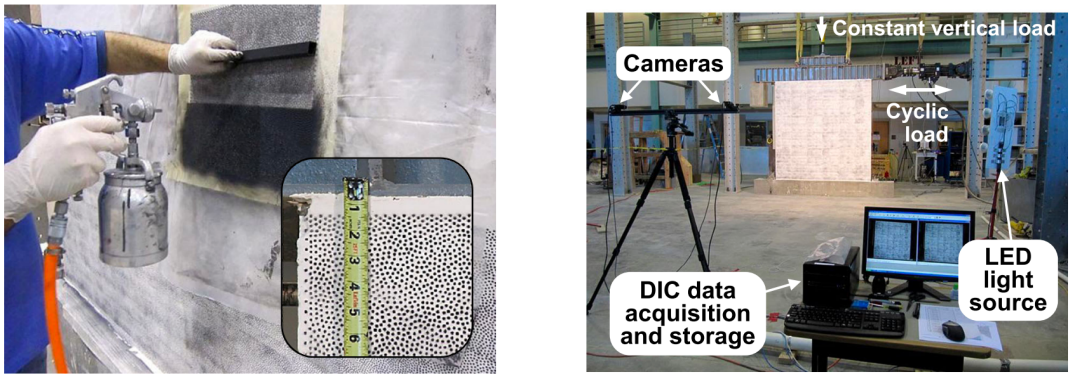
2.2. Imaged-based structural monitoring

A 2D image captured by a conventional digital camera represents a 2D projection of a 3D scene. Given the absence of depth information in 2D images, acquiring accurate measurements on a metric scale using such images often poses significant challenges.

Among all available techniques, Digital Image Correlation (DIC) is frequently regarded as a more established choice for precise displacement tracking (Pan, 2018). Furthermore, displacements obtained from DIC can be differentiated to yield full-field strain (Lava et al., 2010). Therefore, this section will primarily focus on reviewing the principles of DIC and exploring its applications for structural monitoring purposes.

2.2.1. Displacement monitoring

DIC employs one fixed camera to capture digital images from various stages, typically before and after deformation. Correlation is performed on 'features' within those images to identify displacements (Yoneyama, 2016). The surface of the object needs to have sufficient features that serve as carriers of displacement information. Such features may be naturally present or artificially added, for instance, by painting a random pattern or adding high-contrast targets. An example of speckle pattern preparation as used in Ghorbani et al. (2015) is shown in Figure 2.5a. The quality of DIC measurement strongly depends on the quality of features (Pan et al., 2009). Several studies have focused on optimising random pattern preparation (Bomarito et al., 2017; Hua et al., 2011; Sun and Pang, 2007). As a qualitative requirement, the pattern should be highly contrasted, stochastical and isotropic (Lionello and Cristofolini, 2014; Pan, 2018).



(a) (b)

Figure 2.5; (a) Speckle pattern spray-painted on the specimen surface, as used in Ghorbani et al. (2015); (b) DIC setup employed by Ghorbani et al. (2015) to investigate the response of three large confined masonry panels (approximately 2500 × 2500mm) under cyclic loads. Both figures reproduced from Ghorbani et al. (2015).

After capturing the image, the DIC method seeks to match the grey-level distribution of a subset of pixels from the reference image (before deformation) to the target image (after deformation) within the region of interest (ROI) on the monitored surface. Cross-correlation or sum-squared difference measures are used to evaluate the similarity between the subsets in the two states (Feng and Feng, 2018). The position of the subset in the target image is determined by the peak of the correlation coefficients. The difference between positions in the reference and target images represents the displacement of the centre of the subset.

Due to the discrete nature of grey-level values, the difference between positions in the reference and target images cannot detect displacements smaller than one pixel. For improved accuracy, an interpolation scheme is necessary to supply grey-level values between integer pixels, treating the grey-level value at the pixel as the value at the pixel's centre (Yoneyama, 2016). By assuming that neighbouring points in the reference subset remain as neighbours in the target subset, points surrounding the subset centre after deformation can be expressed through a displacement shape function, thereby modelling the displacement transformation. Consequently, the correlation coefficient evolves into a function of displacement and displacement gradient; thus, sub-pixel level displacement can be determined iteratively using various optimisation schemes. Under this setup, DIC accuracy could potentially achieve an accuracy of 0.1 pixels or 0.01mm (Acikgoz et al., 2018).

For a 2D DIC system to make accurate measurements, the surface of the monitored object needs to remain parallel to the camera's CCD sensor during loading; any out-of-plane displacement should be negligible. Moreover, the geometric distortion of the camera of the DIC system should be minimised or compensated for. 3D DIC systems operate, in general, with the same principles as described above, apart from requiring one additional

synchronised camera to provide depth information (through triangulation), to enable displacement tracking in 3D space.

DIC has been successfully applied as an accurate displacement monitoring technique for laboratory investigations, including large-scale testing. Ghorbani et al. (2015) investigated the response of three large confined masonry panels (approximately 2500 × 2500mm) under cyclic loads using a 3D DIC system in a laboratory. A speckle pattern was spray-painted onto the masonry surface, and LED light sources were used to ensure optimal lighting conditions. The displacement results from the 3D DIC system were subsequently compared to benchmark pointwise sensors (PWS), including linear potentiometers and linear displacement transducers installed on the specimen. The comparison demonstrated that the 3D DIC system could provide highly accurate displacement measurements on large-scale specimens. Similarly, Mojsilović and Salmanpour (2016) conducted a study on the deformation capacity of unreinforced masonry walls subjected to in-plane cyclic loading. In this research, the displacements of 10 large masonry specimens (up to 3600 × 2600 × 150mm), each with an applied speckle pattern, were monitored using 2D DIC. The displacement results from the DIC were validated by comparison with 24 installed Linear Variable Differential Transducers (LVDT) and 3 potentiometers. This validation suggested that the 2D DIC system was capable of submillimetre-level displacement measurement in a controlled laboratory environment.

A number of field applications of DIC on displacement monitoring have also been reported. Alhaddad (2016) employed 2D DIC to investigate the settlement profiles and convergence of two sections of the Royal Mail Tunnels and an escalator barrel subjected to new underground construction in London (SCL tunnelling and the construction of a passenger adit). Discrete bullseye-style DIC targets were attached to the tunnel lining to facilitate DIC tracking. The author observed that the convergence and settlement profile results (using

Radius of Curvature) from the 2D DIC were within 10% of those from conventional monitoring (mainly consisting of geodetic surveys using automatic total stations). However, it is worth noting that the DIC monitoring was conducted inside the tunnels, representing a more controlled environment than building monitoring settings, where light changes can be significant. Separately, Tian and Pan (2016) utilised a self-developed video deflectometer, which employed the DIC technique, to monitor the deflection of a section of the Wuhan Yangtze River Bridge in China at night. Six self-illuminating LED lamps were installed on the bridge section and used as targets. Given the oblique angle of the bridge surface to the camera's sensor, the distance between the camera and each target needed to be established using a laser range finder. Initially, the authors verified the accuracy of the video deflectometer by monitoring the LED targets installed on a motorised precision translation stage at varying distances at night. The results showed that at a target-camera distance of 300m, the mean error of measurement was 0.57mm with a standard deviation of 0.58mm. Subsequently, the authors demonstrated that the deflections determined from the deflectometer aligned with the theoretical deflection curve under known loads, although further validation of the field measurements was not provided. In other research, Acikgoz et al. (2018) conducted a case study using 2D DIC to monitor the dynamic response of a masonry railway viaduct in Leeds. Artificial targets with a bullseye-style pattern were installed on the structure, along with other appropriate setup measures to minimise potential tracking errors from the DIC. The comparison between DIC displacement results and the more accurate strain data from Fibre Bragg Grating (FBG) revealed that a significant portion of DIC error was due to out-of-plane displacement, which was subsequently accounted for using a correction method.

Overall, as reviewed above, Digital Image Correlation (DIC) is widely accepted as a reliable technique for displacement monitoring within a laboratory setting, offering accurate, non-

contact, full-field displacement measurements. DIC has also been successfully applied in various large-scale tests under controlled environments, where influences from ambient light, vibration, and out-of-plane movement (in the case of 2D DIC) are minimised. However, DIC typically requires artificial targets—either in the form of speckle patterns or physical high-contrast targets—to provide optimal tracking conditions, and its accuracy is dependent on environmental constraints. These factors considerably limit its field applications.

2.2.2. Strain and crack monitoring

Full-field displacements obtained from DIC can be numerically differentiated to obtain strain after smoothing (Pan et al., 2009). Strains derived from displacement monitoring are often used as indicators of the onset of cracking. Ghorbani et al. (2015) produced a series of crack maps for loaded confined masonry specimens. These maps were based on the maximum principal strain interpreted from the DIC measurements (see an example in Figure 2.6). They then validated the produced crack maps with final hand-drawn versions. Ghorbani et al. (2015) also showcased the potential of DIC for continuous monitoring of crack openings. Rajaram et al. (2017) employed 2D DIC to monitor full-field displacement of a one-storey building subjected to seismic loads. They successfully associated strain localisation patterns with the onset of wall cracking. The distinct strain localisations they observed aligned well with the damage identified during post-mortem visual inspections. Similarly, Howlader et al. (2021) used the maximum principal strain to locate cracks during laboratory experiments investigating the in-plane behaviour of unreinforced masonry (URM) walls containing openings. Once cracks are more widely opened, correlation becomes unfeasible as surface features cannot be matched across the crack. Quantifying such cracks often necessitates defining reference points on either side of the crack to measure relative displacements. For instance, Mirzazadeh et al. (2018) employed 2D DIC to measure the widths of cracks that formed on eight 4200 × 400 × 200 mm reinforced concrete beams.

These beams were subjected to both static and fatigue loading at various temperatures in a laboratory setting. They used a column of patches (64 by 64 pixels) on either side of the crack to measure the crack width.

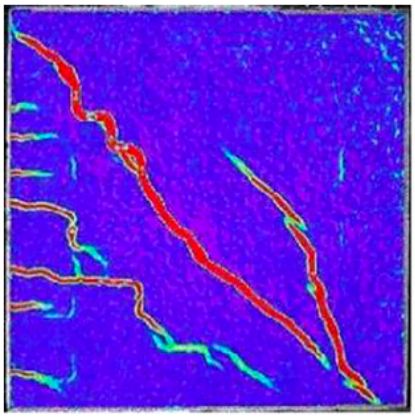


Figure 2.6; DIC maximum principal strain map at first crack developed on the masonry panel specimen SA-R. Red corresponds to +3000 μm/m. Reproduced from Ghorbani et al. (2015).

Alongside DIC, image-based crack detection algorithms utilising machine learning and deep learning techniques have also gained considerable popularity. In recent years, significant efforts have been undertaken to develop pixel-level crack image segmentation models to enhance detection accuracy (Li et al., 2022). Shi et al. (2016) proposed a crack detection algorithm known as 'CrackForest'. This algorithm first uses hand-crafted features to train a random structured forest. The trained forest then predicts structured tokens, representing preliminary crack classification results. These preliminary results are subsequently refined by a second classifier—a Support Vector Machine (SVM)—which provides a more robust and precise crack detection. The validation on the AigleRN dataset showed the proposed algorithm, combined with SVM, could achieve an F_1 score greater than 88%. Zou et al. (2019) proposed a deep neural network (DNN) based algorithm called 'DeepCrack' for automatic crack detection. The deep learning model learns high-level features of crack representation by fusing multiple-level features together through a tailored strategy. In their performance validation, detected cracks were compared to human annotations on a pixel

level. The DeepCrack algorithm was shown to outperform all other competing algorithms on multiple benchmark datasets, achieving an average F_1 score greater than 90%.



(a) (b)

Figure 2.7; (a) Detected cracks on a structured road surface. Reproduced from Zou et al. (2019); (b) Cracks on an unstructured masonry surface with varied brick shapes, colours, and textures. The entire surface, including mortar joints, displays inconsistencies, chips, and other imperfections, with signs of weathering, wear, and the presence of vegetation. Reproduced from Brackenbury (2022).

However, it is important to note that the above algorithms were trained and validated on road cracks, which represent a more structured surface. When applied to unstructured surfaces—for example, a tunnel surface with a layer of shotcrete and mesh—the F_1 scores of these algorithms dropped considerably to less than 60% due to the distinct crack-like texture and shadows caused by surface irregularities (Azhari, 2022). In the context of computer vision for crack identification, masonry surfaces are typically regarded as 'unstructured'. This is due to their variable laying patterns, diverse textures, and the presence of imperfections which can arise from weathering, wear, or even organic growth over time. To visually illustrate the distinction between the two, refer to Figure 2.7, which displays examples of cracks on both structured and unstructured surfaces.

Due to these additional challenges, research for crack detection on masonry surfaces yields less satisfactory results. Brackenbury (2022) developed a CNN-based classifier for detecting cracks on masonry walls. Nonetheless, this classifier tends to produce false positives, reflected in its F_1 score of around 60%. Moreover, as with many neural network-based algorithms, the classifier's performance deteriorates when handling surface conditions not

well-represented in the training dataset. Other works, such as those by Dais et al. (2021) and Loverdos and Sarhosis (2022), which employ a similar CNN architecture for crack detection on masonry surfaces, also display a notable over-reliance on having similar surface representations in their training data. A significant portion of the literature focuses on crack identification. However, for building monitoring applications, quantifying crack widths from images is equally essential. This task is challenging due to the necessity for 3D reconstruction. Even when 3D reconstruction is feasible, for instance, by using multiple images of a crack, the lighting conditions can heavily influence the accuracy of crack width measurements.

Overall, the strain-based crack detection feature of DIC not only provides an indication of crack opening but also offers vital information on the response leading to such damage. There are also reports of successful applications of DIC-based crack monitoring. Nevertheless, the majority of these successful applications were undertaken under strictly controlled laboratory conditions due to the aforementioned constraints.

Separately, as reviewed above, numerous machine learning and deep learning-based pixel-level crack detection algorithms have been developed in recent years, with many finding successful applications in their respective fields. However, it is the author's opinion that these algorithms tend to perform significantly better on structured flat surfaces (e.g. road surfaces, concrete surfaces) than on unstructured irregular ones (e.g. masonry surfaces). Furthermore, obtaining reliable metric measurements from detected crack clusters at the pixel level is a challenge due to the absence of depth information in 2D images. Additionally, since texture-based identification methods depend solely on available surface information without offering insights into displacements leading to crack initiation and progression, they tend to be less favoured from an engineering standpoint.

2.3. Point cloud-based structural monitoring

Point cloud data is a collection of 3D points that represent the external surfaces of a 3D scene. These data can be obtained using a laser scanner or reconstructed from 2D images. In the case of laser scanners, the time-of-flight or phase of the emitted laser beam is used to establish 3D coordinates of the scanned object. The intensity values of the returned signal and the colour of the object surface are also recorded. The efficient, remote, and contactless data acquisition process generates a dense point cloud rich in geometric information. Figure 2.8 shows an example of point cloud data of a building façade. Depending on the setup and external factors, the point accuracy of the point cloud, whether obtained from a laser or reconstructed using Structure from Motion (SfM) and Multi-view Stereo (MvS), is typically at the millimetre level. With terrestrial laser scans (TLS) within an appropriate range, accuracy can reach as high as one to two millimetres.

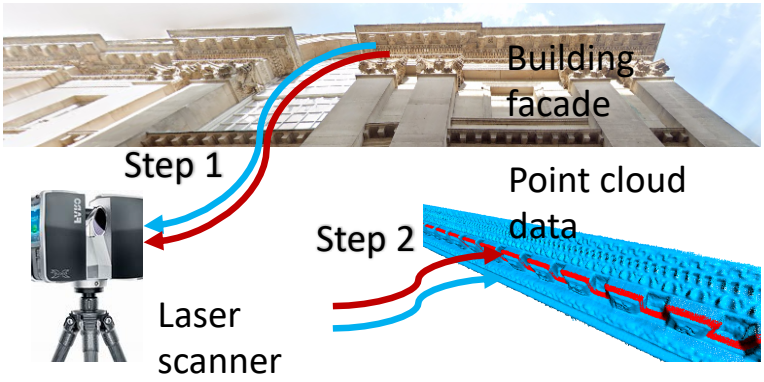


Figure 2.8; Acquisition of point cloud data of the building façade at Mansion House using a laser scanner. The details of the façade ornaments are preserved in the point cloud. Two scans, obtained at different states and shown as red and blue point clouds, are aligned together. For illustrative purposes, only part of the red point cloud is shown. The image of the Mansion House's east façade was extracted from Google Street View. The image of the Faro X330 laser scanner was obtained from image.bing.com under a Creative Commons license.

In the construction industry, it is common practice to use 3D point cloud data, especially from laser scans, to create as-built BIM models upon completion of construction (Wang and Kim, 2019). The data are also widely used for geometric inspection and construction progress tracking. However, the use of point cloud data, particularly unorganised point cloud data, for displacement monitoring is still in its infancy (Mukupa et al., 2017). The first part

of this section will review some recent applications. Conversely, owing to the rich geometric features contained in the point cloud, there have been efforts to use it for crack detection and monitoring. The second part of this section will review some of the representative cases.

2.3.1. Displacement monitoring

To conduct a displacement analysis of the object of interest, point clouds from different instances during a deformation event need to be collected. These collected clouds typically need to be transformed to a common coordinate system first. This is usually done through a rigid transformation using ground control points. Once the point clouds are aligned, the displacement analysis can be conducted by determining the distance between corresponding points in the point clouds. Simple schemes which estimate correspondence according to basic geometric approaches (namely, Cloud-to-Cloud (C2C), Cloud-to-Mesh (C2M), and Multiscale Model-to-Model Cloud Comparison (M3C2) methods) are reviewed below.

The C2C method establishes point correspondence between two point clouds based on the Euclidean distance between points. A point in the undeformed point cloud is matched with its nearest point in the deformed point cloud as a corresponding point pair. The displacement is calculated as the difference in coordinates between the two points. This method is the simplest and fastest for cloud comparison as it does not require calculating surface normals or meshing. However, the correspondence established by the closest point method lacks a physical basis, as displacements can occur in all directions. If the displacements are in the out-of-plane direction (e.g. oriented along the surface normal), the C2C method may give reasonable estimates. Even then, this method is sensitive to outlier measurements (Lague et al., 2013) and variations in point cloud density (Mukupa et al., 2017); these aspects may lead to erroneous displacement interpretations. Examples of the C2C method used for

displacement analysis in recent research related to structural health monitoring include studies by Jafari et al. (2017) and Gawronek et al. (2019).

Alternatively, the C2M method defines point displacement as the distance between a point in the undeformed point cloud and the nearest element of the mesh of the deformed point cloud along its surface normal. This method requires the meshing of the deformed cloud and searching for the nearest meshing element, which is computationally demanding. While this method is able to estimate out-of-plane displacements on flat surfaces (Lague et al., 2013), it cannot be used to predict in-plane displacements. Examples of the C2M method used for displacement analysis in recent research related to structural health monitoring include studies by Caudal et al. (2017) and Mugnai et al. (2019).

The M3C2 method involves selecting core points in the deformed cloud, constructing a cylinder through each core point, and calculating the average distance between points in both point clouds in the cylinder along a predefined direction. Generally, the predefined direction is the surface normal. In this case, the M3C2 method provides broadly equivalent results to C2C and C2M methods, but its averaging step employed reduces measurement noise. Accordingly, the M3C2 method is useful for determining out-of-plane displacements of flat surfaces. Furthermore, in-plane displacements of curved surfaces may influence out-of-plane displacement estimations in this method (Acikgoz et al., 2017). Examples of the M3C2 method used for displacement analysis related to structural health monitoring include studies by Jafari et al. (2017) and Acikgoz et al. (2017).

Cloud comparison-based approaches possess limited capability to capture displacement fields, as they assume point correspondence based on simplistic geometric rules that lack a physical basis. Researchers aimed to improve correspondences by using point cloud registration algorithms, which minimise the distance between undeformed and deformed point clouds. For instance, Teza et al. (2007) presented a piecewise Iterative Closest Point

(ICP) registration algorithm (called PAM, Piecewise Alignment Method) to investigate large landslide displacements using point cloud data. PAM estimates the rigid transformation of point cloud patches to reconstruct non-rigid displacement fields with piecewise rigid displacement estimations. The proposed algorithm achieved a total error of 3cm out of a 20cm annual mean displacement in one case study. Due to its piecewise rigid approach, the displacement field that PAM produces is not continuous and cannot be differentiated to estimate strains. Furthermore, the underlying ICP algorithm establishes correspondences based on nearest-point calculations. As a consequence, PAM is insensitive to in-plane displacements and therefore is not suitable to reconstruct in-plane tunnelling-induced displacements in buildings.

The optimal step N-ICP algorithm for surface registration (referred to as N-ICP algorithm) proposed by Amberg et al. (2007) is a non-rigid point cloud registration algorithm, which aims to find the best affine transformation for each vertex of a point cloud towards another point cloud under additional surface stiffness and landmark constraints. It has the potential to address issues with previously mentioned cloud comparison and PAM methods because: (a) the displacement of each vertex can be recovered by the non-rigid registration of two point clouds; (b) the number of degrees-of-freedom for each vertex and stiffness constraints are compatible with the physics of deformation; (c) with the additional landmark term, the algorithm has the mechanism to reveal in-plane deformation.

During an early stage of this DPhil project, Liu et al. (2022a) adapted the non-rigid ICP (N-ICP) based algorithm for displacement analysis and evaluated its theoretical accuracy on synthetic surface datasets subjected to various in-plane and out-of-plane displacements. The proposed algorithm outperformed C2C, C2M, and M3C2 in terms of interpreted displacements. Nonetheless, it is worth noting the optimisation function in the non-rigid registration-based approach penalises the difference in displacements between adjacent

points. As a result, the proposed method is inherently sensitive to point density and point accuracy.

Primitive shape fitting has also been employed for the displacement analysis of point clouds, with diverse application scenarios in the monitoring of bridges, dams, towers, and tunnels (Neuner et al., 2016). In this approach, point clouds are fitted to a selected primitive shape, such as a plane or curve, and the change in parameters of the fitted shape is used to determine the displacement. For example, Erdélyi et al. (2020) assessed the deflection of Liberty Bridge, Slovakia, using point cloud data collected from a TLS scanner. Segmented point clouds at discrete locations along the bottom of the bridge were fitted to a plane to infer deflection. While this approach provided plausible deflection profiles of the bridge, discrepancies of up to 4mm were observed at monitoring locations situated on the same section of the bridge. Additionally, the assumed primitive shape either does not allow for distortion or is not mechanically meaningful. Although the fitting process reduces some dependence on individual point accuracy, it is likely to obscure small genuine displacements. For this reason, the majority of applications of this approach are limited to relatively large displacements, or they require the point clouds to be further segmented to allow piecewise interpretation.

Overall, based on the preceding review, it is the author's opinion that both cloud comparison-based methods and registration-based methods tend to over-rely on point accuracy and point density. The adopted correspondence introduces further and often biased noise to the displacement results. On the other hand, methods using primitive fitting have shown some reduction in the aforementioned dependencies. However, such fitting does not allow the representation of the structure to deform in a kinematically meaningful way and is limited to large and semi-rigid deformation scenarios. Another point to note is that most reviewed point cloud-based algorithms only validated the displacement results at isolated

points. It is considered that a more comprehensive comparison using displacement results of comparable resolution and higher accuracy would be more suitable and appropriate. Despite the high redundancy of point cloud data, there have been no attempts to capture structural response using a more meaningful kinematic model. Moreover, there is a lack of research on utilising geometric features of point clouds for displacement analysis.

2.3.2. Strain and crack monitoring

The literature on point cloud-based crack detection and monitoring is relatively sparse compared to that on image-based methods. This is largely due to the additional challenges posed by gaps, noise, and irregularities from the scanning process often present in the surfaces represented by point clouds, compared to the more uniform surface representation provided by images.

On the other hand, the intensity data of point clouds from laser scans can sometimes aid crack detection (Stałowska et al., 2022). Zhong et al. (2020) proposed a crack detection and measurement algorithm for pavement cracks using point clouds collected from mobile laser scanners. The differential height and intensity of cracks relative to their neighbours were used for identification purposes. Identified cracks were also quantitatively evaluated for their width and length on their projected 2D image. The authors claimed the proposed algorithm was able to detect cracks of width 1cm and above. Xu and Yang (2019) presented a crack detection algorithm for identifying cracks on tunnel segment linings. In their work, the point cloud of the tunnel lining was projected and converted into 2D grey-scale images based on laser scan intensity. After applying a Gaussian filter to intensity values on the grey image to remove noise, cracks were extracted.

In addition to crack detection using laser intensity data, algorithms based on geometric properties of local surface regions have also been reported, where defects are represented as

deviations from ideal, smooth surfaces. Jovančević et al. (2017) published an algorithm for the detection of dents and scratches on aircraft bodies. In their work, the point cloud was first segmented into damaged and non-damaged regions using local normals and curvatures. The damaged regions were then projected onto a 2D image for further characterisation. The algorithm was shown to be able to detect defects generally larger than 1cm. Madrigal et al. (2017) proposed a damage detection routine based on the hand-crafted Model Point Feature Histogram (MPFH). MPFH is a 3D point descriptor representing the geometric characteristics of a local surface, assessed using fitted models instead of neighbouring points as in the Point Feature Histogram (PFH). The calculated MPFH was then classified into one of five primitives for defect identification.

Furthermore, methods of crack identification using combinations of geometric, intensity, and colour information have also been proposed and attempted for more challenging surfaces. Azhari (2022) developed a Deep Neural Network (DNN) to classify points from unstructured surfaces (e.g. rock cliffs and underground mine tunnels) into damaged or non-damaged regions. A Support Vector Machine (SVM) was then used to further characterise cracks in damaged regions. The author claimed the proposed algorithm outperformed the algorithm in Madrigal et al. (2017) and is able to reliably detect cracks wider than 5mm. However, the validation of the characterisation showed that the estimated crack width often contained large errors, especially with small cracks.

In general, most available crack detection algorithms using point cloud data only work effectively on structured surfaces, where noise is relatively limited, and defects can be determined based on their differences in geometric and/or intensity properties from the surrounding surface. The only exception is the work presented in Azari (2022), where an algorithm was proposed to handle unstructured surfaces. However, the reported crack

detection limit (5mm) and characterisation errors are too high for the purpose of the research described in this thesis.

Consistent with image-based crack detection methods, point cloud-based algorithms approach crack detection and measurement based on the principle of what you can see is what you can analyse. It is worth noting that based on the scanning position (distance to the object and incident angle), intensity and geometric features may become less effective (Laefer et al., 2014; Stałowska et al., 2022). Moreover, the detections and measurements were undertaken based on data representing only one particular state of the concerned object. While such treatment is standard in computer vision, from a structural perspective, modelling the emergence of a crack as distress resulting from underlying deformation featuring distinct kinematic motions on either side of the crack may provide an alternative and perhaps a better solution.

Overall, despite challenges inherent to point clouds, as reviewed above, progress has been made in identifying and quantifying cracks using scanned and reconstructed point clouds. However, it is the author's opinion that the quality of detection and characterisation relies heavily on the scanner's position and the characteristics of the object's surface. Changes in scanner-object distance and incident angle can considerably alter the feature signature of a crack. For small cracks, such changes may result in a crack being indistinguishable from the ambient surface. Similarly, a complex surface would also significantly compromise most algorithms' ability to detect cracks. Moreover, all the reviewed methods approached detection as a 'static' event based on available geometric and/or intensity information contained in one set of point cloud data for a particular moment. From a structural perspective, tracking the formation and propagation of a crack can be more useful.

2.4. Conclusion

For underground construction projects in urban environments, direct strain and crack monitoring on affected buildings are often limited, particularly on a large scale, due to substantial installation requirements and the labour-intensive nature of these tasks. In current practice, assessing damage to individual buildings is typically focussed on interpreting building displacement data with simple mechanical models such as equivalent beams. While these models have become an essential part of monitoring for masonry buildings subjected to settlement, they have not been rigorously validated.

It is evident that the challenges arising from direct strain and crack monitoring on buildings can be mitigated by using non-contact and full-field displacement measurement tools capable of estimating strain and tracking the development of cracks. The review presented in this chapter highlights computer vision techniques, employing both image and point cloud methods, that are potentially capable of providing full-field displacement measurements, estimating strains and quantifying cracks.

The literature reviewed in this chapter reveals that state-of-the-art full-field displacement measurements can be conducted with Digital Image Correlation (DIC). This technique can yield accurate displacement and strain fields, and track the development of cracks when monitoring distinctive surface patterns under constant lighting conditions and stationary camera positions. However, meeting these conditions is typically not feasible in a real project setting. Nevertheless, DIC offers a cutting-edge monitoring technique that can serve to validate new monitoring methodologies under controlled conditions.

On the other hand, laser scanning facilitates the capture of 3D point clouds of engineering structures. Owing to its user-friendly nature, swift and robust data collection, it is preferred in the construction industry over other point cloud generation methods, such as Structure

from Motion (SfM) and Multi-view Stereo (MvS). Laser scanning has minimal data collection prerequisites; there is no need for distinctive surface patterns, constant lighting conditions, or stationary scanner placement. The resulting point clouds, acquired non-intrusively, offer rich geometric data, holding potential for displacement, strain, and crack measurements.

Existing point cloud methods aiming to estimate full-field displacements (e.g. cloud comparison, and both rigid and non-rigid registration-based approaches) struggle to monitor in-plane displacements due to their heuristic approach to point correspondence. Since in-plane displacements play an essential role in strain and crack development, improvements must be made for effective building monitoring during underground construction. Methods based on feature matching might offer an alternative approach, where distinct geometric areas of the point cloud are matched to establish correspondence. Although the displacements derived from feature matching likely contain considerable noise, when combined with appropriate kinematic models, these models can provide additional constraints to refine the displacement field.

Existing research on detecting and measuring cracks using point clouds uses recognition techniques. However, crack detection is complicated by the unstructured masonry surfaces and measurement noise. Beyond detection, it is important for monitoring techniques to quantify the width of cracks. At present, state-of-the-art point cloud algorithms cannot achieve crack localisation and quantification with the required accuracy. However, the ability of DIC-based techniques to locate and quantify cracks from full-field displacements (either via strains or relative displacements) in controlled environments, suggests that a similar approach may be adopted for point cloud data. Such an approach may enable the tracking of the formation and propagation of cracks in field conditions.

3. Introduction to large-scale building settlement test

3.1. Purpose

A large-scale masonry building settlement test campaign, consisting of three half-scale building models with varying opening configurations, floor structures, and weight arrangements, was carried out as part of a collaborative research project. The tests were conducted at the Fibrobeton factory site in Duzce, Turkey, from December 2020 to March 2021. This project was a collaborative effort involving the University of Oxford, Istanbul Technical University, Izmir Institute of Technology, and Fibrobeton with additional financial support from Arup, the Engineering and Physical Sciences Research Council (EPSRC) and the Institution of Structural Engineers (IStructE). The specific role of the author of this thesis in this research project is detailed in Section 3.7. The project comprised several distinct research programs. Specifically, for the purpose of the research presented in this thesis, these tests aimed to: (a) address the scarcity of large-scale tests on masonry building models subjected to settlement; (b) collect high-quality displacement and cracking behaviour data using Digital Image Correlation (DIC); (c) evaluate equivalent beam based interpretation techniques, which have not been rigorously validated in previous research; (d) collect laser scan data to enable the development of innovative point cloud-based displacement, strain, and crack width monitoring techniques.

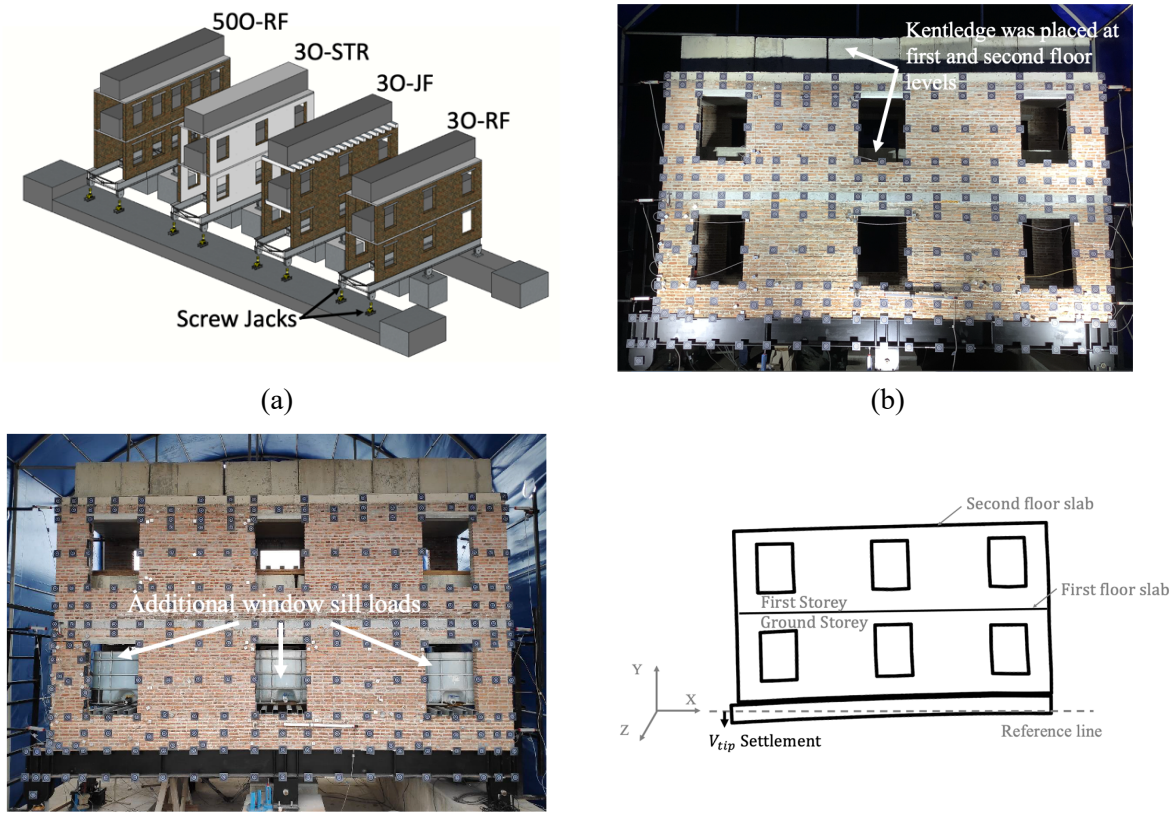
This chapter describes the setup, instrumentation, and implementation of the test campaign and discusses the damage sustained by the building models in each test. Additionally, it presents how the DIC measurements were validated. The work presented in this chapter includes portions of research which the author of this thesis personally contributed to Liu et al. (2022b) and Dalgic et al. (2023).

3.2. Building models

The tests comprise four L: 5.6m $\times W$: 3.2m building models, as shown in Figure 3.1a, with different window openings, weight arrangements and floor types. Each building model consists of two parallel façades constructed using brickwork and connected at first and second floor levels by either rigid reinforced concrete slabs or flexible joists simply supported on the façades. Kentledge was placed at first and second floor levels of the building models to simulate the in-situ stress level of prototype buildings at the model scale (referred to as W1 weight, as shown in Figure 3.1b). The influence of additional loads were also investigated. A test code is assigned to each test according to the number of window openings per floor (e.g. 50O stands for 5 and 0 openings on parallel façades), floor type (i.e. RF refers to rigid slab floor and JF refers to joist floor) and weight code (e.g. W3 refers to a load case with additional window sill loads, achieved by placing filled water tanks on window sills of ground storey through a temporary load distribution setup, as shown Figure 3.1c). The building models are specified in Table 3.1.

Table 3.1; Specification of the building models employed in the test campaign.

Building reference	Description
3O-RF	This building model comprises two similar masonry façades. At ground and first floor levels of each façade, there are three openings (signified by the code 3O). Reinforced concrete slabs (signified by code RF) were cast at first and second floor levels. The building was initially loaded with weight configuration W1 (3O-RF-W1) on 22 December 2020. Since this resulted in minimal damage the building was loaded with a different configuration of weights W3 and tested (3O-RF-W3) again on 28 January 2021.
3O-JF	This building model comprises two similar masonry façades with three openings (signified by the code 3O) at ground and first floor levels. Reinforced concrete joists (signified by code JF to denote 'joist floor') were placed at first and second floor levels. A single test 3O-JF-W1 was conducted on this building on 11 February 2021.
3O-STR	This building model was employed in a separate research activity and is not considered further.
50O-RF	This building model comprises two different masonry façades. One façade had five openings at ground and first floor levels and the other was plain masonry. Reinforced concrete slabs were cast at first and second floor levels. A single test 50O-RF-W1 was conducted on this building on 18 February 2021. Analysis of damage was confined to the façade containing the openings.



(a) (b)

(c) (d)

Figure 3.1; (a) Building models and test setup (after Dalgic et al. 2023). (b) Building model 3O-RF with W1 load arrangement: Kentledge was placed at first and second floor levels of the 3O-RF building model; (c) Building model 3O-RF with W3 load arrangement: In addition to kentledge placed at first and second floor levels of the 3O-RF building model, water tanks were placed on window sills of the ground storey; (d) Schematic of 3O-RF building model under an induced beam tip settlement V_{tip}. The X, Y, Z coordinate system is shown in relation to the building model.

3.3. Test procedure

To conduct a test, downward displacements (referred to as beam tip settlement, V_{tip}, see Figure 3.1d) were applied to the beams supporting the building models by simultaneously pulling down the manual screw jacks at the end of both beams (see Figure 3.1a). This caused the beams to deform in a way that mimics the hogging region of a Gaussian tunnel-induced settlement trough. The beam tip settlement was applied in multiple stages, normally in an increment of 10mm. Once the target beam tip settlement was reached, the test was held for visual damage observations. At the end of each test (i.e. when the building is subjected to the maximum displacement applied in the test) the façade was inspected for damage and visible cracks were recorded. For each individual crack a procedure was conducted in which

the development of crack width was retrieved retrospectively by calculating the relative displacement between DIC targets orthogonal to the crack (see Section 3.4.1).

3.4. Instrumentation details

The deformation of the building models was primarily monitored using a 2D DIC system from Imetrum. One façade of each building model was installed with measurement targets (referred to as the front wall façade, as shown in Figure 3.2a). The displacements of these targets were continuously tracked using a digital image correlation (DIC) system. A typical camera arrangement is depicted in Figure 3.2a.

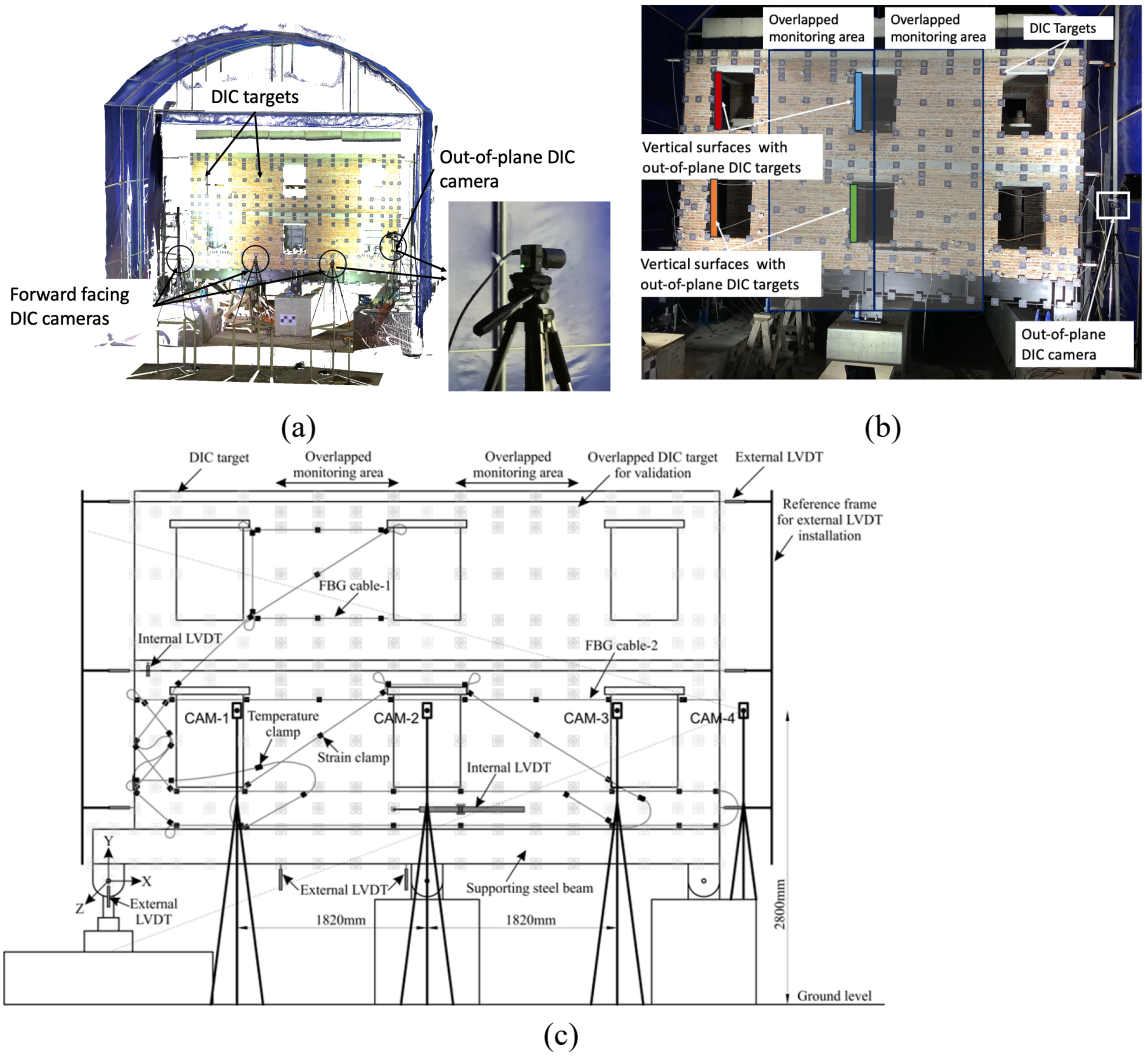


Figure 3.2; (a) A typical camera arrangement for a building model, constructed using laser scan point cloud collected for 3O-RF building model; (b) Arrangements of DIC targets and illustration of overlapped monitoring areas for 3O-RF building model. Vertical surfaces of windows attached with out-of-plane DIC targets and the position of the out-of-plane DIC camera are highlighted and labelled; (c) Key aspects of instrumentation of front wall façade of 3O-RF building model. Reproduced from Dalgic et al. (2023).

Additionally, laser scans of the front wall were conducted before and at the conclusion of each test. Linear Variable Differential Transformers (LVDTs) and Fibre Bragg Grating (FBG) sensors were also employed, but their use was primarily for separate research purposes. They will only be used to validate the DIC measurements in this thesis in Section 3.5.4.

3.4.1. 2D DIC system

In the test campaign, a typical 2D DIC setup comprises three forward-facing GigE cameras, one out-of-plane GigE camera (see Figure 3.2c), and a controller that records and processes all video images. The controller employs 2D DIC techniques to track features in the video images and outputs displacements of the tracked features. All cameras remained fixed in position throughout each test, secured by tripods (in the case of forward-facing cameras, elevated to 2.8m above surface level using a custom-made heavy-duty steel stand to optimise the field of view). The cameras were equipped with a 1/1.2-inch sensor and a 12mm lens. The forward-facing cameras were typically situated approximately 6m from the front façade and 1.85m apart, while the out-of-plane camera was positioned at around 1m from the façade. With the exception of the 3O-JF building model, the image planes of all forward-facing cameras were aligned with the vertical façade plane, enabling tracking of in-plane displacements (referred to as *u*, *v* displacements, corresponding to X and Y directions, see Figure 3.1b) through a simple scale factor calibration. Conversely, the out-of-plane camera had its image plane perpendicular to the façade plane, measuring movement perpendicular to the X-Y plane (referred to as *w* displacement, corresponding to Z direction, see Figure 3.1b). Due to site constraints, the 3O-JF building model necessitated the placement of forward-facing cameras inside an adjacent building model (3O-STR) and their monitoring through the ground floor windows. As a result, the forward-facing cameras were positioned

at an angle to the façade plane to minimise obstructions caused by walls. All cameras were set to have a sampling frequency of 50 Hz.

To enhance tracking performance, discrete DIC targets were fixed to the façade wall using a fast-setting grab adhesive. These DIC targets exhibit high-contrast bullseye-style patterns and have dimensions of 100mm by 100mm, corresponding to a minimum pixel area of 40 by 40 in the camera sensor. Figure 3.2b illustrates a typical arrangement of DIC targets. Generally, more than 200 DIC targets were employed for tracking in-plane displacements of the front wall façade and supporting steel beam, arranged in an approximately regular grid. Additional DIC targets were fixed to the vertical surfaces of ground floor and first floor windows (see Figure 3.2b). Local adjustments were made to avoid interference with FBG cables and LVDTs. Within this configuration, more than 100 in-plane targets were monitored by multiple cameras (referred to as 'overlapped monitoring area' in Figure 3.2b-c). This redundancy in the measurements was exploited to verify the consistency of the data.

To mitigate the influence of ambient light on the 2D DIC system, an industrial tent was erected to shield each building model. Dimmable LED lights were installed in front of the façade during each test to regulate the lighting conditions.

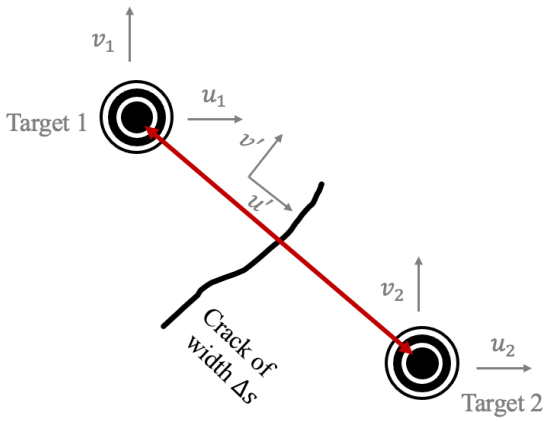


Figure 3.3; Arrangement employed for the 'virtual LVDT'. Two targets spanning a crack are selected to estimate the crack width. The red double arrow line indicates the 'virtual LVDT' that spans the crack. The measured displacements of Target 1 and Target 2 are (u_1, v_1) and (u_2, v_2), respectively. The coordinate system defined by the 'virtual LVDT' is u', v'.

On completion of each test, a thorough examination and mapping of the visible cracks that manifested on the building model were conducted. Along each crack, a series of DIC target pairs were established, perpendicular to its orientation, creating what is referred to 'virtual Linear Variable Differential Transformers (vLVDT)' (refer to Figure 3.3). The crack width Δs is estimated using the measured displacements of Target 1 (u_1, v_1) and at Target 2 (u_2, v_2) to calculate the relative displacement along u', defined by the relative position of Target 1 and Target 2.

Positive values of Δs were taken to indicate a single crack of width Δs between the location of the two targets.

3.4.2. Terrestrial laser scan system

For each test, laser scan point cloud data of the front wall façade were acquired using a FARO Focus S70 scanner both before and after inducing settlement. The scanner was positioned on a tripod, typically situated between the forward-facing DIC cameras and the front wall façade. To simulate a relaxed monitoring condition, the scanner's position was not fixed but generally faced the central section of the façade, maintaining a distance of approximately 3m from it (except 3O-JF-W1 due to space constraints from the adjacent building model). Figure 3.4a shows a typical setup of the scanner for monitoring of the front wall façade. An outdoor HDR scan profile was employed for all scans, with the built-in inclinometer activated. For monitoring purposes, only these central scans were considered. In certain tests, additional scans were conducted from different locations to generate 3D models of the buildings (refer to Figure 3.4b).

Within each test, five checkerboard targets were used to facilitate the initial registration of scans to the same coordinate system using rigid transformation. Three checkerboard targets were typically positioned on the concrete footings adjacent to the façade (see Figure 3.4b),

arranged in a distinctive three-dimensional configuration, while two additional targets were placed on fixed objects elsewhere. The checkerboard targets were positioned at different heights to minimise initial registration errors.



(a) (b)

Figure 3.4; (a) A Faro Laser scanner mounted on a tripod, positioned in front of the 3O-RF building model, illustrating a standard scanning setup; (b) 3D model of the 3O-JF building model constructed from 4 separate scans, with annotation indicating a checkerboard fixed on the concrete footing.

3.5. Export and validation of DIC displacement data

3.5.1. Export of displacement data from video files

The video files collected for each test were first processed using the Video Gauge software developed by Imetrum. To obtain in-plane measurements, a coordinate frame corresponding to the front wall façade was established. Subsequently, a virtual target representing each DIC target was defined within the Video Gauge software. A single scaling factor was determined based on the distance between the camera and the façade. For out-of-plane measurements, it was necessary to use multiple parallel coordinate frames to accommodate the varying distances between the out-of-plane DIC targets, which were attached to different windows, and the out-of-plane camera. In cases where DIC targets were monitored by two adjacent cameras, two virtual targets were defined in Video Gauge, allowing for separate displacement outputs. The Video Gauge software, utilising DIC techniques, then tracked the

movement of each defined virtual target and generated displacement outputs for each time increment (usually 0.02s) throughout the duration of each test.

3.5.2. Evaluation of out-of-plane displacements

When the deformation of the structural surface is planar, under ideal lighting conditions and with cameras free from vibration, 2D DIC has the potential to achieve a measurement accuracy of down to 0.01mm (Acikgoz et al., 2018). The out-of-plane camera was positioned, with its image plane perpendicular to the front wall façade (see Figure 3.2b-c, the out-of-plane camera is labelled as 'CAM-4' in Figure 3.2c), to capture any out-of-plane deformations of the building model. It should be noted that as beam tip settlement is introduced, the out-of-plane targets attached to windows experience movement, which, from the perspective of the fourth camera ('CAM-4'), can be interpreted as out-of-plane motion. Consequently, only the targets fixed to the central windows on the ground floor (the vertical surface shown in Figure 3.2b with green highlight) are considered reliable for estimating the out-of-plane motion of the front wall façade, as the influence from induced settlement movement is expected to be minimal at this place.

Table 3.2; Summary of maximum out-of-plane displacements and its direction of the front wall façade across all tests at 25mm induced beam tip settlement.

Test	Out-of-plane displacement (mm)	Direction (Towards / away from forward-facing cameras)
3O-RF-W1	0.81	Towards
3O-RF-W3	2.86	Towards
5O-RF-W1	0.30	Away from
3O-JF-W1	2.08	Towards

As shown in Table 3.2, across all building models, the maximum measured out-of-plane displacement remained below 2.86mm for a nominal 25mm induced beam tip settlement. By applying established procedures for assessing out-of-plane translations on 2D DIC measurements, as outlined in Sutton et al. (2008), it is found that this maximum out-of-plane displacement corresponds to a maximum potential error in in-plane measurements of less than 0.5mm. Given the small magnitude of this potential error, which represents a worst-

case scenario, compensations for in-plane displacements arising from out-of-plane movements are considered unnecessary.

3.5.3. Assessment of DIC in-plane measurement errors

All tests, with the exception of 3O-JF-W1, involve a significant number of targets monitored simultaneously by two forward-facing cameras. These targets are positioned within the overlapping fields of view of two adjacent cameras (referred to as the 'Overlapped monitoring area' in Figure 3.2b) and, under ideal conditions, are expected to yield consistent displacement results. Therefore, any discrepancies observed in the displacement measurements serve as indicators of DIC measurement errors. However, due to site constraints and the resulting angled camera arrangement, test 3O-JF-W1 has a considerably smaller overlapped monitoring area (only 6 targets monitored by two adjacent cameras compared to over 100 in all other tests) and is therefore excluded from the assessment presented here.

Table 3.3; Summary of evaluated DIC measurement errors. The evaluation is conducted by comparing displacement measurements of targets monitored by two cameras at an applied beam tip settlement of 25mm. In each test, the median and maximum absolute deviations are reported for the X and Y directions (denoted as *u* and *v* displacements, respectively). This table, along with the associated analysis, was originally published in Dalgic et al. (2023) and created by the author of this thesis.

Test	Median Absolute Deviation in *u* (mm)	Maximum Absolute Deviation in *u* (mm)	Median Absolute Deviation in *v* (mm)	Maximum Absolute Deviation in *v* (mm)
3O-RF-W1	0.188	0.402	0.231	0.883
3O-RF-W3	0.193	0.703	0.106	0.469
50O-RF-W1	0.139	1.199	0.127	0.624

To conduct a systematic assessment, a beam tip settlement of 25mm is selected, as it closely approximates the maximum settlement achieved in all tests. For all targets being monitored by two adjacent cameras in each test, the absolute deviations of displacement measurements in the X and Y directions are derived by comparing measurements from one camera to those from another when the beam tip settlement reaches 25mm. Subsequently, the median and maximum absolute deviations are determined by calculating the median and maximum

values from the absolute deviations, respectively. The results for all tests are summarised in Table 3.3.

In Table 3.3, as anticipated, all median absolute deviations—reported across three different tests and in both the X and Y directions—are small. The highest median absolute deviation is less than 0.231mm, indicating the high quality of the data. Moreover, these values are significantly smaller than the potential errors from out-of-plane movements, as estimated in Section 3.5.2. This suggests that the out-of-plane movements of the facade have a negligible impact on errors in the in-plane displacement measurements. It is important to note that the DIC data used in the assessments in Table 3.3 have not been subjected to temporal or spatial smoothing. Therefore, the reported median absolute deviations largely reflect the influence of measurement noise, which is anticipated to be around 0.2mm. On the other hand, while the maximum absolute deviations represent measurement outliers, the fact that the majority are under 1mm further underscores the quality of the measurements.

3.5.4. Cross-validation with FBG and LVDT

The deployment of FBG and LVDTs provides an opportunity to further validate the DIC displacement measurements. In the tests, the LVDT data were not recorded with UTC (Coordinated Universal Time) timestamps, necessitating back-calculation of UTC timestamps based on file metadata and the sampling frequency. On the other hand, FBG measures strain, not displacements. Therefore, to enable a comparison between FBG and DIC, two DIC targets adjacent to FBG clamps are required.

Figure 3.5a shows that two LVDTs were placed next to two DIC targets fixed to the supporting beam during 3O-RF-W1, with their respective LVDT and DIC target identification numbers labelled accordingly. Figure 3.5b compares the vertical displacement time history of these two LVDT and DIC pairs. The results show good agreement between

the measurements from the DIC and LVDT. However, due to a technical fault that caused the LVDT controller to crash, the LVDT records were lost just before maximum settlement was reached.

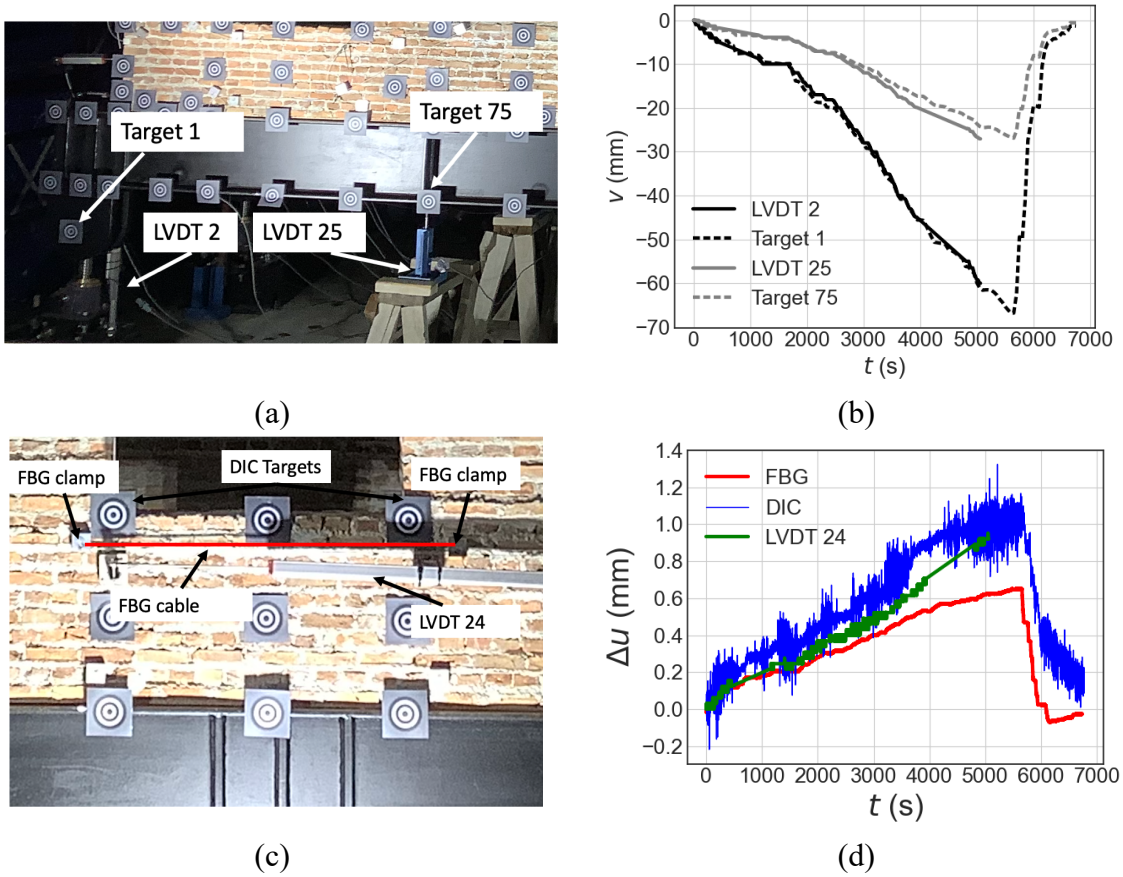


Figure 3.5; (a) Selection of two DIC targets and LVDT pairs for cross-validation of DIC measurements during 3O-RF-W1. The identification numbers of the selected DIC targets and LVDTs are labelled accordingly; (b) Comparison of time histories of vertical displacements at two DIC target locations with those from LVDTs. The X-axis represents elapsed DIC recording time (t) in seconds. This figure, along with associated analysis, was originally published in Dalgic et al. (2023) and created by the author of this thesis; (c) Selection of two DIC targets, a section of FBG cable, and an LVDT (LVDT 24) for cross-validation of DIC measurements during 3O-RF-W1; (d) Comparison of time histories of relative horizontal displacements between two identified DIC pairs with FBG and LVDT (LVDT 24). This figure, along with the associated analysis, was originally published in Dalgic et al. (2023) and created by the author of this thesis.

Figure 3.5c depicts the instrumentation arrangement on the upper part of the middle spandrel on the ground storey for 3O-RF-W1. This arrangement consists of two DIC targets, a section of FBG cable, and a nearby LVDT. Figure 3.5d compares the relative horizontal displacements of two DIC targets fixed to the window corners with results from FBG and LVDT. The distance between the two FBG clamps was 0.78m. For very small relative displacements, the results from DIC, FBG, and LVDT are largely consistent. Although the

DIC time history in Figure 3.5d appears to be considerably noisier than both FBG and LVDT, its magnitude is still small. Furthermore, a vertical crack was observed at the upper part of the spandrel at maximum settlement (around 5800s elapsed time, as shown in Figure 3.5d). Manual crack width measurements taken with a crack ruler were also consistent with the DIC measurements.

These comparisons provide additional assurance regarding the quality of the DIC measurements.

3.5.5. Validation of virtual LVDT results

Manual crack measurements were conducted on 3O-RF-W1, 3O-RF-W3, and 50O-RF-W1 as part of the standard damage record for building models. Mimicking industry standards for crack measurement, Avongard crack rulers were employed, featuring graduations at 0.05mm intervals from 0.1mm to 1mm, and at 0.5mm intervals from 1mm to 7mm. These manual measurements were conducted after reaching the maximum beam tip settlement and before unloading. The data collected are utilised in this section to supplement the quality assurance of the crack width measurements derived from the virtual LVDTs (vLVDT) from the DIC.

Most tests were conducted late at night; hence, building models were typically ‘held’ in place at the maximum beam tip settlement to facilitate manual crack measurements in daylight. Among all conducted tests, 3O-RF-W1 exhibited one small crack in the middle spandrel on the ground storey at the maximum beam tip settlement, measured at 1mm by crack ruler, as discussed in Section 3.5.4. Consequently, this test will not be considered here for the validation of the virtual LVDT results.

Conversely, 3O-JF-W1 exhibited very severe cracks on the first storey, exceeding the measurement range of the Avongard crack rulers. Moreover, the very severe damage

observed on the building model led to a partial collapse of the top lintel. Given the severity of the damage, manual crack measurements were not in this case performed due to health and safety considerations.

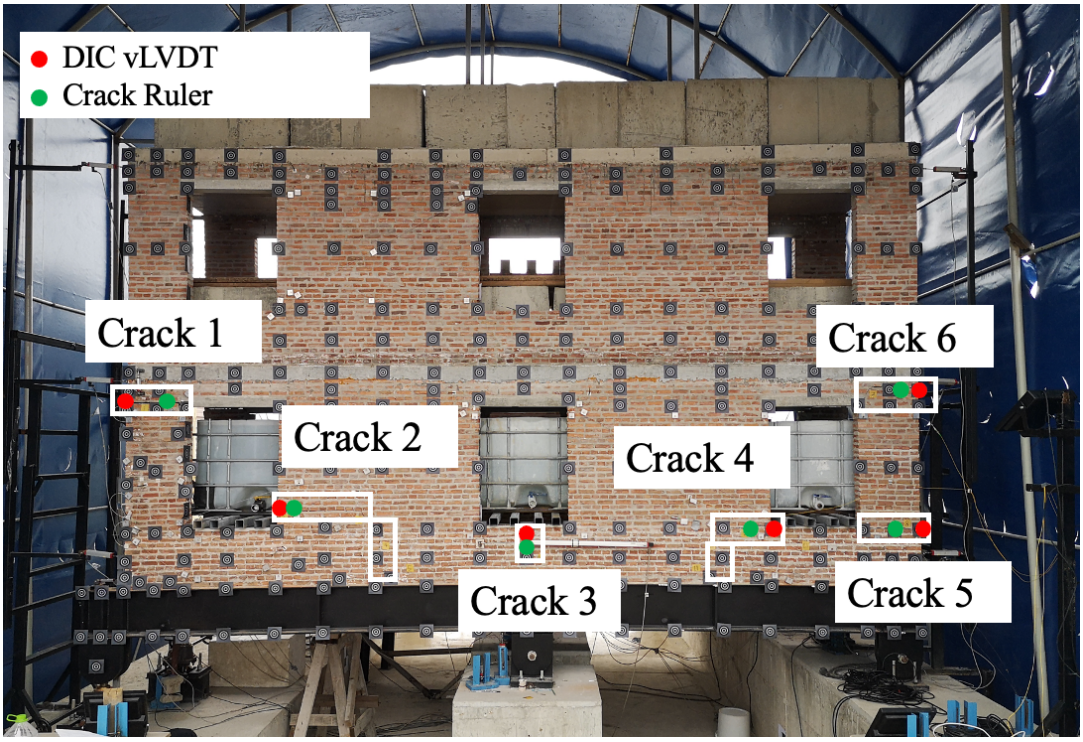
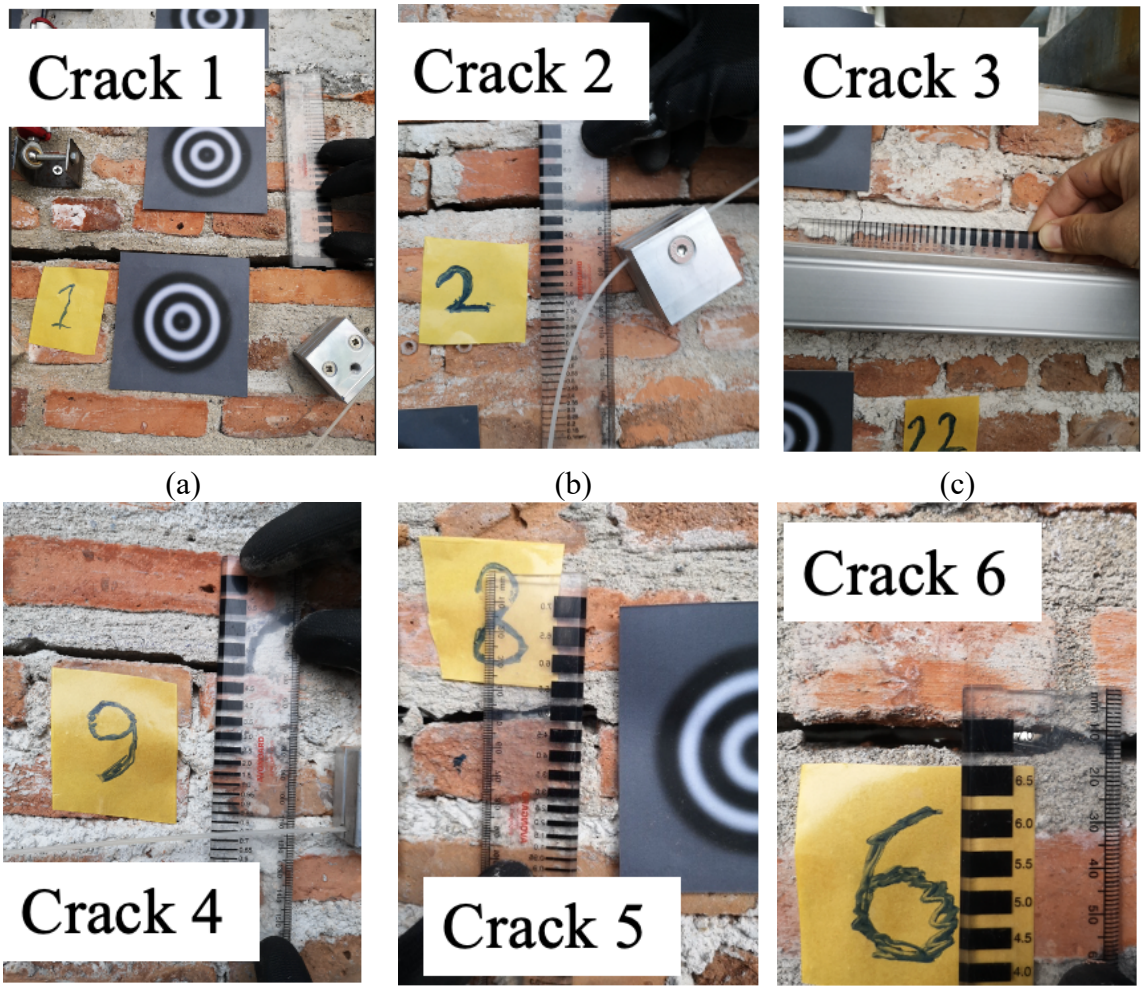


Figure 3.6; Indicative locations of all observed cracks for 3O-RF-W3 at the maximum beam tip settlement. The red and green dots indicate the locations where maximum crack widths were observed for each individual crack, using the virtual LDVT and crack ruler, respectively. Original photo courtesy of Korhan Dalgic and Burcu Gulen.

Figure 3.6 depicts the indicative locations of the observed cracks for 3O-RF-W3 at the maximum beam tip settlement. It is worth noting that the photos in Figure 3.6 and Figure 3.7 were taken during the morning after the day of the test. Crack 6, not observed when the loading reached maximum beam tip settlement during the test, developed into a full split between the spandrel and the masonry unit above. Consequently, the development of Crack 6 after the maximum beam tip settlement was reached was not captured in either the DIC or the laser scan.



(a) (b) (c)

(d) (e) (f)

Figure 3.7; Crack ruler reading for each individual crack on 3O-RF-W3. (a) Crack 1; (b) Crack 2; (c) Crack 3; (d) Crack 4; (e) Crack 5; (f) Crack 6. Original photos courtesy of Korhan Dalgic and Burcu Gulen.

For each crack, multiple measurements using virtual LVDTs and crack ruler were performed along the identified crack paths. In Figure 3.6, the red and green dots indicate the locations where maximum crack widths were observed for each individual crack using the virtual LVDT and crack ruler, respectively. In Cracks 1, 4, and 5, noticeable discrepancies exist between the locations where maximum crack widths are identified by the virtual LVDT and by manual measurement.

Figure 3.7 presents the crack ruler readings at the locations where the maximum crack width was observed for each individual crack on 3O-RF-W3. All cracks observed on 3O-RF-W3 occurred at the brick-mortar interface. Unsurprisingly, these cracks featured uneven crack edges, posing particular challenges for measuring the width.

Table 3.4; Comparison of maximum crack widths determined by virtual LVDT of DIC and crack ruler for all cracks on 3O-RF-W3.

	Maximum crack width – DIC (mm)	Maximum crack width – Crack ruler(mm)
Crack 1	8.03	10
Crack 2	4.24	5
Crack 3	0.64	0.5
Crack 4	3.79	5
Crack 5	6.55	5
Crack 6	1.22	7

Table 3.4 compares the maximum crack widths for all cracks on 3O-RF-W3 as determined by the virtual LVDT of DIC and by crack ruler. With the exception of Crack 6, the results are consistent. In Cracks 1, 4, and 5, discrepancies in the measured crack widths are slightly larger than others. This may be a result of differences in the locations where the virtual LVDT and manual measurements were taken. The substantial difference in measured crack widths for Crack 6 can be attributed to the absence of recorded data from the DIC when the crack developed during the holding period overnight.

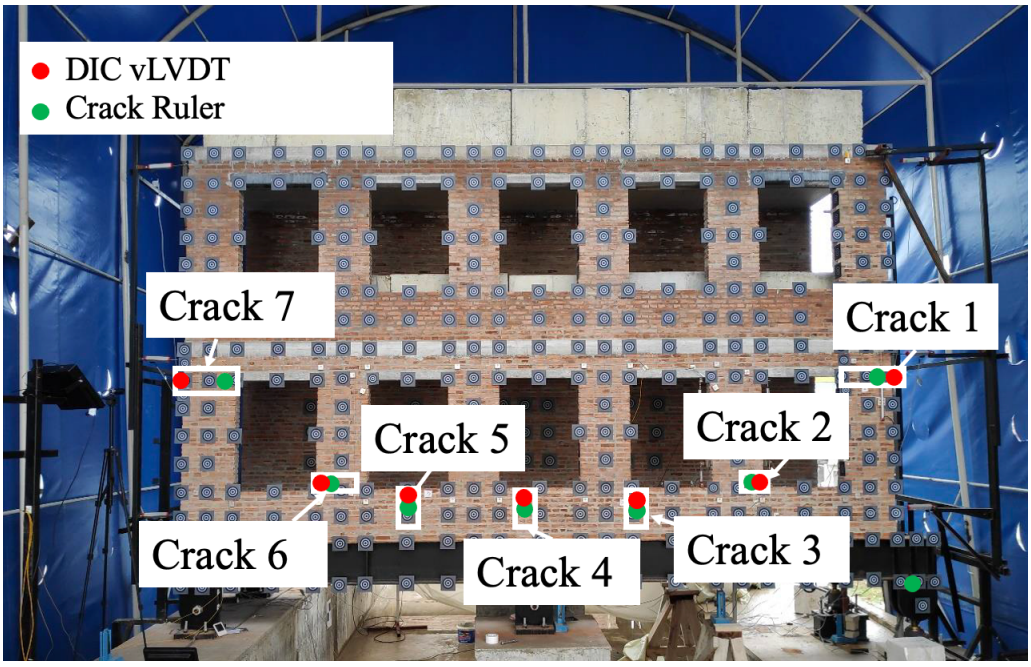


Figure 3.8; Indicative locations of all observed cracks for 50O-RF-W1 at the maximum beam tip settlement. The red and green dots indicate the locations where maximum crack widths were observed for each individual crack, using the virtual LDVT and crack ruler, respectively. Original photo courtesy of Korhan Dalgic and Burcu Gulen.

Figure 3.8 illustrates the indicative locations of all observed cracks for 50O-RF-W1 at maximum beam tip settlement. As with 3O-RF-W3, the photo in Figure 3.8 was taken the

morning after the test. However, unlike 3O-RF-W3, no further development of existing cracks was observed during the holding period. Due to the shorter crack lengths compared to those observed on 3O-RF-W3, only one manual measurement was taken for each crack. As demonstrated in Figure 3.8, with the exception of Crack 7, the locations where manual measurements were taken for each crack largely align with the locations where the virtual LVDT returned the maximum crack width.

Figure 3.9 presents the crack ruler readings for each individual crack on 50O-RF-W1. In comparison to the cracks observed on 3O-RF-W3, the cracks on 50O-RF-W1 are generally narrower, allowing for more reliable manual measurements with less interference from uneven crack edges. Unlike the cracks on 3O-RF-W3, which only went through the brick-mortar interface, Cracks 4 and 5 on 50O-RF-W1 involved cracking of the masonry units themselves.

Table 3.5; Comparison of maximum crack widths determined by virtual LVDT of DIC and crack ruler for all cracks on 50O-RF-W1.

	Maximum crack width – DIC (mm)	Maximum crack width – Crack ruler(mm)
Crack 1	4.10	5
Crack 2	1.93	2
Crack 3	1.27	0.85
Crack 4	0.81	1
Crack 5	1.90	2
Crack 6	3.03	2
Crack 7	5.94	5

Table 3.5 compares the maximum crack widths for all cracks on 50O-RF-W1 as determined by the virtual LVDT of DIC and by crack rulers. The results again show good agreement, even for sub-millimetre cracks.

Overall, the consistent results between the virtual LVDT of DIC and manual measurements using crack ruler further substantiate the reliability of the DIC measurements and the virtual LVDT setup. Perhaps more crucially, compared to manual crack measurement—which could only be performed at discrete stages (in this test campaign, only at the maximum beam tip settlement)—the virtual LVDT enables continuous tracking of crack formation and

propagation. Therefore, for the remainder of this thesis, crack measurements from the virtual LVDT of DIC will be utilised to quantify crack width in the damage assessment of building models, unless explicitly stated otherwise.

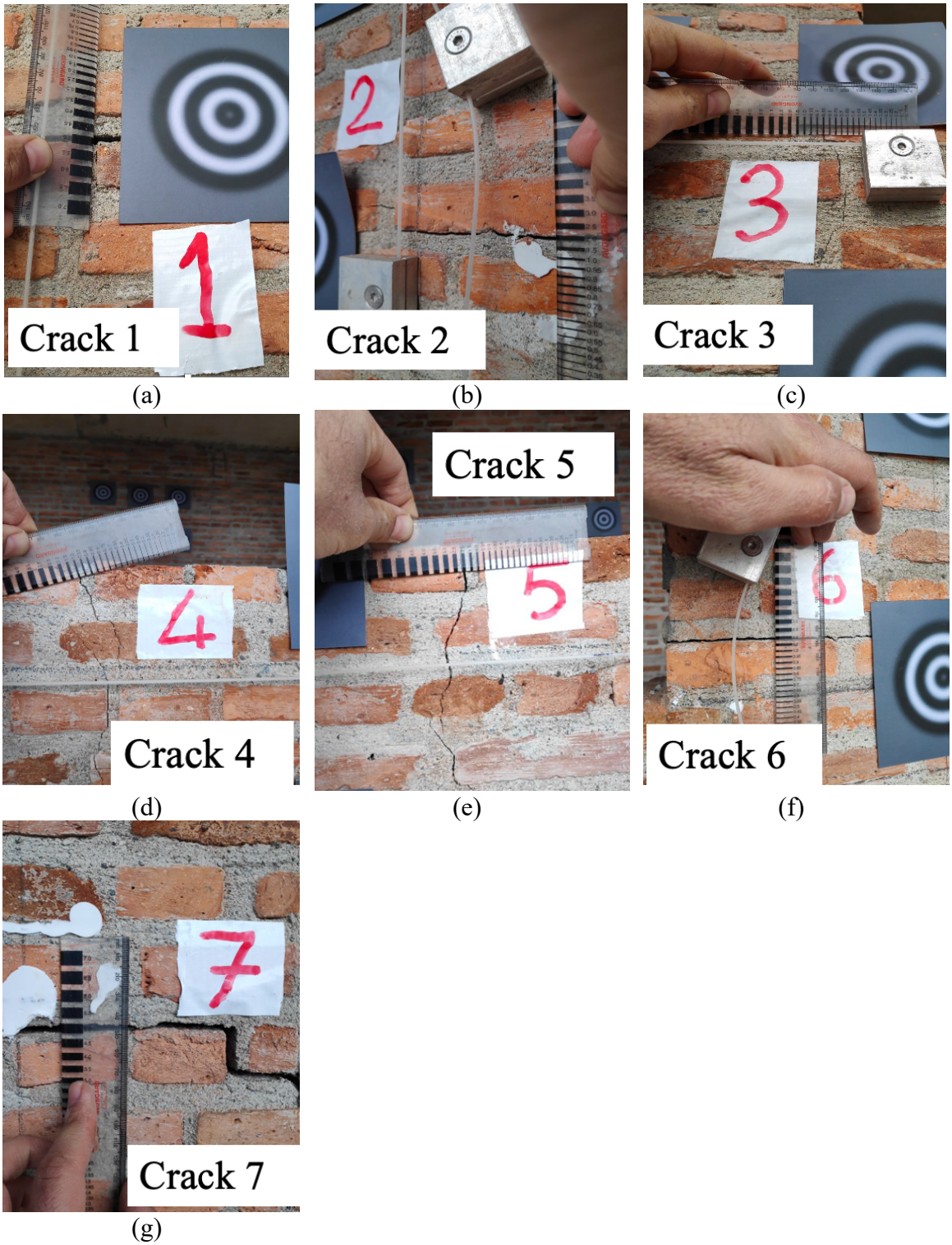


Figure 3.9; Crack ruler reading for each individual crack on 50O-RF-W1. (a) Crack 1; (b) Crack 2; (c) Crack 3; (d) Crack 4; (e) Crack 5; (f) Crack 6; (g) Crack 7; Original photos courtesy of Korhan Dalgic and Burcu Gulen.

3.6. Damage assessment of building models

Damage induced in the building is characterised by the width of cracks that develop in the masonry as the test progressed. Consistent with current industry practice, damage is quantified in terms of a 'damage category' that relates to the width of the widest crack that developed in the building. In the current work the Burland et al. (1977) correlation between crack width and damage category is employed; this correlation is indicated in the leftmost three columns of Table 3.6. Negligible and very slight damage categories are not differentiated in current work (i.e. damage less severe than 'slight' category is indiscriminately labelled as 'negligible'), as such implementation requires significantly more accurate crack measurement and is of little practical significance.

Table 3.6; Damage correlations based on data from Burland et al.(1977) and Boscardin and Cording (1989)

Damage category	Severity	Crack width	Equivalent crack width for half-scale tests	Limiting tensile strain
1	Negligible	Up to 1mm	Up to 0.5 mm	0.05-0.075
2	Slight	Up to 5 mm	Up to 2.5mm	0.075-0.15
3	Moderate	Between 5mm and 15mm or several greater than 3mm	Between 2.5mm and 7.5mm or several greater than 1.5mm	0.15-0.3
4	Severe	15mm to 25 mm	7.5mm to 12.5mm	Greater than 0.3
5	Very severe	Greater than 25mm	Greater than 12.5mm	

Given the one-half geometric scale used in the tests, the crack widths corresponding to the various damage categories are half of their prototype values and are recorded in the fourth column of Table 3.6. This treatment aligns with the principles discussed by Laefer et al. (2011) and Giardina et al. (2012). For a more detailed discussion on the scaling factor applied in the current test campaign, refer to Dalgic et al. (2023). Accordingly, Table 3.7 records the beam tip settlement when the building model first enters a specific damage category based on the width of the observed cracks. Maximum beam tip settlement is also reported in this table.

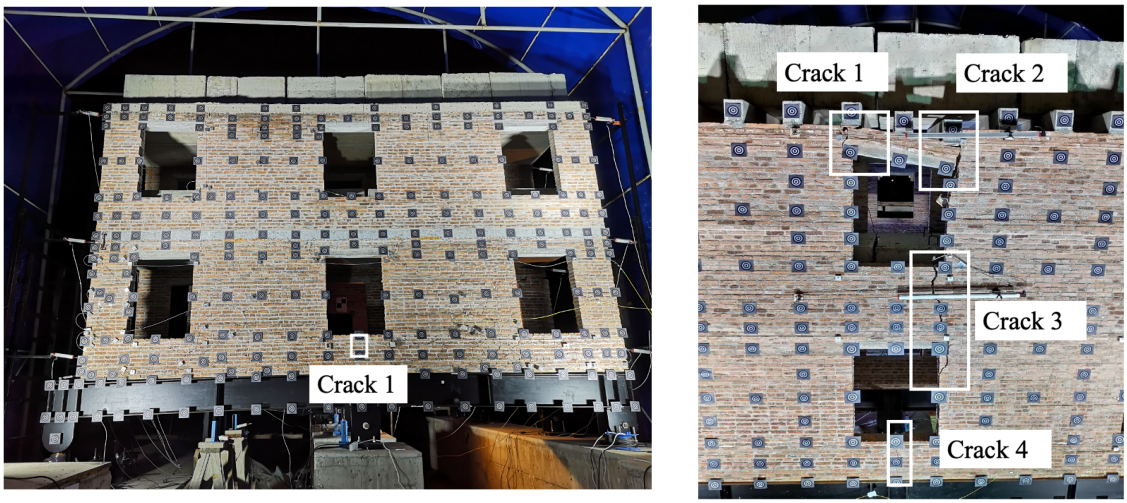
A detailed assessment of the damage induced in each building model, including the influences of the openings and the structural characteristics of the floors, is given in Dalgic

et al. (2023). Key observations from this assessment are as follows: (a) Damage induced in the buildings is strongly influenced by the number of openings; the 5-opening façade of 5O0-RF-W1 experienced significantly more damage than the façades of the equivalent 3-opening model, 3O-RF-W1 (contrast Figure 3.8 and Figure 3.9 with Figure 3.10a); (b) The presence of reinforced concrete slab floors in the RF models act to reduce the incidence of damage in the upper level of the building. While the building with joist floors 3O-JF-W1 suffered extensive damage in the upper level, the corresponding building with reinforced floors 3O-RF-W1 did not (contrast Figure 3.10b with Figure 3.10a); (c) The 3O-RF-W1 building deformed in an essentially rigid manner with minimal observed damage; gaps formed between the base of the building and the supporting beam. When the test was repeated with a higher kentledge load (3O-RF-W3) the building conformed more closely to the applied beam displacements with a consequential increase in the amount of cracking damage (contrast Figure 3.10a with Figure 3.6 and Figure 3.7).

Table 3.7; Summary of test results and damage categories based on the observed crack width. Values recorded under each damage category are the beam tip settlement when the corresponding building model first enters that damage category. The final damage category reflects the damage category of the building model when the maximum beam tip settlement is reached.

Test code	Max beam tip settlement (mm)	Slight (mm) ($0.5 < w < 2.5$) mm	Moderate (mm) ($2.5 < w < 7.5$) mm	Severe (mm) ($7.5 < w < 12.5$) mm	Very severe (mm) ($w > 12.5$) mm	Final damage category (at maximum tip settlement)
3O-RF-W1	67	7.8	-	-	-	Slight
3O-RF-W3	35	9.6	16.7	33.2	-	Severe
50O-RF-W1	26	7.3	15.7	-	-	Moderate
3O-JF-W1	32	9.4	31.9	31.9	31.9	Very severe

It is important to note that according to Burland et al. (1977), the damage category for masonry buildings is determined not only by crack size but also by their ease of repair. However, unlike crack width, the ease of repair is inherently subjective and cannot be quantified. As demonstrated by Dalgic et al. (2023), for all tests conducted in the current campaign, the assignment of damage categories on the basis of observed maximum crack width is largely consistent with the assessments of ease of repair.



(a) (b)

Figure 3.10; (a)(b) Indicative locations of all observed cracks for 3O-RF-W1 and 3O-JF-W1 at the maximum beam tip settlement. Original photos courtesy of Korhan Dalgic and Burcu Gulen.

3.7. The role of the author of this thesis in the test campaign

The role of the author of this thesis in the large-scale building settlement test campaign included: (a) preparing the laser scan instrumentation strategy; (b) developing the data management plan for both DIC and laser scanning; (c) on-site implementation of test 3O-RF-W1, which involved setting up DIC and laser scanning instrumentation, collecting DIC and laser scan data, and recording building damage; (d) exporting DIC data from the Imetrum controller for test 3O-RF-W1; (e) validating, visualising, and analysing the exported DIC displacement data for all tests; and (f) post-processing the laser scan data collected for all tests.

DIC, laser scan data, and building damage records for tests 3O-RF-W3, 3O-JF-W1, and 50O-RF-W1 were collected by the colleague of the author Burcu Gulen after the author had to leave the site due to visa expiry. Additionally, DIC displacement data for 3O-RF-W3, 3O-JF-W1, and 50O-RF-W1 were exported from the Imetrum system by Burcu Gulen. Burcu Gulen and Professor Korhan Dalgic also supplied FBG data and LVDT data to enable cross-validation of DIC measurements with FBG and LVDT at one common location for 3O-RF-W1. The finite element models for 3O-RF-W3 were provided by Professor Korhan Dalgic

and were utilised in the subsequent synthetic validation of the proposed Equivalent Frame Approach (EFA) as well as in the simulations of point cloud displacements for synthetic validation of the proposed Point Cloud-based Equivalent Frame Approach (PC-EFA).

3.8. Conclusion

This chapter provides the setup, instrumentation and implementation details for a unique large-scale masonry building settlement test campaign. In this campaign, displacements across the façades of the masonry building models and their supporting beams were recorded by DIC cameras in a carefully controlled environment. Terrestrial laser scans were conducted to collect point cloud data before and after each test.

The maximum out-of-plane movement for each building model was quantified using readings from a dedicated out-of-plane DIC camera. The collected DIC data were then systematically validated, both internally through overlapping monitoring areas and externally against other measurements. Additionally, virtual LVDT measurements of crack widths were compared with measurements taken using a crack ruler for further validation.

The accurate and continuous DIC displacement measurements provided a detailed capture of the building models' responses to settlement. Through the virtual LVDT setup, the DIC system allowed for precise monitoring of crack widths at multiple locations simultaneously throughout the test. This level of precision in crack monitoring facilitated an accurate reconstruction of crack propagation, a feature not commonly available in conventional settlement test setups. The datasets collected served as the foundation for subsequent research. Displacements and crack measurements obtained from DIC were used to benchmark the performance of tools discussed in subsequent chapters.

4. Estimation of building damage using equivalent beam idealisation

4.1. Purpose

Building response during nearby excavation activities (e.g. tunnelling or deep excavations) is traditionally monitored by conducting displacement measurements. These displacement data are then converted into various distortion measures, which are further utilised to estimate strains using different beam idealisations. For masonry buildings, commonly-used distortion measures include building deflection ratio, angular distortion and average horizontal strain; simple mechanical models and empirical rules are used to define limiting values for estimated strains to identify and control the level of cracking in buildings during construction. This procedure has a profound influence on mitigation and construction activities, and a critical evaluation of its veracity is needed. To this end, results from the large building settlement test campaign on the settlement response of three half-scale masonry building models are examined in this chapter. The systematic DIC displacement measurements allow the calculation of absolute displacements across the façade, as well as crack opening displacements at specific locations. These measurements facilitate a direct comparison between the actual observed damage and the damage category that is indicated by estimated strains.

The work presented in this chapter includes portions of research which the author of this thesis personally contributed to Liu et al. (2022b).

4.2. Methodology

There are three steps to estimate building damage using displacement measurements and equivalent beam idealisations. First, displacement measurements are converted into distortion measures, which describe various differential displacements and rotations experienced across the building. Second, distortion measures are used to estimate strains,

using various beam idealisations. Finally, maximum tensile strains in the equivalent beam model are associated to a damage category, using established correlations.

4.2.1. Distortion measures

To estimate building strains using equivalent beam models, suitable measures of distortion need to be determined from the measured building displacements. Following current practice, the chosen distortion measures are 'deflection ratio', 'angular distortion' and 'average horizontal strain'. Deflection ratio Δ/L is defined as indicated in Figure 4.1a where Δ is maximum vertical settlement with respect to a straight reference line defined by the corners of the building, which has a length of L. The angular distortion β is defined by the overall shear deformation of a particular bay of the building (Figure 4.1b):

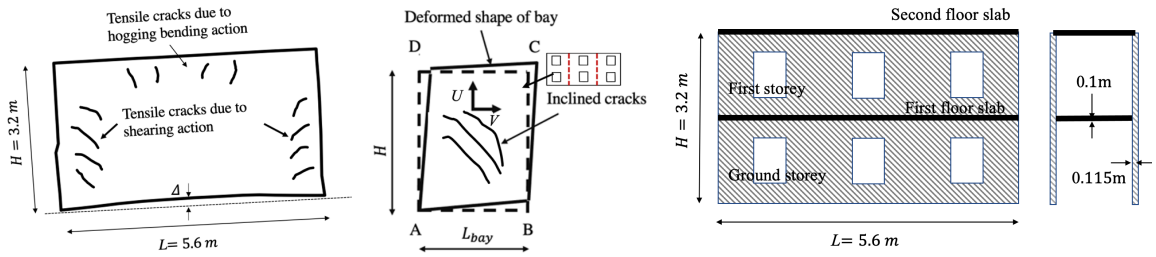
$$\beta_{\mathrm{ABCD}} = -\left[\frac{(V_B + V_C) - (V_A + V_D)}{2L_{bay}}\right] + \frac{(U_D + U_C) - (U_A + U_B)}{2H} \tag{4.1}$$

where U_p, V_p are the horizontal and vertical displacement at a general point P and β_{ABCD} is the angular distortion for a building bay defined by the points A, B, C and D (see Figure 4.1b). The building bay length and height are denoted by L_{bay} and H.

Additionally, values of 'average horizontal strain' are employed in conjunction with deflection ratio and angular distortion. For the building bay in Figure 4.1b, average horizontal strain ε_{AB}^{h} is calculated as follows:

$$\varepsilon_{AB}^{h} = \frac{U_B - U_A}{L_{bay}} \tag{4.2}$$

In the context of the current tests, displacements are obtained from the DIC at a time interval of 0.02s throughout the entire duration of each individual test. Maximum vertical settlement, Δ, is determined using vertical displacement measurements taken at all DIC targets (between 18 to 23 in number) fixed to the bottom row of the façade on each building model.



(a) (b) (c)

Figure 4.1; (a) Assumed deformation mode and potential crack locations for Deep Beam idealisation of a building façade with a neutral axis at the base. The location of diagonal cracks is not prescribed in Burland and Wroth (1974) but is expected to concentrate around the neutral axis; (b) Bay Beam idealisation of a building bay with an imposed angular distortion. The inclination of the cracks will depend on the ratio between angular distortion, β, and average horizontal strain ε_{AB}^{h} at the base of the bay; (c) Sandwich Beam idealisation of a building façade and dimensions of a cross-section of the building models.

4.2.2. Strain estimation

4.2.2.1. Deep Beam Approach (DBA)

In the widely-used approach by Burland and Wroth (1974) the building is represented by a Timoshenko beam with a uniform rectangular cross-section, made from a homogenous elastic material. The presence of openings and floors is neglected. In this chapter, this approach is referred to as the 'Deep Beam Approach' (DBA).

To apply the DBA to a building deforming in hogging (as is the case in the current tests) it is considered that the neutral axis lies at the base of the building. In this case the maximum tensile strain due to bending, ε_b^t, is related to the deflection ratio Δ/L (determined from displacement measurements) by,

$$\frac{\Delta}{L} = \left\{\frac{L}{12H} + \frac{EH}{2LG}\right\}\varepsilon_b^t \tag{4.3}$$

where E and G are Young's and shear moduli of the equivalent beam. The ratio $E/\ G$ is taken as 2.6 following Mair et al. (1996). Separately, the maximum tensile strain due to shear, ε_s^t, is given by,

$$\frac{\Delta}{L} = \left\{1 + \frac{GL^2}{6H^2E}\right\}\varepsilon_s^t \tag{4.4}$$

Additionally, the average horizontal strain ε^h developed at the base of the building (determined from horizontal displacement measurements) is combined with ε_b^t and ε_s^t

(using an appropriate tensor-based approach) to determine the maximum tensile strain ε_{max}^{t} experienced by the building. According to this model, if the maximum tensile strain is due to bending and its magnitude exceeds a limiting value, visible vertical cracks will appear at the top of the building at its midspan location (see Figure 4.1a). Conversely, if shear effects are found to dominate then visible inclined cracks may be expected to occur towards the edges of the façade (Figure 4.1a).

4.2.2.2. Sandwich Beam Approach (SBA)

Finno et al. (2005) proposed an alternative equivalent beam model referred to as Sandwich Beam Approach (SBA). This approach is relevant for buildings which have stiff floor slabs. In SBA, bending resistance is provided by the floors and the masonry walls act only in shear (see Figure 4.1c). SBA incorporates an explicit consideration of floor stiffness and the geometry of openings in the façade.

The SBA approach is only applicable to two building models (3O-RF and 50O-RF) with rigid floors. To apply SBA to these models, two slabs (first floor slab and second floor slab) and two load-bearing walls (ground storey wall and first storey wall) are considered, as shown in Figure 4.1c. When determining the shear stiffness of the wall, the influence of window openings is considered via a reduced wall shear area $A_{v,wall}$. Consistent with DBA, the neutral axis of the sandwich beam is assumed to coincide with the base of the façade. The maximum tensile strain due to bending, ε_b^t, is determined as,

$$\frac{\Delta}{L} = \left[\frac{L}{12\ H} + \frac{E_{slab}\ I_{slab}}{G_{wall}\ \overline{A_{v,wall}}\ L\ H}\right]\ \varepsilon_b^t \tag{4.5}$$

where $E_{slab}\ I_{slab}$ is the bending stiffness of the equivalent sandwich beam, determined by the slab properties, floor area, and the location of the slabs relative to the neutral axis, while $G_{wall}\overline{A_{v,wall}}$ is the shear stiffness of the equivalent sandwich beam, determined by the shear

area and shear modulus of the infill walls. The maximum tensile strain due to shear, ε_s^t, is found by,

$$\frac{\Delta}{L} = \left[\frac{L^2(\, G_{wall}\ \overline{A_{v,wall}})}{18\, E_{slab}\ I_{slab}} + 1\right] \varepsilon_s^t \tag{4.6}$$

Similar to DBA, ε_b^t and ε_s^t are combined with the horizontal strain ε^h the largest value of the resulting tensile strain is considered to be ε_{max}^t.

In the current work, Young's modulus E_{slab} of the reinforced concrete slab and shear modulus G_{wall} of the infilled wall are based on the values employed in the numerical analyses conducted by Dalgic et al. (2021). The second moment of area of the slab I_{slab} and total shear area $\overline{A_{v,wall}}$ are derived based on the dimension of each building model. The relevant data are summarised in Table 4.1.

Table 4.1; The material properties, second moment of area and total shear area used in SBA for 50O-RF-W1 and 3O-RF-W1/W3.

	E_{slab} (GPa)	G_{wall} (GPa)	I_{slab} (m^4)	$\overline{A_{v,wall}}$ (m^2)
50O-RF-W1 (35% window opening ratio)	32	1.435	0.844	0.112
3O-RF-W1/W3 (20% window opening ratio)	32	1.435	0.844	0.138

4.2.2.3. Bay Beam Approach (BBA)

In an alternative mechanical representation (referred to as Bay Beam Approach (BBA)), Son and Cording (2005) considers the building as a series of shear deformable rectangular 'bays' (see Figure 4.1b). The deformation of each bay is defined by the value of angular distortion determined from the monitored displacements. The shear strain is assumed to be uniform within each bay; is therefore equal to the (measured) value of angular distortion. The shear strain is combined with average horizontal strain (averaged over the length of the bay) using a tensor-based approach to determine a value of ε_{max}^t relevant to the façade. Since bending effects are neglected and constant shear and axial deformation is assumed, there is no particular expected location for the emergence of visible cracks. The definition of bays is

somewhat arbitrary, although previous studies define them around façade openings (Cook, 1994; Ritter et al., 2020).

4.2.3. Tensile strain and damage correlation

The value of maximum tensile strain ε_{max}^{t} determined from equivalent beam models is then correlated to a damage category. In the current work the widely-used maximum tensile strain–damage category, based on data from Boscardin and Cording 1989, is employed (see Table 3.6); this correlation is referred to as the 'standard damage correlation'. Standard damage correlations were formulated in an empirical manner, based on data and observations from various laboratory tests and field cases (e.g. Skempton and MacDonald, 1956).

4.3. Performance evaluation of equivalent beam models

4.3.1. 3O-RF

The first building model to be tested in the campaign was 3O-RF. Initially this was loaded with load configuration W1 and then tested to an applied beam tip settlement of 67 mm. The building suffered minimal observable damage, with a single visible crack in a ground storey spandrel (see Figure 4.2c). Data on maximum tensile strain determined using the Timoshenko beam models (DBA and SBA) are shown in Figure 4.2a. To apply the BBA approach the building was considered in three separate bays. Calculated values of ε_{max}^{t} for each of the bays are shown in Figure 4.2b. It is clear that the three approaches deliver broadly consistent values of ε_{max}^{t} as the test progressed. All three modelling approaches indicate that the damage category is 'negligible'. The dominant damage mode of DBA and SBA is bending and shearing, respectively. Their implied damage patterns are shown in Figure 4.2a inset.

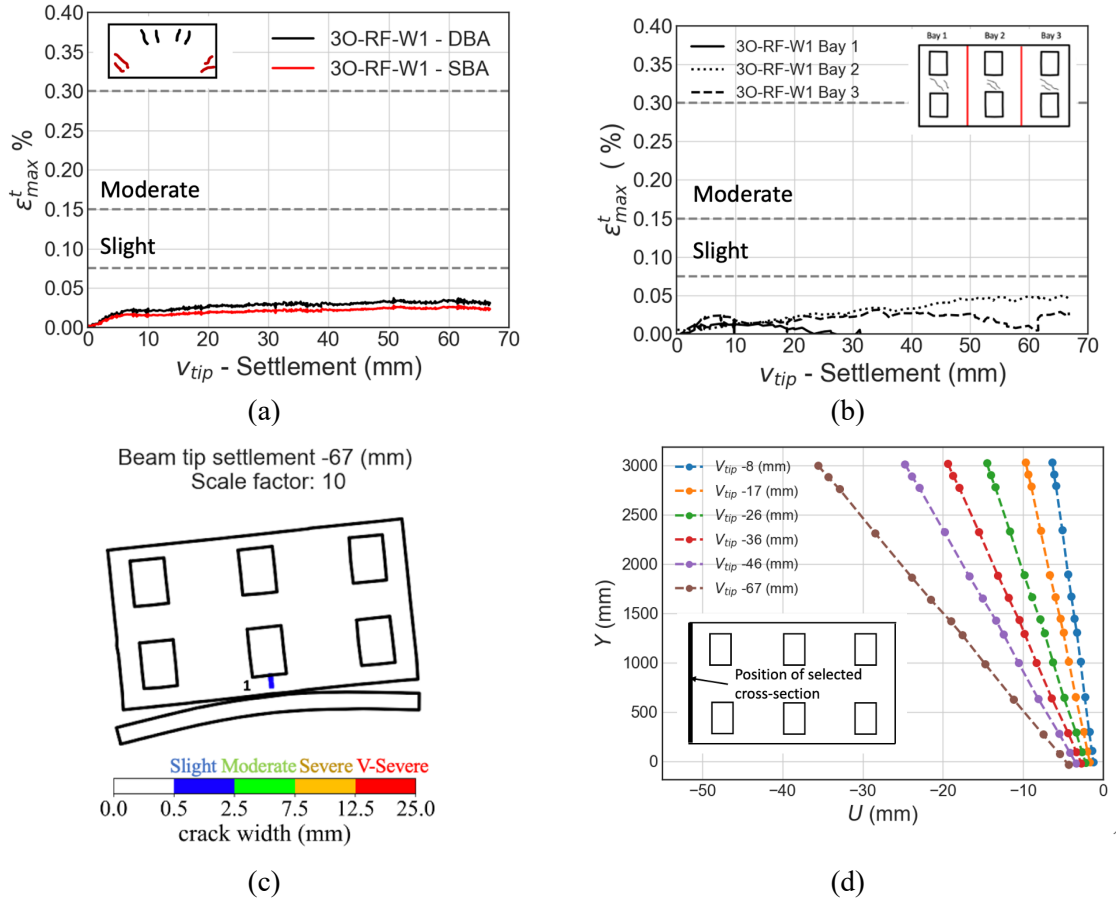


Figure 4.2; (a) Values of maximum tensile strain ε^t_{max} estimated from measured values of deflection ratio and average horizontal strain on 3O-RF-W1 using the DBA(Black) and SBA (Red). Inset, the locations of cracks that would be associated to the measured tensile strains from DBA (Black) and SBA (Red), are illustrated. (b) Values of maximum tensile strain ε^t_{max}determined from angular distortion and average horizontal strain using the BBA on 3O-RF-W1. The division of bays is shown in the inset. (c) Deformed shape of the front façade of 3O-RF-W1 at the beam tip settlement of 67mm, plotted with the crack location and size (indicated by the colour bar). (d) Profiles of the cross-section at the left edge of the building model subjected various beam tip settlements in 3O-RF-W1.

Building deformed shape and crack observations are shown in Figure 4.2c. In contrast to DBA, SBA and BBA predictions, the presence of a crack indicates the damage category as 'slight'. The location of this crack at one of the ground storey lower spandrels also contradicts DBA and SBA indications. The equivalent beam models are therefore unable to provide an indication of the level and location of the actual damage in this case. It appears that the lower spandrel is subjected to a localised hogging displacement with the consequential formation of a vertical crack at its upper edge. Figure 4.2d plots the evolution of horizontal displacements along the left vertical edge of the façade. The linear variation of horizontal displacements along the height indicates a rigid body movement, which was also

evident in the deformed shape in Figure 4.2c. This supports the observation that the damage is localised and does not influence the rigid body rotation of the building model.

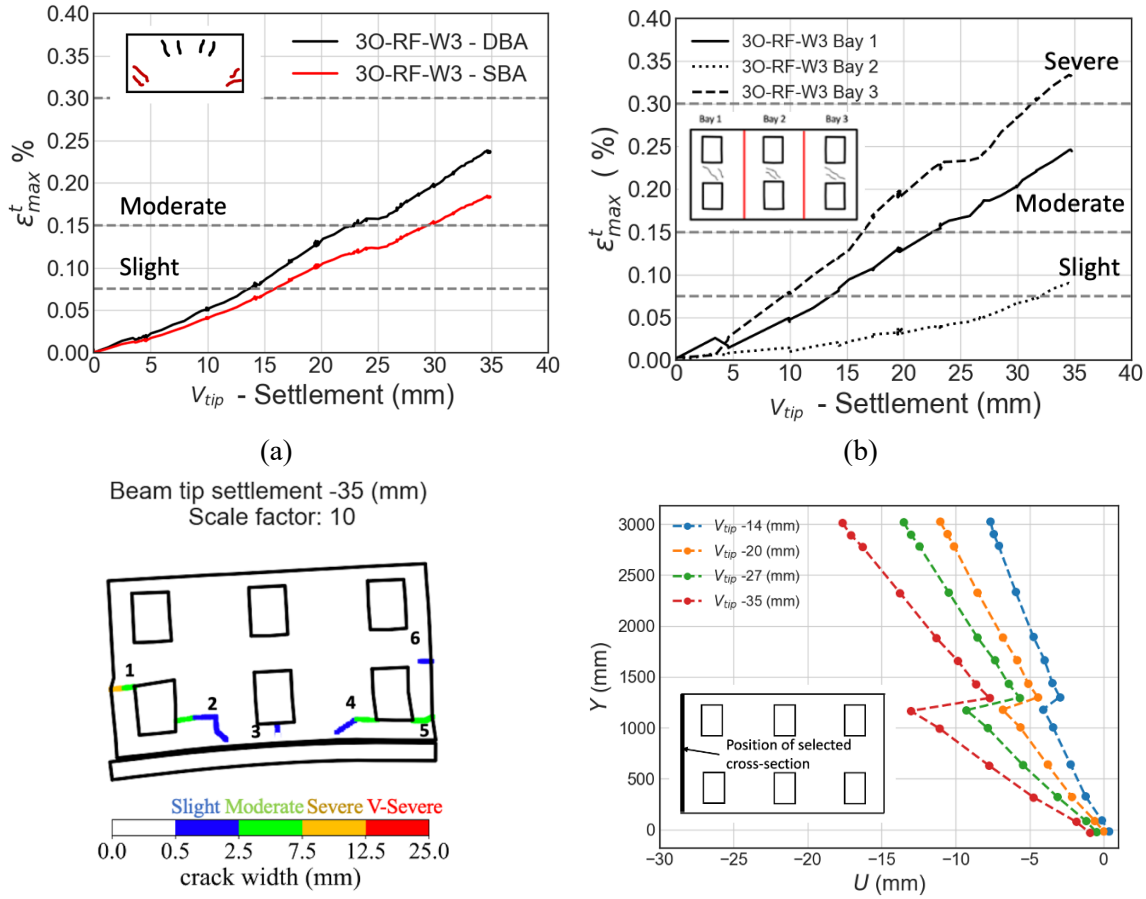


Figure 4.3; (a) Values of maximum tensile strain ε^t_{max} estimated from measured values of deflection ratio and average horizontal strain on 3O-RF-W3 using the DBA(Black) and SBA (Red). Inset, the locations of cracks that would be associated to the measured tensile strains from DBA (Black) and SBA (Red), are illustrated. Horizontal dashed lines indicate boundaries between implied damage categories. (b) Values of maximum tensile strain ε^t_{max}determined from angular distortion and average horizontal strain using the BBA on 3O-RF-W3. The division of bays is shown in the inset. (c) Deformed shape of the front façade of 3O-RF-W3 at the beam tip settlement of 35mm, plotted with the crack location and size (indicated by the colour bar). (d) Profiles of the cross-section at the left edge of the building model subjected various beam tip settlements in 3O-RF-W3.

The slight damage experienced by 3O-RF-W1 provided an opportunity to re-test the building with a larger set of applied weights (W3) in an attempt to induce additional damage to the building. Cracks that developed during test 3O-RF-W3 are shown in Figure 4.3c. In this case significant cracking occurred at the ground storey of the façade; the first storey appeared undamaged. Horizontal cracks were observed at the slender external piers, which appeared to be induced by bending action in these piers. Meanwhile, stockier internal piers

experienced diagonal cracking. On the basis of the width of the visible cracks, at the maximum beam tip settlement (35 mm) the building damage category is classified as 'severe'. Estimated values of ε_{max}^{t} from the beam models are shown in Figure 4.3a-b. It is seen that the most onerous case from the BBA approach (Bay 3) indicates 'severe' damage at the end of the test, consistent with the observed damage state. The DBA and SBA approaches, however, classify the damage as 'moderate'. Location of cracks estimated by DBA and SBA (shown inset in Figure 4.3a) is in stark contrast with the damage observations in Figure 4.3c. The horizontal deformation profiles along the left vertical edge of the building are shown in Figure 4.3d. There appear to be two lines in this figure with distinct deformation trends, corresponding to the ground and first storey deformations. These lines indicate that building cross-sections do not remain plane, violating kinematic assumptions made during the formulation of DBA and BBA.

4.3.2. 3O-JF-W1

Figure 4.4a shows data on beam tip settlement versus tensile strain determined using DBA (since this model does not incorporate a rigid slab, SBA was not examined in this case). At beam tip settlements less than 32 mm, the estimated maximum tensile strains are similar to the data from the corresponding rigid floor test (3O-RF-W1, Figure 4.2a). At a tip displacement of 32 mm the sudden development of significant cracks caused the building to deform and the gaps between the steel beam and the building to close (refer to Figure 3.10b to observe the severity of the damage and contrast the deformed shapes illustrated in Figure 4.2c and Figure 4.4c). The measured deflection ratio increased with a consequential increase in ε_{max}^{t}, as indicated in Figure 4.4a. DBA estimates the final damage state as 'moderate'. The BBA approach (Figure 4.4b) predicts a comparatively low level of strain and estimates 'slight' damage at the final state.

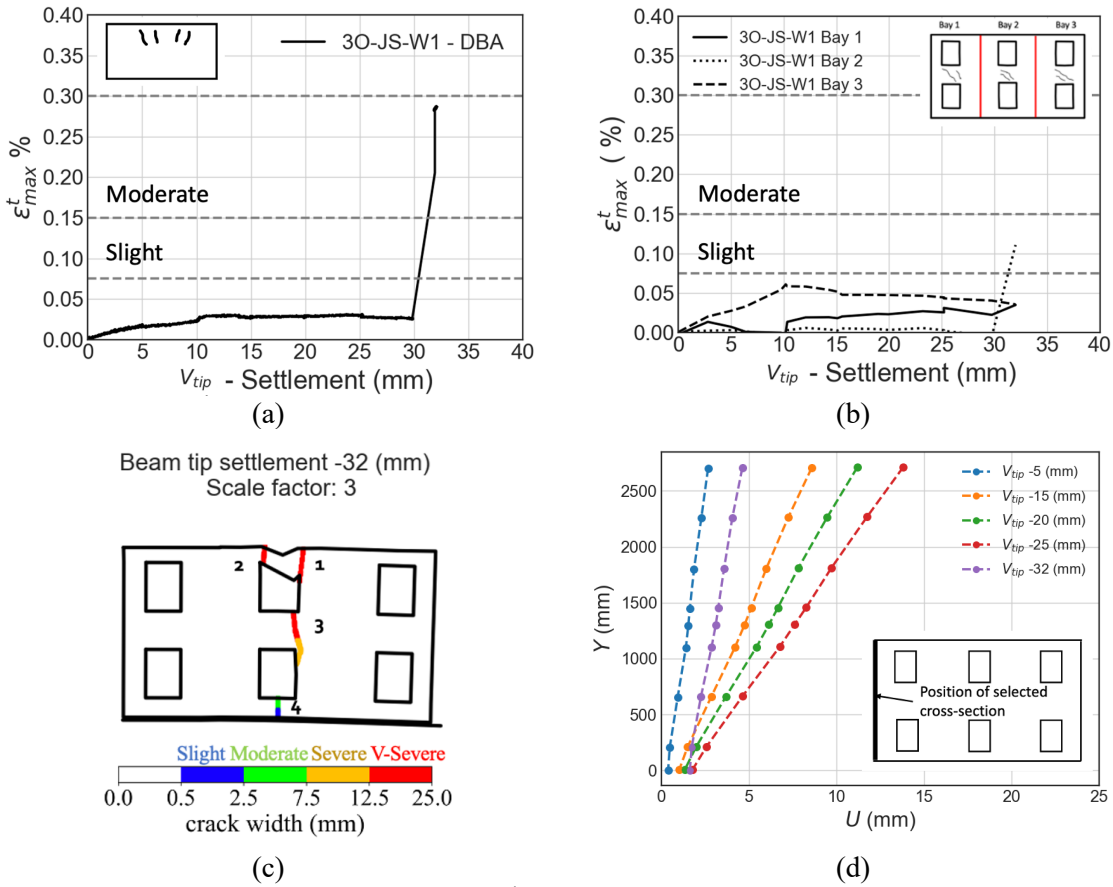


Figure 4.4; (a) Values of maximum tensile strain ε^t_{max} estimated from measured values of deflection ratio and average horizontal strain on 3O-JF-W1 using the DBA(Black). Inset, the locations of cracks that would be associated to the measured tensile strains from DBA (Black) are illustrated. (b) Values of maximum tensile strain ε^t_{max}determined from angular distortion and average horizontal strain using the BBA on 3O-JF-W1. (c) Deformed shape of the front façade of 3O-JF-W1 at the beam tip settlement of 32mm, plotted with the crack location and size (indicated by the colour bar). (d) Profiles of the cross-section at the left edge of the building model subjected various beam tip settlements in 3O-JF-W1.

Deformed shape and crack widths at the maximum beam tip settlement in 3O-JF-W1 test are shown in Figure 4.4c. There was only slight damage in the building until two vertical cracks (cracks 1 and 2 in Figure 4.4c) suddenly appeared at the tip settlement of 32 mm. These led to the development of cracks 3 and 4 at lower levels. A maximum crack width of 40.45mm was observed at the end of the loading for crack 2. This 'very severe' damage caused a partial collapse of the central lintel at the top (refer to Figure 3.10b). Comparing damage observations to equivalent beam predictions, it is clear that damage severity was underestimated by beam models. However, in this case, the location of damage at the first storey of the building at midspan location (shown in Figure 4.4c) was well-predicted by DBA and SBA. This agreement is due to the beam-like behaviour of 3O-JF-W1 highlighted

in Figure 4.4d, where building cross-sections remained plane until severe damage occurred. The beam-like behaviour of 3O-JF-W1 also explains the poor performance of BBA in interpreting damage category. The shear beam kinematics that underlie BBA do not consider bending deformations, resulting in an underestimation of damage at the final loading stage.

4.3.3. 50O-RF-W1

Figure 4.5a shows the estimated maximum tensile strains from DBA due to bending, suggesting that at the end of the test ($V_{tip} = 26\,mm$) the building model has sustained moderate damage. The SBA indicates the building model was at the boundary between slight and moderate damage, with maximum strains due to shear. Figure 4.5b shows that, at the end of the test, building bays 1, 2 and 4 are expected to experience moderate damage according to BBA, whereas bays 3 and 5 experienced very slight and slight damage, respectively. The beam models therefore all provide a consistent indication of moderate damage at the end of the test.

The observed crack damage in 50O-RF-W1 at the end of the test (see Figure 4.5c) comprised horizontal cracks (cracks 1, 2, 6 and 7) at the ground storey external pier boundaries and vertical cracks (cracks 3, 4, 5) on the ground storey spandrels. No diagonal cracks were observed; this is presumably due to the presence of windows resulting in individual slender building components deforming predominantly in bending. The horizontal crack (crack 1) at the top of the right external pier measured 4.10 mm at the final stage, corresponding to moderate damage category. While the damage category indications from DBA and SBA are consistent with this result, crack locations (contrast Figure 4.5c and Figure 4.5a inset) and the kinematics (contrast 'plane cross-section assumption' in beams with deformation profiles in Figure 4.5d) assumed in the equivalent beam formulations disagree with observations.

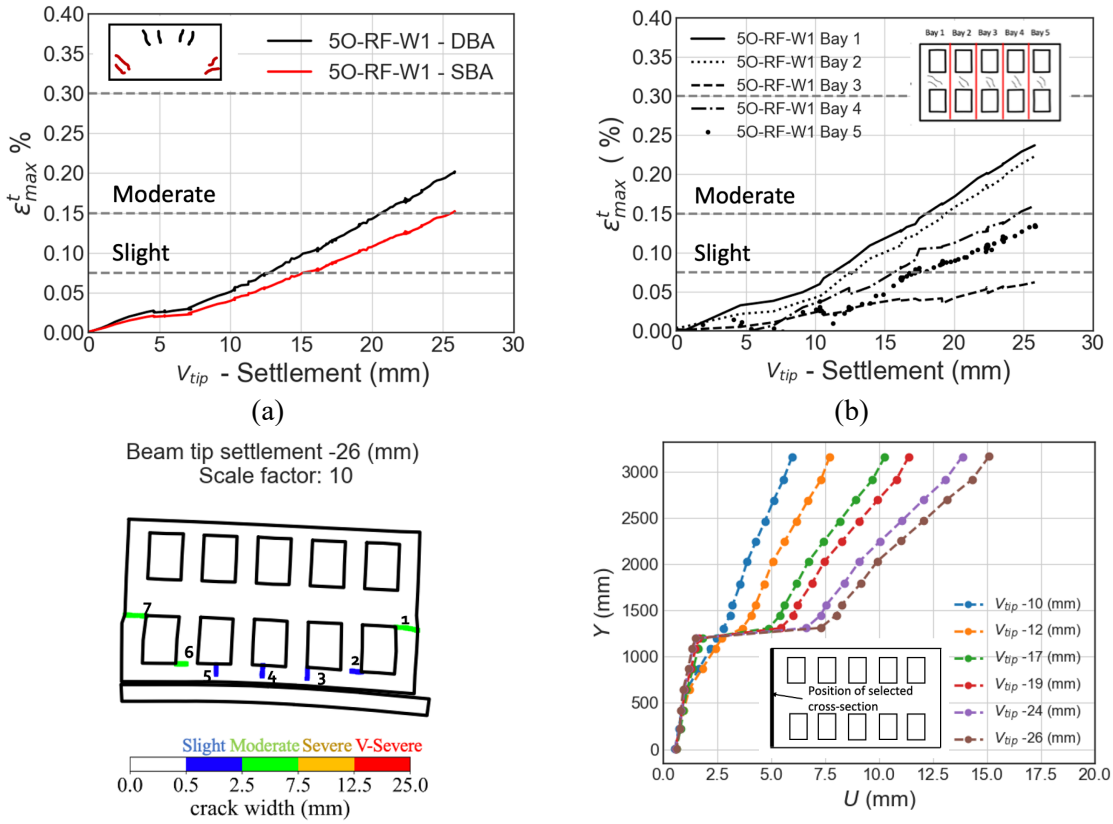


Figure 4.5; (a) Values of maximum tensile strain ε^t_{max} estimated from measured values of deflection ratio and average horizontal strain on 50O-RF-W1 using the DBA(Black) and SBA (Red). Inset, the locations of cracks that would be associated to the measured tensile strains from DBA (Black) and SBA (Red), are illustrated. Horizontal dashed lines indicate boundaries of damage categories. The inset shows the potential damage locations. (b) Values of maximum tensile strain ε^t_{max}determined from angular distortion and average horizontal strain using the BBA on 50O-RF-W1. The division of bays is shown in the inset. (c) Deformed shape of the front façade of 50O-RF-W1 at the beam tip settlement of 26mm, plotted with the crack location and size (indicated by the colour bar). (d) Profiles of the cross-section at the left edge of the building model subjected various beam tip settlements in 50O-RF-W1.

4.4. Overall performance of the equivalent beam models

Table 4.2 summarises the performance of equivalent beam models in indicating damage category and location at the final settlement of each test. It is worth noting that there appears to have a positive correlation between growing crack width and estimated strains, and the effectiveness of damage indication from equivalent beam models varies as a test progresses. Nevertheless, this table highlights that equivalent beam models tend to underestimate damage category and provide a poor indication of damage location.

Table 4.2; Summary of the performance of DBA, SBA and BBA equivalent beam models in terms of indicating damage category and location at the final settlement of each test.

Test ID	Types	Observation[1]	DBA	SBA	BBA[2]
3O-RF-W1	Damage Category	Slight	Negligible	Negligible	Negligible
	Damage Location	-	Poor	Poor	Poor
3O-RF-W3	Damage Category	Severe	Moderate	Moderate	Severe
	Damage Location	-	Poor	Poor	Poor
3O-JF-W1	Damage Category	Very severe	Moderate	-	Slight
	Damage Location	-	Good	-	Poor
5O-RF-W1	Damage Category	Moderate	Moderate	Moderate	Moderate
	Damage Location	-	Poor	Poor	Poor

[1]Based on the maximum measured crack width and correlations presented in Table 3.6; [2]Only the most severe damage category recorded.

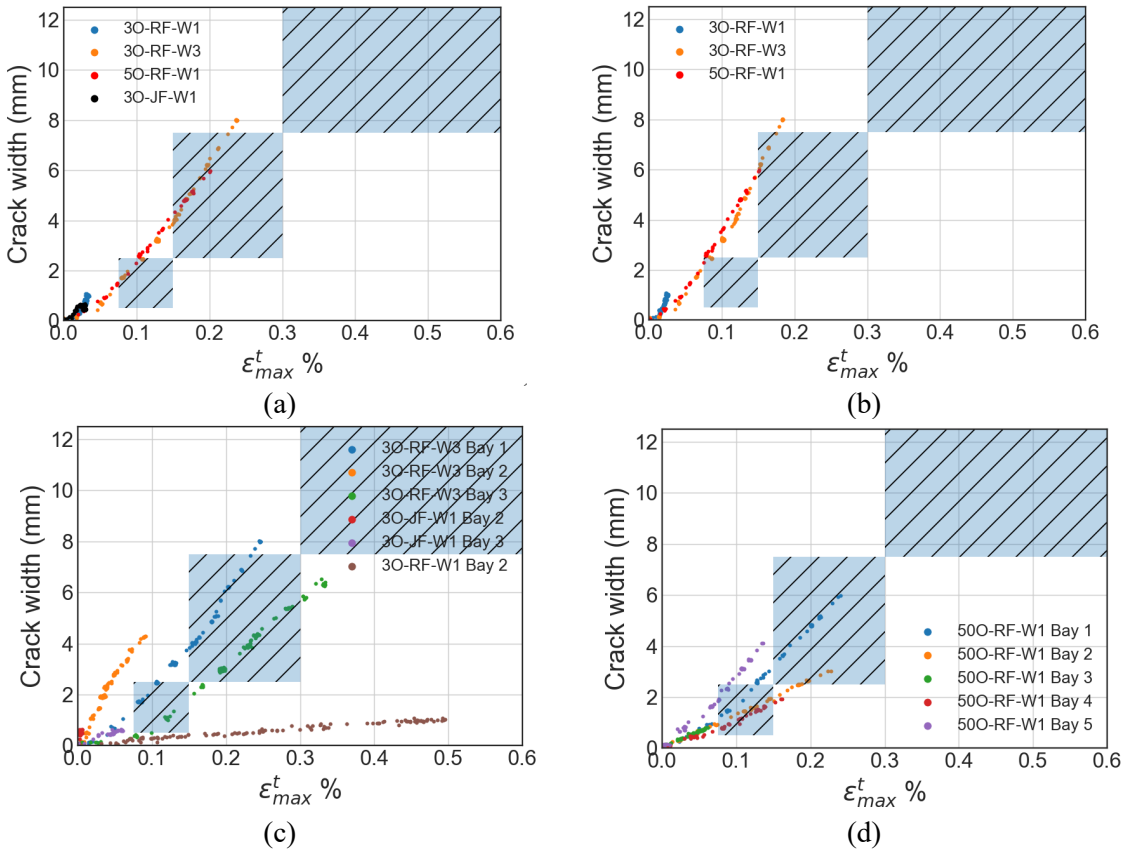


Figure 4.6; Combined data for estimated maximum tensile strain plotted against maximum observed crack width for (a) DBA and (b) SBA (c)(d) BBA models; The hatched grey boxes indicate the standard correlations (see Table 3.6)

The relationship between the maximum tensile strain determined from all equivalent beam models, plotted against actual maximum crack width determined from the DIC measurements is shown in Figure 4.6. The data in Figure 4.6a-b indicate an apparent linear

relationship from the slight damage category up to the upper bound of the moderate damage category. The observed linear relationships suggest that, as the crack width increases, the estimated strain is less responsive than is implied in the standard correlations, leading to the estimated strain underestimating the damage category. The data in Figure 4.6a-b also appear to suggest that strain limits can be calibrated to improve damage estimation. However, it shall be noted that the linear relationship in Figure 4.6a-b no longer holds when very severe cracks are considered according to the 3O-JF-W1 results (beyond the region of Figure 4.6a). On the other hand, when damage is local and small, noticeably in test 3O-RF-W1 in Figure 4.6a-b, the tensile strain–crack width correlation departs from that of other tests, leading to further disagreement with the standard correlations.

Owing to a broadly consistent strain–crack width relationship, the DBA and SBA modelling approaches may be able to correctly identify the damage category when the underlying relationship is in line with the standard correlations (i.e. passing through the hatched boxes in Figure 4.6). The performance of DBA and SBA can be further improved by calibrating the standard correlations to better fit the observed damage categories. However, as noted in Table 4.2, the observed cracking damage tends to occur at locations that are inconsistent with the underlying beam theory assumptions. In particular, when the building incorporates rigid slab floors, these appear to shield the first storey from damage. Models which consider the influence of rigid slab floors, such as SBA, do not account for the complex kinematics involved in the behaviour. Consequently, damage location predictions remain poor in SBA.

Compared to DBA and SBA, the relationship between the calculated tensile strain using BBA and damage (Figure 4.6c-d) in a specific bay, is more scattered. One of the reasons for the scatter relates to the definition of building bays; bays are not structural components, and

their selection is somewhat arbitrary. Moreover, BBA neglects bending deformations, which can be significant. For instance, when predicting the damage category of 3O-JF-W1, which resembled a beam more than any of the other tested building models, the BBA approach was unable to capture the very severe damage level which associated with a bending-type failure mode.

4.5. Conclusion

The use of equivalent beam models (DBA, SBA and BBA) and standard damage–crack width–tensile strain relationships to estimate damage from displacement measurements, provides low fidelity results. A major reason for this is the mismatch between the kinematic assumptions inherent in the equivalent beam models and the actual deformations of the building. It is noted that this empirical damage assessment procedure has been developed over many years; numerical values of the widely-accepted crack width-tensile strain correlations that are embedded in this approach appear to be tailored to provide an approximate match between observed damage on the one hand and estimated tensile strain on the other. Within this context, the standard damage category–crack width–tensile strain correlations should not be regarded as having a fundamental basis; instead, they represent a numerical correlation that—when employed with equivalent beam models—provide an indication of observed building damage. This suggests that the standard numerical damage–tensile strain correlations have effectively been 'tuned' to compensate for deficiencies in the beam modelling approach when applied to real buildings. The application of the equivalent beam-based damage assessment approach to building models has shown that the method appears to be capable of indicating some damage development, but damage categories are often underestimated. While alternative strain and damage correlations can be proposed to improve damage category results, the fundamental limitations of equivalent beam models in capturing building kinematics and locating damage cannot be resolved.

5. Equivalent frame approach

5.1. Purpose

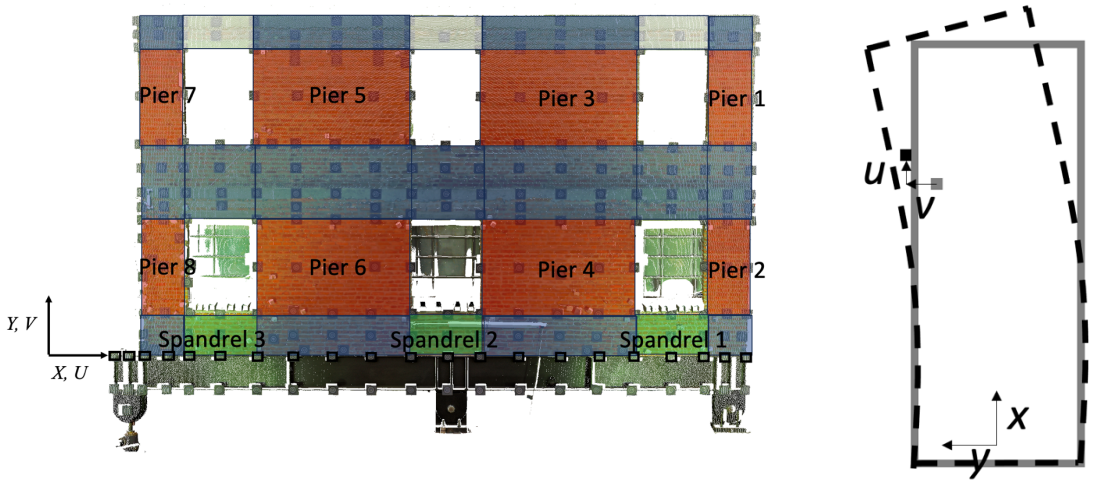
Methods which idealise buildings as equivalent beams, DBA, SBA and BBA, show limited success in categorising and locating damage. Poor performance is in large part due to a mismatch between the kinematics assumed in the equivalent beam models and the deformations actually experienced by the building. An alternative approach is proposed in this chapter, called the Equivalent Frame Approach (EFA), in which the building façade is idealised as an equivalent frame. This approach can be viewed as a higher resolution version of the DBA; in DBA the whole façade is represented as a beam whereas in EFA the beam approximation is employed at the level of individual piers and spandrels. Unlike DBA and SBA, EFA does not require the consideration of additional parameters, such as the position of the neutral axis.

5.2. Proposed methodology

5.2.1. Façade discretisation

Following previous work (e.g. Lagomarsino et al., 2013) building façades are considered to be composed of three types of structural components: piers, spandrels and connectors. Piers (coloured in red in Figure 5.1a) and spandrels at the bottom (coloured in green in Figure 5.1a) are represented by Timoshenko beam elements. The top spandrels, marked in white in Figure 5.1a, are not modelled as beams due to the presence of the second-floor slab (in 3O-RF and 50O-RF building models) and reinforced concrete lintels (in all building models). The ‘connectors’ (coloured in blue in Figure 5.1a) are typically employed to connect the piers and spandrels. In computational models, ‘connectors’ are treated as rigid offset elements, justified by the observation that connector elements rarely experience damage. Similarly, in the current tests, damage was largely confined to the piers and spandrels. For

the building models with slab floors, spandrels in contact with the slabs did not experience any damage and are treated as connectors. No attempt is made in the current work to estimate the strain distributions in the connector elements.



(a) (b)

Figure 5.1; (a) Discretisation of the 3O building model using Timoshenko beam elements and connectors. Red and green colours indicate structural components modelled by a Timoshenko beam element, and blue colours indicate connectors. White colours represent spandrels that cannot be modelled as beams due to the presence of the reinforced concrete slab and/or lintels. DIC targets can be seen affixed to the front wall facade, where displacements are measured. DIC targets outlined with black square boundary lines are affixed to the edge of the support beam and cannot be used to infer displacements of the façade; (b) A Timoshenko beam element subjected to deformation. Displacements of an internal point are illustrated in a local coordinate system.

5.2.2. Strain estimation

In contrast to equivalent beam models, EFA does not require the definition of distortion measures to estimate strain. Displacement field functions from beam theory are directly fitted to the measured displacement data in a least squares sense. Partial derivatives of the displacement fields are then used to obtain the strain fields and estimate the maximum tensile strain in the element.

The settlement-induced displacement field in each beam component is represented by,

$$u(x,y) = -\phi y + fx + e \tag{5.1}$$

$$v(x,y) = c_1x^3 + c_2x^2 + c_3x + c_4 \tag{5.2}$$

where x, y are the position coordinates in the local coordinate system (Figure 5.1b) u and v are local displacements in the x and y directions. Consistent with beam theory, plane sections

remain plane; ϕ is the rotation of the beam cross section. Additional parameters are *f*, *e*, c_1, c_2, c_3 and c_4 . The transverse settlement-induced shear strain is obtained from:

$$\gamma_{xy} = \frac{1}{2}\left(\frac{\partial u}{\partial y} + \frac{\partial v}{\partial x}\right) = \frac{1}{2}\left(\phi + \frac{\partial v}{\partial x}\right) \tag{5.3}$$

To emphasise that this expression for shear strain represents an averaged value over the cross section, the nomenclature $\gamma_{ave} = \gamma_{xy}$ is employed below.

It is considered that a set of displacement data (u_i, v_i) are available at locations (x_i, y_i) in the beam, where $i \in (1,2,\dots,n)$ is the index of the measurement target. The measured displacement data are related to the model parameters by a *B* matrix:

$$\begin{bmatrix} u_1 \\ v_1 \\ u_2 \\ v_2 \\ \vdots \\ u_n \\ v_n \end{bmatrix} = B \times \begin{bmatrix} c_1 \\ c_2 \\ c_3 \\ c_4 \\ f \\ e \\ \gamma_{ave} \end{bmatrix} \tag{5.4}$$

where $B = \begin{bmatrix} -3y_1{x_1}^2 & -2y_1x_1 & -y_1 & 0 & x_1 & 1 & 2y_1 \\ {x_1}^3 & {x_1}^2 & x_1 & 1 & 0 & 0 & 0 \\ -3y_2{x_2}^2 & -2y_2x_2 & -y_2 & 0 & x_2 & 1 & 2y_2 \\ {x_2}^3 & {x_2}^2 & x_2 & 1 & 0 & 0 & 0 \\ \vdots & \vdots & \vdots & \vdots & \vdots & \vdots & \vdots \\ -3y_n{x_n}^2 & -2y_nx_n & -y_n & 0 & x_n & 1 & 2y_n \\ {x_n}^3 & {x_n}^2 & x_n & 1 & 0 & 0 & 0 \end{bmatrix}$

A minimum of four measurement points (n = 4, with displacement in both X and Y directions, amounting to eight data points) are required to estimate the parameters. Ideally, to minimise the influence of measurement errors, more than four measurement points would be employed for the parameter evaluation.

Let unknown model parameters $(c_1, c_2, c_3, c_4, f, e, \gamma_{ave})^T$ in Equation 5.4 be represented as *p*, and the displacement vector $(u_1, v_1 \dots u_n, v_n)^T$ be represented as *d*. The linear equations in Equation 5.4 then become an overdetermined system, and a least squares solution can be found by:

$$\hat{p} = (B^T B)^{-1} B^T d \tag{5.5}$$

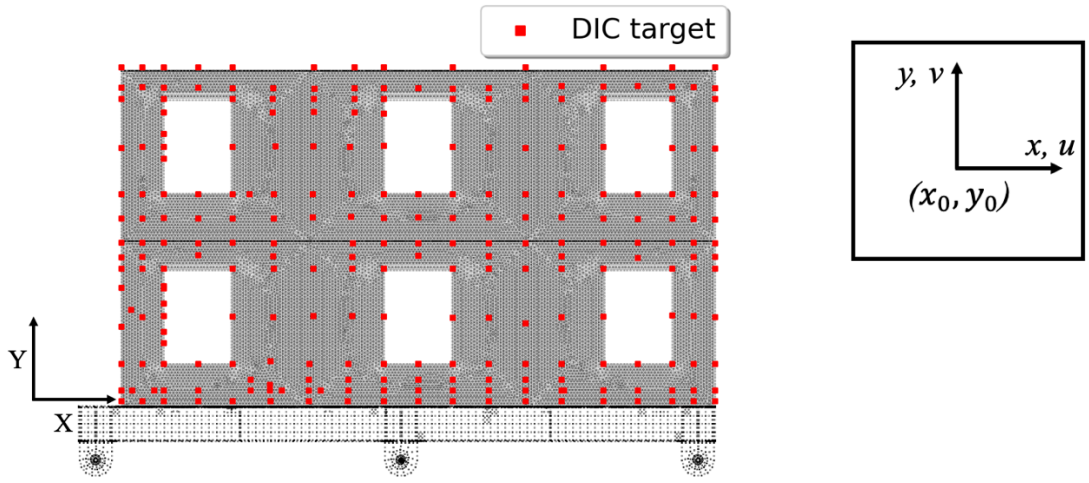
where $\hat{p}$ represents the least square solution of model parameters that minimises $\|d - Bp\|^2$. Once the parameters have been determined, the derived average shear strain γ_{ave} is re-distributed along the cross-section using a parabolic function satisfying zero shear strain conditions on the external fibres of the cross-section. The axial strains within each beam element are then determined straightforwardly from Equations 5.1 and 5.2 and combined with re-distributed shear strains using a tensor-based approach to determine the maximum tensile strain ε_{max}^{t} in each pier and spandrel.

5.3. Validation using 3D finite element models

To evaluate EFA, 3D finite element (FE) models developed by Dalgic et al. (2021) are reused. The FE models have the same geometric properties as the physical test models. The masonry wall and supporting beams are modelled using 6-node triangular shell elements and structural solid elements, respectively. In the linear analysis, all materials behave elastically. In the nonlinear analysis, the total strain crack model (Rots, 1991) is adopted for masonry. The interface between the masonry wall and the beams is represented by 3D line interface elements. The 3D line interface elements have no tension strength in nonlinear analysis but retain their elastic properties in linear analysis. The simulation of the kentledge, positioned on both the first and second floor slabs, involves the application of distributed forces on the upper faces of the floor slab elements. Additionally, to account for the effects of window sill loads (W3), distributed forces are applied along the upper edges of the elements at each window sill. Settlement is added by applying vertical movement to the tip of screw jacks. More details are available in Dalgic et al. (2021).

The validation scheme considers responses from linear (with elastic materials) and nonlinear (with cracking materials) analyses. The EFA routine operates on a small subset of the FE

displacement data (located where DIC targets were placed, as shown in Figure 5.2 with red squares) to estimate strains. For linear models, displacements and strains from EFA are compared to results from FE analysis using statistical measures to evaluate the fitness and prediction accuracy of the underlying beam model. In the nonlinear range, due to softening material models used in the FE analyses, a direct comparison of displacements and strains is less meaningful. Instead, FE strains are regularised to estimate crack bandwidth, which is then correlated to damage via standard correlations (see Table 3.6). The damage class of each structural component determined by crack bandwidth from nonlinear finite element analysis is then compared to the damage class estimated on the basis of EFA to assess the effectiveness of EFA in indicating damage.



(a) (b)

Figure 5.2; (a) DIC targets overlaying finite element mesh of 3O-RF-W3. Red squares are DIC target locations. (b) local coordinate system of a quad/ rigid element.

5.3.1. Validation of EFA with synthetic data from linear FE analysis

5.3.1.1. Methodology

Nodal displacements from the linear analysis of 3O-RF-W3 model subjected to 10mm settlement are first exported. DIC targets used here largely retain their arrangement on the physical building model (contrast Figure 5.2a with Figure 5.1a), except for a few realignments to account for construction imperfection. A row of targets at the base of the

masonry wall, which was attached to the top flange of the supporting beam on the physical building model during the test (refer to DIC targets outlined with black square boundary lines in Figure 5.1a), are placed at the base of the masonry wall for this numerical validation. This allows assessment of the entire spandrel instead of only the upper half. Displacements of DIC targets are determined by assigning the displacements of the nearest FE node to each DIC target through a nearest point search. Since the façade model has a target mesh size of 30mm, the expected distance from the nearest FE node to a DIC target is approximately 15mm. Subsequently, coordinates of DIC targets and the assigned displacements in each structural component are fitted in a least square sense to derive EFA parameters as defined in Equations 5.1-5.5.

The validation in the linear range first evaluates the fitness and accuracy of prediction of the underlying Timoshenko beam model (referred to as 'beam model') used in EFA. To this end, the coefficient of determination (R^2) and root mean square error (RMSE) are assessed for each structural component on the basis of predicted and FE displacements at each finite element node. The B matrix assembled from coordinates of all FE nodes is multiplied to model parameters derived based displacements and coordinates at DIC targets using Equation 5.4 to obtain predicted displacements at FE nodes.

Given that the building model undergoes substantial rigid body motion during the test, a rigid model and a first order quadrilateral model (referred to as 'quad model' in this chapter) are introduced as references to provide additional context for evaluating the beam's performance. As implied by its name, the rigid model does not deform, and its displacements are given by:

$$u(x,y) = u - \omega y \tag{5.6}$$

$$v(x,y) = v + \omega x \tag{5.7}$$

where *x, y* are the position coordinates in the local coordinate system (Figure 5.2b), u and v are local displacements in the *x* and *y* directions. ω is the rigid body rotation around its centroid, x_0, y_0. Conversely, the quad model allows axial deformation as well as shear, and its displacements are assumed to be given by:

$$u(x,y) = a_1 + a_2 x + a_3 y + a_4 xy \tag{5.8}$$

$$v(x,y) = a_5 + a_6 x + a_7 y + a_8 xy \tag{5.9}$$

where *x, y* are the position coordinates in the local coordinate system (Figure 5.2b). a_1 to a_8 are model parameters.

Displacement and coordinates at DIC targets are fitted to Equations (5.6) and (5.7) or Equations (5.8) and (5.9) to derive relevant parameters for each model. Following a similar approach used for the beam model as introduced above, predicted displacements are derived using fitted model parameters and compared with FE displacements at each node.

The second stage of the linear validation assesses the quality of inferred tensile strain from EFA. Since FE strain computations are frequently impacted by stress singularity phenomena around sharp corners, there exists a prevalent dependency of maximum tensile strains on mesh configurations (Yiu et al., 2017). As a consequence of this inherent limitation, maximum strain indicator is considered unsuitable as a validation measure. Instead, the Pearson correlation coefficient (referred to as 'correlation coefficient' or 'correlation result'), calculated between interpreted strain and FE strain at each individual FE node, is employed to shed light on the performance of the model. In contrast to the maximum tensile strain metric, the correlation coefficient provides an assessment that takes into account the entirety of the data points and reflects both strain magnitude and distribution, which is more relevant to characteristic strain that correlates to damage class in the application.

The Pearson correlation coefficient is defined as:

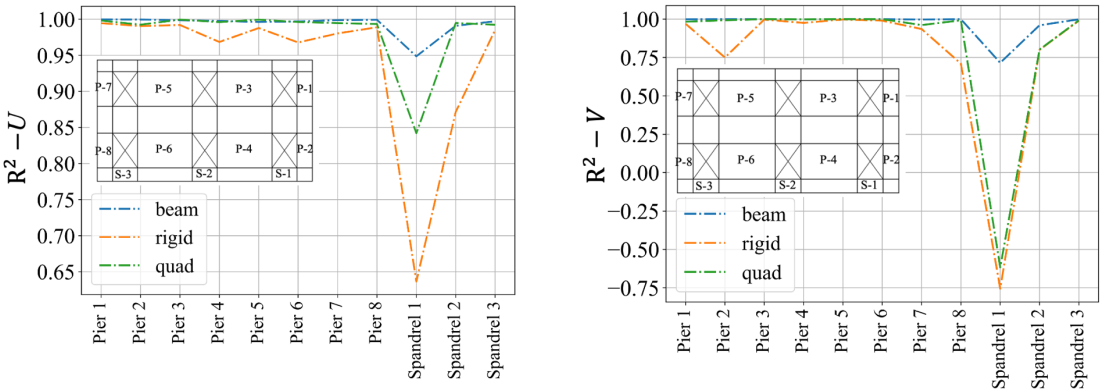
$$R_{ij} = \frac{C_{ij}}{\sqrt{C_{ii}C_{jj}}} \tag{5.10}$$

where C_{ij} is the covariance of two variables, i and j. C_{ii} and C_{jj} are i and j covariance with itself. In the context of the evaluating strain correlation, C_{ii} and C_{jj} may be viewed as the variance of inferred and FE tensile strains, whereas C_{ij} is the covariance between inferred and FE tensile strains.

Consistent with the validation in the first stage, the correlation coefficient of inferred strain using the quad model and FE strain is provided as a reference when assessing the EFA.

5.3.1.2. Evaluation of beam model

In Figure 5.3a-b, remarkably high R^2 values for U, V displacements are observed in both the X and Y directions (as defined in the global coordinate system in Figure 5.1a) for all piers and spandrels (except spandrel 1) when using the beam model, demonstrating excellent fitness. In contrast, the rigid model in Figure 5.3a-b exhibits reduced fitness, particularly at external piers (Piers 2 and 8) on the ground floor, where relatively large distortion is observed. The quad model in Figure 5.3a-b also has good fitness at piers in all directions, though its score falls slightly short compared to the beam model. However, its performance at spandrels is much reduced and significantly worse than the beam model.



(a) (b)

Figure 5.3; R^2 values of the beam, rigid and quad models on displacement fitting at all piers and spandrels. (a) U displacement; (b) V displacement. Piers and spandrels are abbreviated and labelled in the inlet of each figure for ease of reference: 'P-1' for Pier 1, 'S-1' for Spandrel 1, and so on.

The considerable reduction of fitness in all models at Spandrel 1, especially in Figure 5.3b along Y direction, can be attributed to the behaviour of interface elements between the masonry wall and the support beam. In linear analysis, the no-tension property of the interface elements is ignored, and as a result, spandrels are forced to deform together with the support beam, leading to complex responses. In particular, Spandrel 1 is subjected to very small Y displacements due to the constraints from the interface elements, making it prone to 'inflated' reduction in R^2 values for small errors in predictions. On the other hand, Spandrel 3 is least affected due to its close proximity to the screw jack and, therefore, a large displacement experienced. Another factor contributing to the reduced fitness at spandrels is their smaller size relative to piers. As such, the stress concentration near window corners exerts a more significant influence than piers.

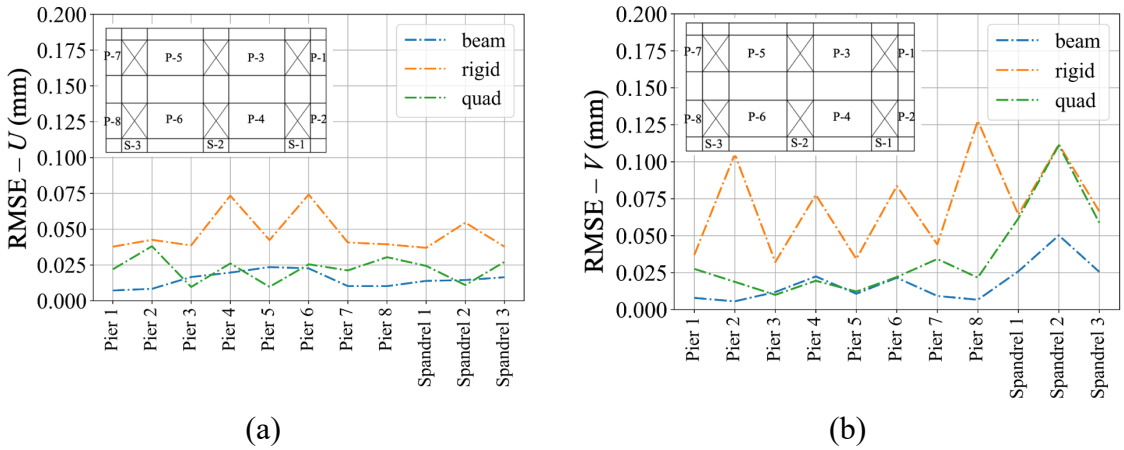


Figure 5.4; RMSE of predicted displacements using the beam, rigid and quad models at all piers and spandrels. (a) *U* displacement; (b) *V* displacement. Piers and spandrels are abbreviated and labelled in the inlet of each figure for ease of reference: 'P-1' for Pier 1, 'S-1' for Spandrel 1, and so on.

In Figure 5.4a-b, the beam model is shown to consistently exhibit low prediction errors across all assessed structural components. Moreover, the displacement predictions from the beam model demonstrate significantly better accuracy at external piers (Piers 1, 2, 7, and 8) and spandrels 1 and 3, when compared to other reference models.

For middle piers (Piers 3, 4, 5, and 6), the quad models in Figure 5.4a show slightly improved predictions along the X direction (*U* displacement) compared to the beam model. This is due

to the shape of the middle piers, which makes them less susceptible to flexure deformation along the width of the pier (X direction). As expected, in Figure 5.4b along the Y direction (i.e. along the length of the pier), both the beam and quad exhibit similar accuracy. On the other hand, the poor performance from the rigid model in Figure 5.4a-b suggests there is considerable distortion experienced in the assessed structural components.

5.3.1.3. Evaluation of EFA strain output

Figure 5.5a-b presents a comparison of inferred strains from all piers and spandrels as derived by EFA using the beam model along with results from FE. Despite the fact that EFA utilises a relatively coarse beam model, the strain distributions across all piers show striking similarity, suggesting the beam model aptly represents the kinematics inherent in those structural components.

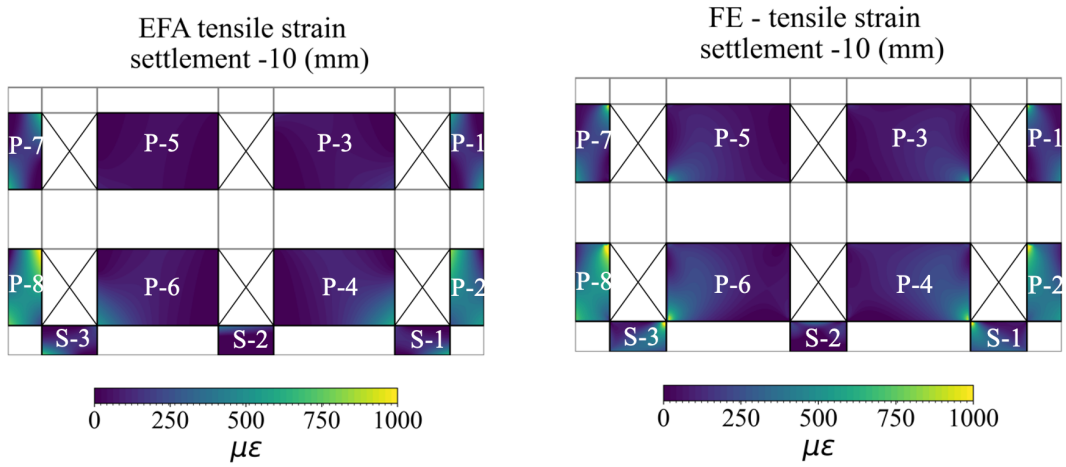
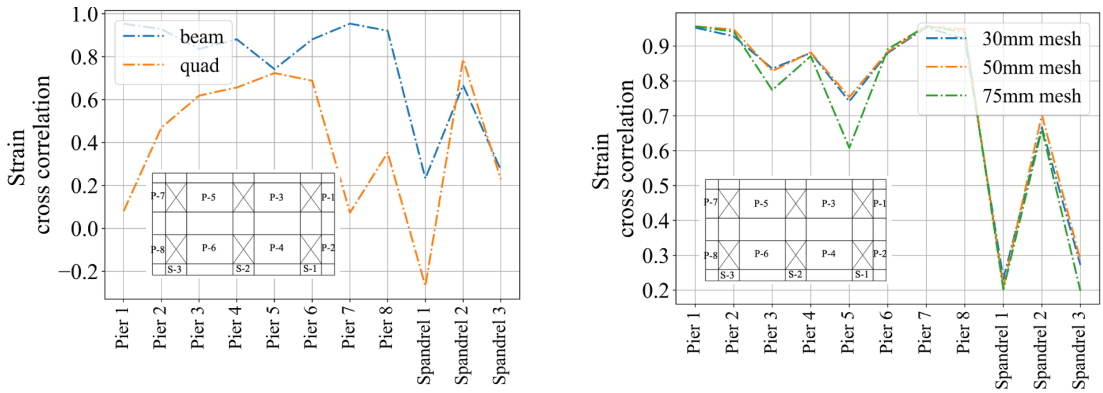


Figure 5.5; (a) Strain distribution interpreted from EFA, employing the beam model at all piers and spandrels. (b) FE strain outputs at all piers and spandrels. Diagonal crosses denote the positions of window openings. Piers and spandrels are abbreviated and labelled in each figure for ease of reference: 'P-1' for Pier 1, 'S-1' for Spandrel 1, and so on.

In Figure 5.5b, the top right corner of Spandrel 1 and the top left corner of Spandrel 3, both exhibit pronounced tensile strain, indicating effects of strain concentration near the window corners. However, the strain pattern elsewhere in these two elements appears to be successfully captured by EFA. Conversely, also in Figure 5.5b, it can be noted that Spandrel

2 exhibits less intense strain concentrations near its top corners. The tensile response at the top of spandrel 2 is clearly represented by EFA.

The notable similarity between strains interpreted from EFA using the beam model and the FE results in piers (as shown in Figure 5.5a-b) is evidenced by the consistently high correlation coefficient (depicted by the blue line in Figure 5.6a). The reduced correlations observed at Piers 3 and 5 can primarily be attributed to their lower strains from deformation – the impacts of errors from target displacement (through nearest node search) and strain concentration start to play a more significant role here.



(a) (b)

Figure 5.6; (a) The correlation between EFA strains derived from both the beam model and the quad model and the corresponding FE outputs at all piers and spandrels. (b) the correlation between EFA strains, computed using the beam model, and the FE outputs at varying mesh sizes of 30mm, 50mm, and 75mm at all piers and spandrels. Piers and spandrels are abbreviated and labelled in the inlet of each figure for ease of reference: 'P-1' for Pier 1, 'S-1' for Spandrel 1, and so on.

In contrast, strains interpreted through the application of the quad model exhibit a significantly poorer correlation with FE results (represented by the amber line in Figure 5.6a), notwithstanding the fact that the model demonstrates reasonable fitness and prediction accuracy with respect to displacements, as shown in Figure 5.3a-b and Figure 5.4a-b. Even in the case of stocky piers (Piers 3, 4, 5 and 6), where the quad model demonstrates marginally superior prediction accuracy in *U* displacement, the strain output in Figure 5.6a from the quad model does not correlate well with FE results.

Also evident in Figure 5.6a, the strains from EFA using the beam model display a reduced correlation with the FE strains at spandrels. The reasons for this are twofold. Firstly, the line interface elements between the spandrels and the supporting beam have constrained the affected spandrels' response in the FE linear analysis, forcing the spandrels to deform with the beam. This phenomenon limits the beam model's ability to accurately capture the response. However, such constraints are considered to be very limited in the physical test, particularly under tension. Secondly, the high-intensity strains resulting from strain concentration overshadow the relatively lower-intensity strain caused by underlying deformation. Given that spandrels are smaller in size than piers, strain concentrations have a more pronounced impact on their correlation coefficient. Spandrel 2, which is least affected by strain concentration (contrast Figures 5.5a and Figures 5.5b), sees the best cross-correlation between strains from EFA and FE among all spandrels. The influence of strain concentrations is expected to diminish as the strains resulting from underlying deformation become more dominant.

Figure 5.6b presents a comparison of correlations between strains interpreted from EFA using the beam model and corresponding FE strains of mesh sizes of 30mm, 50mm and 75mm. It is noteworthy that as the mesh coarseness increases, there is an expectation of increased displacement errors at DIC targets (from which EFA utilises to derive its model parameters). This increase is due to the expected distance from a target location to its nearest FE nodes growing from 15mm with a mesh size of 30mm, to 25mm and 37.5mm as the mesh size expands to 50mm and 75mm, respectively.

Despite the increased target displacement errors, the EFA-interpreted strains generally display consistent correlation results with FE outputs across all piers and spandrels, as evident in Figure 5.6b. This observation supports the assertion that EFA when employing the beam model, can reliably capture the underlying strains resulting from the deformation.

The significant reduction of correlation at Piers 3 and 5 for 75mm mesh size further substantiates the previously mentioned impact of displacement errors at DIC targets on correlation results when the underlying strain from deformation is low.

5.3.2. Validation of EFA with synthetic data from nonlinear FE analysis

5.3.2.1. Methodology

In the nonlinear validation, nodal displacements and crack widths at various tip settlements are exported from the nonlinear FE analyses of 3O-RF-W3. The masonry wall of the nonlinear model utilises a mesh size of 30mm. Displacements of DIC targets and beam model parameters are then determined in the same manner as delineated in Section 5.3.1.1.

Given that the total strain crack model (Rots, 1991) is incorporated in the nonlinear analysis, the linear beam model is not expected to fully capture the kinematics of the damaged structural components. Consequently, the first stage of validation only assesses the predictive accuracy of the beam model with respect to displacements in the presence of cracks using RMSE (root mean square error). This evaluation of the predictive accuracy of the beam model reflects the extent to which the model captures the kinematics. RMSE, concerning the interpreted displacements utilising the beam model and nonlinear FE outputs, is evaluated in the same manner as outlined in Section 5.3.1.1.

Instead of directly evaluating the correlation of strains using the Pearson correlation coefficient, the second validation stage investigates the degree to which the linearly interpreted strain, using the beam model, can reflect the damage state of a structural component. To this end, maximum tensile strains within each structural component are linearly interpreted by EFA employing the beam model. Subsequently, a damage class is assigned to each structural component based on the standard strain-damage correlation

(Table 3.6). These damage class estimations are then contrasted with FE indications for damage class on the basis of predicted crack width.

5.3.2.2. Evaluation of the beam model

The evaluated RMSE, depicted in Figure 5.7a-b, seems to increase primarily in a linear fashion with the widening of the crack width in both directions. The rate of this increase appears to be largely contingent on the crack's direction and location. As depicted in Figure 5.7a-b, it is apparent that up until 0.5mm crack width, the RMSE in both directions remains very low, and is considered comparable to the RMSE assessed in the linear range using the beam model (refer to Figure 5.4a-b).

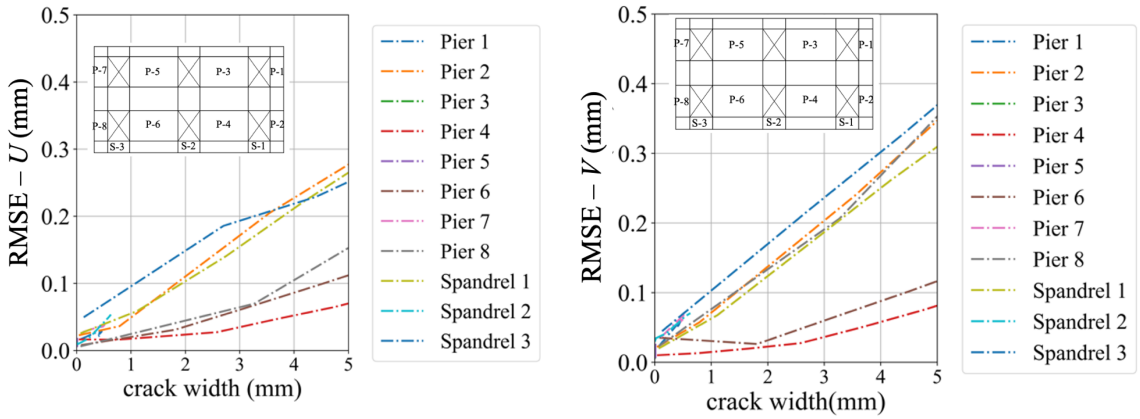


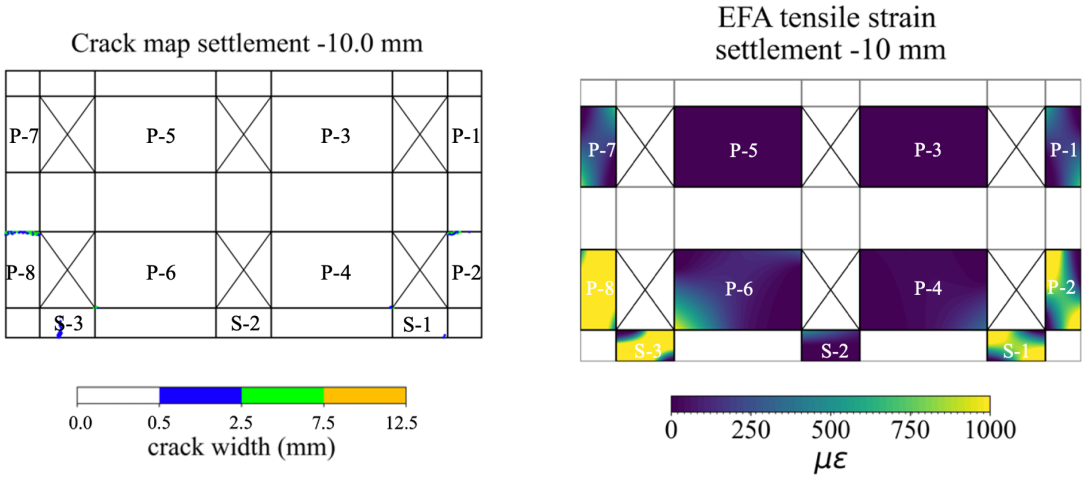
Figure 5.7; RMSE, derived from comparing the interpreted displacements using the beam model and the nonlinear FE outputs for all piers and spandrels. (a) *U* displacement; (b) *V* displacement.

This comparison indicates the model maintains its ability to capture the kinematics until significant cracking occurs. Depending on the specific structural component, from 1mm (as evidenced by Spandrel 3 in Figure 5.7a-b, which exhibits the fastest rate of RMSE increase with crack width) to approximately 5mm crack width (as shown by Pier 4 in Figure 5.7a-b, which exhibits the slowest rate of RMSE increase with crack width), the beam model may still achieve an RMSE less than 0.1mm. This outperforms the rigid model and the quad model in the linear range in some cases (contrast with Figure 5.4). This observation suggests that, for cracks within this range, the beam model may still reflect the underlying

deformation to a certain extent. Beyond a crack width of 5mm, it becomes progressively challenging for the beam model to capture the structural component's response.

5.3.2.3. Evaluation of EFA strain output

At a 10mm beam tip settlement, the FE analysis indicates the development of moderate cracks (as classified by Table 3.6) in several ground-floor structural components. Specifically, as shown in Figure 5.8a, Piers 2, 6, and 8, as well as Spandrels 1 and 3, have registered maximum crack widths of 3.55mm, 3.1mm, 6.98mm, 2.74mm, and 4.4mm, respectively. Concurrently, these elements exhibit significant tensile strains as inferred from EFA, as shown in Figure 5.8b, suggesting a correlation between EFA-derived strain and the structural components' damage state. Moreover, it is worth highlighting the strain distribution within these elements, as displayed in Figure 5.8b; aside from Pier 8, the strain distribution in the other damaged elements appears to continue reflecting the expected underlying deformation at their respective locations, even for crack widths up to 4.4mm (for comparison, see Figure 5.5b). This observation implies that the EFA-derived strain, even after significant damage, may still represent the deformation leading to such damage.



(a) (b)

Figure 5.8; (a) Cracks in all piers and spandrels of 3O-RF-W3 as per nonlinear FE analysis corresponding to 10mm beam tip settlement. The sizes of presented cracks are indicated by the colour bar; (b) Strain distribution interpreted from EFA, utilising displacements from nonlinear FE analysis and employing the beam model at all pier and spandrel locations. Piers and spandrels are abbreviated and labelled in each figure for ease of reference: 'P-1' for Pier 1, 'S-1' for Spandrel 1, and so on.

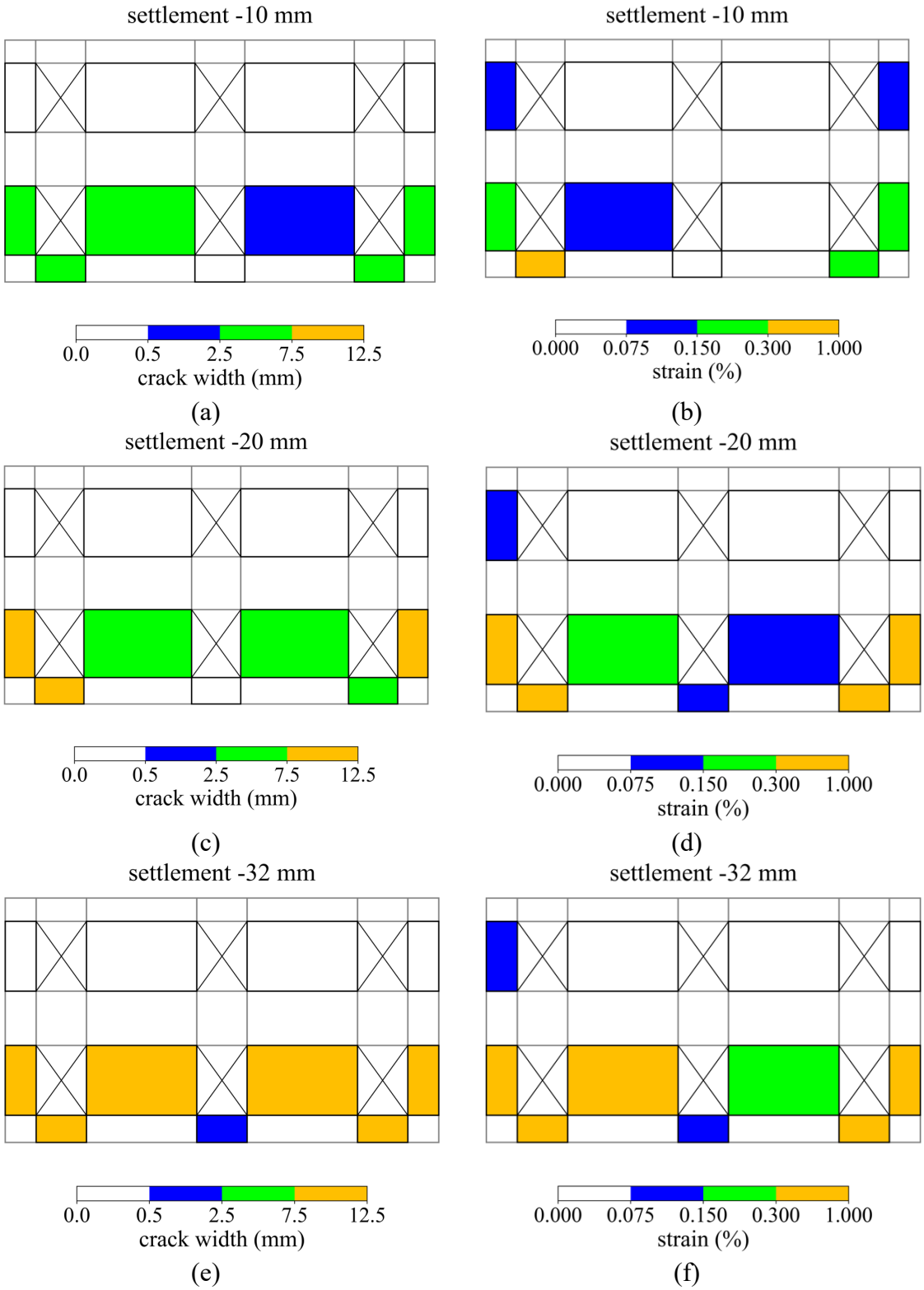


Figure 5.9; (a) (c) (e) Damage category of pier and spandrel components (highlighted with black boundary lines) of 3O-RF-W3, determined based on the maximum FE crack width in that structural component at 10, 20 and 32mm beam tip settlements; (b) (d) (f) Damage category of pier and spandrel components (highlighted with black boundary lines) of 3O-RF-W3, determined based on the maximum interpreted tensile strain from the EFA at10, 20 and 32mm beam tip settlements.

Figure 5.9 compare damage classes determined by crack width as indicated by the FE model (Figure 5.9a,c,e) and by EFA-derived strain (Figure 5.9b,d,f) for each pier and spandrel at

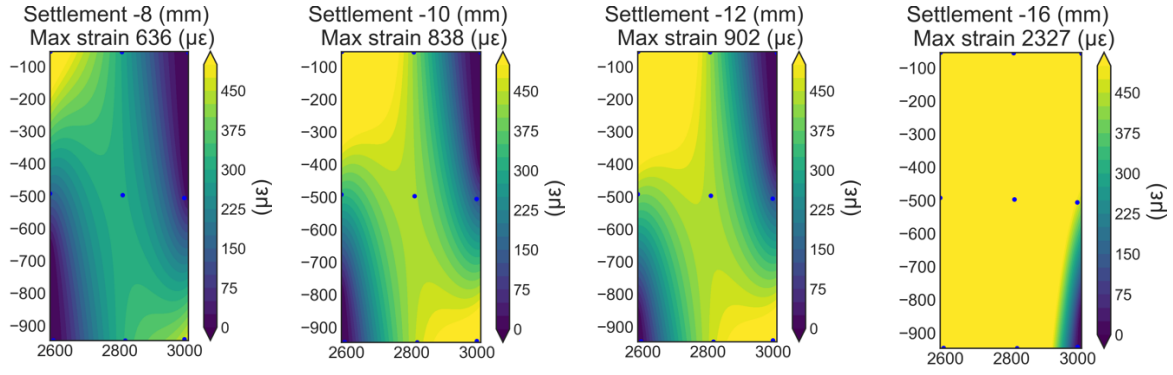
various induced beam tip settlements. Colour codes in Figure 5.9 reflect the corresponding damage class for each structural component, using either the crack or strain criterion, employing the standard strain-damage correlation in Table 3.6. Generally, there is a notable similarity between the damage classes assigned to the structural components using these two approaches. This similarity further supports the proposition that some form of correlation exists between the damage state (measured by maximum crack width) and the EFA-derived strains. The EFA-derived strain demonstrates its ability to track the initiation and progression of damage, despite a few discrepancies regarding severity, particularly at the induced settlements of 10mm and 20mm (as shown in Figure 5.9a-d). Given the total strain crack model used in the analysis tends to smear cracks and underestimate crack width (Rots, 1991), a precise correlation between the EFA-derived strain and crack widths is not further explored at this stage.

5.4. Application to the large-scale building settlement test

5.4.1. Sample strain calculation

When EFA is applied to the large-scale building settlement test, the displacement data of targets are directly taken from DIC measurements. Implementing EFA, Figure 5.10 illustrates the strain distribution of Pier 2 of 3O-RF-W3 at various beam tip settlements. At 8mm settlement, the EFA results in Figure 5.10a show the upper left and lower right corners were subjected to tensile strain concentration. At this stage, no damage was observed on the pier, and the strain distribution derived from EFA conformed to the expected deformation patterns. The RMSE of 6.25×10^{-2} mm between measured and fitted displacements over 9 DIC targets suggests the kinematics of the pier is reasonably captured by EFA. As the settlement increased from 8mm to 10mm, the maximum tensile strain rose from 636 $\mu\varepsilon$ to 838 $\mu\varepsilon$. A crack emerged at the lower right corner of the pier at a 9.6 mm settlement and

was measured at 0.58mm width at a 10mm settlement. The RMSE increased to 8.16×10^{-2} as a result. The location at which the crack was first developed corresponds to a strain concentration area suggested by the EFA. When the settlement reached 12mm, the maximum tensile strain increased to 902 $\mu\varepsilon$, with a maximum crack width of 0.88mm. The RMSE remained relatively small at 1.09×10^{-1}, meaning despite the development of the crack, strain results from EFA are expected to reflect the underlying deformation. As the settlement increased to 16mm, the maximum tensile strain reached 2327 $\mu\varepsilon$, and the crack width widened to 2.17mm. This relatively large crack significantly impacts the interpreted strain results (see Figure 5.10d) and further worsens the RMSE to 4.17×10^{-1}. During the early stage of crack development, it is observed that the maximum tensile strain grows commensurately with crack width, despite the accuracy of displacement fitting suffering a decreased quality. However, the correlation between observed crack widths and the maximum tensile strains derived from EFA in this structural component diverged considerably from the standard correlation in Table 3.6.



(a) (b) (c) (d)

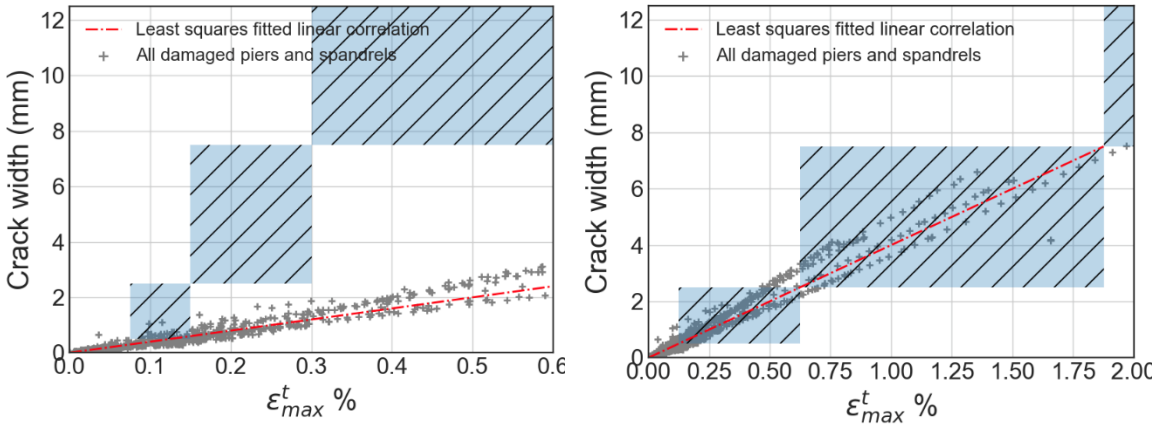
Figure 5.10; Interpreted strain distribution using EFA in Pier 2 of 3O-RF-W3 at the beam tip settlements of (a) 8mm; (b) 10mm; (c) 12mm; (d) 16mm. Corresponding observed crack widths at these settlements are 0mm, 0.58mm, 0.88mm, and 2.17mm, respectively.

5.4.2. Tensile strain – damage correlation

To further explore and generalise the observations in Section 5.4.1, the maximum tensile strain ε_{max}^{t} in each pier and spandrel is determined from the DIC measurements employing the EFA procedures in Section 5.2 at each stage in the test. The maximum crack width

observed in each pier and spandrel via DIC at the same stage is then correlated with the calculated maximum tensile strain in the same pier/spandrel that experienced the crack. This correlation—collected together for all of the four building tests—is illustrated in Figure 5.11a.

The data in Figure 5.11a indicate a remarkably consistent linear correlation between maximum tensile strain and maximum observed crack width. However, the correlation does not map well onto the standard tensile strain–crack width correlations; data from the EFA indicate that maximum observed crack widths correlate with larger strain magnitudes than is the case with the standard correlations. This difference is likely a result of the different 'length measure' embedded in the empirical strain damage–correlation and the length measures considered in the strain interpretation proposed in this chapter. The empirical correlations consider typical building length scales while the proposed interpretation procedures refer to experimental building component (e.g. pier) length scales.



(a) (b)

Figure 5.11; (a) Correlation between maximum tensile strain (ε^t_{max}) estimated from the EFA and observed maximum crack width for all damaged piers and spandrels of all four building tests (14 no. in total), except two piers from 3O-JF-W1 where anomalously large cracks were developed. The hatched grey boxes indicate the standard correlations (see Table 3.6). (b) Re-scaled plot with proposed strain–crack width correlations for the EFA approach.

An alternative strain–damage correlation is therefore proposed as indicated in Table 5.1; these correlations are illustrated in Figure 5.11b. It is clear that the alternative correlations provide an improved representation of the data.

Table 5.1; Proposed damage classification for use with the EFA approach.

Damage category	Crack size (at model scale)	Strain range
Slight	0.5 – 2.5	0.125% - 0.625%
Moderate	2.5 – 7.5	0.625% - 1.875%
Severe	7.5 – 12.5	1.875% - 3.125%

To highlight the need for a new correlation an exercise has been conducted in which—for each building at each stage in the test—values of maximum tensile strain estimated from the beam models are compared with maximum tensile strain (for the façade as a whole) estimated from the EFA approach. Results are plotted in Figure 5.12. It is clear that the strains detected by the EFA are systematically larger than those estimated by the DBA. This is an unsurprising outcome; the presence of openings in the façade would be expected to concentrate building strains in the piers and spandrels. It is not claimed that the data in Table 5.1 represent a definitive correlation for future damage assessment analysis. Further work is needed to confirm the numerical values of the correlations and also to consider whether the correlations should incorporate a representation of masonry material parameters. It is suggested, however, that the appropriate correlations between tensile strain and crack damage—when tensile strains are calculated at the level of individual piers/spandrels—will be expected to differ considerably from the standard correlations.

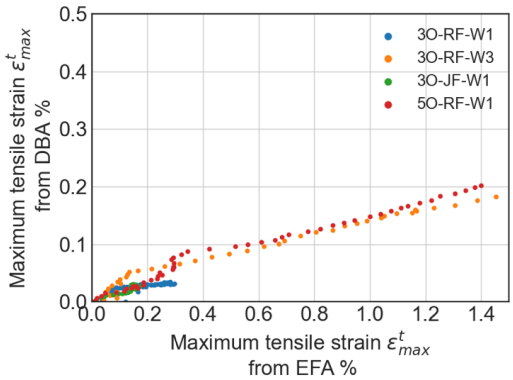
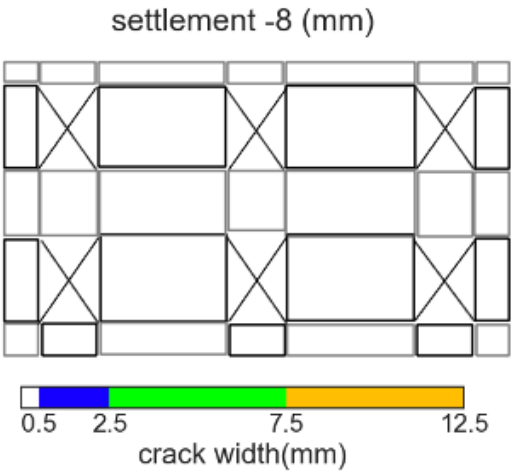


Figure 5.12; Maximum values of estimated tensile strain from the DBA compared with maximum values of estimated tensile strain of all piers and spandrel components of the same building model from the EFA throughout each test.

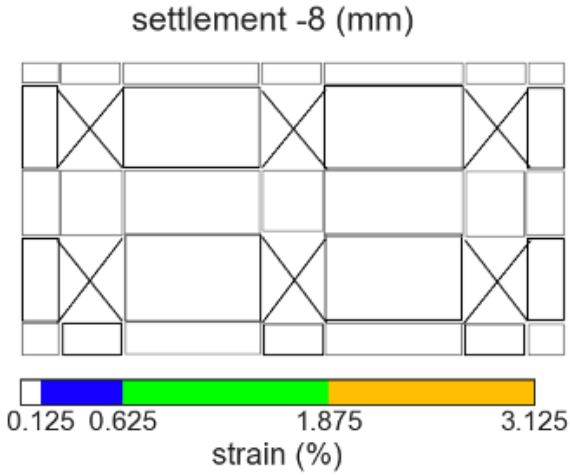
5.4.3. Crack size–tensile strain maps

Consistent with the nonlinear validation of EFA strain in Section 5.3.2.3, maps have been developed in which individual piers and spandrels are colour coded according to their damage category. The damage category is determined in two ways: Approach 1 uses the maximum observed crack width in the pier/spandrel to derive the damage category (following standard crack width and damage correlations in Table 3.6). Approach 2 uses the maximum tensile strain estimated from EFA to determine the damage category on the basis of the correlation in Table 5.1.

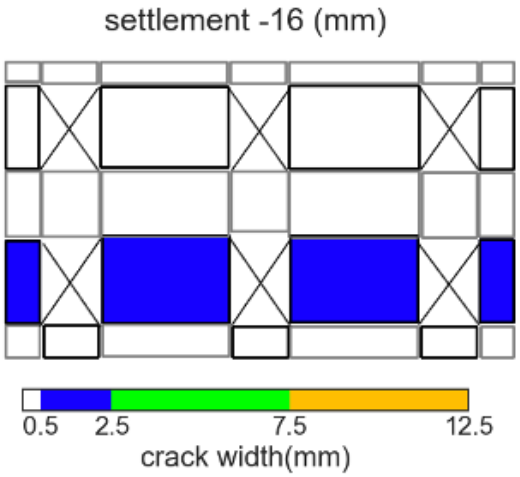
Maps for 3O-RF-W3 are indicated in Figure 5.13, using Approach 1 (left column) and 2 (right column) for increasing beam tip settlements. These maps demonstrate a strong correlation between damage category assigned from crack width observations (Approach 1) and from the proposed crack size–strain correlation (Approach 2). There are, however, a few anomalies. From an early stage in the test the right external pier on the first storey has been assigned a slight damage category, despite no crack being observed in this pier. There is also a slight mismatch between implied damage categories for the right internal pier on the ground storey during the later stages of settlement. On the basis of observed crack width, the damage would be classified as ‘moderate’ whereas—on the basis of the EFA—the damage is classified as ‘slight’. In fact, the EFA estimate for the maximum tensile strain in this pier is only marginally less than the slight-moderate threshold.


settlement -8 (mm)
0.5
2.5
7.5
12.5
crack width(mm)

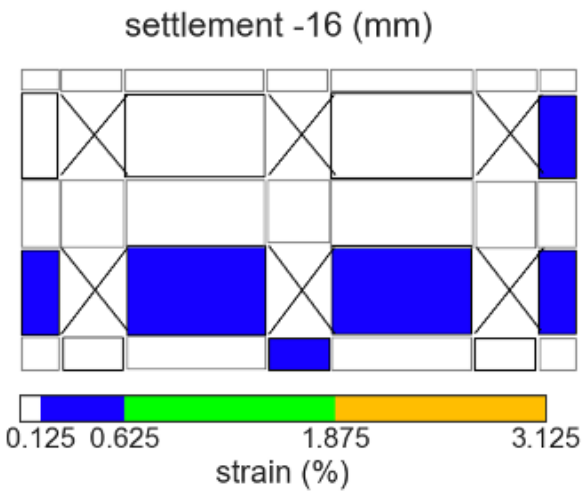
(a)


settlement -8 (mm)
0.125
0.625
1.875
3.125
strain (%)

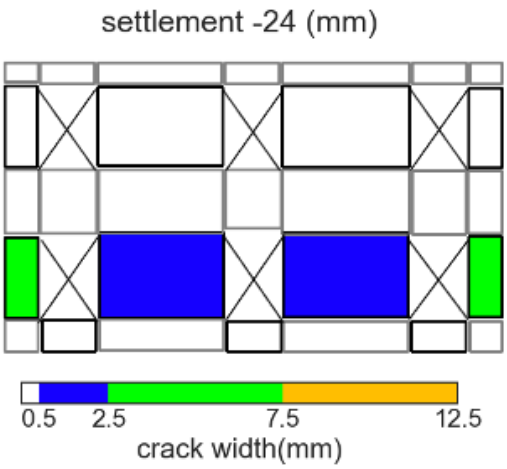
(b)


settlement -16 (mm)
0.5
2.5
7.5
12.5
crack width(mm)

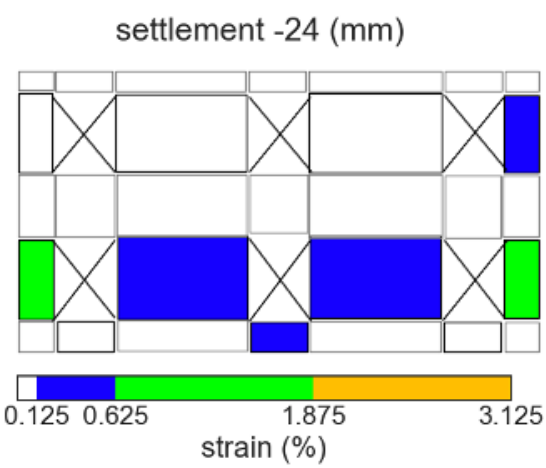
(c)


settlement -16 (mm)
0.125
0.625
1.875
3.125
strain (%)

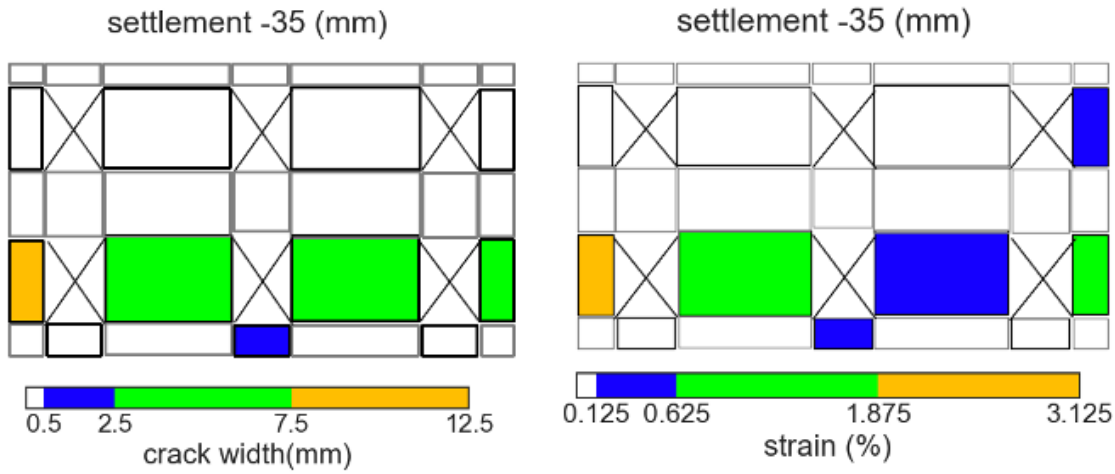
(d)


settlement -24 (mm)
0.5
2.5
7.5
12.5
crack width(mm)

(e)


settlement -24 (mm)
0.125
0.625
1.875
3.125
strain (%)

(f)



(g) (h)

Figure 5.13; (a) (c) (e) (g) Damage category of pier and spandrel components (highlighted with black boundary lines) of 3O-RF-W3 based on the maximum observed crack width at 8,16 and 24 and 35mm beam tip settlements (Approach 1); (b) (d)(f) (h) Damage category of pier and spandrel components (highlighted with black boundary lines) of 3O-RF-W3 based on the maximum interpreted tensile strain from the EFA at 8, 16, 24 and 35 mm beam tip settlements (Approach 2). Two additional targets above the left external pier on the ground storey were used in EFA to derive maximum tensile strain, due to the observed crack (crack 1 in Figure 4.3c) run through DIC targets placed at the top of the pier. The diagonal crosses in the maps denote window opening.

Figure 5.14 shows the maps for 50O-RF-W1 at three values of beam tip settlement. It is clear that the tensile strain criterion in Approach 2 is highly effective at identifying the presence of cracks, although the damage category on the first storey appears to be overestimated. No physical damage was observed on the first storey but it is possible that small cracks (which may qualify the pier for a slight damage category) at this less accessible location were missed. An increase in maximum tensile strains on the first storey is likely a result of the observed considerable bending in external piers. This statement is supported by the distortions evident in Figure 4.5d and earlier numerical simulations by Dalgic et al. (2021).

In all examined cases, the EFA has located and captured the propagation of the damage reasonably well. The method highlights, from early stages, structural components which are experiencing distress, enabling further monitoring and intervention activities.

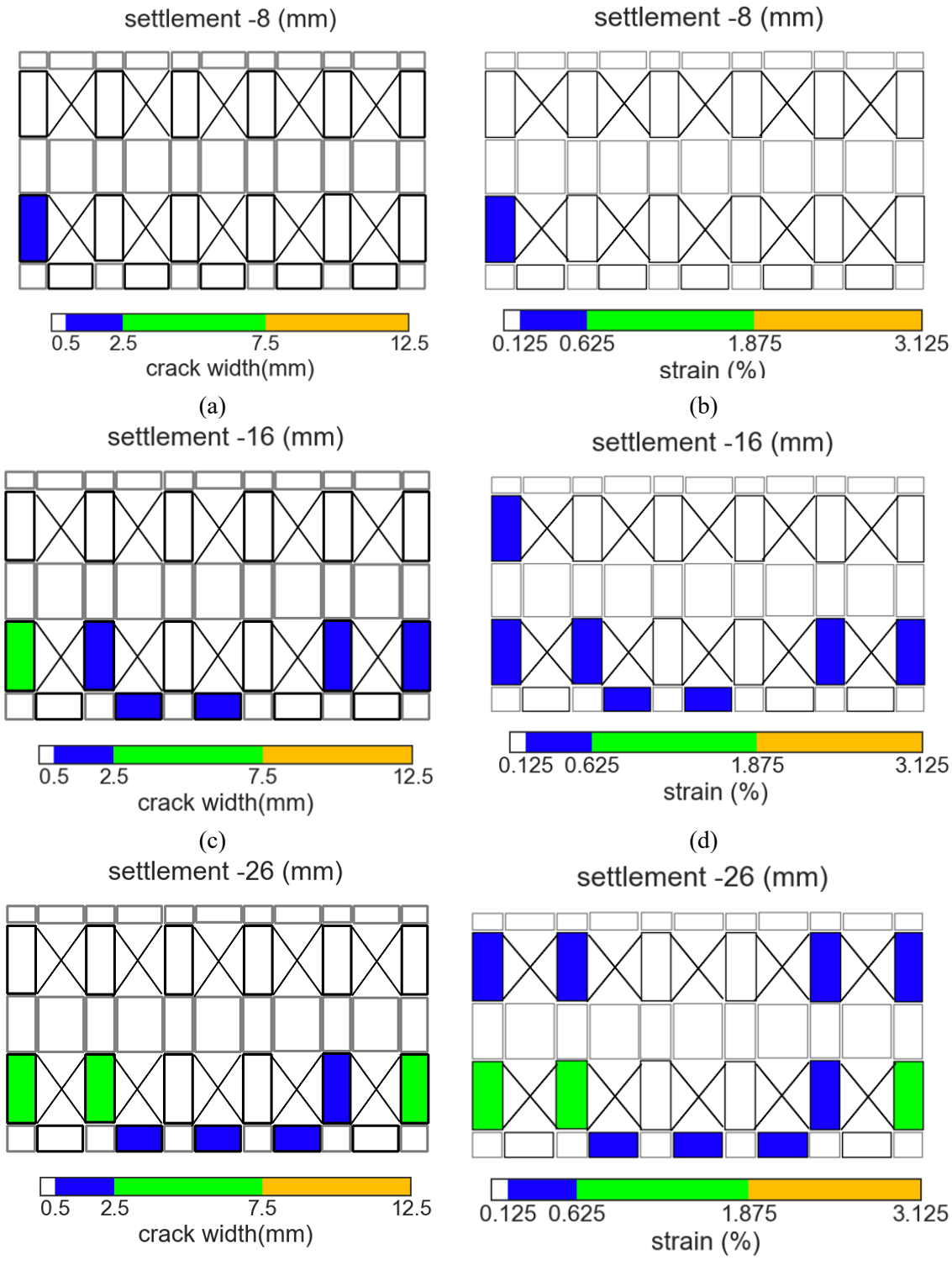


Figure 5.14; (a) (c) (e) Damage category pier and spandrel components (highlighted with black boundary lines) of 50O-RF-W1 based on the maximum observed crack width at 8,16 and 26mm beam tip settlements (Approach 1); (b) (d)(f) Damage category of pier and spandrel components (highlighted with black boundary lines) of 50O-RF-W1 based on the maximum estimated tensile strain from the EFA using DIC displacement data at targets at 8, 16, 26mm beam tip settlements (Approach 2). Three additional targets above the right external pier on the ground storey were used in EFA to derive maximum tensile strain, due to the observed crack (crack 1 in Figure 4.5c) run through DIC targets placed at the top of the pier.

5.5. Conclusion

Compared to equivalent beam methods, the EFA approach presented in this chapter offers a higher fidelity procedure, applying beam models to the individual piers and spandrels in the building. The validity of such representation and discretisation was initially investigated using outputs from linear and nonlinear FE analyses of a reference building model (3O-RF-W3) subjected to induced settlement.

Specifically, the EFA's ability to capture displacements in piers and spandrels was evaluated against FE nodal displacements in those structural components, using statistical measures R^2 and RMSE. Generally, compared to quad and rigid models, the EFA displayed a higher R^2 and significantly lower RMSE, indicating that it captured not only the rigid body motion but also the relative distortion. This assertion was further substantiated by the high correlations between the tensile strains inferred from the beam model and the FE outputs. In the nonlinear range, the beam model demonstrated its capability to continue capturing the kinematics even after the onset of cracks. The results, benchmarked with nonlinear FE outputs, revealed that up to a 0.5mm crack width, the RMSE of the EFA's predictions on displacements remained comparable to the RMSE assessed in the linear range. Furthermore, depending on the specific structural component, up to a 5mm crack, the EFA was able to maintain an RMSE less than 0.1mm. Overall, the FE validation suggests that the EFA method can accurately reflect the underlying kinematics to a considerable degree, even post-cracking.

The nonlinear FE results were also utilised to investigate the EFA method's ability on indicating damage. A notable similarity was observed between the damage classes assigned to the structural components, using the crack width and the maximum strain derived from

the EFA. However, a precise correlation was not further explored at this stage, as the crack model employed in the nonlinear FE analysis tends to smear and underestimate crack width.

When applied to large building settlement tests, the predictions of displacements by the EFA were first compared with DIC measurements to assess RMSE. The findings were consistent with that from FE validation, showing that RMSE remained low until cracks widened considerably. Moreover, the interpreted maximum tensile strains from the EFA appeared to exhibit a linear relationship with crack width. However, the standard crack width–tensile strain correlation does not seem to be appropriate for the EFA model at the level of individual structural components. An alternative correlation—where the limiting tensile strain values are larger than those in the standard correlation, as shown in Table 5.1—is proposed for use with the EFA model. Utilising the proposed correlation, the EFA approach has been demonstrated to provide an excellent indication of damage in terms of both intensity and location.

Although this chapter is concerned with the processing of monitored data, the findings have implications for the prediction of damage categories within a building prior to underground construction. In current practice, the damage category is typically predicted by applying assumed ground movements to an equivalent beam model of the building and classifying the damage on the basis of the standard correlations. If alternative assessment procedures are used in which a higher fidelity structural analysis (such as a finite element model or an equivalent frame model) then the adoption of the standard tensile crack width–tensile strain correlation could lead to over-conservative damage assessments.

The adoption of higher fidelity methods for damage assessment, such as the EFA, would require a larger number of displacement measurement points than currently adopted in practice. While DIC was used to obtain the experimental data in this chapter, surveying techniques commonly used in engineering practice for displacement monitoring, such as

electronic distance measurement using total stations, can be readily used for this purpose. Alternative techniques, such as laser scan displacement monitoring are also an option, which is explored in the following chapters.

6. Introduction to point cloud-based equivalent frame approach (PC-EFA) and validation using synthetic dataset

6.1. Purpose

Chapter 5 highlighted that the adoption of the EFA idealisation in building damage assessment can produce informative strain results that reveal underlying deformation. It also indicates damage in terms of both location and severity. Although the proposed method is versatile regarding its source of input displacement data, applying it with traditional monitoring approaches, such as geodetic surveys, necessitates a large number of monitoring points on each discretised structural component. To overcome this limitation, this chapter introduces a novel method called 'PC-EFA'. This approach leverages the core principles of EFA and uses point clouds from before and after a deformation event as input data. Like EFA, this method provides tensile strain distribution outputs, which can subsequently be used for structural analysis and damage indication. The proposed PC-EFA is systematically validated using synthetic datasets drawn from linear and nonlinear FE models of a typical masonry building under settlement.

6.2. Methodology

Unlike all other point cloud-based displacement monitoring methods reviewed in Chapter 2, the proposed PC-EFA utilises a validated kinematic representation of a structural component to regulate displacement fields obtained from feature matching. Such representation constrains the solution space while retaining the ability to unveil the underlying distortion. Strain, owing to its differentiative nature, is inherently sensitive to noise present in displacements. As discussed in Chapter 2, displacement analysis using point clouds is generally much noisier than most traditional monitoring methods. For this reason, few researchers have attempted to derive strain measurements from point cloud data. On the

other hand, as demonstrated in the previous chapter, tensile strain has a strong association with damage, especially concerning cracks appearing in masonry. Utilising the EFA idealisation and the beam model to represent piers and spandrels offers a chance to filter out noisy displacements and regulate the strain response accordingly.

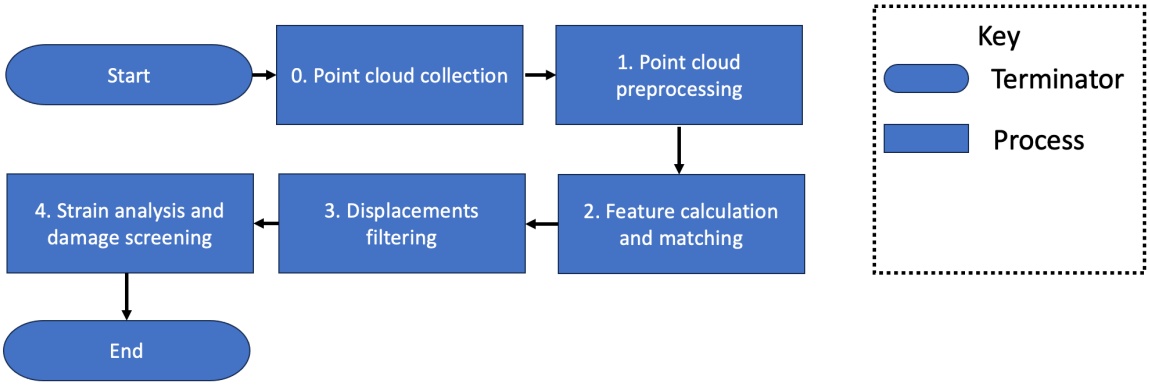


Figure 6.1; Flowchart illustrating the main PC-EFA process.

Figure 6.1 depicts the primary steps of the proposed PC-EFA method. The subsequent sections will describe each step in greater detail.

The proposed method is implemented by a custom Python package, developed as part of this research. The package makes use of several general-purpose libraries, namely 'Open3D' (Zhou et al., 2018) for routine 3D point cloud processing, 'NumPy' (Harris et al., 2020) for conducting numerical operations, and 'Pandas' (The Pandas development team, 2023) for data manipulation and analysis. Unless specifically stated, the 'Matplotlib' (Hunter, 2007) Python library is used for visualising the results in this chapter. Any additional libraries utilised for specific tasks are detailed in the corresponding sections where those tasks are discussed.

It is worth noting that point cloud registration (a substep in Step 1: Point cloud preprocessing) is implemented in Faro Scene. Faro Scene is proprietary software developed by Faro Technologies, tailored for processing and managing point cloud data.

6.2.1. Point cloud collection

The point cloud collection process typically involves performing laser scans of the building under investigation before and after a settlement event. In practice, this can be achieved by conducting routine laser scans at regular intervals during underground construction. While the discussion in this chapter primarily concerns point clouds from terrestrial laser scanning (see Figure 6.2), point clouds from other sources may also be utilised. For instance, these can be obtained through mobile laser scanning, where the scanner is mounted on a moving platform, or reconstructed from 2D images using Structure from Motion (SfM) and Multi-view Stereo (MvS).

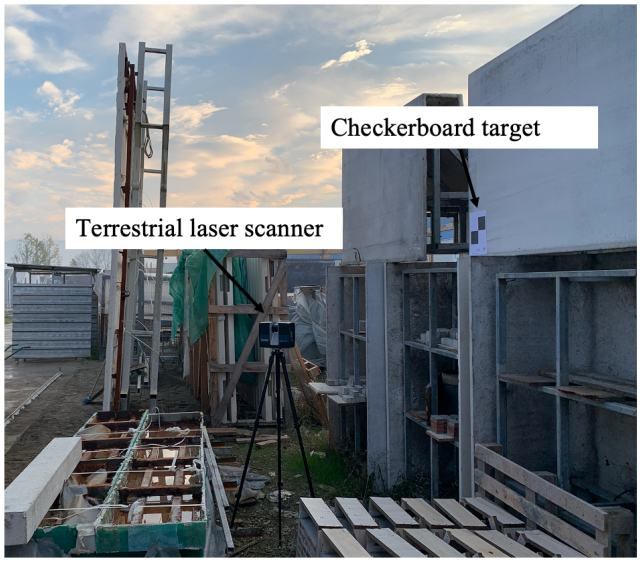


Figure 6.2; A terrestrial laser scanner collecting point cloud data in a factory, with a checkerboard target affixed to a stationary surface.

For displacement monitoring, stationary reference points, such as checkerboard targets with known coordinates, can enhance the accuracy of registering point clouds onto a common coordinate system, a process referred to as ‘registration’ (Section 6.2.2.1). Essentially, checkerboard targets or other artificial targets serve as reference points across multiple scans. Their design facilitates easy identification and coordinate extraction.

6.2.2. Point cloud preprocessing

Point cloud preprocessing involves three standard steps of point cloud manipulation, as depicted in Figure 6.3. It takes raw point clouds as input and outputs segmented clouds for each structural component.

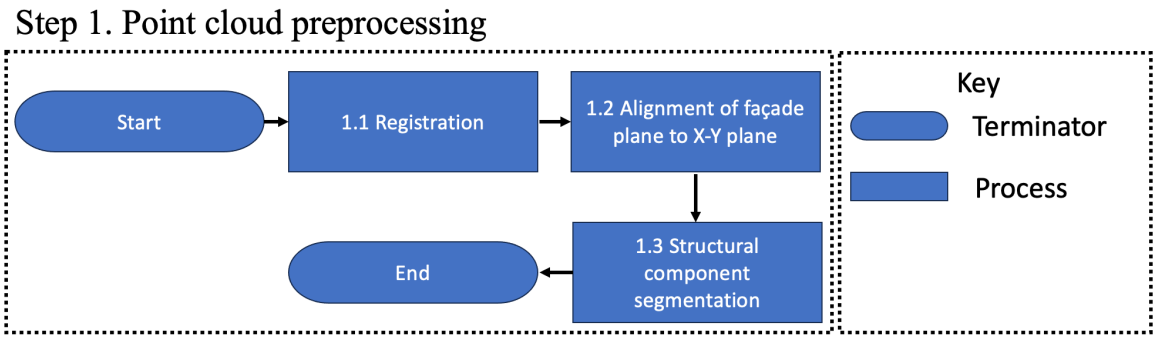


Figure 6.3; Flowchart detailing the point cloud preprocessing steps.

6.2.2.1. Registration

The initial step in point cloud preprocessing involves registering point clouds to a common coordinate system. These point clouds, captured before and after a deformation event, are denoted as pre-test and post-test point clouds, respectively. Here, 'test' signifies a conceptual phase of observation and is concerned with the timing of data collection relative to the deformation event. Typically, a common coordinate system is defined by designating one of the point clouds as the reference and adopting its coordinate system. When a scan is performed, the acquired point cloud resides in a local reference system, specific to the scanner's position and orientation. Figure 6.4 illustrates this concept by visualising the point clouds of a stationary object (an Emirates cabin crew doll) collected at two distinct time instances. Without registration, when plotted together in the coordinate system of Point Cloud 2, the stationary object appears at disparate locations in the visualisation space, as evidenced by the positions of Point Cloud 1 and Point Cloud 2 in Figure 6.4.

The registration of pre-test and post-test point clouds is undertaken using Faro Scene software. Consistent with the software's user manual (FARO Technologies Inc, 2023), Faro

Scene recognises artificial targets within individual point clouds and extracts the coordinates of these targets. When checkerboard targets are utilised, the high contrast between the black and white squares assists Faro Scene in detecting the targets' edges and corners, leveraging variations in laser intensity and geometric properties (Fryskowska, 2019). Conversely, when sphere targets are employed, their distinct geometric properties are utilised for identification.

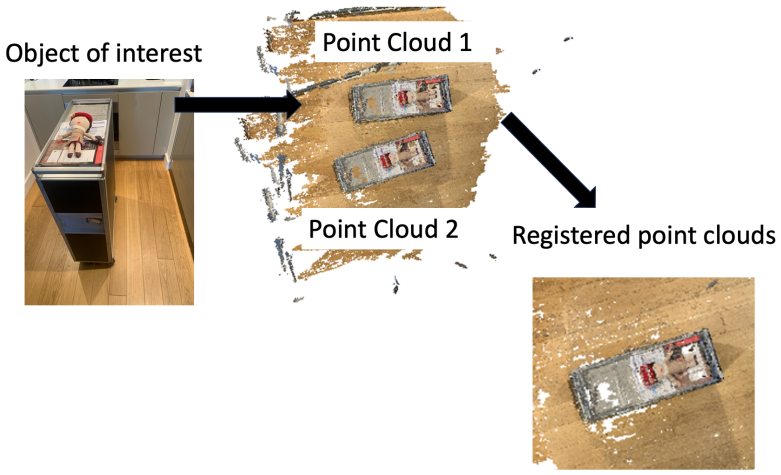


Figure 6.4; Illustration of the process of registering two point clouds of an Emirates cabin crew doll. In this example, Point Cloud 2 serves as the reference cloud. The point clouds, designated as Point Cloud 1 and Point Cloud 2, were collected at separate time instances. When visualised without registration in Point Cloud 2's coordinate system, they appear at different locations within the visualisation space. During the registration, a rigid transformation is applied to Point Cloud 1 to align it to Point Cloud 2's coordinate system. The point clouds were reconstructed using VisualSfM (Wu, 2011) from 47 2D photographs taken by an iPhone.

These automatically identified points, present in both pre- and post-test scans, are typically considered high-confidence point sets, ensuring reliability during registration. This automated method likely offers greater accuracy in determining target positions than manual point picking. Once these point pairs, known as 'tie points', are selected, their positions across different scans help define a rigid transformation relative to the specified reference point cloud. By applying this transformation, another point cloud is registered to the coordinate system of the reference cloud (as illustrated in Figure 6.4). Additionally, if the scanner's inclinometer is used, Faro Scene can leverage the additional information to align the vertical axis of the point clouds to the vertical axis defined by the inclinometer (gravitational vertical) during registration (FARO Technologies Inc, 2023). This reduces both the complexity of registration and the occurrence of errors.

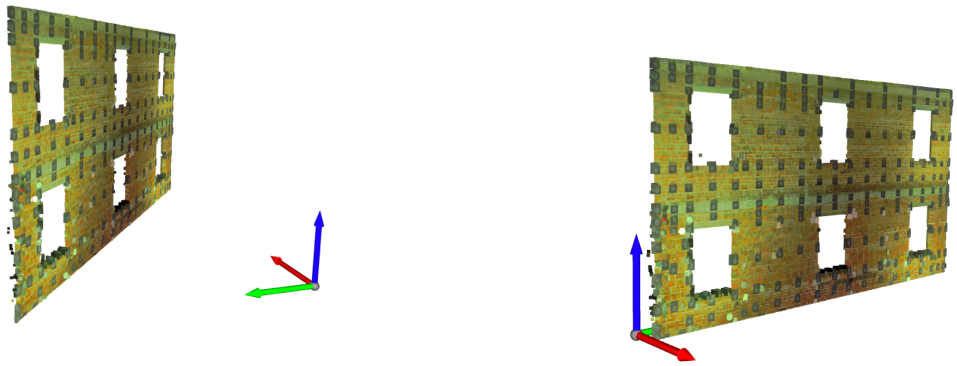
After completing registration, unrelated objects in the registered point clouds are excluded using a bounding box. For buildings, only the point clouds of the masonry façade under investigation are retained; these point clouds are referred to as façade clouds.

It is worth noting that the aforementioned process presumes that checkerboard targets are stationary, meaning there is no relative movement between them. If this is not the case, the absolute coordinates of these checkerboard targets need to be surveyed to compensate for the registration errors, as such errors will subsequently influence the displacement results. Conversely, the derived strains remain unaffected by these errors, as their rigid nature does not induce distortion or additional strain. This concept will be further elaborated on later in this chapter.

6.2.2.2. Alignment of façade plane to X-Y plane

To facilitate displacement and strain calculations, it is beneficial to align the façade surfaces in the registered point clouds to the X-Y plane. Figure 6.5a displays a point cloud of a masonry façade situated in the reference coordinate system following registration. Assuming the scanner's inclinometer was active, implying the scanner's vertical axis aligns with the gravitational vertical (Y direction, upright relative to the earth's surface, as indicated by the blue arrow in Figure 6.5), the plane alignment issue reduces to aligning the façade plane's normal with the desired coordinate plane's normal. In this context, the façade plane's normal is ascertained using principal component analysis (PCA); after centre-aligning the façade points, a covariance matrix is formulated and subsequently decomposed to retrieve eigenvectors. The eigenvector $\bar{v}$ corresponding to the smallest eigenvalue signifies the façade plane's normal. For example, to align the façade plane with the X-Y plane (as outlined in Figure 6.5), an angle between $\bar{v}$ and Z axis is determined. This angle then informs

the creation of a rotational transformation to align the façade cloud. Figure 6.5b illustrates the resultant alignment of the façade cloud to the X-Y plane.



(a) (b)

Figure 6.5; (a) A point cloud of a masonry façade situated in the reference coordinate system following registration; (b) The point cloud of the masonry façade after aligned with the X-Y coordinate plane. The green, blue and red arrows denote the X, Y, and Z directions, respectively.

6.2.2.3. Structural component segmentation

The third step encompasses segmenting piers and spandrels from the façade clouds, in accordance with the façade discretisation strategy outlined in Section 5.2.1. This process employs a bounding box, delineated by the coordinates of a structural component's four corners from the pre-test cloud, with added offsets. These offsets ensure the complete inclusion of the structural component in both pre-test and post-test segmented clouds.

6.2.3. Feature calculation and matching

The feature calculation and matching step establishes the displacement profile of a structural component. This involves four distinct phases, as illustrated in Figure 6.6. The process uses segmented clouds in the X-Y plane from preprocessing as input and yields re-sampled clouds and a correspondence set. For the remainder of this thesis, the term 'point feature' within the context of point cloud processing refers to local geometric properties of a point in its vicinity. While properties of a point, such as colour and intensity values, could also be included in the point feature, these properties generally depend more on the ambient

environment, like light, and on the setup conditions, such as the scanner's position. For this reason, this implementation considers solely geometric properties.

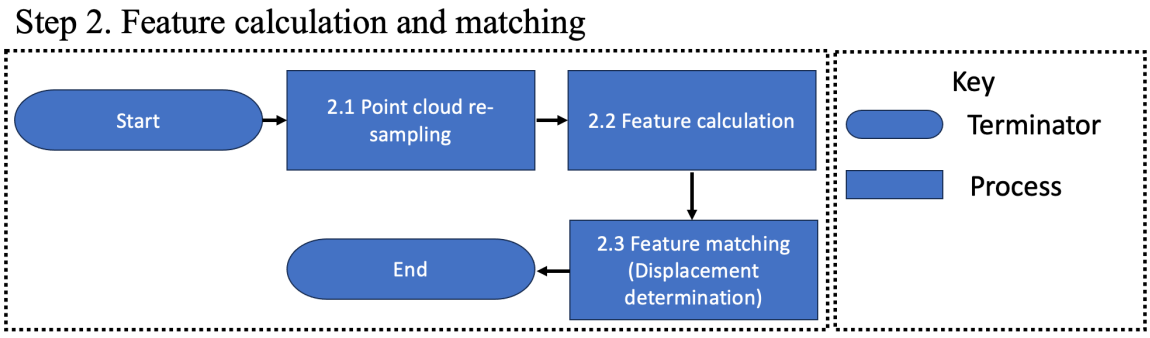


Figure 6.6; Flowchart detailing the feature calculation and matching steps.

6.2.3.1. Point cloud re-sampling

The first phase involves the re-sampling of segmented clouds. This is a standard step in point cloud processing to down-sample a point cloud to a more even density before the calculation and matching of point features. In this thesis, the term 'point density' refers to the average nearest point distance in the point cloud. This provides a more tangible and intuitive measure of point spacing. Under this definition, a smaller average point spacing denotes a denser point cloud, whereas a larger point spacing indicates a sparser point cloud. The re-sampling process generally yields more consistent feature descriptors. This consistency is paramount since subsequent procedures aim to establish correspondences based on feature descriptor matching of pre- and post-test point clouds.

Various factors can produce inconsistent densities across the point cloud. The primary reason for such variations is laser beam divergence. When an object is positioned at a sharp angle relative to the scanner, the effective area impacted by the laser beams on the object's surface expands, leading to fewer points per given area (resulting in a larger nearest neighbour distance).

Because of potential variations in scanner positioning and settings, the densities of pre-test and post-test point clouds for specific structural components might differ. Consequently, in

this method, both the pre-test and post-test point clouds of each structural component are re-sampled based on the higher value of their average nearest neighbour distances. For instance, if the average nearest neighbour distances for the pre- and post-test point clouds of a given structural component are 1mm and 1.2mm respectively, the 1.2mm is multiplied by a factor to set the re-sampling size. In this implementation, voxel size re-sampling is the chosen method, and the factor is fixed at 1.2. This factor ensures that both the pre- and post-test point clouds maintain a similar point density throughout the structural component while retaining the majority of the detail. As illustrated in Figure 6.7, during voxel size re-sampling, the specified re-sampling size (referred to as 'voxel size') is employed to construct a 3D grid over the point cloud space. Each point in the cloud is allocated to a voxel. If multiple points are situated in a single voxel, a new point, obtained by averaging the coordinates of all points within that voxel, is retained.

In this implementation, the voxel-based re-sampling is handled by the Python library Open3D (Zhou et al., 2018).

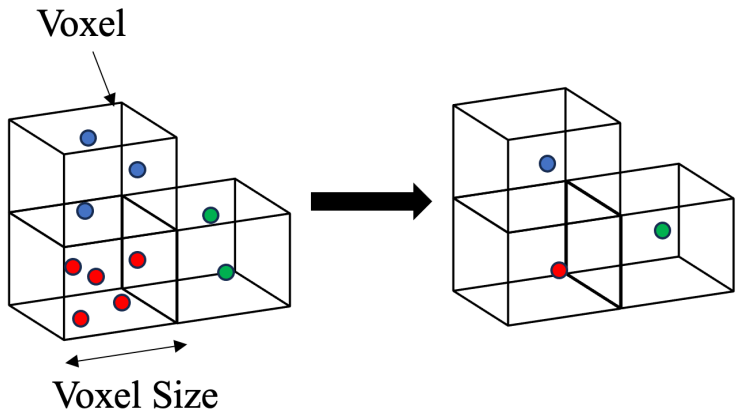


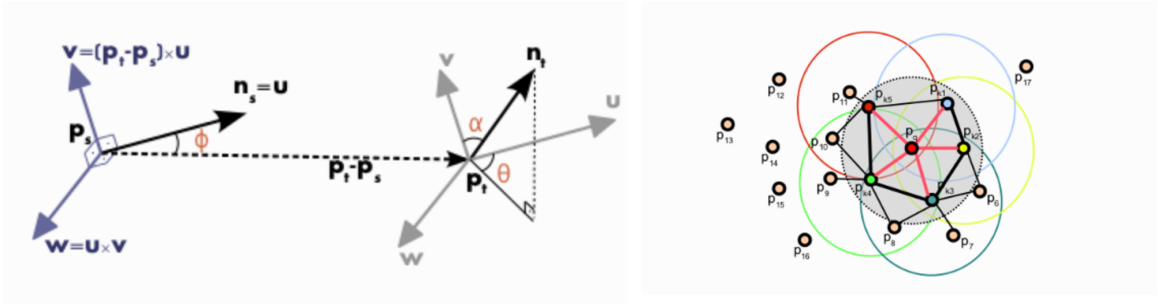
Figure 6.7; Illustration of the voxel size down-sampling process. The specified re-sampling size (referred to as 'voxel size') is employed to construct a 3D grid over the point cloud space. Each point in the cloud is allocated to a voxel. If multiple points are situated in a single voxel, a new point, obtained by averaging the coordinates of all points within that voxel, is retained.

6.2.3.2. Feature calculation

In point cloud processing, features describing certain characteristics or patterns around a point within a local neighbourhood often aid tasks like feature matching and object

recognition. If the local neighbourhood is sufficiently small and the underlying deformation does not drastically alter the feature descriptor, these features or point descriptors can establish correspondence between points in the pre-test and post-test point clouds. Given that the point clouds are registered in the preprocessing step, displacements may be derived using the established correspondences.

In this implementation, the Fast Point Feature Histogram (FPFH) is used as the point feature descriptor. FPFH, a handcrafted descriptor introduced by Rusu et al.(2009), builds on the Point Feature Histogram (PFH) (Rusu et al., 2008) to achieve quicker computation. Essentially, SFPH quantifies each point's normal, geodesic and torsional curvature using histograms and FPFH aggregates Simplified Point Feature Histograms (SPFH) of a point and its neighbours. The SPFH of a point p_s is calculated as follows with a specific radius of *r*:



(a) (b)

Figure 6.8; (a) A point pair and their local *uvw* frame. The relative orientation between points p_s and p_t is characterised by the angles α, ϕ, and θ. (b) The influence region for FPFH. The FPFH of point p_q is determined by its own SPFH as well as the SPFHs of its neighbours (points located inside the shaded area). Both figures reproduced from Rusu et al. (2009).

For the point p_s, a local *uvw* frame is defined, as shown in Figure 6.8a. p_t is a point within radius *r* from p_s. In the local *uvw* frame:

$$u = n_s \tag{6.1}$$

$$v = u \times \frac{(p_t - p_s)}{\|p_t - p_s\|_2} \tag{6.2}$$

$$w = u \times v \tag{6.3}$$

where p_s and p_t are 3 ×1vectors representing coordinates of specific points in 3D space and n_s represents the estimated normal of point p_s. The symbol '×' denotes the cross-product operator and the notation ' $\| \|_2$' represents the second norm operator, which measures the length of a vector.

For point p_s and its neighbouring point p_t, the following angles are determined:

$$\alpha = v \cdot n_t \tag{6.4}$$

$$\phi = u \cdot \frac{(p_t - p_s)}{\|p_t - p_s\|_2} \tag{6.5}$$

$$\theta = \arctan\ (w \cdot n_t, u \cdot n_t) \tag{6.6}$$

where n_t is the estimated normal of point p_t. The symbol '·' denotes the dot-product operator.

The computation is executed for all neighbouring points within radius *r* from p_s. The angles α, ϕ and θ of all neighbouring points are then binned into three histograms and concatenated to form the SPFH of point p_s. Typically, each angle is clustered into 11 bins, leading to 33 bins in total. The SPFH calculation then repeats for every point in the point cloud.

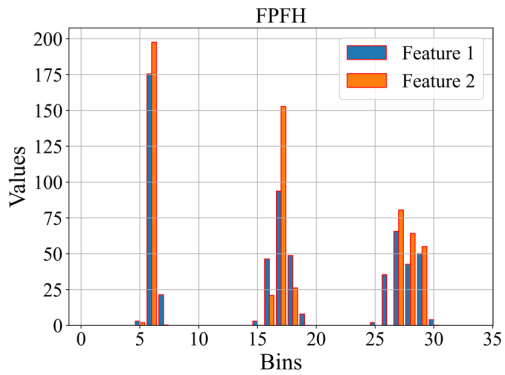
As depicted in Figure 6.8b, the FPFH of a point p_q is an aggregation of its own SPFH and SPFHs of its neighbours. It is defined by,

$$FPFH(p_q) = SPFH(p_q) + \frac{1}{k}\sum_{i=1}^{k}\frac{1}{\omega_i} \cdot SPFH\ (p_i) \tag{6.7}$$

where p_i is a point within radius *r* from point p_q, ω_i is the Euclidean distance between points p_q and p_i. In this way, the FPFH of p_q reflects not only the local geometry of its immediate surroundings (shaded area in Figure 6.8b) but also the surroundings of its

neighbours (areas inside the coloured circles in Figure 6.8b). The above FPFH calculation using Equation 6.7 is repeated for all points within pre- and post-test point clouds.

Figure 6.9a illustrates the FPFH features of two points from a representative structural component on a masonry façade (referred to as 'Structural Component A'), with the radii for normal and FPFH determination being 3 and 6 times the re-sampling voxel size (3.7mm), respectively. Despite the façade's overall planar nature, the combination of brick units and mortar joints introduces unique local variations (see Figure 6.9b), each reflected in the distinct FPFH features of the points.



(a)



(b)

Figure 6.9; (a) FPFH signatures of two points from a representative structural component on a masonry façade (referred to as 'Structural Component A'). The point cloud was re-sampled using a voxel size of 3.7mm; (b) Detailed image of the surface of a masonry façade, highlighting rich and unique local variations.

This implementation primarily considers the following when determining the size for normal and FPFH calculations: (a) a larger radius typically signifies richer geometric properties and a more distinctive FPFH, which enables more reliable correspondence; (b) the deformable nature of the structural component means that with a larger radius, the feature is more susceptible to variations from deformation. Particularly in the event of cracking, this can lead to lost correspondence or incorrect matches; (c) coarser point clouds often necessitate a larger radius to compensate for limited information in the local region.

Further discussions on the selection of FPFH and normal radii is presented in the subsequent chapter, within the context of building settlement tests and the application of PC-EFA. In

this implementation, the computation of FPFH is conducted using the Python library Open3D (Zhou et al., 2018).

6.2.3.3. Feature matching

The settlement caused by underground construction is usually relatively small due to stringent construction control and advancements in construction techniques. Settlement reports are often generated before construction, providing expected settlement values at various stages of a project's lifecycle. While the accuracy of these estimations is influenced by numerous factors, this prior knowledge can enhance the efficiency and precision of feature matching. Given that pre- and post-test clouds are approximately aligned, for example, it does not make sense to seek matches for points separated by more than about a metre, as such large deformation in a structural component due to settlement is unrealistic. Consequently, suppose the local search region has a radius of `r`, and the aligned point clouds, `s`, `t` have FPFHs, calculated as `pt_fpfh_s`, `pt_fpfh_t`, respectively. The following local region-based feature matching procedure is proposed:

```
Function Local_Region_Feature_Matching(s, t, pt_fpfh_s, pt_fpfh_t, r):
    correspondences_s = []
    correspondences_t = []

    FOR each_point_s IN s:
        idx_s = Index(each_point_s, s)
        fpfh_s_i = pt_fpfh_s[idx_s]
        local_dist_neighbours = []

        FOR each_point_t IN t:
            IF Distance(each_point_s, each_point_t) <= r:
                ADD each_point_t TO local_dist_neighbours
            END IF
        END FOR

        nearest_neighbour_idx = NULL
        min_fpfh_dist = INFINITY

        FOR each_neighbour IN local_dist_neighbours:
            idx_t = Index(each_neighbour, t)
            fpfh_t_j = pt_fpfh_t[idx_t]
            current_dist = FPFH_Distance(fpfh_s_i, fpfh_t_j)

            IF current_dist < min_fpfh_dist:
                min_fpfh_dist = current_dist
                nearest_neighbour_idx = idx_t
            END IF
        END FOR

        IF nearest_neighbour_idx IS NOT NULL:
            ADD  (idx_s,  nearest_neighbour_idx)  TO  correspondences_s,
correspondences_t
        END IF
    END FOR

    RETURN correspondences_s, correspondences_t
END FUNCTION
```

Figure 6.10; Pseudocode of function `Local_Region_Feature_Matching` implementing local region-based feature matching.

In the pseudocode in Figure 6.10, The point clouds, `s` and `t`, store the coordinates of their respective points in arrays of dimensions `p` by 3 and `q` by 3, respectively, where `p` and `q` represent the number of points in each point cloud. The arrays, `pt_fpfh_s` and `pt_fpfh_t`, are of dimensions `p` by 33 and `q` by 33, respectively, and they contain the FPFH signatures of each corresponding point in the point clouds `s` and `t`. The notation `pt_fpfh_s[idx_s]` represents the selection of an FPFH signature from `pt_fpfh_s` based on the index `idx_s`. Similarly, `pt_fpfh_t[idx_t]` denotes the selection from `pt_fpfh_t` using the index `idx_t`. The `Index` function accepts a query point and a point cloud as inputs, returning the index of the query point in the cloud. The `Distance` function calculates the Euclidean distance between two given points, while the `FPFH_Distance`

function computes the distance between the FPFH signatures of two points in the FPFH space. For simplicity, the pseudocode does not include the spatial structure for nearest neighbour search. In this work, the KD-Tree implementation in C++ from the Python library Scipy (Virtanen et al., 2020) is employed for both local neighbour search and feature space search. Essentially, a KD-tree is a technique that partitions data to optimise the efficiency of nearest point queries (Maneewongvatana and Mount, 1999).

To improve matching reliability, this procedure can be repeated for each point in point cloud `t` to find the best matches in point cloud `s`. Once done, the two collections of matched points can be used to enforce a 'mutual best match': suppose a point `p_s` in point cloud `s` has a matched point `p_t` in point cloud `t`, and the matched point of `p_t` is also `p_s`. Then, this pairing is accepted since both points are mutual best matches. If this condition is not met, the pairing is rejected.

By leveraging domain knowledge, this procedure employs a 3-dimensional local search to reduce the search space for the more computationally intensive high-dimensional feature search (33 dimensions for FPFH). Such constraints can also refine match results, particularly when the object's surface displays repetitive patterns. The radius, `r`, which defines the local neighbourhood, primarily depends on expected settlement and initial registration errors. A too-small neighbourhood might inadvertently eliminate genuine matches due to deformation. Conversely, an overly large neighbourhood might overconsume computational resources.

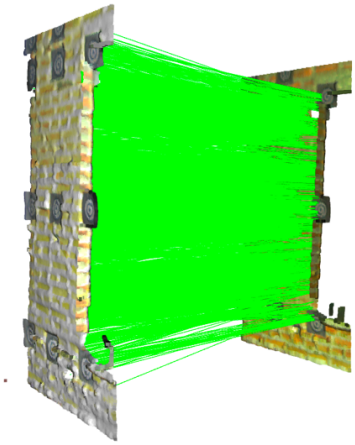


Figure 6.11; Correspondence set found between pre- and post-test point clouds of Structural Component A using the proposed local region-based feature matching method. The matching process implemented the 'mutual best match' strategy. The post-test point cloud (front) is offset along the plane normal for visualisation purposes. The visualisation is implemented using the Python library Open3D.

Figure 6.11 depicts the correspondences found on the pre- and post-test clouds of Structural Component A. In this example, the structural component was subjected to a maximum settlement of 35mm, and a relaxed local neighbour radius of 150mm was used in the local region-based feature matching to account for uncertainties related to estimated settlements and registration errors in the real-world application. After re-sampling using a voxel size of 3.7mm, the pre-test cloud of the structural component contained 41,938 points. A total of 16,723 mutual best match correspondences were identified. Displacement can be derived straightforwardly by subtracting the coordinates of corresponding points in the pre-test point clouds from those in the matched post-test point clouds. While many of the correspondences in Figure 6.11 seem sensible upon visual inspection, there are also some evident mismatches. This suggests that displacements derived from feature matching should be subjected to a series of filters to remove erroneous ones before interpretation.

6.2.4. Displacement filtering

Displacements derived from correspondence matches inevitably contain significant noise. This noise arises from several sources, as described below:

Feature mismatches. Objects with similar feature signature, for example due to repetitive patterns on the surface, are more susceptible to feature mismatches due to reduced distinctiveness of feature descriptors. This often leads to mismatched correspondences, resulting in considerable displacement errors.

Random error due to point density. When two points are matched using FPFH (or any point feature descriptor) from point clouds, the distance between these matched points is always subjected to a random error. This error is inherently tied to point density. It is analogous to the variability one might expect from the distance between two randomly selected points within a cube (or within a square, in the case of a planar object).

Initial registration errors. Any errors in initial registration directly influence the displacements derived from feature matching.

This section presents a three-stage displacement filter specifically designed to address and process the aforementioned noise before any structural interpretation. The primary goal of these filters is to remove significant errors arising from feature mismatches, while preserving feature points that offer authentic insights into the structural response. Although these preserved points might be exposed to random noise due to point density, the filters guarantee that no bias is introduced. Generally, the larger the variance of the noise, the more likely it is for imbalances to occur in the error (resulting in a non-zero mean).

The process is depicted in Figure 6.12. The displacement filtering process takes downsized pre- and post-test point clouds (from Step 2.1), along with the correspondence set, as input. The output is a refined set of correspondences, which can then be used for strain interpretation in the subsequent stage.

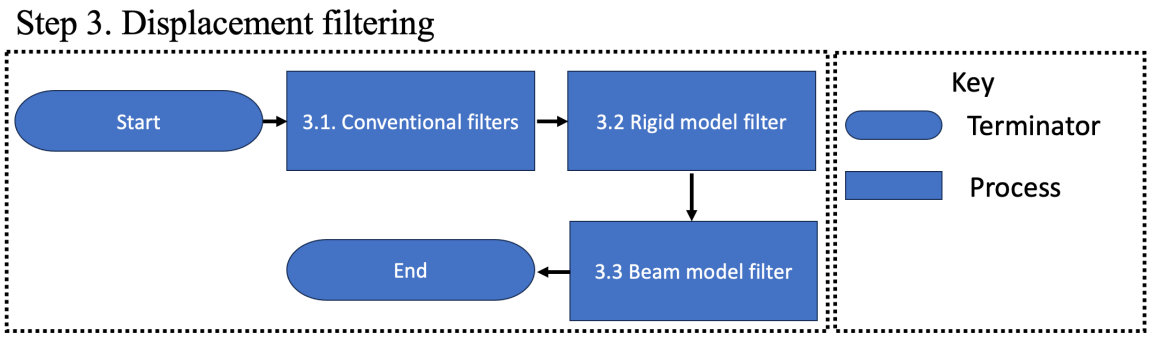


Figure 6.12; Flowchart detailing the displacement filtering steps.

6.2.4.1. Conventional filters

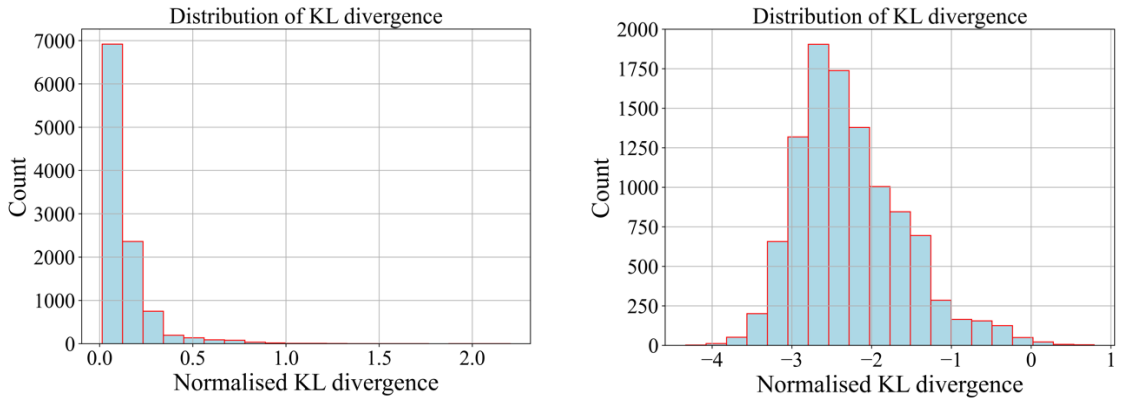
In this implementation, several conventional filters are utilised, as described below:

Boundary filter. When segmenting point clouds, a bounding box representing a space larger than the actual structural component is employed. This ensures that the features of the structural component are entirely captured in both the pre- and post-test point clouds. However, for strain interpretation in the next stage, only the displacements of points within the structural component are considered. Therefore, points from the pre-test cloud that lie outside the area of the structural component are excluded based on the pre-test boundary coordinates. Corresponding points in the post-test cloud that match those removed from the pre-test cloud are also discarded. This filter employs the coordinates of the structural component's corner points as the threshold.

Feature quality filter. The KL divergence from the mean FPFH histogram of all points is commonly used to assess the distinctiveness of an individual point's FPFH signature (Rusu et al., 2008). It measures how different a point's FPFH signature is from the mean histogram and is defined by:

$$D_{KL}(\text{FPFH}||\text{MeanFPFH}) = \sum_{j=1}^{33}\left(p_{i,j}^{f} - \mu_j\right)\ln\frac{p_{i,j}^{f}}{\mu_j} \tag{6.8}$$

where D_{KL} is the KL divergence of a query point, p_i, and $p_{i,j}^{f}$ represents the feature value of the query point p_i at the j^{th} bin. μ_j is the mean feature value of the entire dataset at the i^{th} bin.



(a) (b)

Figure 6.13; (a) Distribution of KL divergence of FPFH for all matched points in pre-test cloud of Structural Component A;(b) Distribution of KL divergence of FPFH for all matched points in pre-test cloud of a representative masonry structural component after log-transformation.

Figure 6.13a presents the distribution of KL divergence values for the FPFH of all matched points in the pre-test cloud of Structural Component A (the same structural component presented in Figure 6.9). A high KL divergence value implies that the FPFH of that point distinctly varies from the mean, while a lower KL divergence value suggests a weaker feature. The KL divergence values determined in this manner resemble a log-normal distribution, as illustrated in Figure 6.13a. In this implementation, the natural logarithm is applied to each KL divergence value, transforming the distribution to a normal distribution, as seen in Figure 6.13b. Points with KL divergence values (on the log scale) exceeding the mean are regarded as having an above-average distinctiveness. The level of distinctiveness can also be adjusted by specifying a threshold in terms of standard deviations from the mean on the log scale. The filter uses the number of standard deviations from the mean as its threshold.

Distance filter. The distance filter is a straightforward method to assess the distance between two corresponding points. This filter calculates the distances of these points and uses a scalar value as the distance threshold.

Normal filter. The normal filter is a straightforward method to assess the relative orientation of the normals for two matching points. This filter calculates the dot products of the normals for these corresponding points and uses a scalar value as the normal threshold.

6.2.4.2. Rigid model filter

The overall motion of a structure subjected to settlement can typically be characterised by a dominant rigid transformation accompanied by a relatively small distortion. These kinematic observations serve to refine the displacement field derived from feature matching (after passing conventional filtering).

The rigid model filter relies on a rigid body model, as introduced in Chapter 5, and is defined by:

$$u(x,y) = u - \omega y \tag{6.9}$$

$$v(x,y) = v + \omega x \tag{6.10}$$

where *x, y* are the position coordinates, and u and v are local displacements, both expressed in the local coordinate system (as shown in Figure 5.2b). ω is the rigid body rotation.

Points whose displacements do not conform to the rigid motion—within a given tolerance—are flagged as outliers and subsequently removed. Conversely, points that conform to the underlying rigid motion, are treated as inliers.

Given that the displacements derived from feature matching often contain considerable noise, the RANSAC (Random Sample Consensus) method is employed to estimate the rigid motion. RANSAC, introduced by Fischler and Bolles (1981), uses an iterative method to estimate the parameters of a mathematical model from a dataset featuring noise.

Suppose the pre-and post-test point clouds are represented by `s` and `t`, respectively. The indices of their corresponding points are given by `correspondence_s` and `correspondence_t`. The maximum number of iterations is denoted as `iterations`. The number of samples in each draw is denoted as `n`. The `threshold` is the maximum distance a data point can be away from the model prediction to be considered as 'inlier'.

The implementation of the `Rigid_Model_Filter` is detailed as follows:

```
FUNCTION Rigid_Model_Filter(s, t, correspondences_s, correspondences_t,
iterations, n, threshold):

    best_inliers = []
    best_inlier_count = 0
    d = Calculate_Displacements(s[correspondences_s], t[correspondences_t])

    FOR i FROM 1 TO iterations:
        correspondences_s_sample,        correspondences_t_sample        =
Random_Select(correspondences_s, correspondences_t, n)
        d_sample = d[correspondences_s_sample]
        model_paras   =   Determine_Parameters(s[correspondences_s_sample],
d_sample)
        d_predicted      =      Predict_Displacements(s[correspondences_s],
model_paras)

        current_inliers = []

        FOR idx IN correspondences_s:
            IF ABS(d_predicted[idx] - d[idx]) < threshold:
                ADD idx TO current_inliers
            END IF
        END FOR

        IF LENGTH(current_inliers) > best_inlier_count:
            best_inliers = current_inliers
            best_inlier_count = LENGTH(current_inliers)
        END IF
    END FOR

    RETURN best_inliers
END FUNCTION
```

Figure 6.14; Pseudocode of function `Rigid_Model_Filter` implementing RANSAC-based filtering using rigid body model.

In the pseudocode, the point clouds, `s` and `t`, store the coordinates of their respective points in arrays of dimensions `p` by 3 and `q` by 3, respectively, where `p` and `q` represent the number of points in each point cloud. `correspondence_s` and `correspondence_t` are both 1D arrays of the same length and contain the index numbers of corresponding points in point clouds `s` and `t`. The notation `s[correspondence_s]` denotes the selection of points

from point cloud `s` based on the indices specified in `correspondence_s`. Similarly, `t[correspondence_t]` denotes the selection from point cloud `t` based on indices in `correspondence_t`. The `Calculate_Displacements` function computes the displacements between input corresponding points. The `Random_Select` function randomly selects `n` sets of corresponding indices from correspondence sets. The `Determine_Parameters` function uses input coordinates and displacements to compute the parameters of the rigid model in a least squares sense, as introduced in Section 5.3.1.1. The `Predict_Displacements` function uses the derived parameters of the rigid model to predict displacements for each point in the input set, following the approach outlined in Section 5.3.1.1. The `ABS` function returns the absolute values of the input array. The `LENGTH` function returns the number of items in the input variable.

The success of the above filtering hinges on the condition that, during some iteration, all samples drawn in `Random_Select` function are inliers. Assume that the required probability of success is *p*, the ratio of outliers in implied displacements from correspondence is *w*, and the sample size in each draw is *n.* The number of iterations *k* required can be expressed as:

$$k = \frac{\log(1-p)}{\log(1-(1-w)^n)} \tag{6.11}$$

In this implementation, the threshold is determined by multiplying the re-sampling voxel size by a factor, typically ranging between 1.5 and 2, to ensure distortions are preserved. The number of samples in each draw is set to 3. With this setup, the maximum number of iterations is limited to 3,000, ensuring coverage for extreme cases where *w* can rise to 0.85 with a probability of success of 99.99%.

The process returns indices of points in both pre- and post-test clouds that pass through rigid model filter.

6.2.4.3. Beam model filter

The beam model filter operates similarly to the rigid model filter. The primary distinction lies in the model used to determine parameters in the `Determine_Parameters` function: the beam model filter employs the beam model introduced in Section 5.2.2 instead of the rigid model as used in Section 6.2.4.2. Notably, when fitting with the beam model, there is a directional nuance: displacement variations along the beam's length are interpreted differently than those along its width. Additionally, to capture the inherent distortion, samples in each draw must be spatially separated. Given these considerations, rather than selecting samples randomly, points across the structural component are first clustered based on their coordinates. A sample is subsequently drawn from each cluster individually.

Suppose the pre-and post-test point clouds are represented by `s` and `t`, respectively. The indices of their corresponding points are given by `correspondence_s` and `correspondence_t`. The maximum number of iterations is denoted as `iterations`. The number of samples in each draw is denoted as `n`. The `threshold` is the maximum distance a data point can be away from the model prediction to be considered as 'inlier'.

The implementation of the `Beam_Model_Filter` is as follows:

```
FUNCTION Beam_Model_Filter(s, t, correspondences_s, correspondences_t,
iterations, n, threshold):

    best_inliers = []
    best_inlier_count = 0
    d = Calculate_Displacements(s[correspondences_s], t[correspondences_t])
    clustered_correspondence_s = Cluster_Points(s[correspondences_s], n)

    FOR i FROM 1 TO iterations:
        correspondences_s_sample = []

        FOR cluster IN clustered_correspondence_s:
            selected_sample = Random_Select(cluster, 1)
            ADD selected_sample TO correspondences_s_sample
        END FOR

        d_sample = d[correspondences_s_sample]
        model_paras = Determine_Parameters(s[correspondences_s_sample],
d_sample)
        d_predicted = Predict_Displacements(s[correspondences_s],
model_paras)
        current_inliers = []

        FOR idx IN correspondences_s:
            IF ABS(d_predicted[idx] - d[idx]) < threshold:
                ADD idx TO current_inliers
            END IF
        END FOR

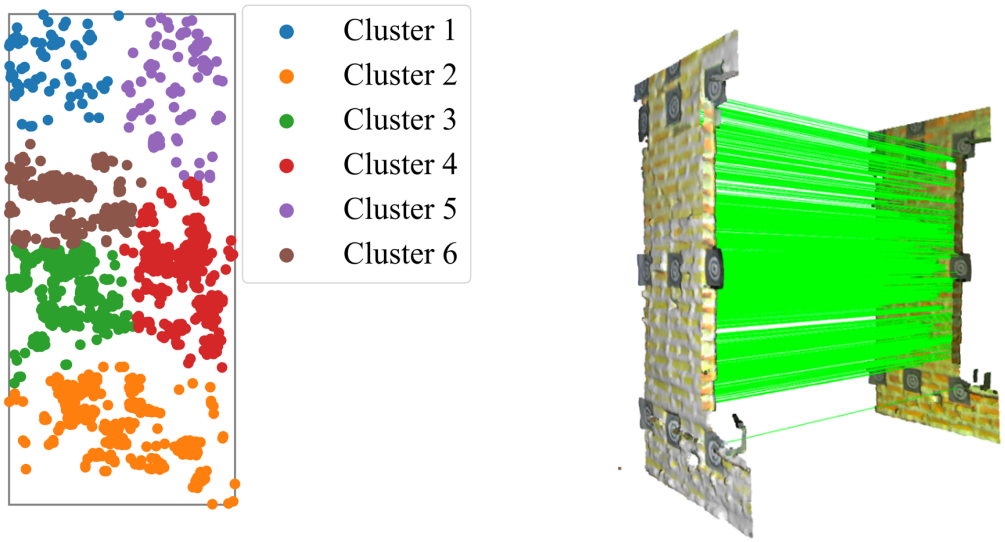
        IF LENGTH(current_inliers) > best_inlier_count:
            best_inliers = current_inliers
            best_inlier_count = LENGTH(current_inliers)
        END IF
    END FOR

    RETURN best_inliers
END FUNCTION
```

Figure 6.15; Pseudocode of function `Beam_Model_Filter` implementing RANSAC-based filtering using Timoshenko beam model.

In the pseudocode above, the point clouds, `s` and `t`, store the coordinates of their respective points in arrays of dimensions `p` by 3 and `q` by 3, respectively, where `p` and `q` represent the number of points in each point cloud. `correspondence_s` and `correspondence_t` are both 1D arrays of the same length and contain the index numbers of corresponding points in point clouds `s` and `t`. The notation `s[correspondence_s]` denotes the selection of points from point cloud `s` based on the indices specified in `correspondence_s`. Similarly, `t[correspondence_t]` denotes the selection from point cloud `t` based on indices in `correspondence_t`. The `Calculate_Displacements` function computes the displacements between input corresponding points. The

`Clustering_Points` function employs K-means clustering to group points into `n` clusters, using the input coordinates. The K-means clustering applied within `Clustering_Points` is facilitated by the Python library, scikit-learn. The `Random_Select` function randomly selects 1 set of corresponding indices from each cluster. The `Determine_Parameters` function uses input coordinates and displacements to compute the parameters of the beam model in a least squares sense, as introduced in Section 5.2.2. The `Predict_Displacements` function uses the derived parameters of the beam model to predict displacements for each point in the input set, following the approach outlined in Section 5.2.2. The `ABS` function returns the absolute values of the input array. The `LENGTH` function returns the number of items in the input variable.



(a) (b)

Figure 6.16; (a) Points of Structural Component A clustered based on their coordinates using `Clustering_Points` function (employing K-means clustering) in the beam model filter; (b) Correspondence set between pre- and post-test point clouds of Structural Component A after filtering. The post-test point cloud (front) is offset along the plane normal for visualisation purposes. The visualisation is implemented using the Python library Open3D.

Figure 6.16a illustrates an example of clustered points from Structural Component A during beam model filtering. A noticeable void can be seen in the lower left corner. This absence

is attributed to a significant crack in the area; the displacements resulting from this crack were filtered out by the rigid body filter. This behaviour is explored later in this chapter.

The beam model requires a minimum of four samples to compute its parameters. To accurately capture distortions, however, more samples may be required. Given the number of samples needed in each draw and in light of Equation 6.11, a high outlier ratio could demand a prohibitive high number of iterations. However, applying the rigid model filter first eliminates most significant noise, especially those arising from feature mismatching. This leaves the beam model filter to handle a dataset with a high percentage of inliers. Such a design has demonstrated efficiency in application. Figure 6.16b depicts the correspondences between the pre- and post-test clouds of the representative masonry structural component after filtering, with no apparent mismatches remaining in the dataset.

For the current implementation, the threshold is set equal to the re-sampling voxel size. The number of samples for each draw is set at 6, and the maximum number of iterations is capped at 10,000. The maximum iteration of 10,000 can handle an outlier rate of up to 65% with a successful rate of 99.99%.

6.2.5. Strain analysis and damage screening

The final stage of PC-EFA involves strain analysis and damage screening. This phase utilises refined correspondences from displacement filtering to infer tensile strain in the structural component. These interpreted strains provide crucial insights into the structural response. They can serve as early warning indicators of potential damage and can also be used for damage screening.

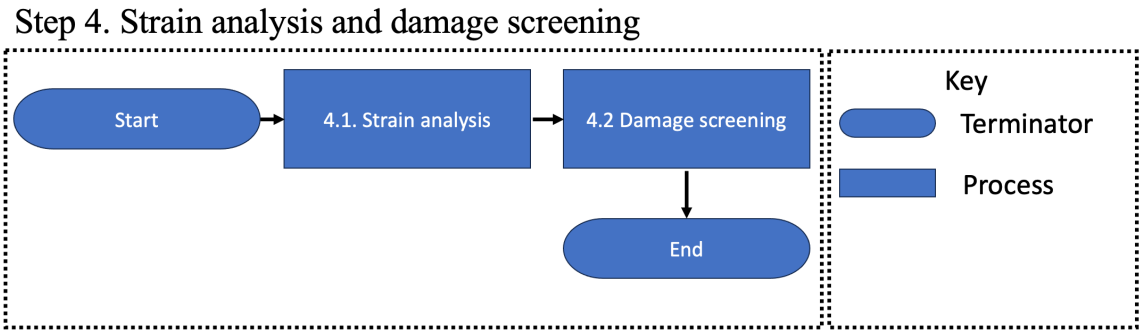


Figure 6.17; Flowchart detailing the strain analysis and damage screening steps.

6.2.5.1. Strain analysis

The displacement filters described in the previous section are expected to effectively eliminate most of the noise resulting from feature mismatches. While noise from the initial registration will persist, it is not anticipated to influence the strain output. Since the threshold in the latest beam model filter is set to the re-sampling voxel size, noise attributed to point density remains. Figure 6.18a illustrates the distribution of feature points for a representative structural component (referred to as 'Structural Component B') after applying the displacement filters, with 6709 feature points remaining. Notably, while most reliable features align along mortar joints, local point concentrations lead to an irregular distribution of feature points.

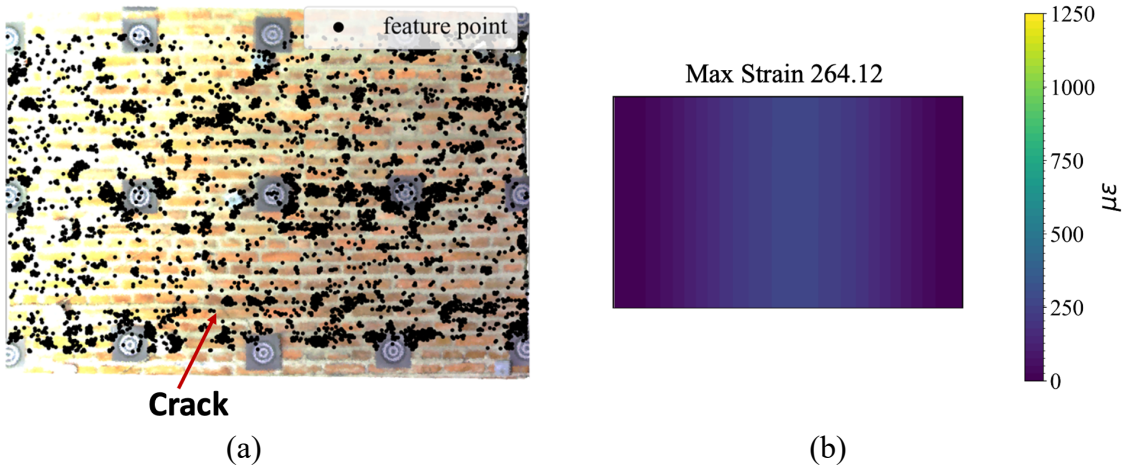


Figure 6.18; (a) Remained feature points of Structural Component B after passing displacement filters. Feature points are plotted overlaying the coloured post-test cloud; (b) Strain derived by fitting all displacements of all remaining 6709 feature points to the beam model.

Directly fitting all feature points to the beam model is unlikely to yield satisfactory results. This approach might obscure local distortions, thereby losing vital information, or it could be disproportionately influenced by local point concentrations, leading to skewed strain results. One example of the strain results from direct fitting all feature points is shown in Figure 6.18b – despite a visible crack appeared near the left corner of Structural Component B, the maximum interpreted tensile strain remained low at 264.12 microstrain, resulting in underestimation of the structural response.

To overcome this limitation, an iterative sampling and fitting approach is proposed. In this method, multiple samples are drawn, and each is fitted to the beam model, under the following assumptions: (a) the filtered displacements from feature matching capture the small local distortions of the structural component; (b) The primary sources of error in the filtered displacements are random noise from point density and potential rigid transformation errors due to initial registration; (c) random noise arising from point density is not substantially biased; (d) The influence of the spatial distribution of samples on the fitting process is minimised, each draw can be considered as an independent and identically distributed (i.i.d.) random variable. According to the Central Limit Theorem (CLT), given a sufficiently large number of draws (thus a large set of parameter estimates), the distribution of these parameter estimates will approximate a normal distribution. Furthermore, based on the Law of Large Numbers (LLN), when samples are drawn and beam parameters are estimated for each draw, the average of these estimates will converge to the expected value of the entire population (reflecting the underlying distortion). This convergence ensures that, despite variability in individual estimates, the aggregated result provides a reliable approximation of the true parameters.

Consistent with the beam model filter, points across the structural component are first clustered based on their coordinates before sampling. In the validation later, it is shown such handling can considerably reduce the influence of special variation on estimation parameters.

Suppose the pre-and post-test point clouds are represented by `s` and `t`, respectively. The indices of their corresponding points are given by `correspondence_s` and `correspondence_t`. The maximum number of iterations is denoted as `iterations`. The number of samples in each draw is denoted as `n`. The number of parameters to determine is `k`.

The proposed Iterative Sampling and Fitting-based Strain Interpretation (ISFSI) is implemented in the `strain_interpreation` as follows:

```
FUNCTION Strain_Interpretation(s, t, correspondences_s, correspondences_t,
iterations, n, k):
    model_parameters_collection = Initialise_2D_Array(iterations, k, 0)
    clustered_correspondence_s = Cluster_Points(s[correspondences_s], n)
    d = Calculate_Displacements(s[correspondences_s], t[correspondences_t])

    FOR i FROM 1 TO iterations:
        correspondences_s_sample = []

        FOR cluster IN clustered_correspondence_s:
            selected_sample = Random_Select(cluster, 1)
            ADD selected_sample TO correspondences_s_sample
        END FOR

        d_sample = d[correspondences_s_sample]
        model_paras   =   Determine_Parameters(s[correspondences_s_sample],
d_sample)
        model_parameters_collection[i] = model_paras
    END FOR

    mean_parameters = Initialise_2D_Array(k, 1, 0)

    FOR parameter_idx FROM 1 TO k:
        sum = 0
        FOR j FROM 1 TO iterations:
            sum += model_parameters_collection[j][parameter_idx]
        END FOR
        mean_parameters[parameter_idx] = sum / iterations
    END FOR

    interpreted_strains = Interpret_Strains(mean_parameters)
    RETURN interpreted_strains
END FUNCTION
```

Figure 6.19; Pseudocode of function `Strain_Implementation`, implementing the proposed Iterative Sampling and Fitting-based Strain Interpretation (ISFSI).

In the above pseudocode, the point clouds, `s` and `t`, store the coordinates of their respective points in arrays of dimensions `p` by 3 and `q` by 3, respectively, where `p` and `q` represent the number of points in each point cloud. `correspondence_s` and `correspondence_t` are both 1D arrays of the same length and contain the index numbers of corresponding points in point clouds `s` and `t`. The `Calculate_Displacements`, `Clustering_Points`, `Random_Select`, and `Determine_Parameters` functions share the same definitions as those in Function `Beam_Model_Filter`. The `Initialise_2D_Array` function initialises a 2D array with a specified shape and populates the array with a specified scaler. The `Interpret_Strains` function calculates axial and shear strains using Equations 5.1, 5.2, and 5.3, and combines them using a tensor-based approach.

The resolution of the strain interpretation is directly influenced by the number of samples taken in each draw. A larger number of samples typically yields higher resolution. However, with the use of location-based point clustering, increasing the number of samples often results in smaller and potentially imbalanced clusters. Such imbalances can lead to the underlying deformation being underrepresented or exaggerated, which might compromise the accuracy of the interpretation.

Neither CLT nor LLN specifies a particular rate of convergence. Nonetheless, based on observations from both synthetic validations (discussed later in this chapter) and applications (covered in the next chapter), the proposed method tends to converge relatively quickly, providing a reasonable estimation of strains. Samples from populations with lower variance typically converge faster than those from high variance populations. This topic will be delved into further in the subsequent sections.

6.2.5.2. Damage screening

For the purpose of damage screening, the maximum tensile strain interpreted for each structural component can be correlated to a damage category based on a strain-damage correlation (e.g. the one proposed in Table 5.1).

6.3. Validation with synthetic data from FE model

This section aims to validate the proposed rigid model filter (Step 3.2), beam model filter (Step 3.3), and the Iterative Sampling and Fitting-based Strain Interpretation method (Steps 4.1 and 4.2) within the PC-EFA process. The validation employs synthetic displacement data derived from FE analyses, augmented with artificial noise characterised by two distinct profiles: (a) larger magnitude noise simulating errors from feature mismatching, and (b) smaller magnitude noise mimicking errors due to point density variations. Within this framework, each node in the FE model represents a feature point in the point cloud. The displacements, determined through feature matching of pre- and post-point clouds, are simulated by the FE nodal displacements with the inclusion of specified noise.

The effectiveness of both the rigid model filter and beam model filter is gauged by examining the noise level present in their outputs. The objectives of both filters are to remove large errors due to feature mismatch while retaining points with genuine information on the structural response without introducing bias. Since the beam representation of piers and spandrels was validated in Chapter 5, the strains deduced from PC-EFA, taking into account the effect of the simulated noise, are compared against the results from EFA interpretations. EFA interpretations use displacements at DIC targets (see Figure 6.20), which are assigned similarly to Chapter 5 without the additional noise.

Discussion on point cloud pre-processing (Step 1), feature calculation and matching (Step 2), and the performance of conventional filters (Step 3.1) is reserved for Chapter 7, where they are presented alongside point cloud data from the building settlement test.

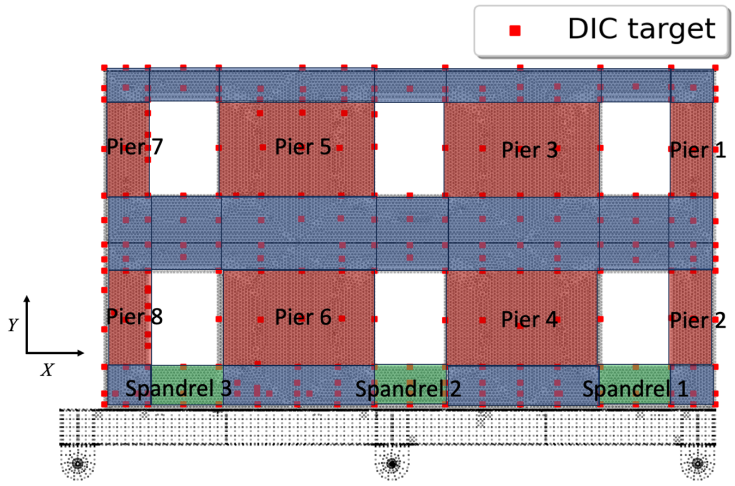


Figure 6.20; Discretisation of the 3O-RF-W3 building model using Timoshenko beam elements and connectors. Piers are highlighted in red and spandrels in green, both modelled by Timoshenko beam elements, while connectors are indicated in blue. Piers and spandrels are labelled following a top-to-bottom and left-to-right convention. DIC targets, overlaid on the finite element mesh of 3O-RF-W3, are shown in the background.

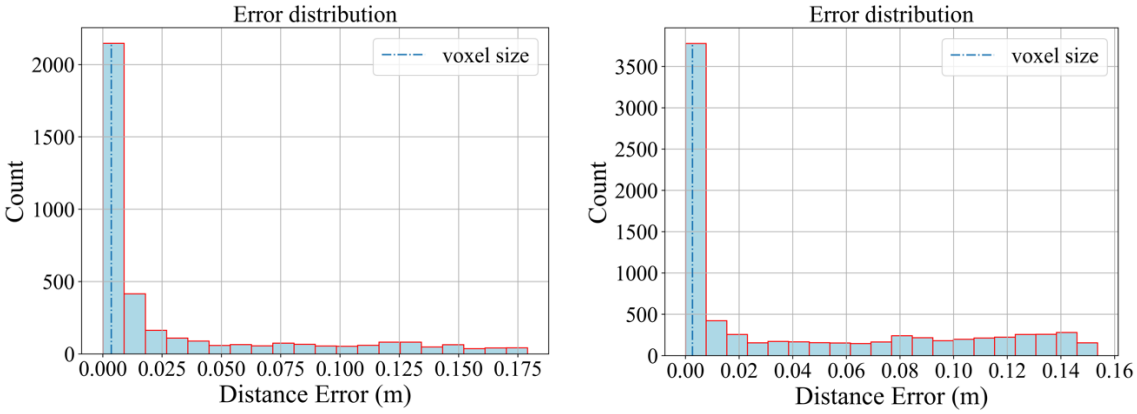
The linear and nonlinear FE models of 3O-RF-W3, as used in Chapter 5, are employed in this section. As depicted in Figure 6.20, the targeted mesh size for the masonry façade in both FE models is 30mm. Consistent with the approach in Chapter 5, the masonry façade was segmented into 8 piers and 3 spandrels. Each structural component is distinctively labelled in Figure 6.20, following a top-to-bottom and left-to-right convention.

6.3.1. Sample validation of a pier

Before exploring noise simulation and synthetic validation, it is beneficial to examine the distribution of displacement errors resulting from feature matching in real-world scenarios. Figure 6.21a-b depict the distributions of these errors in Pier 8 of 3O-RF-W3 and 3O-JF-W1. These errors were determined by comparing point cloud displacements, derived through feature matching in the PC-EFA process (Steps 1 to 3.1), with interpolated displacements from DIC at target locations. The DIC displacements at target locations were obtained following the process described in Section 3.5.1.

In both instances shown in Figure 6.21a-b, there is a noticeable concentration of smaller errors, which are believed to be linked to the point density. Concurrently, there is a relatively

uniform distribution of larger errors over an extended range, which are thought to be related to mismatched features.



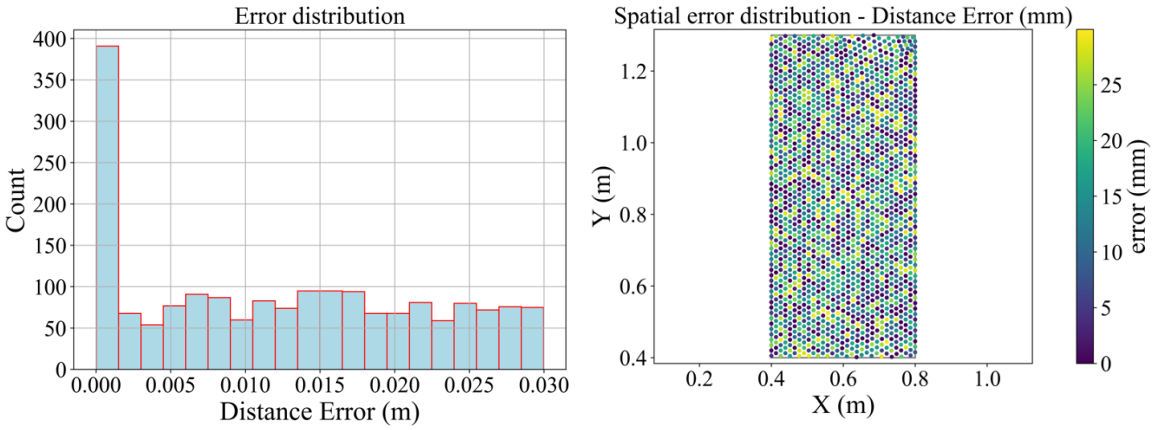
(a) (b)

Figure 6.21; (a) Displacement error profile from feature matching for Pier 8 in 3O-RF-W3; (b) Displacement error profile from feature matching for Pier 8 in 3O-JF-W1.The displacement errors are obtained by comparing with interpolations of corresponding displacements from DIC at target locations. Displacements from feature matching were derived as per the PC-EFA process (Steps 1 to 3.1), while DIC displacements were obtained following the procedures detailed in Section 3.5.1.

To simulate the observed error distribution, two independent uniform distributions were used. First, a percentage and a boundary for the error related to point density were defined. For the simulations described below, the percentage of points affected by this error is fixed at 40%, and the range is set from 0 to 1mm. This implies that within any given structural component, 40% of the points experience a uniformly distributed error of up to 1mm. These errors, in the form of their X and Y components, were assigned to randomly selected points and then added to their respective FE nodal displacements. The boundary was adjusted later to study the effects of greater point density. The remaining 60% of the points were subjected to another uniform error distribution ranging from 1mm to 30mm. These simulated errors were tied to feature mismatching and were incorporated similarly to the point density-related errors.

The uniformly distributed random error for each point was generated using polar coordinates. First, a distance (radius), *r*, was selected randomly from a uniform distribution within the

specified boundary. Next, a random angle θ was chosen between 0 to $2\,\pi$. The X and Y components of the error were given by, r sin (θ) and $r\cos(\theta)$, respectively.



(a) (b)

Figure 6.22; (a) Simulated displacement error profile for Pier 8 in 3O-RF-W3; (b) Spatial distribution of the simulated displacement errors for Pier 8 in 3O-RF-W3.

The distribution of simulated displacement errors for Pier 8 in 3O-RF-W3 is illustrated in Figure 6.22a, which bears a resemblance to Figure 6.21a-b. These simulated errors were then allocated to randomly chosen feature points across the structural component, as depicted in Figure 6.22b. The simulated displacements at each feature point were derived by combining the simulated errors with the corresponding FE nodal displacements. For the purpose of this section, the nodal displacements from the linear analysis of 3O-RF-W3 subjected to a 10mm beam tip settlement were used.

Pier 8 of the 3O-RF-W3 linear FE model comprises 1848 nodes. Of these, 40% experienced simulated errors related to point density of up to 1mm. The remaining 60% were affected by errors attributed to feature mismatching, ranging from 1mm to 30mm. These feature point coordinates and their corresponding displacements were subsequently forwarded to both the rigid model filter and the beam model filter for additional processing.

In PC-EFA, both the pre- and post-point clouds are re-sampled during the pre-processing stage. This ensures that the point density (or average nearest point distance) of both clouds is uniform and aligns with the re-sampling voxel size. Consequently, errors related to point

density are confined to the re-sampling voxel size. With this consideration in mind, filter thresholds are established. For the validations presented in this chapter, as well as for applications discussed in Chapter 7, the following parameters are applied: for the rigid model filter and the beam model filter, the thresholds are set at twice and equal to the re-sampling voxel size, respectively. The rigid and beam model filters sample 3 and 6 points, respectively, in each iteration. The maximum iteration counts for the rigid and beam model filters are set at 3,000 and 10,000, respectively. Since the re-sampling and feature matching processes are not directly simulated in the current chapter, the upper bound of the point density-related error is used as the sampling voxel size to establish the thresholds for both filters.

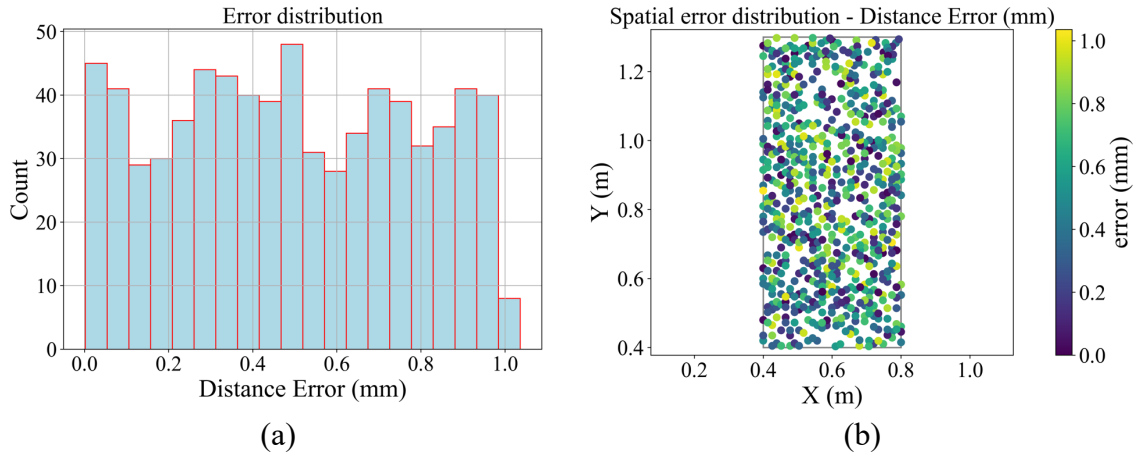
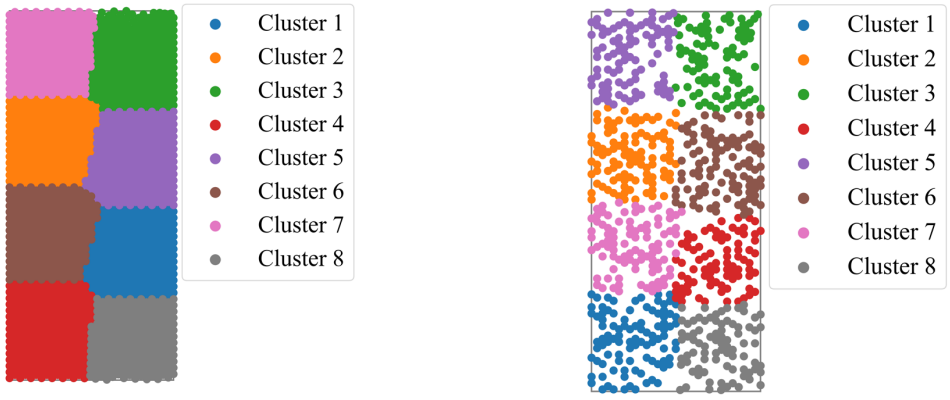


Figure 6.23; (a) Simulated displacement error profile of remaining feature points for Pier 8 in 3O-RF-W3 after application of both the rigid model filter and the beam model filter; (b) Spatial distribution of simulated displacement errors for the remaining feature points of Pier 8 in 3O-RF-W3, following application of the rigid model and beam model filters.

Of the total number of points, 39.2% (equivalent to 724 points) successfully passed through both the rigid model and beam model filters. Notably, 99.8% of feature points with added displacement errors greater than 1mm (representing simulated feature mismatching errors) were filtered out, while 97.5% of feature points with added errors of 1mm or less (representing simulated point density-related errors) were retained. The distributions of displacement errors for the points that navigated both filters are presented in Figure 6.23a, with a peak displacement error of 1.035mm. It is worth noting that, similar to real-world

scenarios, the remaining feature points often are not uniformly distributed across space, as depicted in Figure 6.23b.

Before evaluating the performance of the proposed ISFSI strain interpretation method, it is important to examine the impact of spatial variations in sampled points on estimated parameters. It is evident that when all points are clustered in one corner of a structural component, they may not capture the representative response of the entire component. Thus, a location-based clustering and sampling strategy is introduced to achieve spatially distributed samples. However, even within a cluster, any point can be chosen, so the potential influence of their spatial variations on parameter estimation within these clusters needs to be assessed.

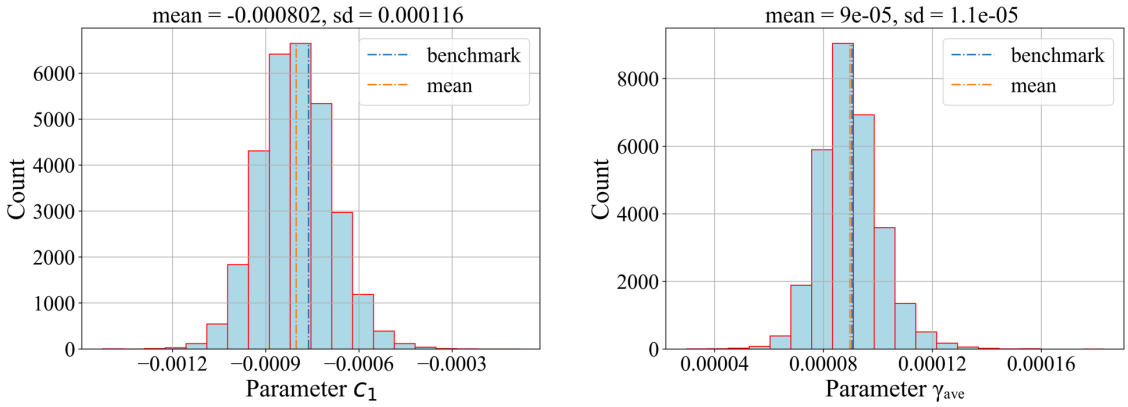


(a) (b)

Figure 6.24; (a) Clustering of all 1,848 simulated feature points in Pier 8 of 3O-RF-W3 based on their coordinates; (b) Clustering of simulated feature points that passed both the rigid model filter and the beam model filter, based on their coordinates.

To investigate this, all 1848 nodal points of Pier 8 in 3O-RF-W3 were grouped into 8 clusters based on their coordinates, as illustrated in Figure 6.24a. Consistent with the approach suggested in the ISFSI strain interpretation method, one sample was selected from each cluster per iteration, resulting in 8 samples for every iteration. For clarity, all 1848 points were assigned their true FE nodal displacements. These selected samples and their respective displacements were subsequently fitted to the beam model to estimate the 7 beam parameters

using Equation 5.4. This procedure was repeated across 30,000 iterations, with the values of each estimated beam parameter being collated into a histogram.



(a) (b)

Figure 6.25; (a) Variation in the individual determination of beam parameter c_1 over 30,000 iterations; (b) Variation in the individual determination of beam parameter γ_{ave} over 30,000 iterations. The benchmark value depicted in each figure was derived using the EFA approach, interpreting displacements at fixed DIC target locations within Pier 8. The mean value was calculated by averaging all derived values of the beam parameter. The 'sd' values in the title reflect the standard deviation of the parameter's distribution.

Figure 6.25a-b depict the distribution of the individual determination of beam parameters c_1 and γ_{ave} in each iteration under the above setup. The distributions of the other parameters are similar. All distributions naturally converge to a normal distribution consistent with the Central Limit Theorem (CLT). The standard deviations observed are remarkably small in all instances (labelled as 'sd' in the title box of Figure 6.25a-b). For instance, the standard deviation of the parameter γ_{ave} is 11 microstrain. These results suggest a negligible influence from the spatial variation of sampled points on the estimated parameters given the current setup.

With the assurance from the above results, the 724 simulated feature points that passed both the rigid model filter and beam model filter were used for parameter estimations and strain interpretations. For the validations presented in this chapter, the following parameters were applied. The proposed ISFSI strain interpretation method sampled 8 points each time (except for stocky piers (Piers 3, 4, 5 and 6 in 3O-RF-W1, W3 and 3O-JF-W1) where 12 points are sampled), with a maximum iteration count set at 30,000.

Figure 6.24b depicts the clustering of the remaining 724 points. In each iteration, the selected samples and their displacements were fitted to the beam model, as described in Section 5.2.2, to determine the 7 beam model parameters (referred to as 'individual determination'). Figure 6.26a-b illustrate the variations in estimated values of parameters c_1 and γ_{ave} over 30,000 iterations. The estimated value of a parameter was calculated by taking the running average of all individual determinations up to that iteration. For instance, the estimated value of a parameter at the 1000^{th} iteration is determined by averaging the first 1,000 individual determinations. The results in Figure 6.26a-b suggest that the estimated values of parameters $c_1$and γ_{ave} converged before 5,000 iterations. All other estimated parameters also converged before 5,000 iterations, except for parameter *e*, which is not associated with any position coordinate variables (see Equation 5.1), implying it does not influence strain determination. Variations in individual determinations of beam parameters c_1 and γ_{ave} are depicted in Figure 6.26c-d, where both distributions converged to a normal distribution. The value of the estimated parameter was determined by taking the mean of all individual determinations and is labelled as 'mean' in Figure 6.26c-d. The benchmark value shown in each figure was derived using the EFA approach, interpreting displacements at fixed DIC target locations (without added noise) within Pier 8. The benchmark and estimated values of parameters c_1 are -0.00076 and -0.00081, respectively. For parameter γ_{ave}, the benchmark and estimated values are 9.0×10^{-5} and 7.7×10^{-5}, respectively, representing a difference in average shear strain of 13 microstrain. All other parameters followed the same trend and converged very close to their respective benchmark values.

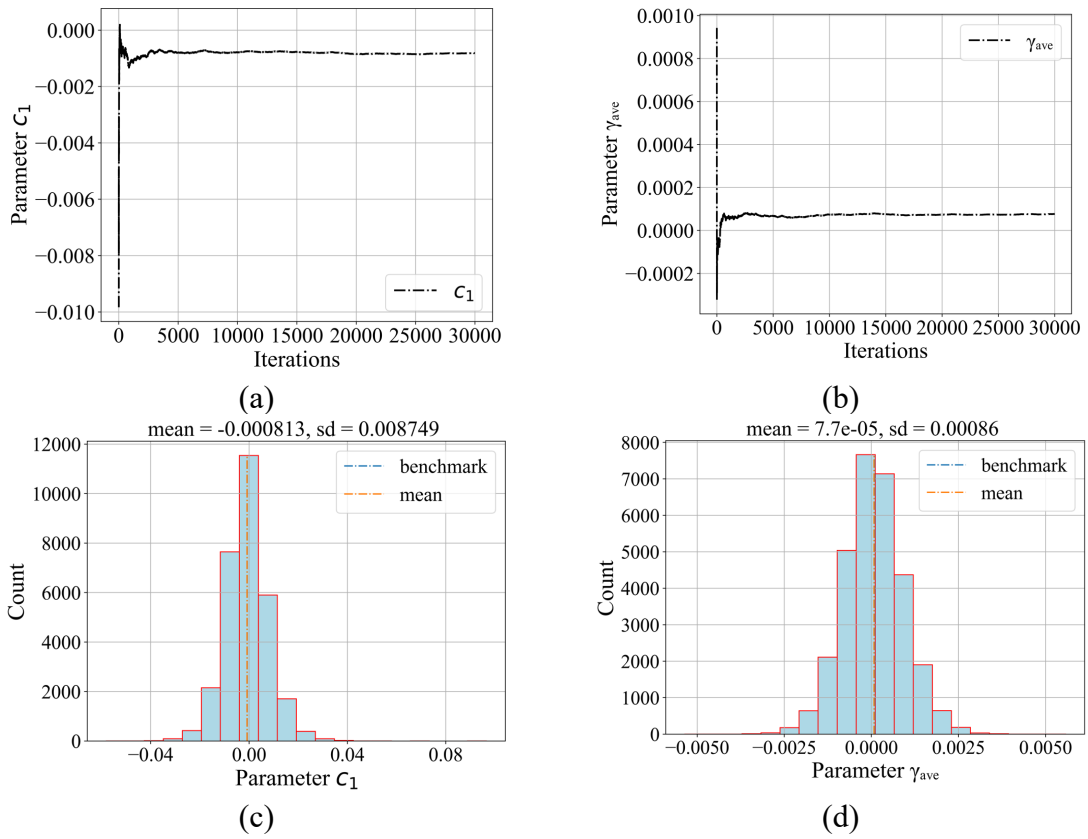
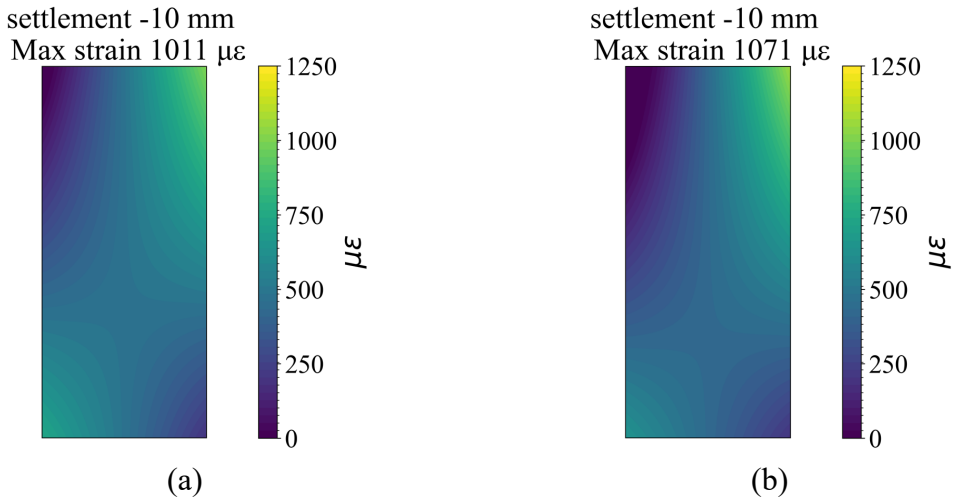


Figure 6.26; (a) Variations in the estimated value of parameter c_1 over 30,000 iterations; (b) Variations in the estimated value of parameter γ_{ave} over 30,000 iterations. The estimated value of a parameter is determined by taking the running average of all individual determinations up to that iteration; (c) Variation in the individual determination of beam parameter c_1 over 30,000 iterations; (d) Variation in the individual determination of beam parameter γ_{ave} over 30,000 iterations. The benchmark value, the mean value, and the 'sd' values in (c) and (d) have the same meanings as described in Figure 6.25.

Lastly, the estimated beam model parameters were employed to estimate the distribution of tensile strain. The strain estimation followed the approach in Section 5.2.2. Figure 6.27a-b compares the EFA-derived tensile strain distribution with the PC-EFA-derived distribution. Despite PC-EFA operating with a substantially noisy dataset (in contrast, the EFA interpretation used assigned DIC target displacements without added noise), the two strain distributions are remarkably similar. The correlation coefficient between EFA strains and PC-EFA strains is 98%, signifying minimal influence from the added noise. The maximum tensile strain results from PC-EFA and EFA are also very close, standing at 1071 microstrain from PC-EFA and 1011 microstrain from EFA.



(a) (b)

Figure 6.27; (a) Interpreted strain distribution using EFA in Pier 8 of 3O-RF-W3 using displacements assigned at DIC target locations based on nodal displacements from the linear FE model subjected to a 10mm beam tip settlement without added noise; (b) Interpreted strain distribution using PC-EFA in Pier 8 of 3O-RF-W3 using synthetic data constructed based on nodal displacements from the linear FE model subjected to a 10mm beam tip settlement with added noise.

6.3.2. Validation with synthetic data from linear FE analysis

In this section, validations conducted on Pier 8 were extended to all other piers and spandrels in 3O-RF-W3. For Case 1, the simulated displacement errors of feature points, following Table 6.1, were added to randomly selected nodal displacements of each structural component. As in the validations in Section 6.3.1, nodal displacements from the linear FE analysis of 3O-RF-W3, subjected to a 10mm beam tip settlement, were utilised. Subsequently, the simulated feature points in each structural component, along with their respective displacements augmented with noise, were processed through the rigid model and beam model filters. The parameters employed in both filters, as detailed in Section 6.3.1, are summarised in Table 6.2.

Table 6.1; Error profiles used to simulate displacement errors from point cloud feature matching (Case 1).

Error profile	Percentage of points	Boundary (mm)	Distribution
Error profile -1 Point density-related error	40%	0 – 1mm	Uniform
Error profile -2 Feature mismatch-related error	60%	1 – 30mm	Uniform

The outcomes in Table 6.3 indicate that the implemented filters effectively eliminated most significant feature mismatching-related errors. Such errors, due to their substantial variance, could skew local cluster interpretations if left unchecked. Conversely, over 97% of points

influenced by density-related errors were retained, suggesting minimal bias was introduced. The maximal errors of points that passed both filters ranged from 1mm to 1.14mm. Given their sparse presence, they are unlikely to affect the strain interpretation significantly.

Table 6.2; Summary of parameters employed in the three steps of the PC-EFA process for validations with synthetic data derived from linear FE analysis. The upper bound of Error profile -1 was utilised as the re-sampling voxel size.

Process	Outlier Threshold	Sample drawing method	Number of clusters	Number of samples in each draw	Maximum iterations
Rigid model filter (Step 3.1)	2 × re-sampling voxel size	Random	-	3	3000
Beam model filter (Step 3.2)	1 × re-sampling voxel size	Clustered draw	6	6	10,000
ISFSI strain interpretation (Step 4.1)	-	Clustered draw	8 (12 for stocky piers)	8 (12 for stocky piers)	30,000

Table 6.3; Evaluation of the performance of the rigid model filter and the beam model filter. Maximum errors were calculated by comparing the displacements of remaining points that passed both filters to the corresponding FE nodal displacements. Percentages of removed points were ascertained by comparing indices of points assigned feature mismatch errors with those removed by both filters. Similarly, percentages of retained points were determined by comparing indices of points assigned point density-related errors with those retained by both filters.

Structural Component	Maximum error (mm)	Percentage of points assigned with feature mismatching errors removed	Percentage of points assigned with point density error retained
Pier 1	1.00	100.00%	99.06%
Pier 2	1.10	99.82%	97.42%
Pier 3	1.10	99.92%	97.08%
Pier 4	1.02	99.95%	97.62%
Pier 5	1.01	99.95%	97.77%
Pier 6	1.14	99.82%	97.32%
Pier 7	1.14	99.91%	98.25%
Pier 8	1.04	99.82%	97.57%
Spandrel 1	1.00	99.86%	98.09%
Spandrel 2	1.00	100.00%	98.15%
Spandrel 3	1.02	99.72%	97.65%

Despite PC-EFA-derived strains using displacements with considerable added noise, the strains interpreted using both PC-EFA and EFA, as depicted in Figure 6.28, reveal striking similarities across the façade in terms of both tensile strain intensity and distribution. The average correlation coefficients in all slender piers and spandrels are 97% and 81%, respectively. However, the stockier piers, with their subdued strain intensity, exhibit reduced correlation, possibly because minor localised imbalances in noise overshadow the modest underlying strains.

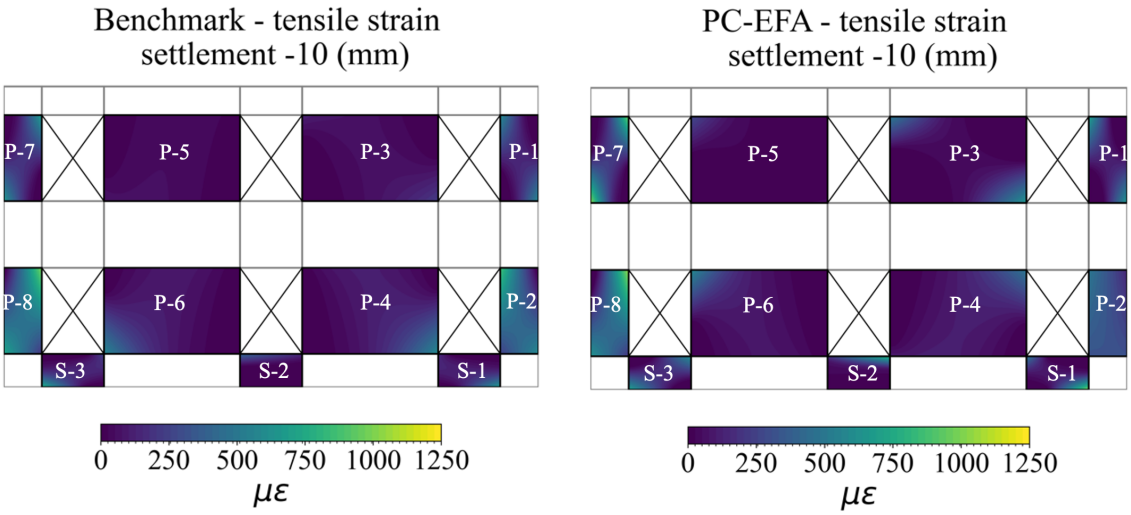


Figure 6.28; (a) Interpreted strain distribution using EFA in all piers and spandrels of 3O-RF-W3 using displacements allocated at DIC target locations based on nodal displacements from the linear FE model, subjected to a 10mm beam tip settlement without added noise; (b) Interpreted strain distribution using PC-EFA in all piers and spandrels of 3O-RF-W3 using synthetic data crafted from nodal displacements from the linear FE model, subjected to a 10mm beam tip settlement with added noise (Case 1). Parameters utilised in strain interpretation are summarised in Table 6.2. Piers and spandrels are abbreviated and labelled in the figure for ease of reference: 'P-1' for Pier 1, 'S-1' for Spandrel 1, and so on.

The above process was repeated with an alternate error combination (Case 2). The boundary of error profile 1 was adjusted to between 0 – 2mm, while other parameters remained consistent with Case 1, as outlined in Table 6.4. Consistent with Case 1, these simulated errors were added to the nodal displacements of each structural component from the linear FE model, which underwent a 10mm beam tip settlement. The corresponding feature matching displacements and feature point coordinates were relayed to both filters, which operated under the parameters specified in Table 6.2 (same as Case 1).

Table 6.4; Error profiles used to simulate displacement errors from point cloud feature matching (Case 2).

Error profile	Percentage of points	Boundary (mm)	Distribution
Error profile -1 Point density-related error	40%	0 – 2mm	Uniform
Error profile -2 Feature mismatch-related error	60%	1 – 30mm	Uniform

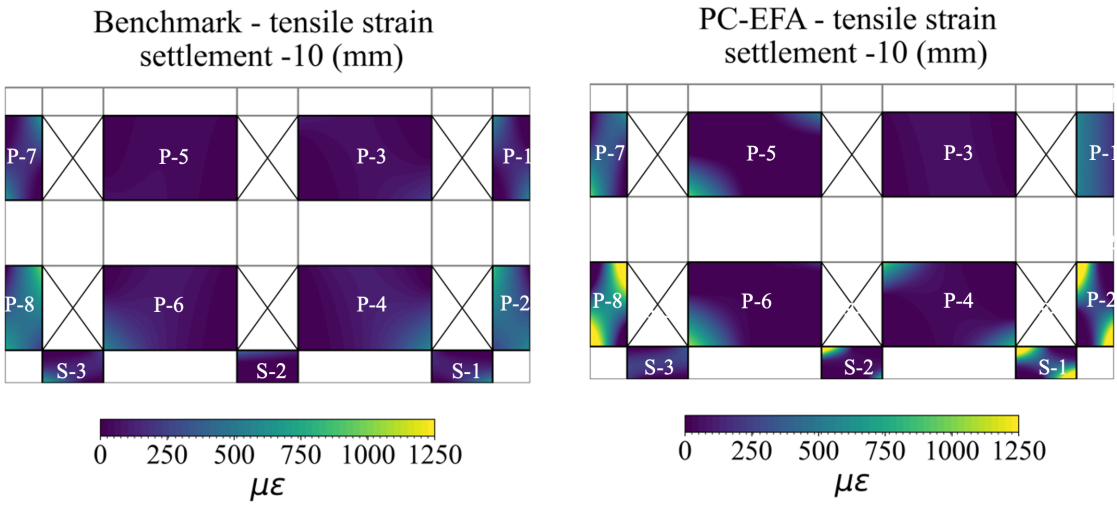


Figure 6.29; (a) Interpreted strain distribution using EFA in all piers and spandrels of 3O-RF-W3 using displacements assigned at DIC target locations, based on nodal displacements from the linear FE model, subjected to a 10mm beam tip settlement without added noise; (b) Interpreted strain distribution using PC-EFA in all piers and spandrels of 3O-RF-W3 using synthetic data formulated from nodal displacements from the linear FE model, subjected to a 10mm beam tip settlement with added noise (Case 2). Piers and spandrels are abbreviated and labelled in the figure for ease of reference: 'P-1' for Pier 1, 'S-1' for Spandrel 1, and so on.

When compared to the benchmark EFA strain results in Figure 6.29a, the tensile strain distribution from PC-EFA (Figure 6.29b) remains largely consistent. There are instances, notably in Pier 2, Pier 8, and Spandrel 1, where PC-EFA overestimates the strain. Additionally, in Spandrel 2, PC-EFA-derived strains differ from those of EFA.

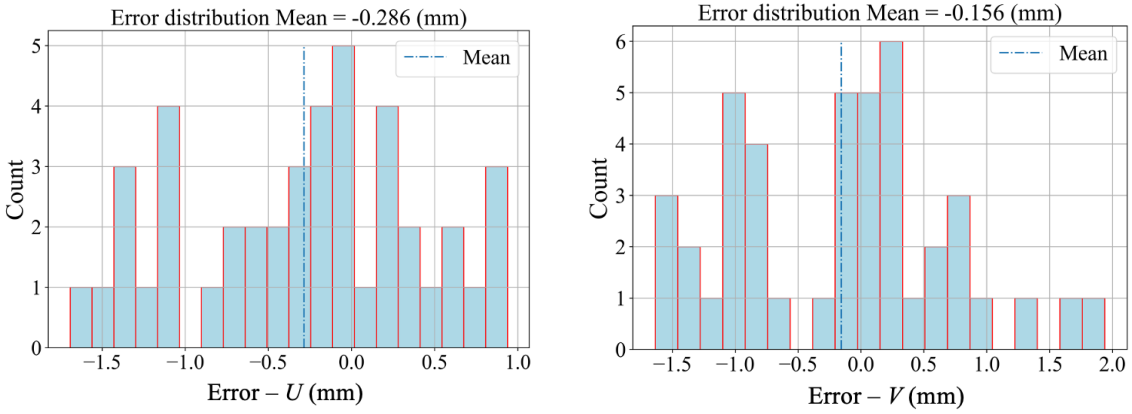
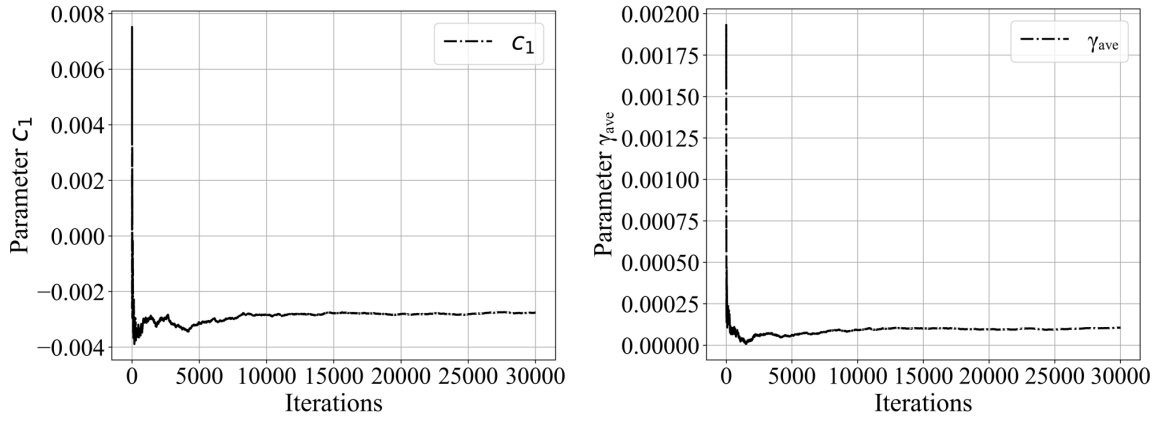


Figure 6.30; Simulated displacement error distribution of remaining feature points in cluster 2 of Pier 8 in 3O-RF-W3 after applying both the rigid model filter and the beam model filter; (a) Error distribution of *U* displacements; (b) Error distribution of *V* displacements. Case 2 error profiles were employed to simulate feature displacements.

On closer inspection, these discrepancies in strain outcomes are attributed to localised imbalances in noise, especially within cluster 2 (refer to Figure 6.30a-b). The mean errors in *U* and *V* displacements in this cluster are -0.289mm and -0.156mm, respectively. Such

imbalances are more probable in structural components with fewer feature points and a broader noise variance. Here, spandrels, being smaller than piers and thus having fewer FE nodes, are more susceptible.

Contrasting Figure 6.31a-b with Figure 6.26a-b reveals that with increased variance in point density-related noise, both parameters, c_1 and γ_{ave}, require more iterations to converge. Similar observations were made with other parameters.



(a) (b)

Figure 6.31; (a) Variations in the estimated value of parameter c_1 for Pier 8 in 3O-RF-W3 over 30,000 iterations; (b) Variations in the estimated value of parameter γ_{ave} for Pier 8 in 3O-RF-W3 over 30,000 iterations. The estimated value of a parameter is determined by taking the running average of all individual determinations up to that iteration. Case 2 error profiles were used to simulate feature displacements.

While the results from Case 2 are deemed reasonable and offer valuable insights into inherent deformation, these findings confirm the notion that PC-EFA yields more reliable predictions when functioning within denser point clouds. It is worth emphasising that the noise level presented in the simulation, even after the application of both filters, poses a significant challenge to any strain interpretation routines. A variance of 1mm in displacement errors could lead to a variance of 2000 microstrain axial strain over a 1m gauge length. Their influence on strain intensifies as the gauge length diminishes. With this in mind, the proposed PC-EFA can be regarded as performing exceptionally well in handling such challenges.

6.3.3. Validation with synthetic data from nonlinear FE analysis

The validation with synthetic data from nonlinear FE analysis primarily aims to assess the performance of the proposed PC-EFA in indicating certain types of cracks using the interpreted maximum tensile strain. For this purpose, the nodal displacements and crack widths from the nonlinear FE model of 3O-RF-W3 (discussed in Chapter 5, Section 5.3.2) at various beam tip settlements were utilised. Noise was added to nodal displacement to simulate displacements of feature points using the error combinations presented in Table 6.1. As in previous examples, the simulated feature points and their associated displacements underwent filtering (Steps 3.2 and 3.3) and strain interpretation (Step 4.1). The parameters used in both filters and strain interpretation remained consistent with those reported in Table 6.2.

When the beam tip settlement was 3mm, the crack map in Figure 6.32a reveals that no cracks developed in the pier and spandrels. Concurrently, neither EFA nor PC-EFA interpretation identified significant strains across all piers and spandrels, as depicted in Figure 6.32c-e. At a 6mm beam tip settlement, two main cracks appeared on Pier 7 and Spandrel 3 (Figure 6.32b). Specifically, one crack was observed spanning the top section of Pier 8, with a maximum crack width of 3.3mm. Another crack, with a maximum width of 2.7mm, was identified on the lower section of Spandrel 3. The maximum width of the crack seen at the upper left corner of Pier 2 was measured at 0.79mm. Figure 6.32d shows that EFA detected high strains in both Pier 8 and Spandrel 3, with maximum tensile strains of 2355 microstrain and 4152 microstrain, respectively. The PC-EFA in Figure 6.32f indicates that the maximum tensile strain in Spandrel 3 was 4224 microstrain. The distribution of interpreted strains in Spandrel 3 by EFA and PC-EFA (contrasting Figure 6.32d and Figure 6.32f) exhibits striking similarity, with a correlation coefficient of 0.98. The maximum tensile strains reported by EFA and PC-EFA in Pier 2 are 646 microstrain and 583 microstrain, respectively.

Once again, the strains interpreted from both methods correlate well, with a correlation coefficient of 0.91.

It is noteworthy that PC-EFA did not detect high strains in Pier 8 when the beam tip settlement was 6mm (see Figure 6.32f). Such behaviour is anticipated as the crack in Pier 8 ran through its entire width, causing a complete alteration in the pier's kinematics. The simulated feature points and their consequent displacements above the crack were identified as outliers by both the rigid body filter and beam model filter since the displacements related to this type of cracking do not resemble typical beam response. As a result, the subsequent strain interpretation only reflects the post-damage state of the main pier following stress release (maximum tensile strain reported at 226 microstrain). Conversely, in Pier 2 and Spandrel 3, even though cracks had formed, the structural components' response could still be approximated by the beam model, with a proportionate increase in interpreted strain corresponding to the extent of cracking. Moreover, Spandrel 1 in Figure 6.32f had developed some strain concentration near the lower right corner, which subsequently led to cracking at a beam tip settlement of 10mm (see Figure 6.33).

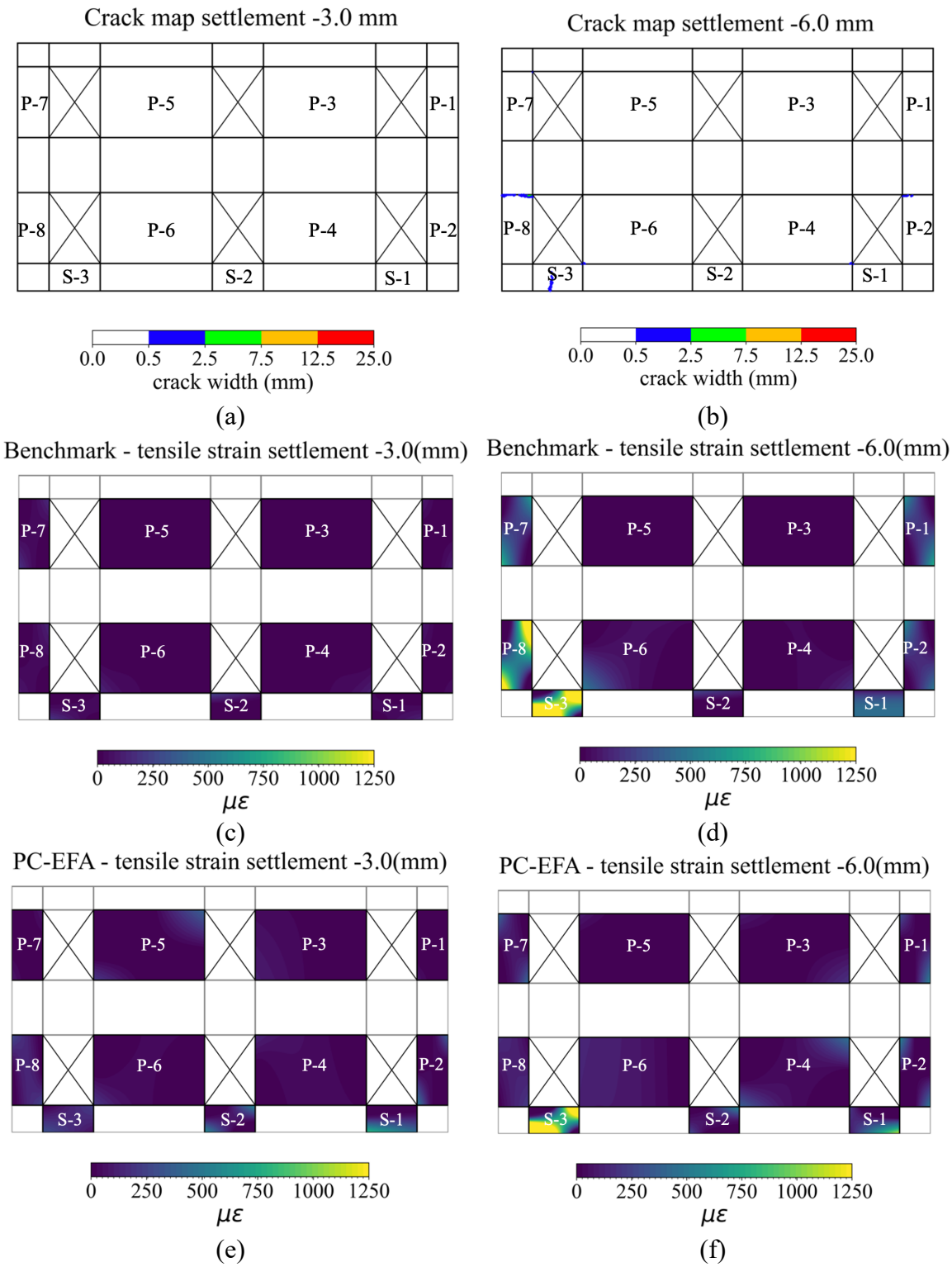


Figure 6.32; (a) Cracks in all piers and spandrels of 3O-RF-W3 from nonlinear FE analysis at 3mm and (b) 6mm beam tip settlement. The sizes of presented cracks are indicated by the colour bar; (c) Interpreted strain distribution using EFA in all piers and spandrels of 3O-RF-W3, based on displacements assigned at DIC target locations from the nonlinear FE model, for 3mm and (d) 6mm beam tip settlement without added noise; (e) Interpreted strain distribution using PC-EFA in all piers and spandrels of 3O-RF-W3, formulated from nodal displacements from the nonlinear FE model, for 3mm and (f) 6mm beam tip settlement with added noise. Piers and spandrels are abbreviated and labelled in the figure for ease of reference: 'P-1' for Pier 1, 'S-1' for Spandrel 1, and so on.

The results in this section demonstrate that the proposed PC-EFA can capture the intrinsic response from the structural components reliably in a noisy environment. The interpreted tensile strains offer crucial insights into early damage indications as well as post-mortem damage state. This section also highlights that the proposed PC-EFA is not designed to capture damage associated with a complete split along the boundary interface, as such damage cannot be represented by the linear beam model. A more general suite for crack identification and measurement using point clouds, which can efficiently manage this type of crack, will be elaborated upon in Chapter 8.

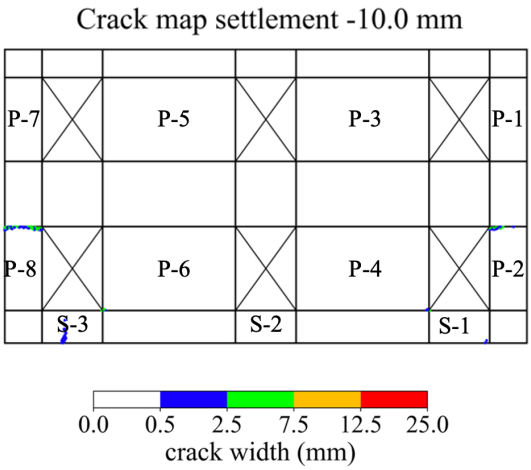


Figure 6.33; Cracks in all piers and spandrels of 3O-RF-W3 as determined by nonlinear FE analysis corresponding to 10mm beam tip settlement. The widths of presented cracks are indicated by the colour bar. Piers and spandrels are abbreviated and labelled in the figure for ease of reference: 'P-1' for Pier 1, 'S-1' for Spandrel 1, and so on.

6.4. Conclusion

To address limitations inherent in traditional monitoring approaches, this chapter introduces a novel method termed the Point Cloud-based Equivalent Frame Approach (PC-EFA) for monitoring buildings subjected to settlement. This method incorporates the fundamental principles of EFA, utilising easily obtainable pre- and post-settlement point clouds of the building façade as input data. Similar to EFA, the acquired façade point clouds are segmented into structural components represented by the beam model. In the proposed

method, the collected point clouds are first registered to a common coordinate frame before aligning the façade for in-plane displacement and strain analysis.

To compute displacements, FPFH features of the pre- and post-settlement point clouds are determined and matched using a local region-based scheme. Leveraging domain knowledge on expected settlement, this local region-based feature matching utilises a computationally less intensive 3-dimensional local neighbour search to narrow the search space for the more demanding high-dimensional feature search (33 dimensions for FPFH).

To address the substantial noise present in the displacement data determined from feature matching, a series of carefully designed filters are deployed. Among these, two kinematic-based filters—namely, the rigid model filter and the beam model filter—utilise the RANSAC approach to estimate model parameters and omit feature points that do not conform to the predominant kinematic motions. Feature points that pass through all filters are then utilised for strain interpretation. Given the inherent noise related to point density, an Iterative Sampling and Fitting-based Strain Interpretation (ISFSI) method is proposed to reliably estimate model parameters and derive strains. Compared to displacement results, the derived strains offer a more tangible indication of the structural component's response and can serve as damage indicators through strain-damage correlations.

The proposed method was validated through synthetic data acquired from both linear and nonlinear FE analyses of a masonry building model subjected to settlement. In the linear range, the method proved robust against noise and provided accurate strain indications compared to EFA benchmarks. Within the nonlinear range, it consistently yielded strain results comparable to the EFA benchmarks and identified damage both in terms of locations and intensities. Additionally, most parameters used in this method can be determined based on physical evidence, eliminating the need for additional experiments or fine-tuning. However, the method displayed lower efficacy in identifying certain types of cracks,

especially those developing along the boundaries of the structural component. The performance of this approach in real-world scenarios will be evaluated in the subsequent chapter within the context of building settlement tests.

7. Application of point cloud-based equivalent frame approach (PC-EFA) to the large-scale building settlement test

7.1. Purpose

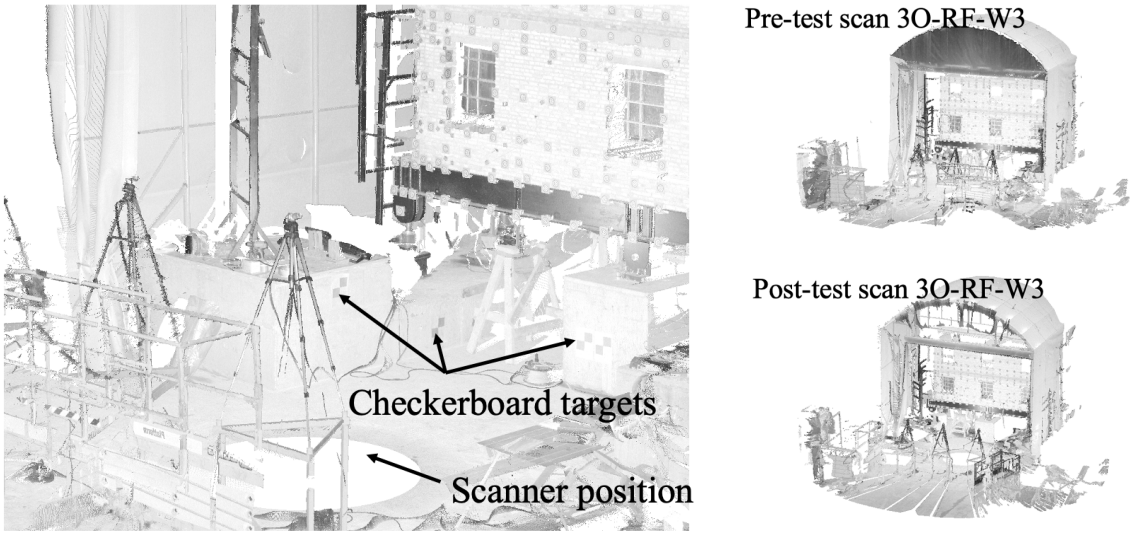
A novel method, termed PC-EFA (Point Cloud-based EFA), is described in Chapter 6. The current chapter explores the detailed application of the proposed method in the context of the large building settlement test and subsequently discusses its performance.

7.2. Application to the large-scale building settlement test

The application of PC-EFA to the large building settlement test was conducted using a custom Python package, developed specifically for this research. The sole exception was the initial registration during point cloud pre-processing, for which the Faro Scene software was utilised. All ensuing applications and analyses were executed on a 2019 MacBook Pro, featuring a 2.4 GHz Quad-Core Intel Core i5 processor and 8GB of RAM.

7.2.1. Overview

Eight scans are used in this chapter, representing four building settlement tests: 3O-RF-W1, 3O-RF-W3, 3O-JF-W1, and 50O-RF-W1. For each test, a point cloud of the façade was captured both before the test commenced (referred to as the pre-test point cloud) and after the maximum induced settlement was achieved (known as the post-test point cloud). These captures were performed using a Faro Focus S70 scanner, using an outdoor HDR profile with inclinometer activated. Figure 7.1 depicts a typical laser scanning setup used for the tests, illustrated using the pre-test scan of 3O-RF-W1 as an example. The scanner was typically positioned approximately 3m from the façade's centre and raised about 1.5m above ground level. The sole exception was for 3O-JF-W1, where scans were taken from a range of between 1m and 1.5m, due to spatial constraints imposed by an adjacent building model.



(a) (b)

Figure 7.1; (a) Close-up of the pre-test scan of 3O-RF-W3, highlighting the checkerboard targets affixed to the concrete footing and the position of the scanner; (b) Visualisation of the pre-test and post-test point clouds without registration, showing they appear at different locations in the visualisation space;

7.2.2. Point cloud pre-processing

7.2.2.1. Registration

Faro Scene was utilised predominantly for target-based bundle registration. As described earlier, a minimum of three checkerboard targets were fixed to a stable surface (e.g. concrete footing) for each test, serving as a shared reference between pre- and post-test point clouds. To execute the registration, both pre- and post-test point clouds are first imported into Faro Scene. Subsequently, the checkerboard targets are recognised using the 'Detect Targets' function. If any targets are not automatically detected, manual identification is initiated. Upon identification of all targets within each point cloud's view, the Faro Scene software undertakes the registration by pairing corresponding targets between pre- and post-test point clouds. The quality of the registration can be gauged through target statistics, which Faro Scene provides post-registration. The maximum and average target errors for each test are listed in Table 7.1. The discrepancies in Table 7.1 correspond to the variance between the observed and anticipated target positions post-registration. It is essential to note that 'horizontal' and 'vertical' pertain to the respective target coordinate plane and are not

necessarily congruent with the reference coordinate frame. Although best practice was rigorously followed on site, some registration discrepancies persist. Most mean errors presented in Table 7.1 oscillate between 0 and 2.5mm. However, there are two notable deviations (3O-RF-W3 and 50O-RF-W1), both concerning horizontal errors. Given the distance between the scanner and the targets, coupled with the point density, these error margins are deemed acceptable.

Table 7.1; Errors from initial registration as reported by Faro Scene. The errors presented in this table highlight the discrepancies between observed and expected target positions post-registration. Note that 'horizontal' and 'vertical' refer to the target's coordinate plane and may not align with the reference coordinate frame.

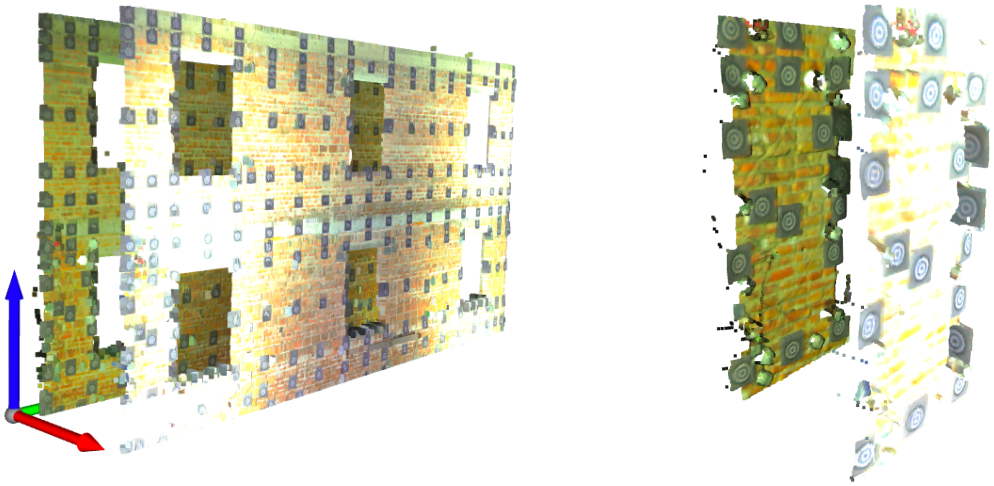
Building model	Maximum horizontal error (mm)	Maximum vertical error (mm)	Mean horizontal error (mm)	Mean vertical error (mm)
3O-RF-W1	3.3	5.5	1.5	2.1
3O-RF-W3	5.2	1.3	3.7	0.8
3O-JF-W1	1.4	2.3	1.0	1.5
50O-RF-W1	7.9	2.9	6.9	1.9

After registration, unnecessary portions of the point clouds were removed using the selection tools within Faro Scene, retaining only the point clouds of the façade. The refined pre- and post-test point clouds were then exported in ASCII format for subsequent procedures.

7.2.2.2. Alignment of façade plane to X-Y plane and structural component segmentation

To enable in-plane deformation analysis, the pre- and post-test point clouds of each test were aligned to the X-Y plane using a PCA-based method. The resultant pre- and post-test point clouds of 3O-RF-W3 after the alignment are shown in Figure 7.2a. The post-test point cloud (the point in front in Figure 7.2a) was offset along the Z direction (indicated by the red arrow) for visualisation purposes. Once point clouds were aligned with the X-Y plane, they were segmented together into individual piers and spandrels, in line with the EFA discretisation strategy. The segmentation was performed by employing a bounding box, delineated by the coordinates of a structural component's four corners from the pre-test cloud, with added offsets. These offsets ensure the complete inclusion of the structural component in both pre-

test and post-test segmented clouds. An example of segmented clouds of Pier 8 in 3O-RF-W3 is shown in Figure 7.2b.



(a) (b)

Figure 7.2; (a) Pre- and post-test point cloud of 3O-RF-W3 façades plotting together. Front: Post-test point cloud; Back: Pre-test point cloud. Post-test point cloud was offset along Z direction (indicated by the red arrow) for visualisation purposes. The green, blue and red arrows denote the X, Y, and Z directions, respectively. (b) segmented pre- and post-test point clouds of Pier 8 in 3O-RF-W3. Point clouds visualised using Python Open3D package.

7.2.3. Feature calculation and matching

7.2.3.1. Point cloud re-sampling

Due to varying scanning setups and conditions (e.g. scanner position, weather, lighting) before and after each test, the resultant point clouds display differences in point density at the level of individual structural components. For illustration, in the case of 3O-RF-W1, the point densities for pre- and post-test clouds (approximated by the average distance to the nearest point) of each structural component are presented in Figure 7.3a-b. Here, a colour code is assigned to each structural component based on its point density. From the figures, it is evident that the pre-test point clouds for all structural components are considerably denser than those from the post-test. To provide a specific example, the point densities of Pier 4 (the stocky pier on the ground storey to the right in Figure 7.3a-b-c-d) in the pre- and post-test clouds are 0.99mm and 1.97mm, respectively.

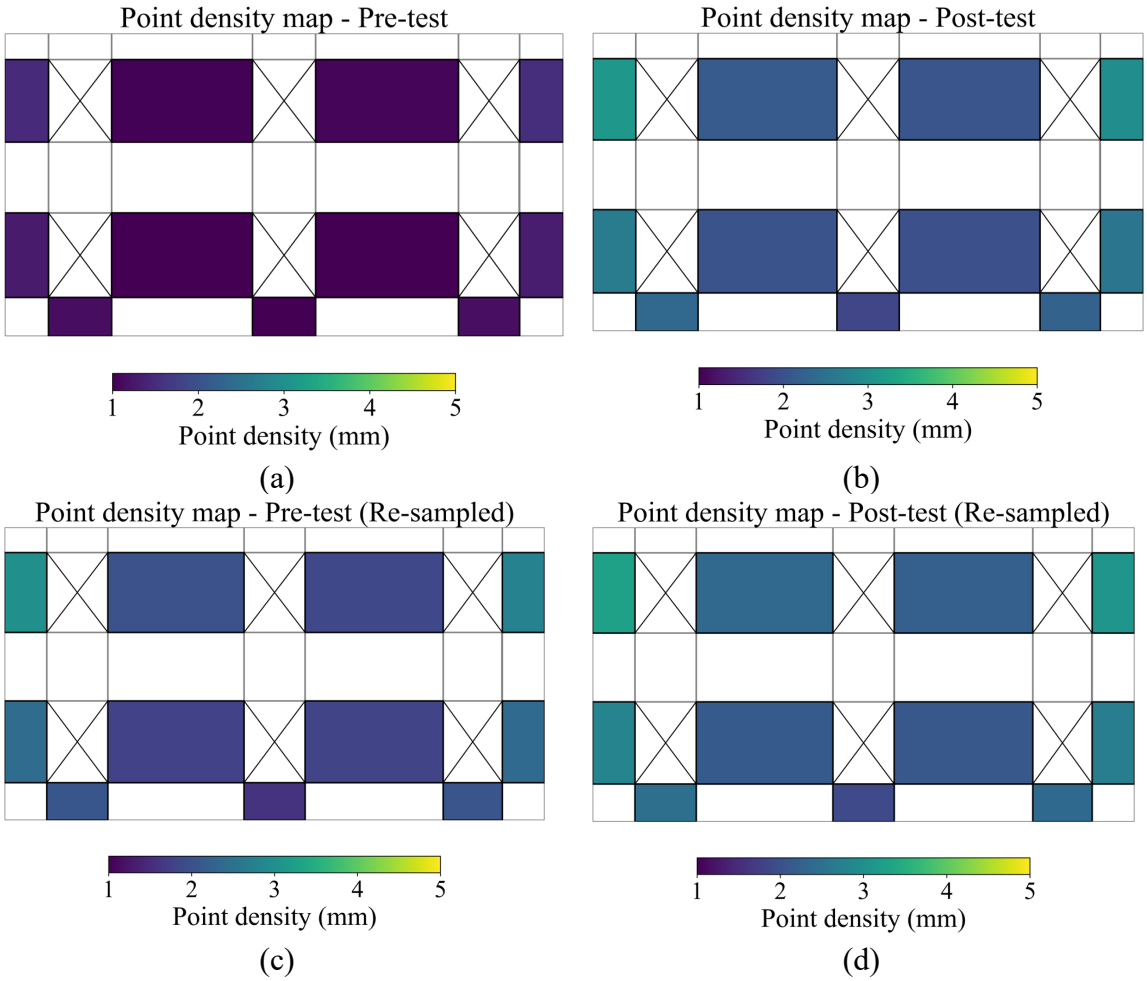


Figure 7.3; Point density of structural components in the 3O-RF-W1 point clouds, approximated by average nearest point distance. (a) Pre-test point density; (b) Post-test point density; (c) Pre-test point density after voxel-based re-sampling; (d) Post-test point density after voxel-based re-sampling. The point density is represented by a colour code for each structural component, as indicated by the colour bar.

Since subsequent feature calculations depend on point density, it is essential to achieve consistent point densities between pre- and post-test clouds for each structural component to ensure reliable feature matching. The chosen voxel size for re-sampling was determined by taking the greater of the point densities from the pre- and post-test point clouds for each structural component and then multiplying by a factor of 1.2 (the re-sampling factor, applied for all tests). The point densities after this re-sampling process are presented in Figure 7.3c-d. Notably, the disparity in point densities between re-sampled point clouds has been substantially reduced. Revisiting the example of Pier 4, the densities for the re-sampled pre- and post-test point clouds are 1.80mm and 2.08mm, respectively. It is worth mentioning that

while a higher re-sampling factor can lead to more consistent point densities across re-sampled point clouds, it also risks eroding finer details.

For 3O-RF-W3, as illustrated in Figure 7.4a-b, discrepancies in point density between the pre- and post-test point clouds were observed, though they were less pronounced than in the 3O-RF-W1 case. Specifically, the point densities for Pier 4 (the stocky pier on the ground storey to the right in Figure 7.4a-b-c-d) in the pre- and post-test clouds stood at 2.56mm and 2.05mm, respectively. Following re-sampling, point densities became more uniform across the façade, as highlighted in Figure 7.4c-d. For Pier 4, the densities in the re-sampled pre- and post-test clouds were 2.68mm and 2.52mm, respectively.

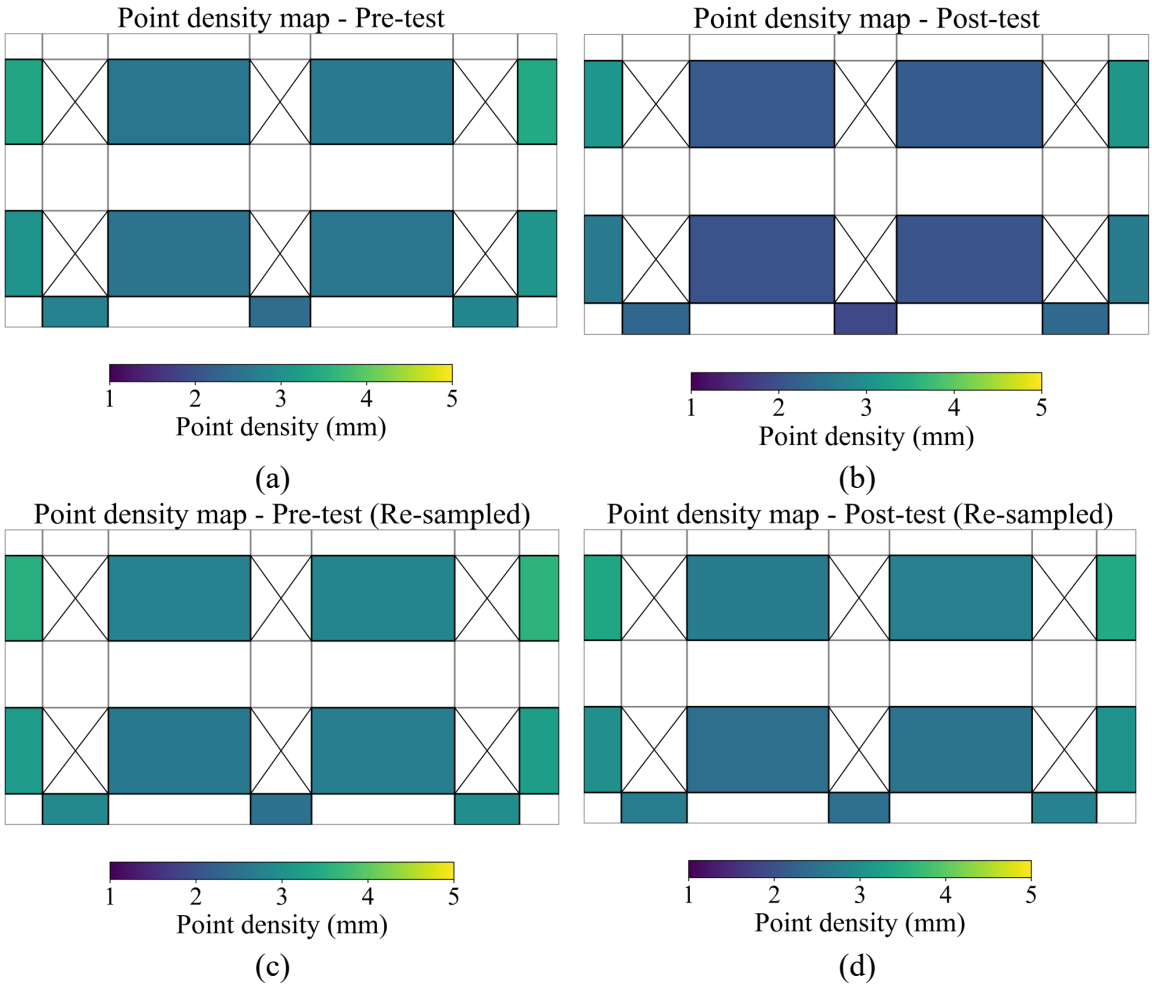


Figure 7.4 Point density of structural components in the 3O-RF-W3 point clouds, approximated by average nearest point distance. (a) Pre-test point density; (b) Post-test point density; (c) Pre-test point density after voxel-based re-sampling; (d) Post-test point density after voxel-based re-sampling. The point density is represented by a colour code for each structural component, as indicated by the colour bar.

Conversely, 3O-JF-W1 exhibited the most consistent point densities between pre- and post-test clouds among all four tests, due to the shorter distance between the scanner and the façade, as demonstrated in Figure 7.5a-b. Taking Pier 4 as a consistent example, the point densities in the pre- and post-test clouds were 1.42mm and 1.63mm, respectively. As shown in Figure 7.5c-d, re-sampling further narrowed these discrepancies. For Pier 4, the re-sampled densities for the pre- and post-test clouds were 1.68mm and 1.76mm, respectively.

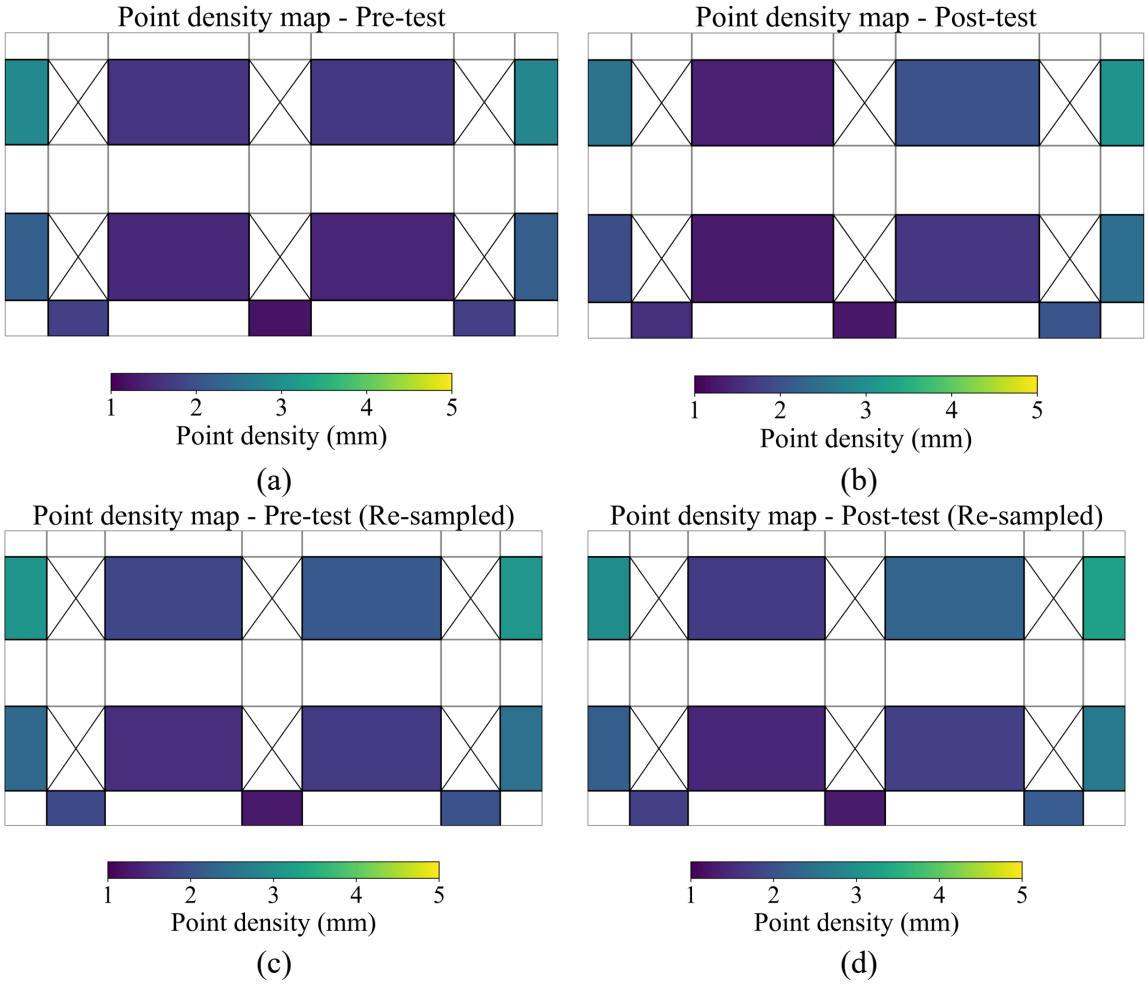


Figure 7.5; Point density of structural components in the 3O-JF-W1 point clouds, approximated by average nearest point distance. (a) Pre-test point density; (b) Post-test point density; (c) Pre-test point density after voxel-based re-sampling; (d) Post-test point density after voxel-based re-sampling. The point density is represented by a colour code for each structural component, as indicated by the colour bar.

50O-RF-W1 had the lowest average point density among all structural components across all four tests, particularly in the post-test clouds. As shown in Figure 7.6a-b, there were also considerable discrepancies in point density between the pre- and post-test clouds at the level of individual structural components. For example, the point densities for Pier 11 (the

external pier on the first storey to the left) were 3.52mm and 4.43mm in the pre- and post-test clouds, respectively. After re-sampling, although more uniform point densities were largely achieved (as shown in Figure 7.6c-d), the resulting densities for both clouds became too low to be useful for further strain interpretation. Using Pier 11 as an example again, the point densities for the pre- and post-test clouds after re-sampling were 4.21mm and 4.61mm, respectively. For this reason, 50O-RF-W1 will not be discussed further from this point onward.

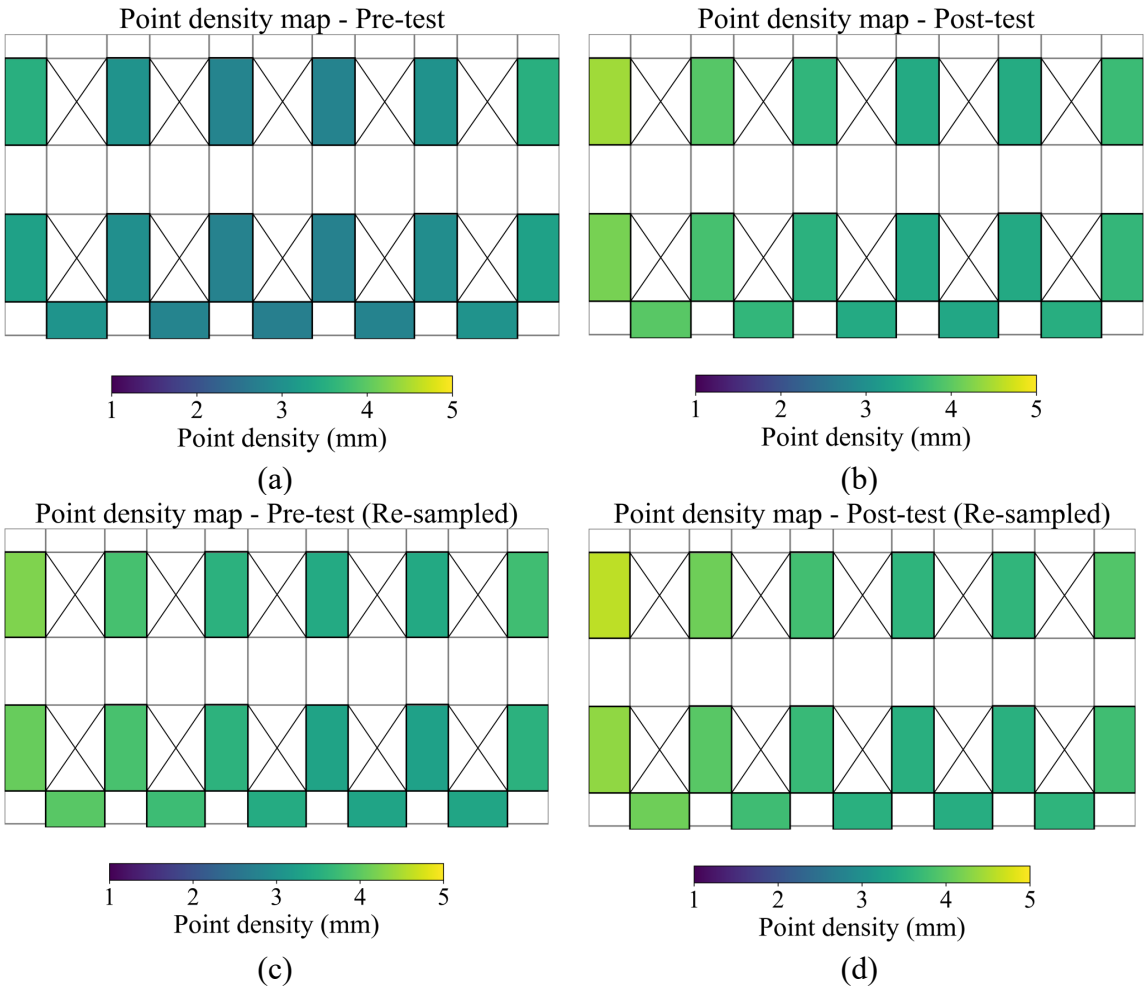


Figure 7.6; Point density of structural components in the 50O-RF-W1 point clouds, approximated by average nearest point distance. (a) Pre-test point density; (b) Post-test point density; (c) Pre-test point density after voxel-based re-sampling; (d) Post-test point density after voxel-based re-sampling. The point density is represented by a colour code for each structural component, as indicated by the colour bar.

It is also worth noting that for both pre- and post-test point clouds across all tests, the external piers/spandrels tend to have a lower density than the middle piers/spandrels. The structural components on the first storey generally exhibit a lower density than those on the ground

storey. These discrepancies arise from the scanner's position, which is typically placed facing the middle of the façade and positioned about 1.5m above the ground.

7.2.3.2. Feature calculation and feature matching

The PC-EFA employs FPFH as the point feature to establish point correspondence between pre- and post-test point clouds. For this application, the same set of parameters (summarised in Table 7.2) was used to calculate FPFH features and to perform local region-based feature matching across various tests. The radius multipliers listed in Table 7.2 were multiplied by the re-sampling voxel size to determine the radii for normal and FPFH calculations. A sensitivity analysis on the selection of these two multipliers is provided later in Section 7.2.4.4. This analysis employs the pass rate of the rigid model filter and beam model filter as performance indicators and is, therefore, discussed in a subsequent section.

The local search radius of 150mm was chosen conservatively to demonstrate the overall applicability of the proposed method. For future applications, a local search radius can be selected more closely aligned with expected settlements. In all applications, mutual best-match correspondences were enforced.

Table 7.2; Parameters used in FPFH feature calculation and local region-based feature matching filter as part of the PC-EFA process for applications to the large building settlement test.

Radius multiplier of normal calculation	Radius multiplier of FPFH calculation	Local search radius (mm)	Mutual best match correspondences
3	6	150mm	On

Table 7.3 details the feature registration and matching for all structural components in 3O-RF-W3. Approximately 40% of points in the pre-test point cloud found their mutual best correspondences in the post-test point cloud, across a varying re-sampling voxel size range of 2.9mm to 4.1mm.

Table 7.3; Details of feature registration and matching for all structural components in 3O-RF-W3. The percentage is calculated based on the number of mutual correspondences.

Structural Component	Re-sampling voxel size (mm)	Number of points (re-sampled pre-test cloud)	Number of points (re-sampled post-test cloud)	Number of mutual best match correspondences	Percentage
Pier 1	4.1	32775	33040	13463	41.08%
Pier 2	3.7	41398	42994	16723	40.40%
Pier 3	3.2	161258	174970	70394	43.65%
Pier 4	3.1	203243	217456	82743	40.71%
Pier 5	3.1	183129	199711	77483	42.31%
Pier 6	3	175823	187944	69805	39.70%
Pier 7	4	31627	34290	13116	41.47%
Pier 8	3.6	43833	47830	15981	36.46%
Spandrel 1	3.4	38510	41644	14868	38.61%
Spandrel 2	2.9	43055	48103	15682	36.42%
Spandrel 3	3.3	33293	36537	13001	39.05%

In 3O-JF-W1, a similar proportion of points in the pre-test point cloud found their mutual best correspondences in the post-test point cloud. However, in the case of 3O-RF-W1, only about 31% of points found their mutual best correspondences. This relatively low percentage is likely due to the significant discrepancies in point densities between the pre- and post-test clouds before re-sampling. Even after re-sampling, some non-negligible discrepancies still exist. For instance, the 0.28mm discrepancy in point density at Pier 4 in 3O-RF-W1 after re-sampling (see Section 7.2.3.1) is the largest among all three tests, in contrast to the 0.08mm in 3O-JF-W1 and the 0.16mm in 3O-RF-W3. While 31% is the lowest percentage of all tests, the number of mutual best match correspondences available was still considered enough for further processing.

7.2.4. Displacement filtering

7.2.4.1. Conventional filters

It is worth noting that the decision to search for correspondences for all points in the point clouds, as described in Section 7.2.3.2, was made for research purposes rather than for computational efficiency. Having a complete set of correspondences allows for the conducting of various sensitivity studies on parameters without having to rerun the feature

matching process. Although local region-based searching confines the high-dimensional search to a relatively smaller area, from a computational efficiency standpoint, it is more efficient to filter out points either before or during feature matching using the lightweight filters proposed in the following section. For example, points with a KL divergence smaller than the mean may not require a search for correspondence, as their featureless descriptor is unlikely to find the correct match. Similarly, points with an established distance greater than a pre-established threshold in the first round of correspondence matching can be excluded from subsequent mutual best-match searches.

In this application, four conventional filters were utilised, and their parameters are summarised in Table 7.4. Since mutual best match correspondences were already searched for all points, these parameters were set in a relaxed manner. Boundary filters were implemented by removing points in the pre-test point cloud that lay outside the boundary of the structural component, as defined by its four corner points in the pre-test cloud. A feature quality filter was implemented by selecting points that lay more than 0.1 standard deviations above the mean (with a Z-score greater than 0.1) in terms of KL divergence on the log scale. The distance threshold and normal threshold were set to 150mm and 0.8, respectively.

Table 7.4; Parameters used in conventional filters during displacement filtering filter as part of the PC-EFA process for applications to the large building settlement test.

Boundary filter	Feature quality filter (Number of standard deviation)	Feature quality filter (Selecting on log scale)	Distance threshold (mm)	Normal threshold
Corner points	0.1	Yes	150	0.8

As shown in Table 7.5, approximately 41% of points within the boundary of structural components in 3O-RF-W3 passed the feature quality filter, and about 98% of those that passed the feature quality filter also passed the normal filter (the distance threshold was set equal to the local search radius, so no points failed to pass).

In 3O-RF-W1 and 3O-JF-W1, a similar percentage of points passed both the feature quality filter and the normal filter. 3O-JF-W1 had a slightly higher pass rate for the normal filter at 99%.

Table 7.5; Details on the number of points (correspondences) that passed each conventional filter during displacement filtering as part of the application of PC-EFA to 3O-RF-W3.

Structural Component	Number of mutual correspondences	Number of correspondences passed boundary filter	Number of correspondences passed feature quality filter	Number of correspondences passed other conventional filters
Pier 1	13463	9355	4334	4281
Pier 2	16723	10557	4254	4227
Pier 3	70394	52849	22165	22098
Pier 4	82743	58157	23121	22755
Pier 5	77483	53063	19918	19734
Pier 6	69805	60577	24796	24309
Pier 7	13116	9488	4519	4404
Pier 8	15981	10513	3868	3670
Spandrel 1	14868	7925	3228	3117
Spandrel 2	15682	9365	4020	3828
Spandrel 3	13001	8622	3308	3229

7.2.4.2. Assessment of displacements derived from feature matching

The DIC measurements of the facades provided a unique opportunity to assess the quality of the established correspondence and the derived displacements. To do this, a dense grid of 50×50 points was generated over each structural component, as shown in Figure 7.7. The displacements at each grid point were determined by interpolating DIC displacements. Since the beam representation of piers and spandrels had already been validated in Chapter 5, for undamaged structural components, the displacements at each grid point were determined directly using Equation 5.4. In this equation, the B matrix was established using the coordinates of each grid point, and model parameters were derived through interpreting displacements at DIC targets following the EFA approach. Benchmark feature displacements were then established by locating the closest grid point for each feature.

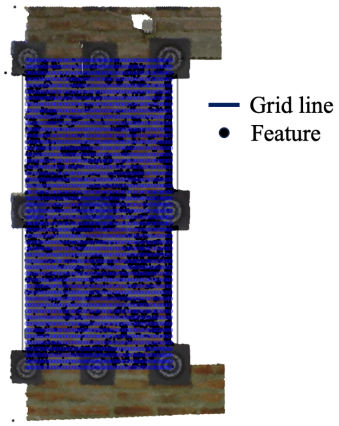


Figure 7.7; A dense grid plotted, overlaying the pre-test point cloud of Pier 8 in 3O-JF-W1 along with feature points that passed the conventional filters.

By comparing displacements derived from feature matching (those that passed the above-mentioned conventional filters) with benchmark feature displacements, the error distributions for feature-derived displacements were established, as shown in Figure 7.8a-b-c-d. Here, Pier 1 in 3O-RF-W3 and Pier 8 in 3O-JF-W1 were used as examples, but the observations made on these cases also appeared in other undamaged structural components. In Figure 7.8a-b-c-d, it is evident that the distribution of errors in both *U* and *V* displacements tends to concentrate near the centres, dropping abruptly outside the region near the centre. This suggests that some displacements from feature matching do carry information about the underlying deformation of the structural component. If correspondences from local region-based feature matching had been established in a completely random fashion, the distribution would look similar to that of the coordinates of points generated uniformly at random within a circle of 150mm radius (the local region-based search radius) centred at the origin (resulting in a semi-circle shape). Since in both tests the maximum induced beam tip settlements were less than 35mm, the results in Figure 7.8 also suggest that substantial noise exists in the displacement data at this stage.

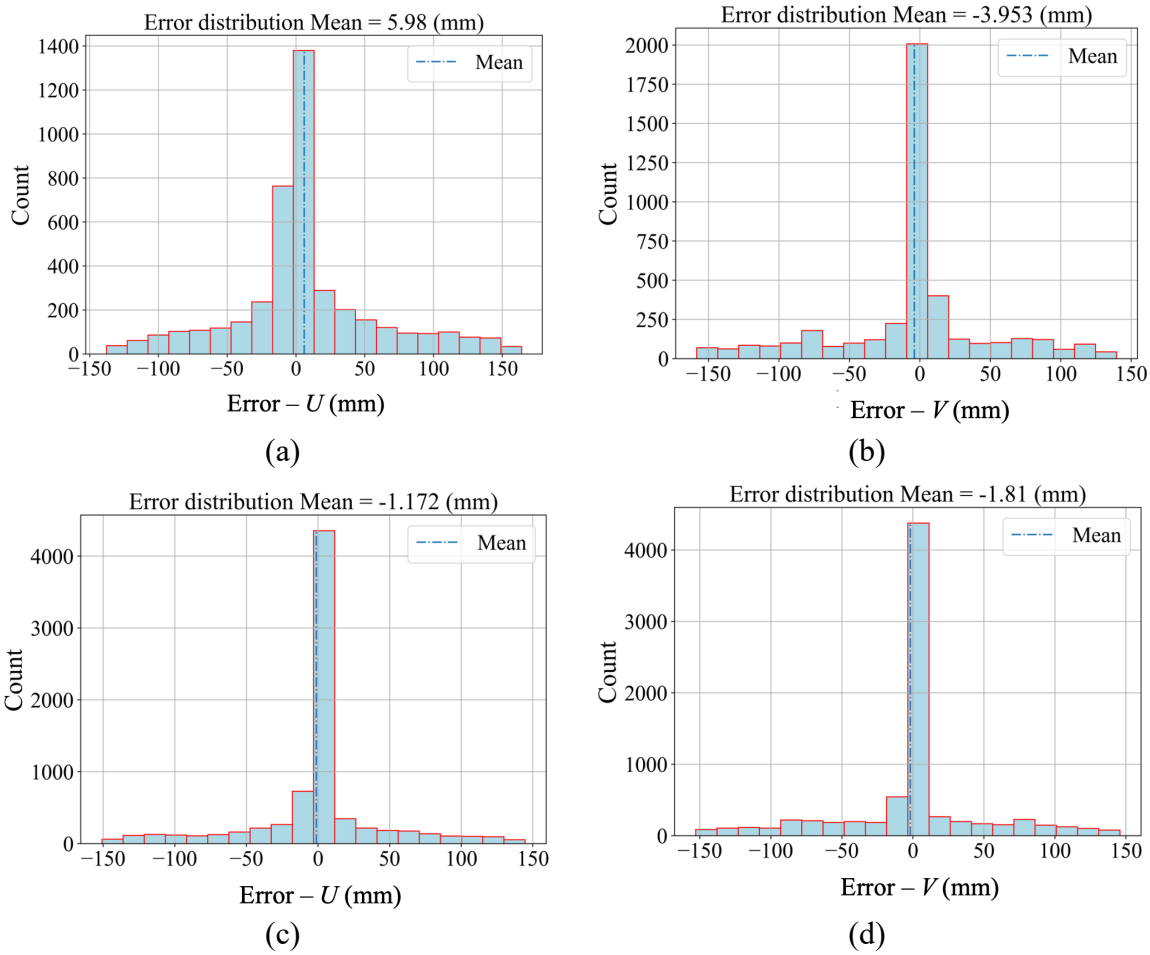


Figure 7.8; Error distribution of displacements after passing conventional filters. (a-b) For *U* and *V* displacements of Pier 1 in 3O-RF-W3, respectively. (c-d) For *U* and *V* displacements of Pier 8 in 3O-JF-W1, respectively.

7.2.4.3. Rigid model filter and beam model filter

The parameters utilised in the rigid model filter and beam model filter are summarised in Table 7.6. The outlier thresholds were determined by using the re-sampling voxel of each structural component.

Table 7.6; Summary of parameters employed in the rigid model filter and beam model filter as part of the PC-EFA process for applications to the large building settlement test.

Filter	Outlier Threshold	Sample drawing method	Number of clusters	Number of samples in each draw	Maximum iterations
Rigid model filter	2 × re-sampling voxel size	Random	-	3	3000
Beam model filter	1 × re-sampling voxel size	Clustered draw	6	6	10,000

As shown in Table 7.7, there were on average 28% points that passed the conventional filter passed both rigid model filter and beam model filter. The pass rate for each filter also

indicates that, within the maximum number of iterations, each filter operated with a success rate of at least 99.99% (see Equation 6.11). It is also evident that the piers on the ground storey had a higher pass rate than piers on the first storey. Spandrels on the ground floor had the highest pass rate than piers. The same was also observed in 3O-RF-W1 and 3O-JF-W1. These observations are believed to be related to the difference in feature quality – the features from denser point clouds on the ground storey are more reliable than the ones on the first storey.

Table 7.7; Details on the number of points (correspondences) that passed the rigid model filter and beam model filter during displacement filtering as part of the application of PC-EFA to 3O-RF-W3.

Structural Component	Number of correspondences passed conventional filters	Number of correspondences passed rigid model filter	Number of correspondences passed beam model filter
Pier 1	4281	1347	835
Pier 2	4227	2017	1473
Pier 3	22098	5694	3581
Pier 4	22755	9625	6703
Pier 5	19734	5815	3764
Pier 6	24309	9830	6737
Pier 7	4404	1049	651
Pier 8	3670	1955	1348
Spandrel 1	3117	1671	1246
Spandrel 2	3828	1868	1391
Spandrel 3	3229	1834	1405

The assessment method outlined in Section 7.2.4.2 was reapplied to evaluate the quality of points that successfully passed both the rigid model filter and the beam model filter. As examples, the resulting error distributions for Pier 1 in 3O-RF-W3 and Pier 8 in 3O-JF-W1 are illustrated in Figure 7.9. These distributions appear to exhibit a triangular shape, aligning with expectations for the U and V displacements between two random points within a voxel (unit square). The maximum deviations from the mean in these distributions are limited by the re-sampling voxel sizes: 4.1 mm for Pier 1 in 3O-RF-W3 and 2.6 mm for Pier 8 in 3O-JF-W1. Notably, the means are not perfectly centred, which is likely attributable to initial registration errors. Aside from these shifted means, no significant skewness is evident in the distributions. These findings suggest that the points passing both the rigid and beam model

filters are primarily subject to random, density-related errors and initial registration errors. Similar observations were made for all other undamaged piers in all tests. It should be noted that spandrels were not assessed, as DIC targets only covered the upper part of each spandrel.

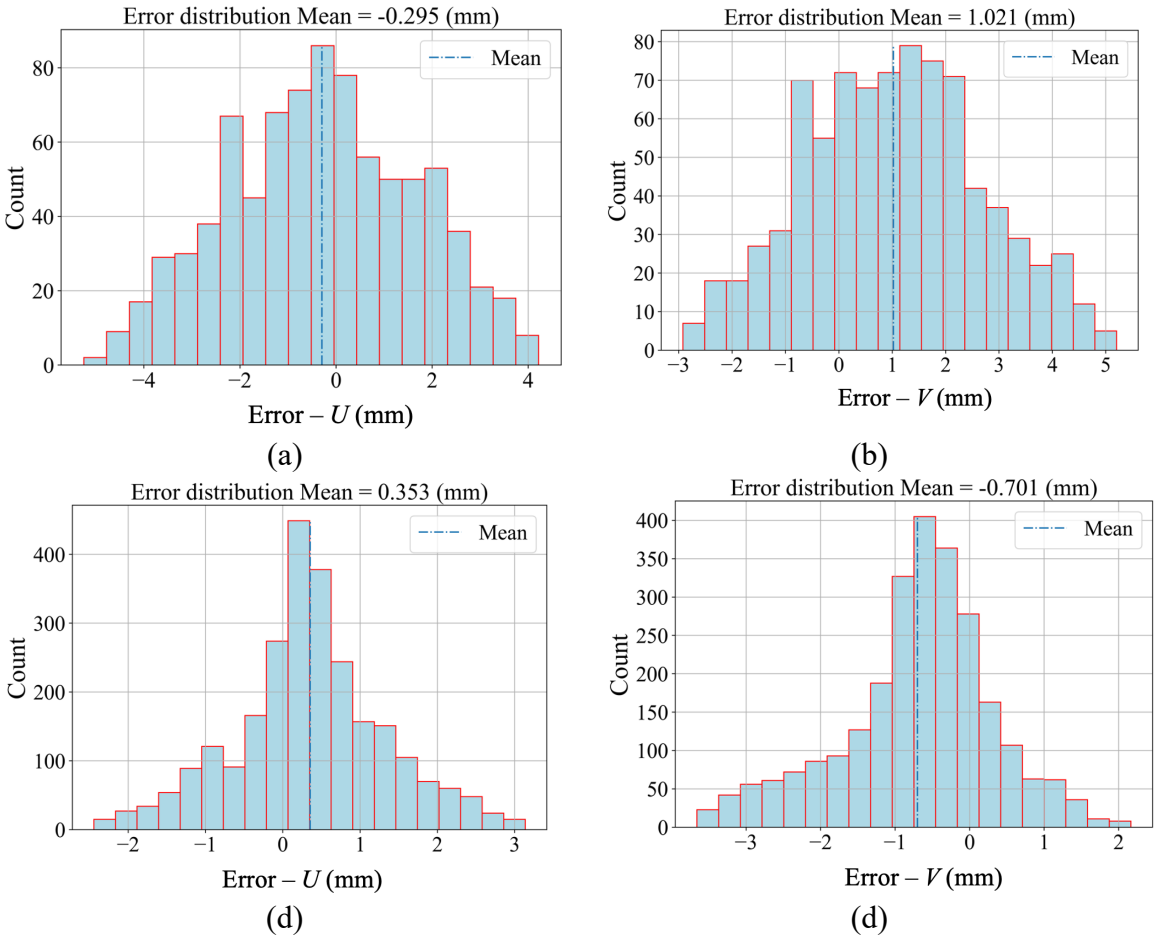


Figure 7.9; Error distribution of displacements after passing the rigid model and beam model filters. (a-b) For *U* and *V* displacements of Pier 1 in 3O-RF-W3, respectively. (c-d) For *U* and *V* displacements of Pier 8 in 3O-JF-W1, respectively.

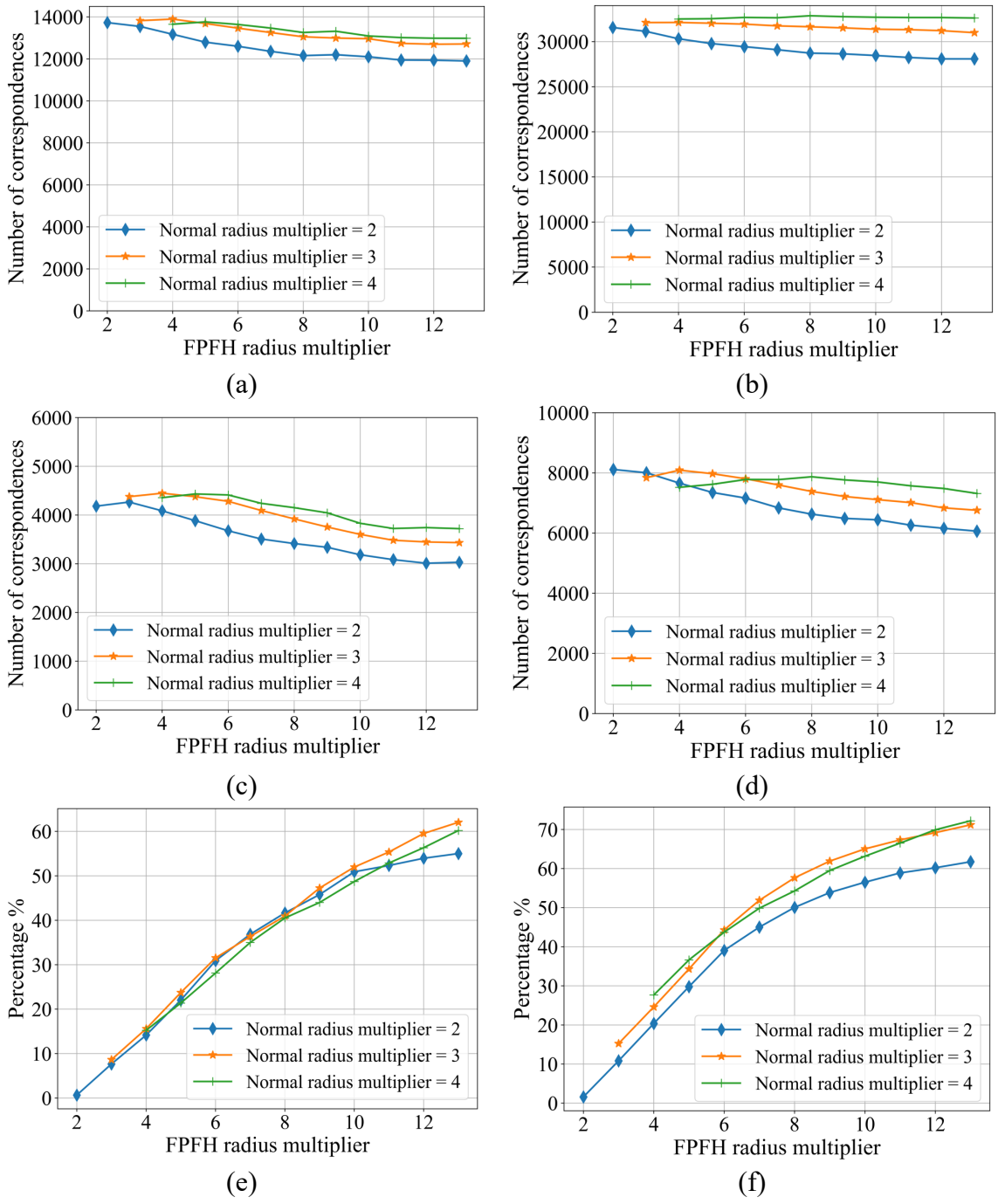
It is also worth noting that some small registration errors are almost inevitable, given the laser scan ranging errors and point density. Although checkerboard targets were used in the building settlement test, there remained some minor residual registration errors at the level of individual structural elements. However, as will be demonstrated later, such errors have no impact on the strain results.

7.2.4.4. Sensitivity analysis on the influence of radius multipliers of normal calculation and FPFH calculation

Before delving into strain interpretation, this section employs the pass rate of the aforementioned filters as a quality indicator to assess the influence of radius multipliers for normal calculation and FPFH calculation on the reliability of feature calculation and matching. To achieve this, Pier 1 from 3O-RF-W3 and Pier 8 from 3O-JF-W1 were selected. These two piers represent undamaged slender piers with contrasting point densities.

Initially, FPFH feature descriptors were calculated for each point in both pre- and post-test point clouds. This was done using a total of 33 combinations of integer radius multipliers for normal calculation and FPFH calculation. The calculation started with radius multipliers of 2 for normal calculation and 2 for FPFH calculation, and progressed up to radius multipliers of 4 for normal calculation and 13 for FPFH calculation. The selected multipliers were then multiplied by the re-sampling voxel size (4.1mm for 3O-RF-W3 Pier 1 and 2.6mm for 3O-JF-W1 Pier 8) to determine the respective radii for normal and FPFH calculations. For each combination case, the calculated feature descriptors were used to establish correspondences, which were subsequently passed through conventional filters and rigid and beam model filters. All filter parameters remained consistent with those recorded in Table 7.4 and Table 7.6. The results for Pier 8 from 3O-RF-W3 are presented in the left column of Figure 7.10 while the results for Pier 1 from 3O-JF-W1 are in the right column. Figure 7.10 a-b present the number of established mutual best match correspondences for each case of the selected piers. For both piers, as the FPFH calculation radius multiplier increases, the number of correspondences slightly decreases. For the same FPFH calculation radius multiplier, a smaller normal calculation radius multiplier (e.g. 2) tends to yield fewer correspondences, while a greater normal calculation radius multiplier (e.g. 4) does not necessarily lead to more correspondences. However, the impact is considered marginal, and a similar trend is observed in Figure 7.10c-d for the number of correspondences passing the conventional filters.

The percentages presented in Figure 7.10e-f-g-h were assessed by dividing the number of correspondences passing the rigid model filter (Figure 7.10e-f) and the beam model filters (Figure 7.10g-h) by the corresponding number of correspondences from each case that passed the conventional filters (as shown in Figure 7.10c-d).



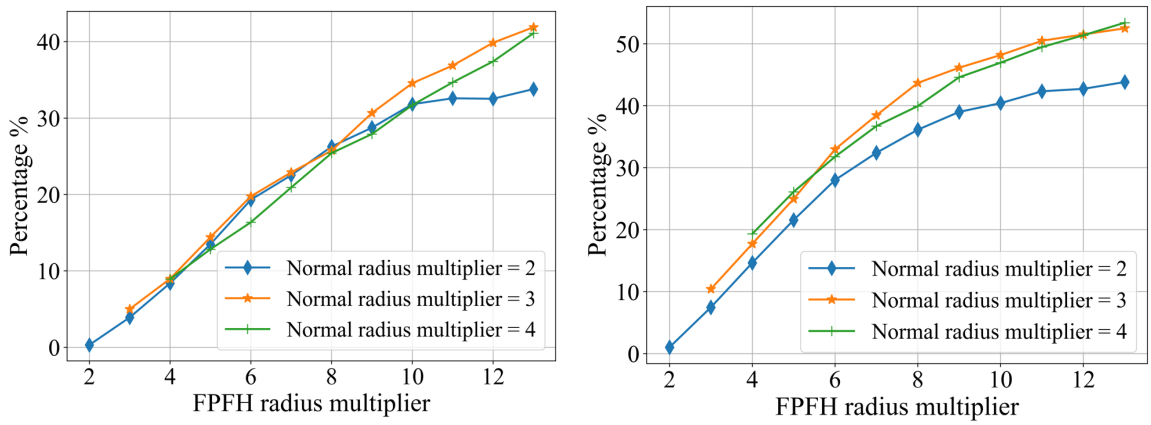


Figure 7.10; Variation in the number of mutual best match correspondences and the pass rates through the rigid and beam model filters for Pier 8 of 3O-RF-W3 (a, e, g) and Pier 1 of 3O-JF-W1 (b, f, h) with different combinations of integer radius multipliers for normal calculation and FPFH calculation. Changes in correspondences passing conventional displacement filters are also depicted for 3O-RF-W3 Pier 8 (c) and 3O-JF-W1 Pier 1 (d).

As demonstrated in Figure 7.10e-f, regardless of the normal calculation radius multipliers, the pass rate of the rigid model filter in both piers tends to increase linearly with the FPFH calculation radius multiplier until it reaches a value between 6 and 10, after which the increase in the pass rate begins to drop slightly. Conversely, for a given FPFH calculation radius multiplier, there is no significant difference in the pass rate among varying normal calculation radius multipliers. Similar observations are made in the pass rates of the beam model filter for both piers, as shown in Figure 7.10g-h.

Additionally, it is noteworthy that Pier 8 in 3O-JF-W1 outperformed Pier 1 in 3O-RF-W3 for the same combination of normal calculation radius multiplier and FPFH calculation radius multiplier, in terms of the pass rate for both the rigid model filter and beam model filter. The denser point clouds for Pier 8 in 3O-JF-W1 resulted in considerably more feature points available for strain interpretation. Furthermore, since the thresholds of both the rigid model filter and beam model filter are related to the re-sampling voxel size, the feature points from Pier 8 in 3O-JF-W1 that passed both filters were subjected to less random point density-related errors than Pier 1 in 3O-RF-W3.

Instead of assigning normal and FPFH calculation radii to specific values, using relative radii based on the re-sampling voxel size provides better flexibility when working with varying point densities. The similar pass rate of both filters facilitates estimating the number of correspondences available for subsequent strain interpretation. Given that denser point clouds generally yield better results, the normal calculation and FPFH calculation radius multipliers can be assigned based on the point clouds of the structural component with the lowest point density, considering the number of correspondences available for strain interpretation.

The parameters employed in this application (normal calculation radius multiplier of 3 and FPFH calculation radius multiplier of 6) are not necessarily optimal in terms of the number of correspondences available for subsequent strain interpretation. However, as will be demonstrated in the following sections, this setup already yields satisfactory results in both strain interpretation and damage indication.

Additional considerations when deciding the normal calculation radius multiplier and FPFH calculation radius multiplier are needed in cases involving cracking. Larger calculation radii may result in the loss of features in the adjacent regions of cracks. Also, when dealing with large datasets, larger radii could lead to noticeable increased computational efforts for feature calculation.

7.3. Results and discussion

7.3.1. Overview

After applying displacement filtering, the remaining feature points were subjected to the ISFSI strain interpretation process. During strain interpretation, the parameters outlined in Table 7.8 were employed. Subsequently, the estimated maximum tensile strain of each

structural component was correlated with a damage category based on the strain-damage correlation proposed in Table 5.1.

To assess the performance of the proposed approach, the damage categories assigned by PC-EFA using pre- and post-test point clouds were compared with the damage categories determined by EFA using DIC data for each test (using the same strain-damage correlation as proposed in Table 5.1). Both sets of results were presented and discussed in conjunction with the observed damage.

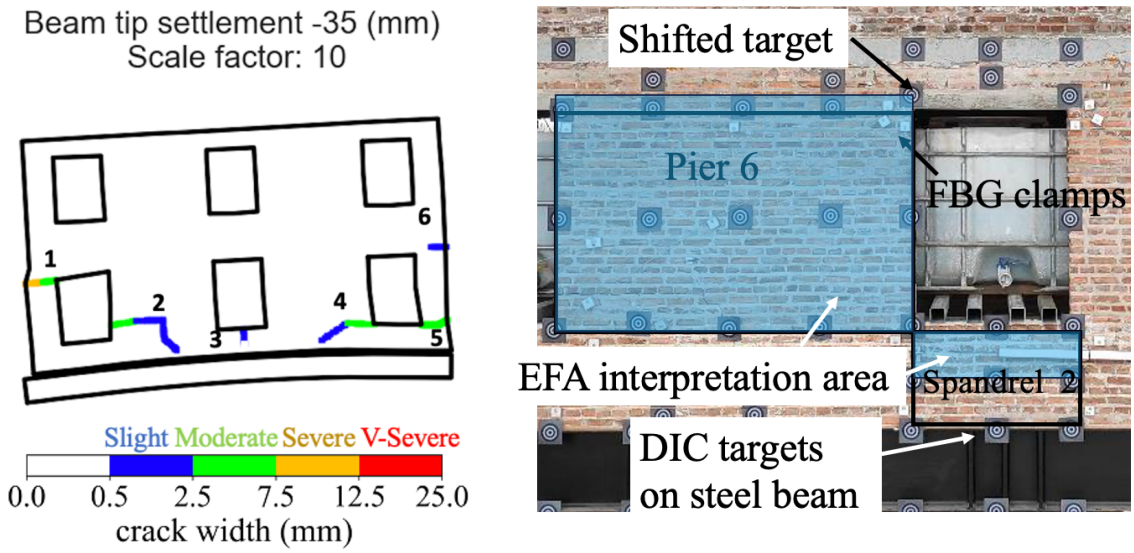
Table 7.8; Summary of parameters used in the strain interpretation process as part of the PC-EFA application to the building settlement test.

Process	Sample drawing method	Number of clusters	Number of samples in each draw	Maximum iterations
ISFSI strain interpretation (Step 4.1)	Clustered draw	8 (12 for stocky piers)	8 (12 for stocky piers)	50,000

7.3.2. 3O-RF-W3

At an induced beam tip settlement of 35mm, significant cracking occurred at the ground storey of the façade, as depicted in Figure 7.11a. Horizontal cracks (labelled as Cracks 1, 5, and 6 in Figure 7.11a) were evident at the slender external piers, likely resulting from bending action in these piers. Conversely, the stockier internal piers exhibited diagonal cracking (Cracks 2 and 4 in Figure 7.11a). Additionally, a vertical crack (Crack 3 Figure 7.11a) was observed on the middle spandrel of the ground storey.

One of the DIC targets (referred to as the ‘shifted target’ in Figure 7.11b) had to be moved to accommodate three FBG clamps, leading to a larger EFA strain interpretation area than the actual extent of Pier 6. Furthermore, DIC targets positioned near the base of Spandrel 2 (and all other spandrels) were situated on the top flange of the steel beam (shown in Figure 7.11b), rendering them unsuitable for EFA strain interpretation of spandrels. Consequently, the EFA interpretation area only covered half of the size of Spandrel 2.



(a) (b)

Figure 7.11; (a) Deformed shape of the front façade of 3O-RF-W3 with a beam tip settlement of 35mm, showing crack locations and sizes (indicated by the colour bar); (b) Annotated image illustrating EFA strain interpretation areas (blue shaded) for Pier 6 and Spandrel 2, along with the extents (black box) of these components. A DIC target (labelled as 'shifted target') was moved for 3 FBG clamps, resulting in a larger EFA interpretation area than the structural component. Additionally, DIC targets near the base of Spandrel 2 (and other spandrels) were placed on the top flange of the steel beam, not used for EFA interpretation, leading to EFA's interpretation area being half the size of Spandrel 2.

Despite the variations in strain interpretation areas, Figure 7.12a-b-c-d present a comparison of the estimated tensile strain distributions between EFA and PC-EFA for Pier 6 and Spandrel 2. In Figure 7.12a-b, the maximum tensile strains estimated by both EFA and PC-EFA indicate a 'moderate' damage category, consistent with the maximum observed crack width illustrated in Figure 7.11a (Crack 2). Furthermore, the strain distributions exhibit a striking similarity. The areas of high strains depicted in Figure 7.12a-b also correspond with the observed diagonal crack (as seen in Figure 7.13a). On Spandrel 2, as shown in Figure 7.12c-d, both EFA and PC-EFA suggest a 'slight' damage category. Again, the strain distribution displays considerable similarity, despite EFA only interpreting the upper half of the spandrel. Similar to Pier 6, the region of high strain indicated in Figure 7.12d corresponds to the observed damage (Crack 3) at the middle span (as shown in Figure 7.13b). Notably, the results from PC-EFA on Spandrel 2 were obtained despite considerable occlusion overshadowing the damaged area, as depicted in Figure 7.13b.

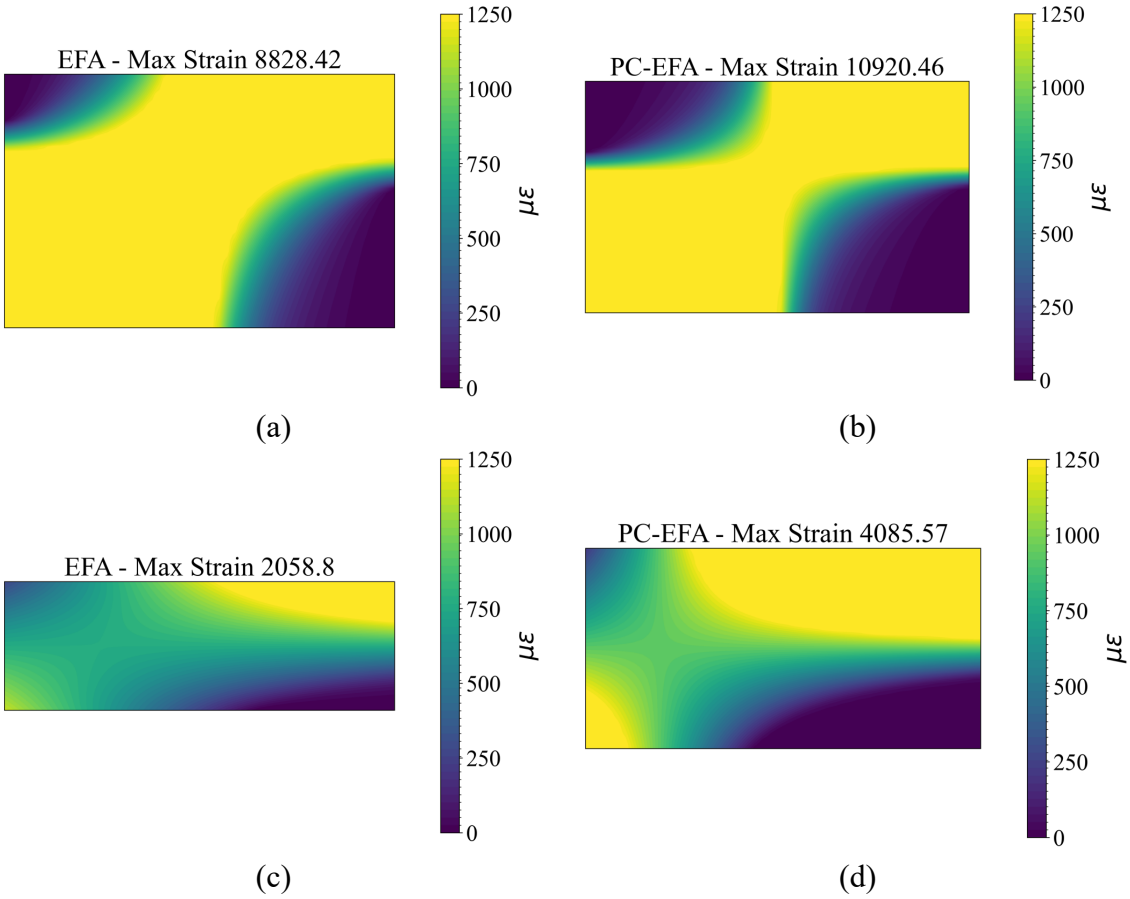


Figure 7.12; (a) Tensile strain distribution of Pier 6 in 3O-RF-W3 derived by EFA using DIC data; (b) Tensile strain distribution of Pier 6 in 3O-RF-W3 derived by PC-EFA using pre- and post-test point clouds; (c) Tensile strain distribution of Spandrel 2 in 3O-RF-W3 derived by EFA using DIC data; (d) Tensile strain distribution of Spandrel 2 in 3O-RF-W3 derived by PC-EFA using pre- and post-test point clouds.

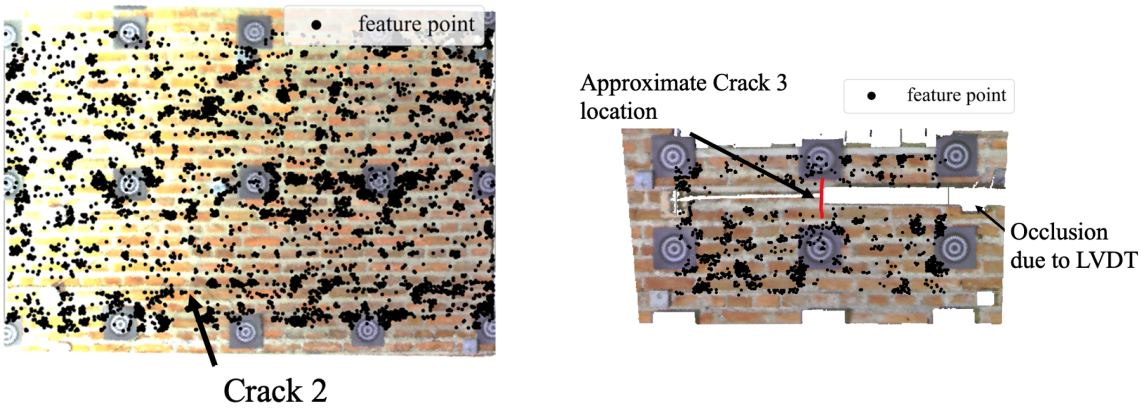


Figure 7.13; (a) Feature points of Pier 6 in 3O-RF-W3 utilised by PC-EFA for strain interpretation, overlaying the post-test point cloud and showing their relative positions to a visible crack (Crack 2); (b) Feature points of Spandrel 2 in 3O-RF-W3 utilised by PC-EFA for strain interpretation, overlaying the post-test point cloud. The vertical crack (Crack 3) observed was highlighted with a red line due to its occlusion in the post-test cloud.

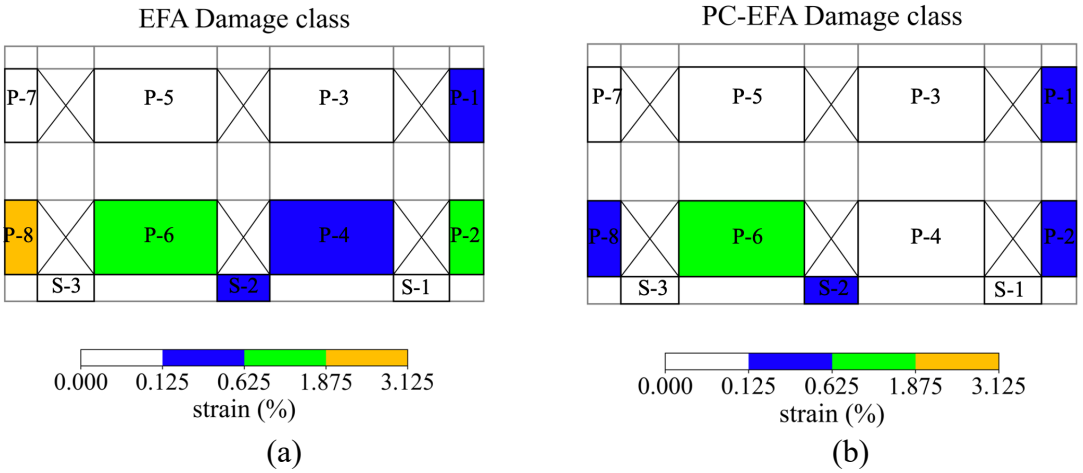


Figure 7.14; (a) Damage category of piers and spandrels (highlighted with black boundary lines) in 3O-RF-W3 based on EFA's maximum interpreted tensile strain at 35mm beam tip settlement. Additional targets above the left external pier were used for EFA to derive maximum tensile strain due to a crack (Crack 1 in Figure 7.15c) running through DIC targets placed on the top of the pier; (b) Damage category of piers and spandrels (highlighted with black boundary lines) in 3O-RF-W3 based on PC-EFA's maximum interpreted tensile strain at 35mm beam tip settlement. Diagonal crosses denote window openings. Piers and spandrels are abbreviated and labelled in the figure for ease of reference: 'P-1' for Pier 1, 'S-1' for Spandrel 1, and so on.

Elsewhere, as shown in Figure 7.14a-b, Cracks 1, 5, and 6 were detected by both EFA and PC-EFA, but PC-EFA had underestimated the extent of the damage categories. While Crack 4 was identified by EFA, it was missed by PC-EFA. Upon closer examination, as depicted in Figure 7.15a, Crack 6 was observed beyond the boundary of Pier 2, and Crack 5 aligned with the lower boundary. It is worth noting that in Figure 7.15a, no feature points are present near the damaged area. This is attributed to the presence of the crack significantly altering the feature descriptors within the local region of the post-test point clouds. As a result, the chance of establishing correspondences between feature points within this local region was largely reduced. Moreover, any established correspondences on the other side of the crack would be treated as outliers in the beam model filter as the damage along the interface does not resemble a typical beam response. Consequently, the estimated maximum strain derived from PC-EFA only reflects the residual strain after the occurrence of damage. Similar instances were observed for Crack 4 on Pier 4 and Crack 1 on Pier 8, as illustrated in Figure 7.15b-c. Separately, Pier 1 on the first storey in Figure 7.14a-b was assigned a 'slight' damage category by both EFA and PC-EFA despite no crack being observed in this pier.

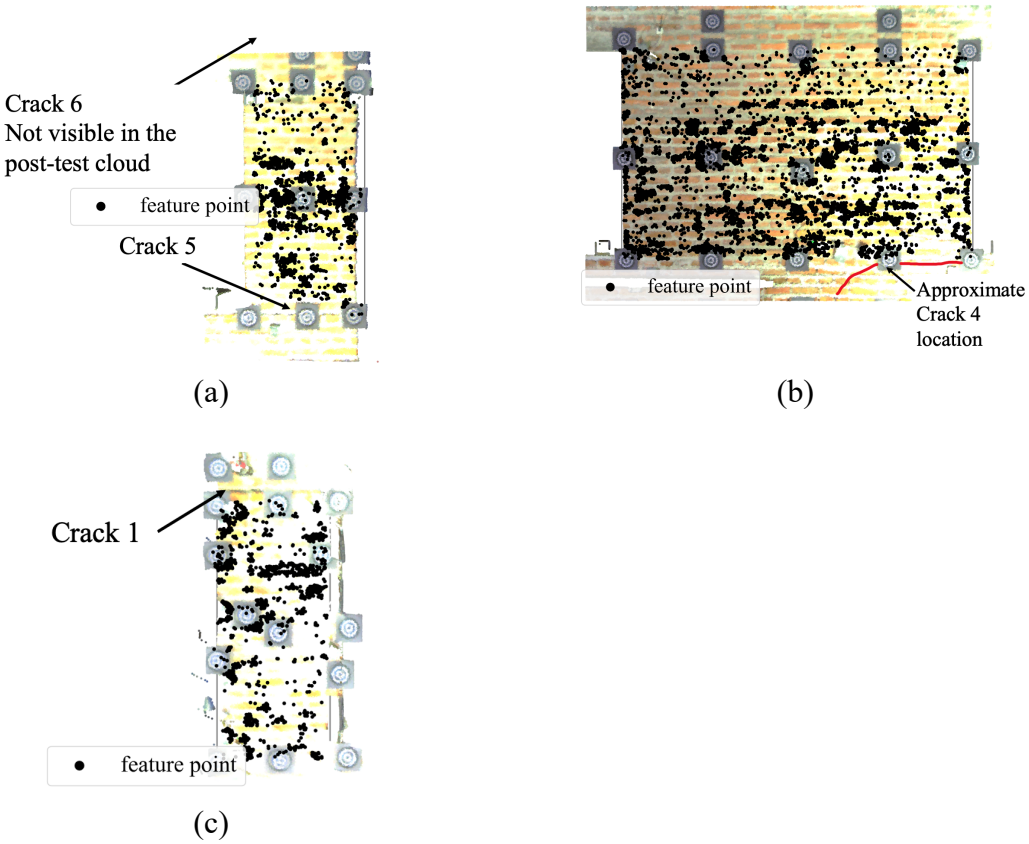
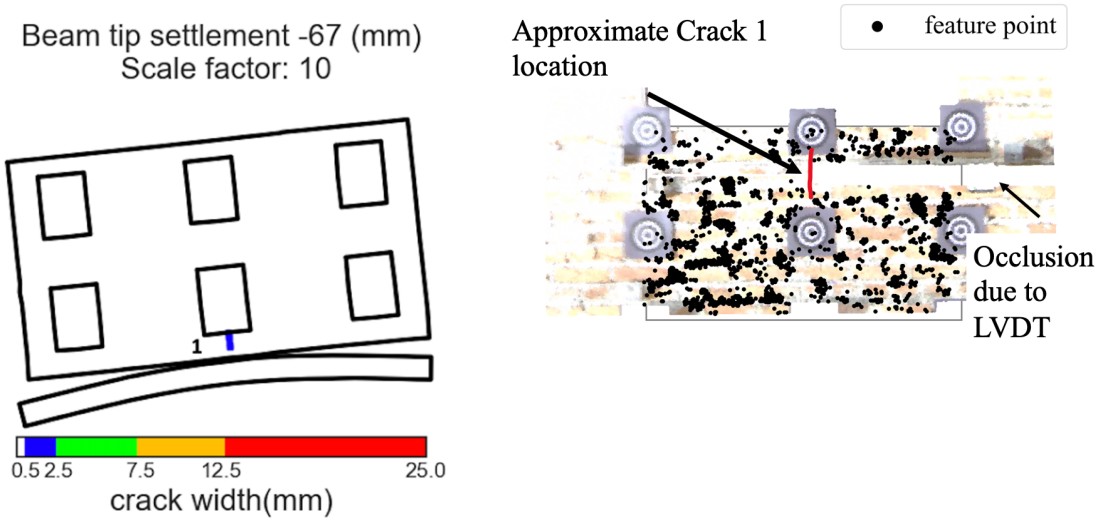


Figure 7.15; (a) Feature points of Pier 2 in 3O-RF-W3 used by PC-EFA for strain interpretation, overlaying the post-test point cloud, showing their relative positions to a visible crack (Crack 6); (b) Feature points of Pier 4 in 3O-RF-W3 used by PC-EFA for strain interpretation, overlaying the post-test point cloud. The diagonal crack (Crack 4) observed on the structural component was highlighted with a red line due to light reflection. (c) Feature points of Pier 8 in 3O-RF-W3 used by PC-EFA for strain interpretation, overlaying the post-test point cloud, showing their relative positions to a visible crack (Crack 1).

7.3.3. 3O-RF-W1

At an induced beam tip settlement of 67mm in 3O-RF-W1, the only observed crack was located on the ground storey's Spandrel 2, as depicted in Figure 7.16a-b. The tensile strain distributions of Spandrel 2, derived using both EFA and PC-EFA, are compared in Figure 7.17a-b. Despite EFA's coverage being limited to the upper half of the spandrel, there are noticeable similarities in the derived distributions on the upper portion. Additionally, both methods indicate that the damage falls within the 'slight' category, consistent with the maximum crack width, as shown in Figure 7.16a. The high strain regions indicated by both approaches correspond to the crack's location on the spandrel. These PC-EFA results were obtained despite significant occlusion.



(a) (b)

Figure 7.16; (a) Deformed shape of the front façade of 3O-RF-W1 with a beam tip settlement of 67mm, showing crack locations and sizes (indicated by the colour bar); (b) Feature points of Spandrel 2 in 3O-RF-W1 utilised by PC-EFA for strain interpretation, overlaying the post-test point cloud. The vertical crack (Crack 1) observed was highlighted with a red line due to its occlusion in the post-test cloud.

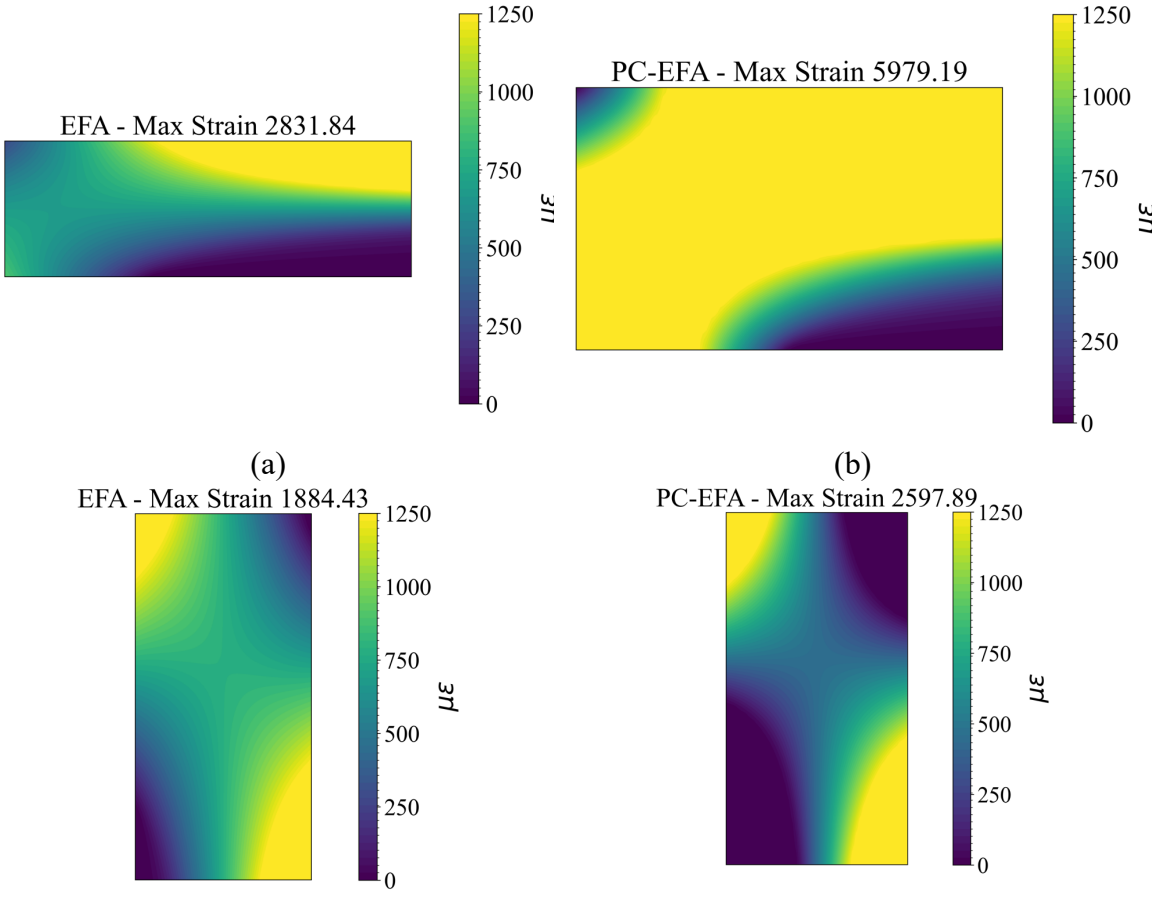


Figure 7.17; (a) Tensile strain distribution of Spandrel 2 in 3O-RF-W1 derived by EFA using DIC data; (b) Tensile strain distribution of Spandrel 2 in 3O-RF-W1 derived by PC-EFA using pre- and post-test point clouds. (c) Tensile strain distribution of Pier 2 in 3O-RF-W1 derived by EFA using DIC data; (d) Tensile strain distribution of Pier 2 in 3O-RF-W1 derived by PC-EFA using pre- and post-test point clouds.

In Figure 7.18a-b, both EFA and PC-EFA have assigned a ‘slight’ damage category to Pier 2 and Pier 4, despite the absence of observed cracking on these piers. Additionally, PC-EFA identifies Pier 8 as having ‘slight’ damage, even though no physical damage was observed there.

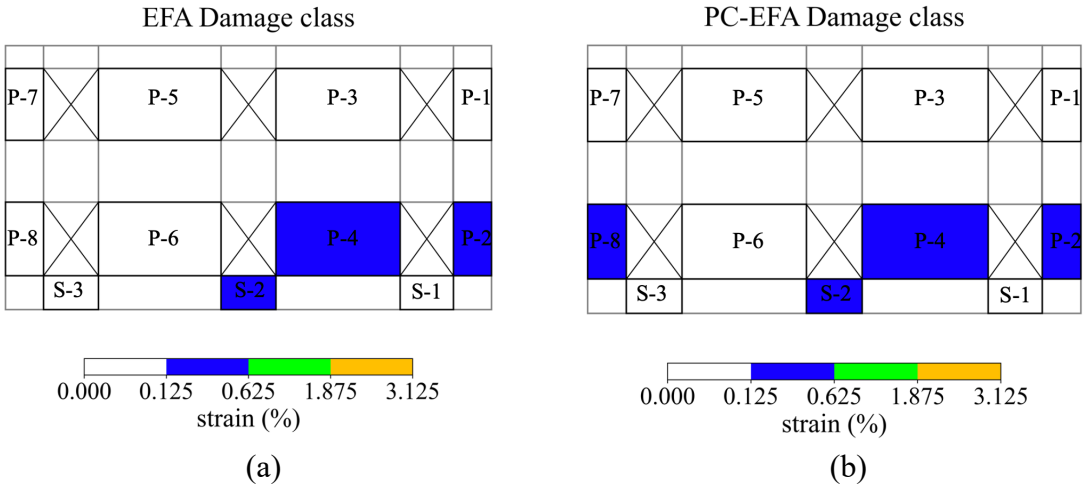
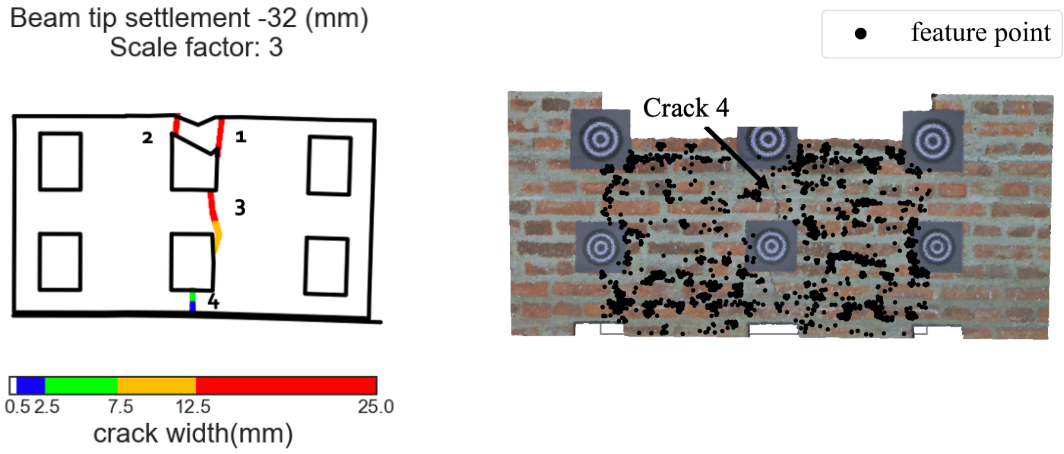


Figure 7.18; (a) Damage category of piers and spandrels (highlighted with black boundary lines) in 3O-RF-W1 based on EFA’s maximum interpreted tensile strain at 67mm beam tip settlement. (b) Damage category of piers and spandrels (highlighted with black boundary lines) in 3O-RF-W1 based on PC-EFA’s maximum interpreted tensile strain at 67mm beam tip settlement. Diagonal crosses denote window openings. Piers and spandrels are abbreviated and labelled in the figure for ease of reference: ‘P-1’ for Pier 1, ‘S-1’ for Spandrel 1, and so on.

However, it is worth noting that the opposing pier of Pier 2 on the rear façade experienced a brittle split at the bed joint (as observed in Dalgic et al. (2023)), suggesting considerable strain on Pier 2. Tensile strain distributions derived from EFA and PC-EFA for Pier 2 are presented in Figure 7.17c-d, indicating a similar distortion with a correlation coefficient of 94.3%.

7.3.4. 3O-JF-W1

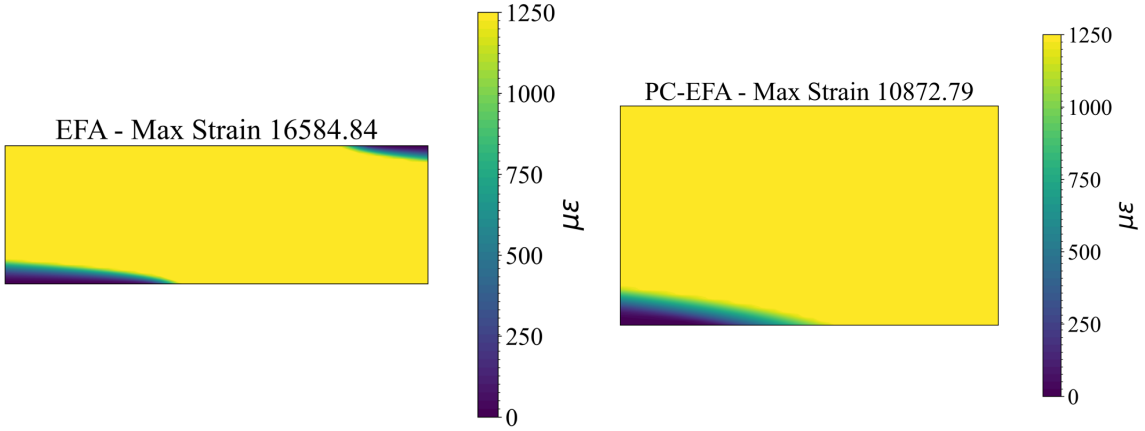
In 3O-JF-W1, when the beam tip settlement reached 32 mm, two vertical cracks (cracks 1 and 2 in Figure 7.19a) suddenly appeared. These initial cracks led to the development of cracks 3 and 4 at lower levels. The ‘very severe’ damage caused by Cracks 1 and 2 resulted in a partial collapse of the central lintel at the top.



(a) (b)

Figure 7.19; (a) Deformed shape of the front façade of 3O-JF-W1 with a beam tip settlement of 32mm, showing crack locations and sizes (indicated by the colour bar); (b) Feature points of Spandrel 2 in 3O-JF-W1 used by PC-EFA for strain interpretation, overlaying the post-test point cloud, showing their relative positions to a visible crack (Crack 4);

According to Figure 7.19a, the lower middle spandrel (Spandrel 2) developed a crack (Crack 4) at the middle span, indicating a 'moderate' damage category based on its maximum crack width. Both EFA and PC-EFA captured this crack, and the derived maximum tensile strains in Figure 7.20a-b also suggested a 'moderate' damage category, consistent with the crack width correlation. As shown in Figure 7.19b, Crack 4 extended the full depth of the spandrel, leading to elevated strain across the entire spandrel, as evident in Figure 7.20a-b.



(a) (b)

Figure 7.20; (a) Tensile strain distribution of Spandrel 2 in 3O-JF-W1 derived by EFA using DIC data; (b) Tensile strain distribution of Spandrel 2 in 3O-JF-W1 derived by PC-EFA using pre- and post-test point clouds.

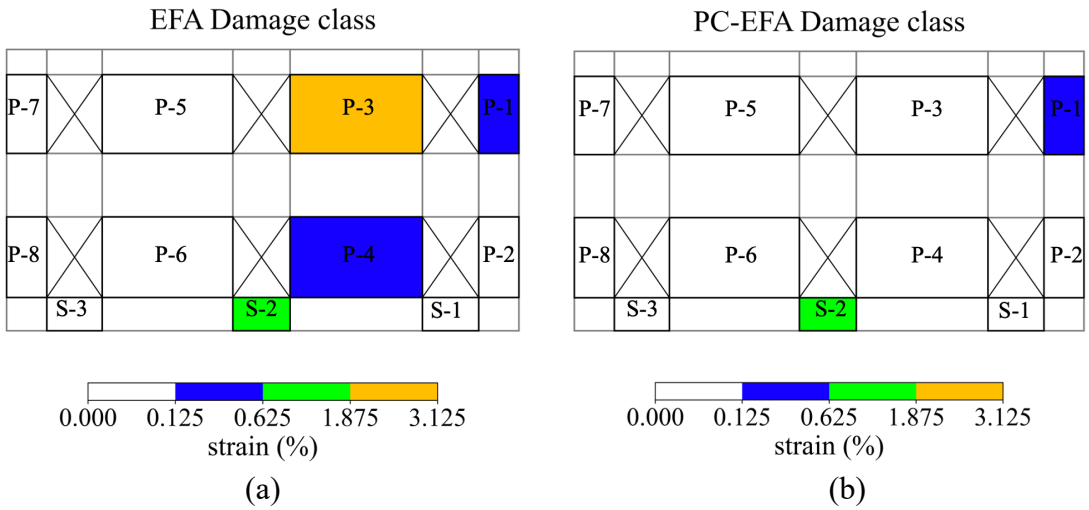
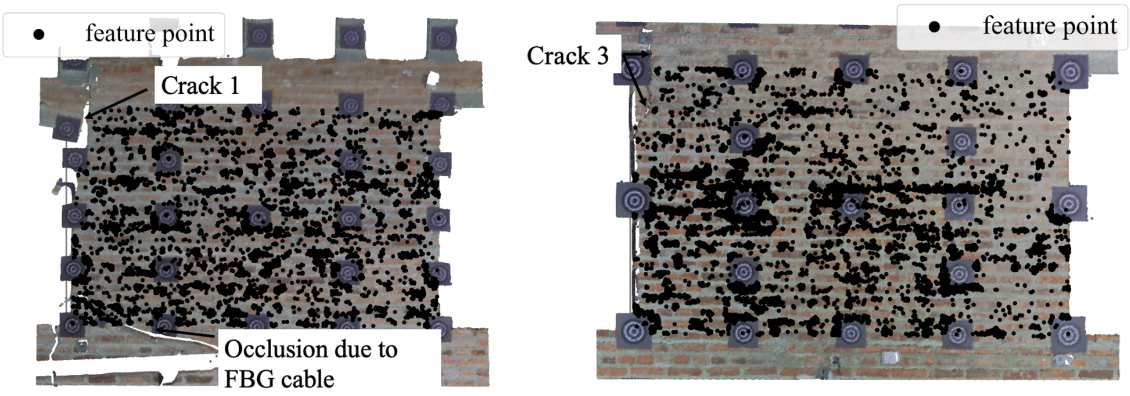


Figure 7.21; (a) Damage category of piers and spandrels (highlighted with black boundary lines) in 3O-JF-W1 based on EFA's maximum interpreted tensile strain at 32mm beam tip settlement. (b) Damage category of piers and spandrels (highlighted with black boundary lines) in 3O-JF-W1 based on PC-EFA's maximum interpreted tensile strain at 32mm beam tip settlement. Diagonal crosses denote window openings. Piers and spandrels are abbreviated and labelled in the figure for ease of reference: 'P-1' for Pier 1, 'S-1' for Spandrel 1, and so on.

On the other hand, Cracks 1 and 3 were detected by EFA (Figure 7.21a), but their severity was underestimated. These cracks, highlighted in Figure 7.22a-b, developed along the boundary of Piers 3 and 4, rendering their inclusion in the beam interpretation of PC-EFA post-damage unfeasible. Specifically, in Figure 7.22a-b, no feature points were present to the left of Cracks 1 and 3, implying that their damage and the resulting displacements do not conform to a beam response. Consequently, these feature points were removed during displacement filtering before strain interpretation.

Furthermore, both EFA and PC-EFA indicated a 'slight' damage category for Pier 1, despite the absence of any observed cracking in this pier (Figure 7.22a-b). Crack 2 was not interpreted, as it did not pertain to any specific structural component under investigation. In fact, this crack was the sole observed crack that did not correspond to any structural components represented by the beam model in all four tests.



(a) (b)

Figure 7.22; (a) Feature points of Pier 3 in 3O-JF-W1 used by PC-EFA for strain interpretation, overlaying the post-test point cloud, showing their relative positions to a visible crack (Crack 1); (b) Feature points of Pier 4 in 3O-JF-W1 used by PC-EFA for strain interpretation, overlaying the post-test point cloud, showing their relative positions to a visible crack (Crack 3);

7.4. Conclusion

This chapter presents the application of the proposed PC-EFA to large-scale building settlement tests. The strains derived from PC-EFA, utilising pre- and post-test point clouds, were validated and benchmarked against the EFA method that employed DIC data. Despite the more relaxed monitoring conditions, the proposed PC-EFA has demonstrated its capability to provide results comparable in strain interpretation and damage classification to the EFA method employing DIC.

Moreover, nearly all parameters used in the proposed PC-EFA are determined based on physical evidence and do not require experimentation or tuning. The method has also exhibited robustness against challenges arising from varying and low point densities.

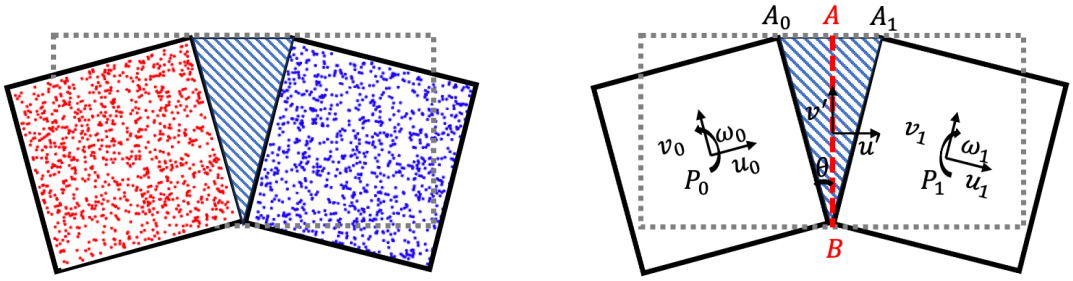
In this application, PC-EFA was implemented by utilising FPFH to establish correspondences and employing the beam model to represent piers and spandrels. It is worth noting that, theoretically, the proposed PC-EFA protocol should also work for other feature descriptors and kinematic representations, as long as the established correspondences can capture the underlying deformation without introducing significant bias and the kinematic representations do not involve an excessive number of parameters.

For cases involving damage along the interfaces of structural components, as demonstrated in Chapter 6, PC-EFA proves more useful, providing indications of strain accumulation before the onset of cracking. In scenarios that require identification and measurements post-damage along the interface, PC-EFA can be complemented by the method termed ‘Point Cloud-based Crack Detector and Quantifier’ (PC-Cr), to be introduced in Chapter 8.

8. Point cloud-based crack detection and crack measurements

8.1. Purpose

In current practice, the identification and quantification of individual cracks form a crucial component of the damage assessment process. However, direct crack monitoring on buildings affected by underground construction is often limited, particularly on a large scale, due to the substantial installation requirements and the labour-intensive nature of these tasks. The PC-EFA, proposed and validated in Chapters 6 and 7, proves to be effective in providing indications of strain accumulation before the onset of cracking. The PC-EFA has also been useful for indicating certain cracks through strain-damage correlation. However, it is worth highlighting that the continuum model (i.e. the beam model) employed in the PC-EFA can only approximate the kinematic behaviour post-cracking to a certain degree. Inevitably, some cracks whose kinematics can no longer be approximated by the continuum model will not be detected by the PC-EFA.



(a) (b)

Figure 8.1; (a) Schematic of a cracking event, where the cracking is indicated by the blue-shaded area. The red and blue points represent simulated feature points on either side of the crack; (b) The proposed segmented rigid-body crack model, in which cracking (indicated by the shaded area) is characterised by two distinct rigid-body motions. These motions are inferred from matched feature points and their respective positions before and after a deformation event, such as settlement. The idealised cracking event results from rotations around Point B by an angle θ in opposite directions. When angle θ is small, the crack planes $\overline{A_0B}$ and $\overline{A_1B}$ can be approximated by a crack path represented by $\overline{AB}$. Under this configuration, crack width is defined as separation of crack planes perpendicular to the crack path (e.g. $\overline{A_0A_1}$ along u' direction), while crack slip is defined as relative movement along the crack path (v' direction).

To address this limitation, this chapter introduces and validates a more general-purpose point cloud-based crack detector and quantifier, termed PC-Cr. Unlike other point cloud-based crack detection and quantification methods reviewed in Chapter 2, the proposed method

employs a newly formulated segmented rigid-body crack model (refer to Figure 8.1a-b), identifying and quantifying cracks using a kinematic-based approach. In this approach, cracking is conceptualised as discontinuities in material (referred to as 'crack path') and characterised by multiple distinct rigid-body motions resulting from these discontinuities, as detailed in Figure 8.1a-b. Consistent with industry practice, crack quantification in this methodology is performed by measuring the 'crack width', representing the separation of crack planes perpendicular to the crack path. Furthermore, this approach enables the quantification of relative movement along the crack path, termed 'crack slip'. The rigid-body motions utilised for identification and quantification of cracks in the proposed model are determined by displacements of feature points. These are inferred from matched feature points and their respective positions before and after a deformation-inducing event, such as settlement. The proposed segmented rigid-body crack model does not prescribe crack locations. Instead, it segments feature points into different clusters based on their kinematic motions. Unlike algorithms which use laser scan intensity to identify crack locations (as reviewed in Chapter 2), the treatment proposed in this chapter allows for the identification of cracks even when the crack itself is not captured by the point cloud (i.e. even when there are no points on the new surfaces created by the cracks). The kinematic properties used for identification and quantification can be inferred from adjacent feature points, thereby further relaxing monitoring requirements.

8.2. Methodology

8.2.1. Overview

Figure 8.2 illustrates the primary steps of the proposed PC-Cr method. Step 0 involves point cloud collection, Step 1 involves point cloud pre-processing, and Step 2 focuses on feature calculation and matching. These steps are consistent with the PC-EFA introduced in Chapter

6 and therefore will not be repeated here. Subsequently, each segmented structural component (comprising both pre- and post-test point clouds as well as feature correspondences) from Step 2 is subdivided into a series of overlapping rolling windows. Within these windows, displacement filtering (Step 3), feature clustering, crack identification (Step 4), and crack measurement (Step 5) are carried out. The detected crack locations and measurements from each rolling window are then assembled and pruned in Step 6 at the level of each structural component.

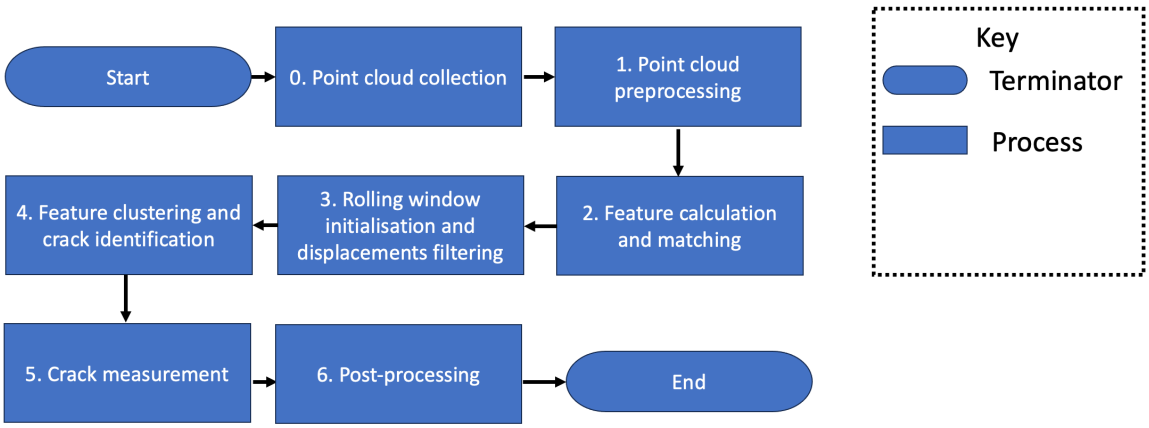


Figure 8.2; Flowchart illustrating the main PC-Cr processes.

The proposed method is implemented by a custom Python package, developed as part of this research, except for initial point cloud registration (a substep in Step 1: Point cloud preprocessing), where Faro Scene is utilised. This package makes use of several general-purpose libraries, namely 'Open3D' (Zhou et al., 2018) for routine 3D point cloud processing, 'NumPy' (Harris et al., 2020) for conducting numerical operations, and 'Pandas' (The Pandas development team, 2023) for data manipulation and analysis. Unless specifically stated, the 'Matplotlib' (Hunter, 2007) Python library is used for visualising the results in this chapter. Any additional libraries utilised for specific tasks are detailed in the corresponding sections where those tasks are discussed.

8.2.2. Rolling window initialisation and displacement filtering

Step 3 involves two distinct phases: rolling window initialisation and displacement filtering, as illustrated in Figure 8.3. As discussed in Chapter 5, structural components, when subjected to settlement, experience dominant rigid-body motion along with distortions, such as bending and shearing. Due to the presence of these distortions, the rigid-body model is considered to more accurately reflect the kinematics within a smaller region than it does for an entire pier or spandrel. Since the proposed segmented rigid-body crack model identifies cracks by detecting distinct rigid-body motions, a smaller search region also aids in identifying more localised cracking. Once the rolling windows are initialised, corresponding feature points within the boundary of each rolling window are selected and passed on for displacement filtering.

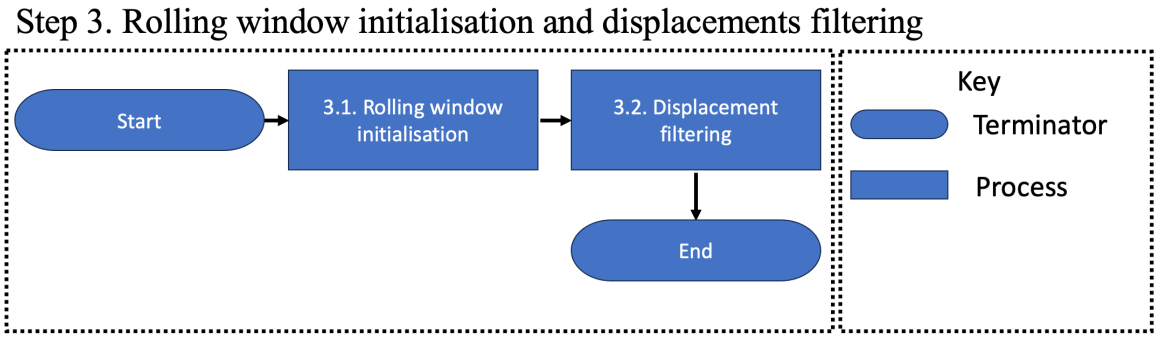


Figure 8.3; Flowchart detailing rolling window initialisation and displacement filtering steps.

The rolling window initialisation and displacement filtering process takes downsized pre- and post-test point clouds, as well as the correspondence set for each structural component, as input. The output is a refined set of correspondences for each rolling window within the structural component.

8.2.2.1. Rolling window initialisation

The rolling windows essentially divide the structural components into multiple smaller regions, which are then used for subsequent crack detection and measurement. The boundary of each structural component is defined by four corner points in the pre-test point cloud.

Because cracking may occur along the boundary of the structural component, the rolling windows need to cover an area slightly larger than the structural component itself. This is achieved by specifying a scan region with offsets from the boundary of the structural component, as illustrated in Figure 8.4. The exact offsets depend on the type of structural component. For example, there is not much point in having a large offset along the horizontal direction for piers, if they are adjacent to window openings along that direction (therefore, no feature points). On the contrary, some offset along the vertical direction for piers can help in the identification of cracks along the boundary.

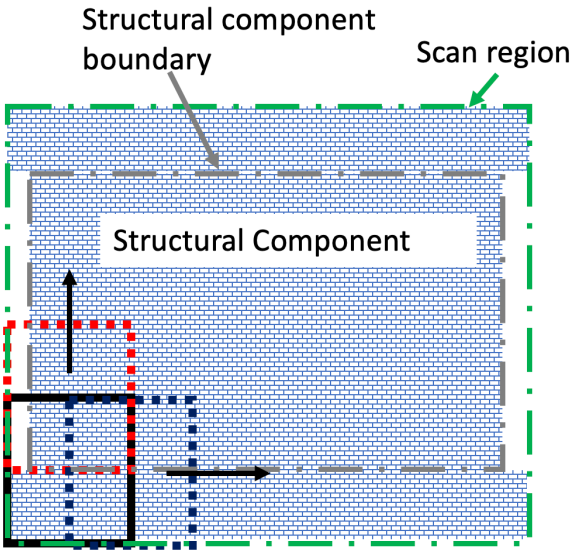


Figure 8.4; Illustration of the rolling window concept. The starting window is outlined with solid black boundary lines, while adjacent windows are shown with dashed boundary lines. The rolling window first moves upwards until it reaches the upper boundary of the scan region, then shifts to the left before travelling upwards again. This process is repeated until the entire structural component/scan region is covered. Green and grey long-dash-dot lines indicate the scan region and the boundary of the structural component, respectively.

Since the boundary of each window is arbitrarily determined, cracks may also coincide with the boundary of rolling windows, resulting in non-detection. To avoid this, overlapping windows are used; the overlap area corresponds to half of the width/height of each rolling window (see Figure 8.4).

A smaller window size generally enables the algorithm to detect more localised motion and trace cracks more accurately. However, this also means that more windows are required to

cover the entire structural component, leading to a longer processing time. The selection of window size is thus a balance between resolution and computational effort. Moreover, excessively small windows may result in a limited number of feature points in each window, leading to a potentially skewed distribution of errors (more discussion on this in Section 8.2.3) and greater inaccuracies in parameter estimation.

8.2.2.2. Displacement filtering

The displacement filtering step comprises four conventional filters, identical to those introduced in Chapter 6 Section 6.2.4.1. The only difference lies in the application of the boundary filter. Instead of using the boundary of the structural component, the boundary of each rolling window is utilised. Feature points located inside the rolling window are then passed through the feature quality filter, distance filter, and normal filter.

8.2.3. Feature clustering and crack identification

As illustrated in Figure 8.5, Step 4 comprises two iterative steps operating on feature point sets in each rolling window. Steps 4.1 and 4.2 are interleaved and continue as long as the new cluster exhibits a rigid motion that is substantially different from that of the previously identified clusters. In this context, a 'cluster' is a subset of feature points whose kinematics can be described by a rigid-body motion within a specified tolerance.

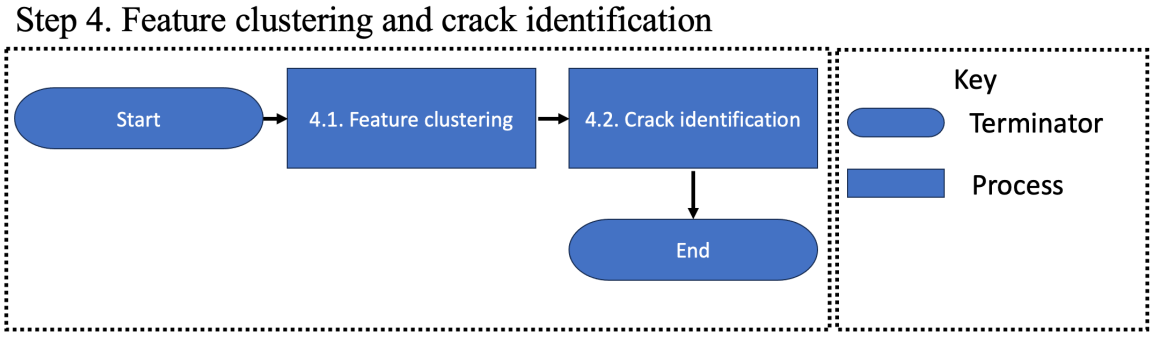


Figure 8.5; Flowchart detailing feature clustering and crack identification steps.

In an uncracked scenario, there is only one dominant rigid motion, with feature points spanning the entire rolling window. The term ‘dominant rigid-body motion’ refers to the motion that describes the kinematics of the largest number of feature points. For feature points that cannot be described by this dominant motion, no secondary rigid motion exists that is substantially different from the dominant one. On the other hand, during a cracking event, at least two distinct rigid motions are typically observed, with their respective centroids considerably separated from each other.

For each rolling window and given feature point set, the variable `crack_flag` is initialised as `True`, and the implementation is conceptualised in the following five subroutines:

While `crack_flag` is `True`:

- Determine the dominant rigid-body motion within the feature point set, `set_a`, and identify a subset, `set_a'`, that conforms to this motion (Subroutine 1).
- Find the optimal rigid model parameters/motion within `set_a'`, and identify a further refined subset, `set_a''`, that conforms to this optimal motion (Subroutine 2).
- Remove the points in `set_a''` from set_a (Subroutine 3).
- Evaluate cracking criteria and update the crack_flag (Subroutine 4).
- If `crack_flag` remains `True`, locate the crack (Subroutine 5).

Figure 8.6; Conceptualisation of crack identification process using 5 subroutines.

In the above conceptualisation, the best rigid model parameters (also referred to as the optimal motion) are the set that yields the smallest RMSE within the subset of feature point `set_a'`. Essentially, Subroutines 1 and 2 handle the feature clustering task (Step 4.1), while Subroutines 4 and 5 are responsible for crack identification (Step 4.2). Subroutine 3 serves as a supportive process, updating the correspondence set for the next iteration. It is worth noting that in the first iteration, crack identification (Subroutines 4 and 5) is skipped; this is because only one cluster exists at that stage. Further details will be provided in the subsequent sections.

Separately, although the algorithm in its current form can identify multiple cracks within a single rolling window—characterised by more than two clusters with distinct rigid body

motion—this capability complicates subsequent discussions on crack identification, measurement, and path optimisation. To concentrate on the fundamental principles of the proposed algorithm, the maximum number of clusters in each rolling window is limited to two for the following discussion and application. Under this setup, multiple individual cracks (in contrast to interconnected cracks) can still be detected and quantified separately in structural components. As is discussed later in this chapter, this treatment is already sufficient for applications, unless there is a specific need to trace interconnected cracks.

Overall, the process for feature clustering and crack identification takes downsized point clouds and feature point correspondences from each rolling window within the structural component as input. It outputs the rolling windows where cracks have been identified, along with their corresponding crack segments.

8.2.3.1. Feature clustering

In each clustering process, the feature clustering step comprises two sub-routines: (a) determining the dominant rigid-body motion; and (b) finding the best rigid model parameters/motion. The determination of the dominant rigid-body motion is carried out by the `Rigid_Model_Filter` function, introduced in Chapter 6. This function employs the rigid-body model:

$$u(x,y) = u - \omega y \tag{8.1}$$

$$v(x,y) = v + \omega x \tag{8.2}$$

where x, y are the position coordinates in the local coordinate system (as shown in Figure 5.2b). u and v are local displacements in the x and y directions. ω is the rigid body rotation.

Since the function implements a standard RANSAC process, it returns the rigid-body motion that yields the largest number of inliers, thereby determining the dominant rigid-body motion. Similar to the PC-EFA method, the RANSAC threshold is set slightly larger than

the re-sampling voxel size to allow for small distortions. The purpose of this process is to filter out feature points that do not conform to the dominant motion before optimal parameter determination. The number of iterations required is determined using Equation 6.11.

Once the subset of points that conform to the dominant motion is determined, they are passed to an iterative clustering process (`Rigid_Model_Clustering` function) to determine optimal rigid-body motion and the associated cluster.

The optimal u, v, and ω would require a pair of feature points with the smallest displacement errors. The displacements estimated using these optimal parameters are expected to yield the smallest RMSE for the subset of points that conform to this motion, subject to a tolerance related to the point density. However, finding the true optimal set requires substantial computational effort. For example, for 1,000 feature points that pass the `Rigid_Model_Filter`, a total of 499,500 iterations would be required to compare all point-pair combinations.

In many cases, selecting point pairs with sufficiently small errors is more practical. Chapter 7 (Figure 7.9) shows that the distributions of u, v displacement errors in the X, Y directions of feature points passing the rigid model filter roughly follow a triangular distribution and are bounded by the re-sampling voxel size. According to the probability density function of the triangular distribution, the probability of selecting a feature point with u or v displacement error that falls within a ±10% interval around the mean (shown in Figure 8.7 with red shading, for a 2mm re-sampling voxel size, this interval represents an error range between -0.2mm to 0.2mm) is 19%. Therefore, the probability of selecting a feature point with both u and v displacement errors within a ±10% interval around the mean is 3.61%. According to Equation 6.11, this inlier rate suggests that with two samples in each draw, 7,063 iterations would yield two points with both u and v displacement errors within a ±10% interval around the mean at a confidence level of 99.99%.

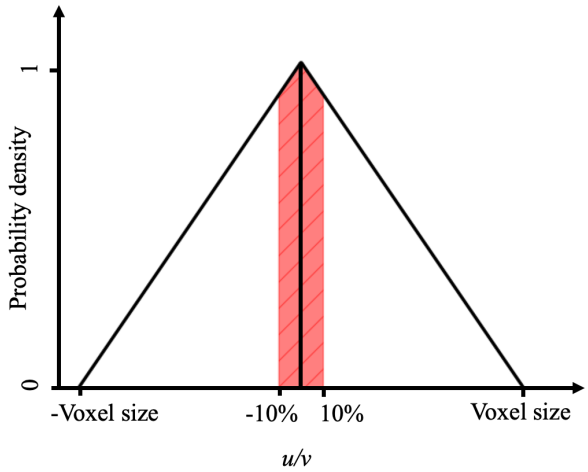


Figure 8.7; Expected error distribution of *u*/*v* displacements of feature points passing the rigid model filters. The red shading highlights the ± 10% interval around the mean.

Suppose the pre-and post-test point clouds are represented by `s` and `t`, respectively. The indices of their corresponding points that have passed the rigid model filter in each rolling window are given by `correspondence_s` and `correspondence_t`. The maximum number of iterations is denoted as `iterations`. The number of samples in each draw is denoted as `n`. The `threshold` is the maximum distance a data point can be away from the model prediction to be considered as 'inlier'. The `min_percent` parameter specifies the minimum size that a cluster must have, expressed as a percentage of the size of `correspondence_s`.

The implementation of the `Rigid_Model_Clustering` is as follows:

```
FUNCTION Rigid_Model_Clustering(s, t, correspondences_s, correspondences_t,
iterations, n, threshold, min_percentage):

    best_cluster = []
    best_model_paras = []
    best_rmse_score = INFINITY
    d = Calculate_Displacements(s[correspondences_s], t[correspondences_t])

    FOR i FROM 1 TO iterations:
        correspondences_s_sample,         correspondences_t_sample         =
Random_Select(correspondences_s, correspondences_t, n)
        d_sample   =   Calculate_Displacements(s[correspondences_s_sample],
t[correspondences_t_sample])
        model_paras   =   Determine_Parameters(s[correspondences_s_sample],
d_sample)
        d_predicted      =      Predict_Displacements(s[correspondences_s],
model_paras)

        current_cluster = []
        total_sq_diff = 0

        FOR each_point IN correspondences_s:
            IF ABS(d_predicted[each_point] - d[each_point]) < threshold:
                ADD each_point TO current_cluster
                total_sq_diff += (d_predicted[each_point] - d[each_point])^2
            END IF
        END FOR

        current_rmse_score = SQRT(total_sq_diff / LENGTH(current_cluster))

        IF    LENGTH(current_cluster)    >    min_percentage    /100    *
LENGTH(correspondences_s) AND current_rmse_score < best_rmse_score:
            best_cluster = current_cluster
            best_model_paras = model_paras
            best_rmse_score = current_rmse_score
        END IF
    END FOR

    RETURN best_cluster, best_model_paras
END FUNCTION
```

Figure 8.8; Pseudocode of function `Rigid_Model_Clustering`. This function implements a clustering process utilising the root mean square error (RMSE) score of all inliers to identify the optimal cluster and determine the rigid body motion that minimises the RMSE score.

In the pseudocode above, the notation `s[correspondence_s]` denotes the selection of points from point cloud `s` based on the indices specified in `correspondence_s`. Similarly, `t[correspondence_t]` denotes the selection from point cloud t based on indices in `correspondence_t`. The `Calculate_Displacements` function computes the displacements between input corresponding points. The `Random_Select` function randomly selects `n` sets of corresponding indices from correspondence sets. The `Determine_Parameters` function uses input coordinates and displacements to compute the rigid model's parameters in a least squares sense, following the method

introduced in Section 5.3.1.1. The `Predict_Displacements` function predicts displacements for each point in the input set based on the derived rigid model's parameters, using the approach presented in 5.3.1.1. The `ABS` function returns the absolute values of the input array. The `SQRT` function returns the square root of the input array, and the `LENGTH` function returns the number of items in the input variable.

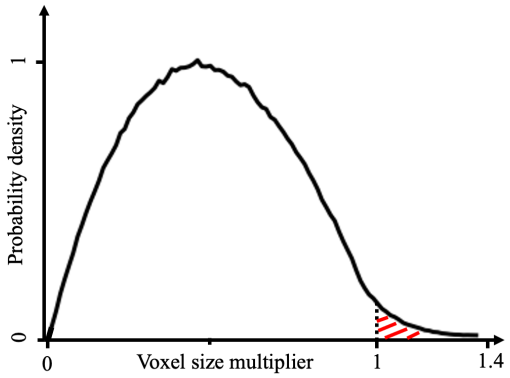


Figure 8.9; Expected total distribution of combined *u*, *v* displacements of feature points passing the rigid model filters. The red shading highlights the probability density of errors greater than the re-sampling voxel size. The graph is generated based on 1,000,000 simulations of the distance measurement between two random points in a unit square.

The number of `iterations` is determined by the probability of selecting a feature point with both *u* and *v* displacement errors within a ±10% interval around the mean. As discussed in Chapter 6, the error distribution of combined *u*, *v* displacements of feature points subject to point density-related error is analogous to the distance distribution of two random points in a unit square. As illustrated in Figure 8.9, although the maximum distance error could exceed the re-sampling voxel size—up to 1.41 times that size—the probability of this occurring is relatively low (less than 3%, as represented by the red-shaded area in Figure 8.9). To include as many feature points carrying genuine displacement information as possible without sacrificing too much resolution (setting the threshold at 1.41 times the re-sampling voxel size would increase the minimum detectable crack width by 41%, discussed further in subsequent sections), it is recommended to set the `threshold` in the `Rigid_Model_Clustering` equal to the re-sampling voxel size.

The min_percent parameter serves two purposes: (a) to ensure that the algorithm does not get trapped in a local minimum, and (b) to define the context in which the optimal motion is determined in Rigid_Model_Clustering. A local minimum occurs when only a handful of feature points conform to the detected motion but yield the smallest RMSE error. Such situations can be avoided by setting a reasonably large min_percent value. However, the value should not be set too high; otherwise, Rigid_Model_Clustering will simply return a motion similar to that produced by Rigid_Model_Filter. In the presence of smaller cracks (relative to the re-sampling voxel size or threshold of Rigid_Model_Filter), Rigid_Model_Filter may attempt to find a compromised motion to maximise the number of inliers. This is also the reason why, in PC-EFA, feature points may still pass both Rigid_Model_Filter and Beam_Model_Filter in the presence of small cracks. In such cases, feature points that conform to this compromised motion may span the crack, and min_percent must be set in a way that allows Rigid_Model_Clustering to 'recover' from this. In this implementation, this percentage is set at 50%, meaning the optimal motion determined by Rigid_Model_Clustering must represent the majority of the feature points that passed through Rigid_Model_Filter. A smaller percentage, such as 30% or 40%, may also work but could alter the sequence of detection and necessitate more iterations in Rigid_Model_Clustering (as it further reduces the probability of selecting feature points within 10% intervals from the mean).

Following the execution of the Rigid_Model_Clustering, the identified best_cluster is removed from correspondence_s and correspondence_t to enable the subsequent iteration identifying the dominant motion and optimal option among the remaining feature points.

8.2.3.2. Crack identification

Crack identification is initiated as soon as two clusters are formed. The identification process consists of two subroutines: (a) checking the cracking criteria (Subroutine 4), and (b) locating the crack, if it exists (Subroutine 5).

The cracking criteria in Subroutine 4 are based on: (a) the relative locations of the identified clusters, and (b) differences in their kinematics. Specifically, the relative locations of the identified clusters are evaluated by measuring the distance between their centroids. For example, Figure 8.10 depicts an idealised cracking event in which a crack is formed as a result of rigid rotations around Point B in opposite directions. For a small rotation angle θ, crack planes A_0B and A_1B may be approximated by a line segment $\overline{AB}$. This line segment is referred to as 'crack line $\overline{AB}$', or 'crack $\overline{AB}$' for simplicity. Points P_0 and P_1 are the centroids of Cluster 0 (represented by red points) and Cluster 1 (represented by blue points), respectively. The distance between P_0 and P_1 is used to assess whether the identified clusters are sufficiently distant from each other. The threshold for this test, known as the 'minimum centroid distance threshold', should be set to less than half of the shortest dimension of the rolling window at a minimum. In practice, this value is often set even lower to account for the uneven distribution of feature points. If the centroids of the two clusters are too close to each other, this often indicates that the last cluster is reflecting secondary global motion related to bending or shearing, rather than a genuine cracking event.

Following the pass of the first test, the second test examines whether the kinematics of the two identified clusters are sufficiently different. To do this, the predicted displacements at the centroids of both clusters are calculated based on the optimal motions determined during the feature clustering stage (Step 4.1). The relative displacement between the centroids is used to assess if the implied crack opening is likely below the minimum detectable limit.

Geometrically, this relative displacement reflects the crack severity, as illustrated in Figure 8.10. Utilising the displacements at the centroids offers a quick means of screening for crack severity, without requiring inference about the relative positions of the clusters at this stage. Since the `Rigid_Model_Filter` and `Rigid_Model_Clustering` cluster points within a tolerance equal to the re-sampling voxel size, an insignificant kinematic difference between the two clusters is more likely a result of errors in estimated model parameters. Consequently, the 'difference of centroid displacement threshold' is set relative to this voxel size, governing the differences in the relative displacement of the centroids of the two clusters. Further discussion on this subject in the context of minimum detectable limit can be found in Section 8.3.

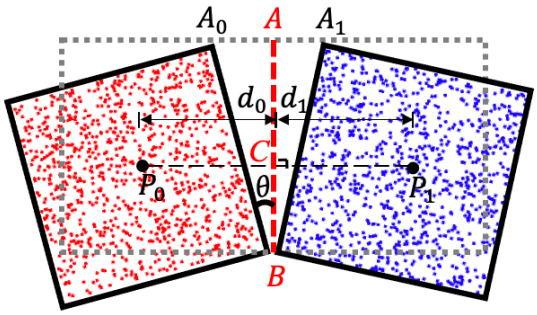


Figure 8.10; Schematic of the crack identification process involving two clusters in an idealised cracking event. A crack, represented by $\overline{AB}$, is formed as a result of rotations around Point B by a small angle θ in opposite directions. Red and blue points represent simulated feature point clusters for Cluster 0 and Cluster 1, respectively. Points P_0 and P_1 are the centroids of Clusters 0 and 1, respectively. The grey dashed boundary represents the rolling window. Measures d_0 and d_1 indicate the spreads of Clusters 0 and 1, respectively. Points A_0 and A_1 are the positions of Point A, after formation of the crack.

As noted in Section 8.2.3.1, the majority of feature points that pass the `Rigid_Model_Filter` are also expected to conform to the optimal motion identified by `Rigid_Model_Clustering`. As an optimisation, the centroid of the second cluster can be approximated using the set of feature points that pass the `Rigid_Model_Filter`. If the second cluster is not sufficiently distant from the first, executing `Rigid_Model_Clustering` becomes unnecessary.

If the two identified clusters pass both tests in Subroutine 4, their geometric properties are used to locate the crack (Subroutine 5). First, a line is drawn between the centroids of the two clusters, which is depicted in Figure 8.10 as $\overline{P_0P_1}$. Then, for each cluster, the median distance of all points to the centroid serves as the measure of spread. This median distance is used instead of the maximum distance because it is less sensitive to outliers.

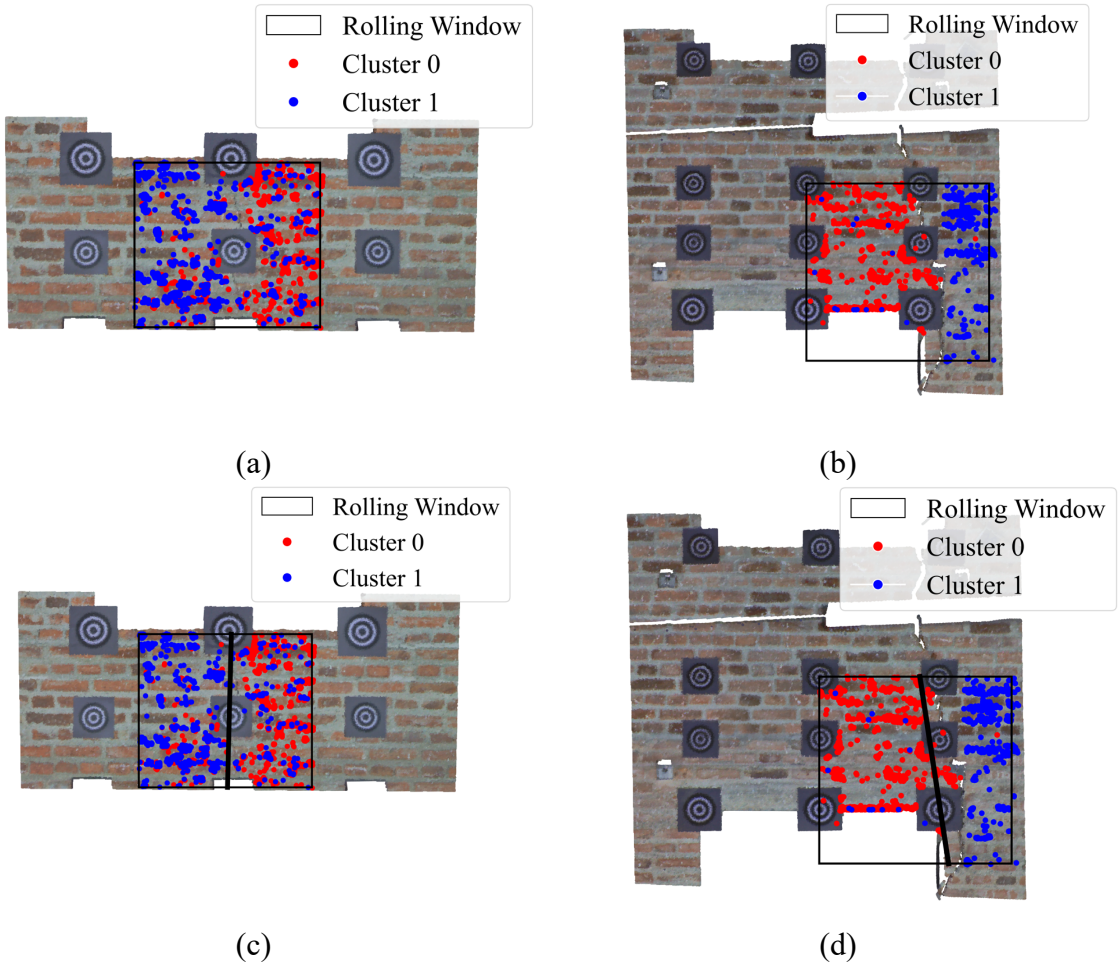


Figure 8.11; (a) Result of the application of the feature clustering step in the presence of a 'slight-moderate' crack in a real-world example; (b) Result of the application of the feature clustering step in the presence of a 'severe-very severe' crack in a real-world example; (c) Result of the application of the crack identification step in the presence of a 'slight-moderate' crack in a real-world example; (d) Result of the application of the crack identification step in the presence of a 'severe-very severe' crack in a real-world example.

For smaller cracks, the clusters tend to span both sides of the crack. As examples, Figure 8.11a-b show the clustering results in real-world scenarios for a 'slight-moderate' crack (Figure 8.11a) and a 'severe-very severe' crack (Figure 8.11b). In the case of the 'slight-moderate' crack depicted in Figure 8.11a, the two clusters are not fully separated and both span the crack at the middle of the rolling window. For Cluster 0, it is apparent that the

feature points are much denser in the region to the right of the crack than to the left. Similarly, for Cluster 1, the feature points are denser in the region to the left of the observed crack than to the right. In contrast, for larger cracks, such as the one presented in Figure 8.11b, the clusters are more clearly separated, consistent with the presence of the crack.

Once the spread of each cluster is determined—using Figure 8.10 as an example—a crack line is established in the following manner: (a) Point *C* is determined along $\overline{P_0P_1}$ in proportion to the spreads d_0 and d_1; (b) A crack line is drawn from Point *C*, perpendicular to $\overline{P_0P_1}$. Its intersections with the boundary of the rolling window are Points *A* and *B*.

Figure 8.11c-d present examples of the application of the above approach, based on the clustering results shown in Figure 8.11a-b, in real-world scenarios. For the 'slight-moderate' crack shown in Figure 8.11a-c, even though the clusters are not fully separated, the method described above is able to accurately locate the crack. This is illustrated as the black line inside the rolling window in Figure 8.11c, which almost overlaps with the observed crack. Figure 8.11b-d present a 'severe-very severe' crack to the right of the rolling window. The proposed method also locates the observed crack with relatively high accuracy. It is worth noting that this was achieved despite the presence of a large void in the bottom-left corner of the rolling window, due to the physical window opening. Nevertheless, such a spatial imbalance of feature points (as shown in Figure 8.11d) is expected to have a greater influence on the detected crack location as the rolling window becomes larger.

Once a crack is located, its intersections with the boundary of the rolling window are passed to the next step for measurements.

8.2.4. Crack measurement

The crack measurement procedure is invoked when a crack is located and its intersections with the boundary of the rolling window are determined. This procedure comprises two steps:

displacement estimation (Step 5.1) and crack quantification (Step 5.2), as shown in Figure 8.12. The crack measurement process takes the coordinates of crack segment intersections within a rolling window and the model parameters of each cluster as inputs, and it outputs the measured crack widths and slips at these intersection points.

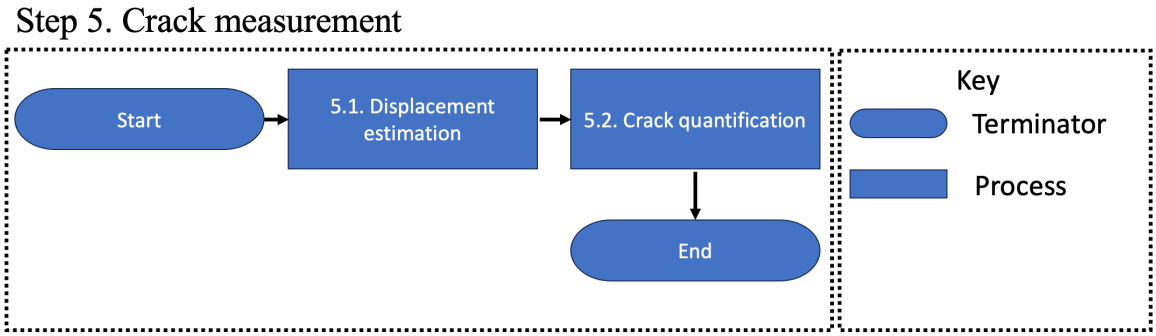


Figure 8.12; Flowchart detailing crack measurement steps.

8.2.4.1. Displacement estimation

In the displacement estimation phase, the u, v displacements of the points where the identified crack intersects the boundary of the rolling window are assessed in the local coordinate system. These are based on the optimal motions of the two clusters. Specifically, using the idealised crack event shown in Figure 8.10 as an example (which is reproduced in Figure 8.13a with additional information), the inferred positions of Point A post-cracking, according to the optimal motions of Clusters 0 and 1, are at Points A_0 and A_1, respectively. The displacements of Points A_0 and A_1 are estimated using the optimal rigid-body parameters obtained in the feature clustering step. These displacements are labelled as u_{A_0}, v_{A_0} and u_{A_1}, v_{A_1} in Figure 8.13a.

8.2.4.2. Crack quantification

In the crack quantification phase, the crack is measured relative to a different coordinate system, depicted as (u', v') in Figure 8.13a and referred to as the 'crack coordinate system'. This system is defined by the crack line $\overline{AB}$ in Figure 8.13a, where u' is perpendicular to the crack line and v' is aligned with it. In most cases, the absolute relative displacements of

a point on the crack face along u' reflect the crack width, unless the implied kinematics suggest that the two clusters have crossed each other at that point (as shown in Figure 8.13d). In such instances, the absolute relative displacement along u' would indicate a crack width that does not exist and is generally not kinematically permissible. On the other hand, the relative displacement along v' indicates the crack slip, and the sign of these relative displacements reflects the direction of slipping.

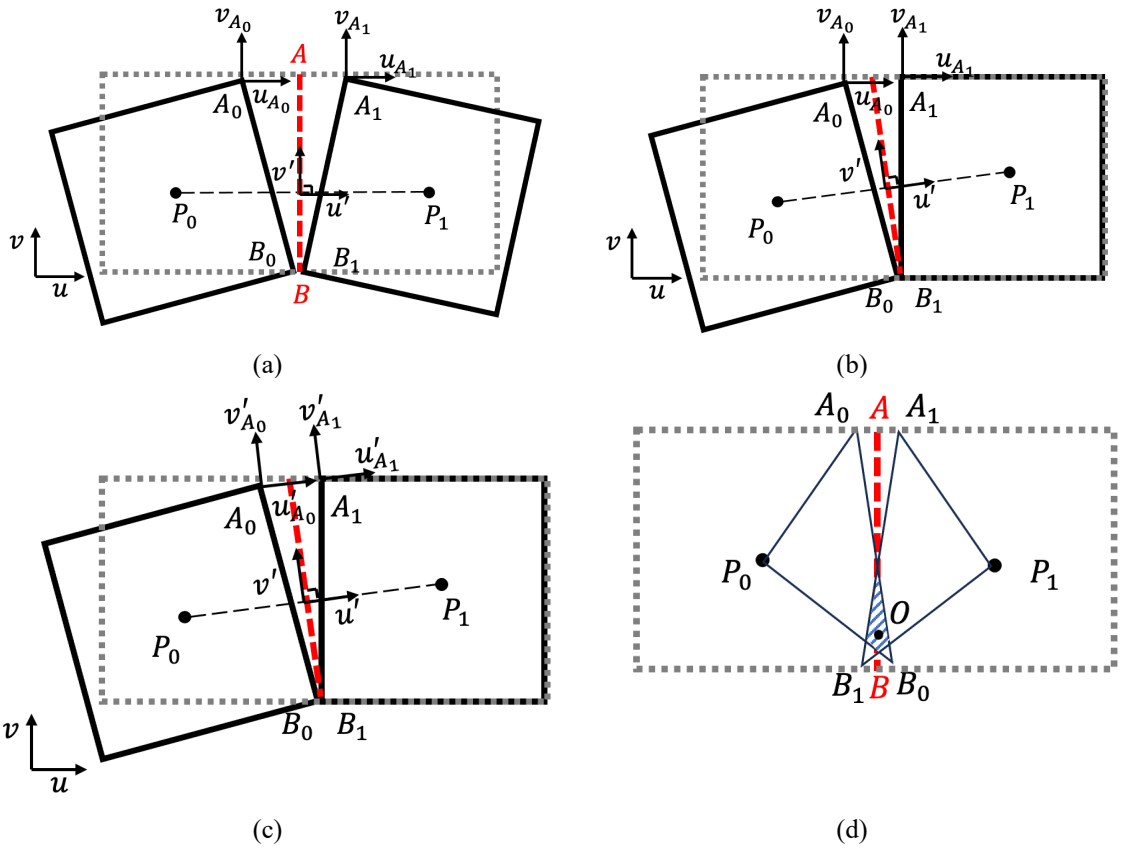


Figure 8.13; (a) Schematic illustrating the crack measurement process with two clusters in an idealised cracking event. A crack, represented by $\overline{AB}$, is formed as a result of rotations around Point B by a small angle in opposite directions.; (b) Schematic showing the crack measurement process where a crack, represented by $\overline{AB}$, forms as a result of the left block (cluster) rotating around Point B; (c) Inferred displacements at Points A_0 and A_1 projected onto the crack coordinate system; (d) Schematic illustrating the test for an overlapping area; Points P_0 and P_1 are the centroids of Clusters 0 and 1, respectively. Points A_0, A_1 and B_0, B_1 represent the inferred locations of Points A and B, based on the optimal motions of Clusters 0 and 1, respectively. The grey dashed boundary represents the rolling window. Feature points are omitted for clarity. Coordinate systems (u,v) and (u',v') are referred to as the local coordinate system and the crack coordinate system, respectively.

In the example shown in Figure 8.13a, the local coordinate system (u,v) aligns with the crack coordinate system (u',v'). In this specific scenario, the absolute difference between u_{A_0} and

u_{A_1} represents the crack width at Point *A*, while the difference between v_{A_0} and v_{A_1} indicates the crack slip at the same point (in this particular case, there is no slip). However, as shown in Figure 8.13b, it is more common for the local coordinate system to not align with the crack coordinate system. When this occurs, the derived displacements u_{A_0}, v_{A_0} and u_{A_1}, v_{A_1} at Points A_0 and A_1 are projected onto the crack coordinate system (*u',v'*), as illustrated in Figure 8.13c. The crack width and slip at Point *A* are then evaluated within the context of the crack coordinate system. This same process is repeated for another intersection point, Point *B*.

Before returning the crack measurement results, the final procedure involves validating these measurements by checking the relative positions of the implied crack planes. Due to errors associated with parameter estimation, the implied crack faces could potentially cross each other, as shown in Figure 8.13d. In this case, the absolute relative displacement between Points B_0 and B_1 is not a valid measure of crack width.

To execute a more general check, for each cluster, the final positions of the intersection points and the centroid are connected to form a triangle. In the example presented in Figure 8.13d, these triangles are $\triangle P_0 B_0 A_0$ and $\triangle P_1 B_1 A_1$. If there is an overlapping area between these triangles, as shown in Figure 8.13d with blue shading, then the centroid of this overlapping area is determined. For simplicity, the crack width at the intersection point closest to the centroid of the overlapping area is set to 0. As will be demonstrated in the following chapters, this approximation has already yielded satisfactory estimations of crack width.

It is worth noting that the above approach does not account for the scenario where two clusters completely overlap each other, resulting in an overlapping area that spans the entire crack face $\overline{AB}$. In such instances, the relative locations of intersection points to the centroid

of the overlapping area become irrelevant. However, such occurrences are deemed to be rare and were not observed in any of the crack cases examined during the extensive settlement test campaign.

Finally, once all rolling windows have been exhausted for a given structural component, the identified crack segments—along with their respective intersections with the rolling window and assessed crack widths and slips—are passed on for post-processing.

8.2.5. Post-processing

As shown in Figure 8.14, the post-processing has three distinct steps: (a) crack path optimisation (Step 6.1), (b) crack measurement interpolation (Step 6.2), and (c) crack measurement pruning (Step 6.3).

The post-processing procedure takes the coordinates of crack segment intersections and crack measurements from all rolling windows within a structural component as inputs and outputs the connected crack paths along with the associated measurements.

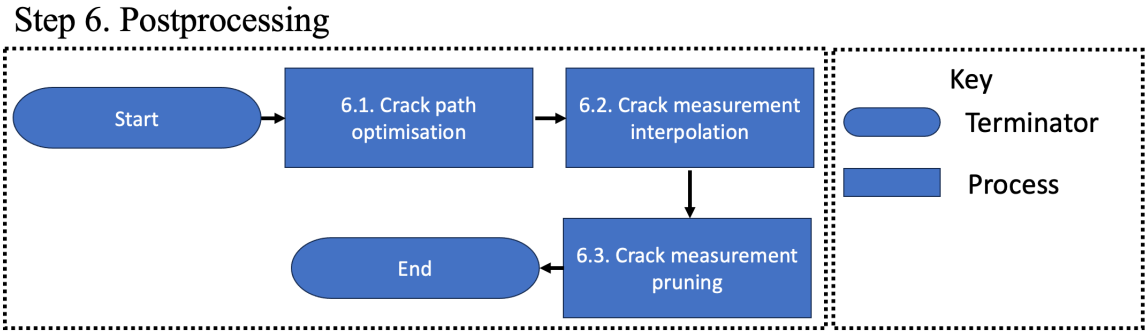


Figure 8.14; Flowchart detailing post-processing steps.

8.2.5.1. Crack path optimisation

The primary goal of crack path optimisation is to connect detected crack intersection points into a continuous polyline. This is modelled as a classic open-loop travelling salesman's problem, where each intersection point is treated as a node. The objective becomes visiting each node exactly once, following the shortest path, without returning to the starting point.

In this implementation, the open-loop travelling salesman's problem is solved using the branch-and-bound search method, as discussed in Winston's 'Artificial Intelligence', specifically in Chapter 4, 'Exploring Alternatives', under the section 'Finding the Best Path' (1984).

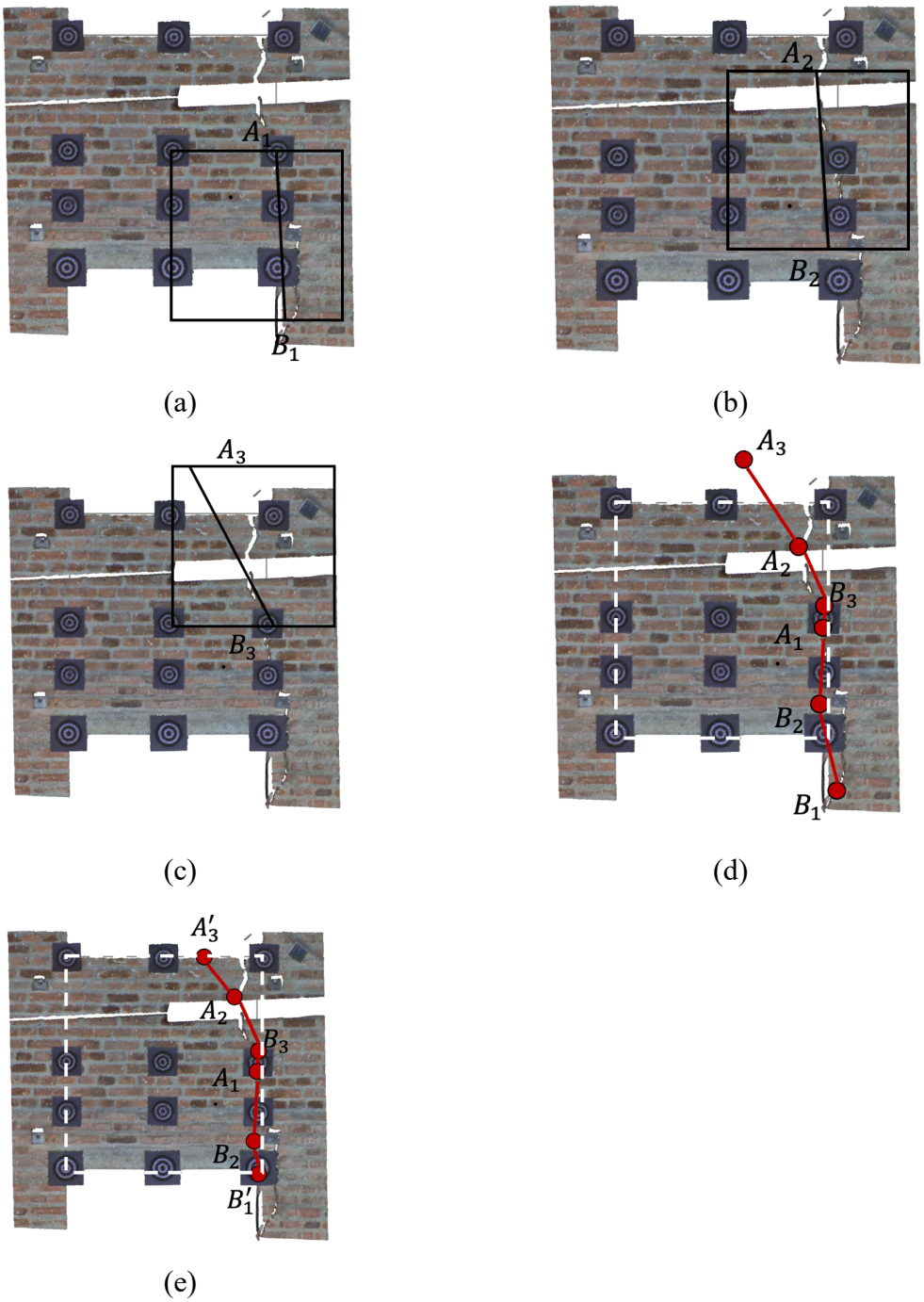


Figure 8.15; (a)(b)(c) Positions of the rolling window (black rectangle) and identified crack segments (black lines across the rectangles) with their intersections with the rolling window boundary labelled accordingly; (d) All crack intersection points connected using branch-and-bound search. The white dashed line indicates the boundary of the structural component; (e) The identified crack within the boundary of the structural component after the crack measurement pruning stage.

Since continuous cracks are expected to be found in adjacent rolling windows, the adjacency list is pruned to remove pairs of nodes (or edges) that exceed a certain distance. This distance is known as the 'maximum node distance threshold' and is typically set to the size of the rolling window, thereby reducing the problem's complexity.

To illustrate the idea of crack path optimisation in Step 6.1, a real-world example is used where a 'severe-very severe' crack is found near the boundary of the structural component. In this example, the crack is detected by three adjacent rolling windows, as shown in Figure 8.15a-b-c. The points where these cracks intersect the boundary of the rolling windows are labelled in the respective figures.

Figure 8.15d depicts all intersection points in relation to the observed crack and the structural component. The red line in Figure 8.15d represents the best route found by the branch-and-bound search, connecting all intersection points with the shortest route (referred to as the crack path).

Even with a relatively large rolling window size, as shown in Figure 8.15d, the crack path identified through the proposed method largely and accurately reflects the observed crack trajectory. The only exception is the segment between A_2A_3. This is due to uneven feature point distribution in the local area and a large void due to the presence of the physical LVDT. A more detailed discussion on the performance of the proposed method will be provided in the 'Results and Discussion' section later.

The branch-and-bound search is followed by a check on the connected nodes in case multiple, non-connecting cracks exist. If there are unconnected nodes (indicating that these nodes belong to a different crack), the branch-and-bound search process is repeated for these missing nodes.

8.2.5.2. Crack measurement interpolation

The crack measurement interpolation is a straightforward process used to interpolate crack widths and slips between adjacent nodes on the crack path. For instance, for the crack path shown in Figure 8.15d, interpolation is first carried out for $\overline{A_2A_3}$ before proceeding to $\overline{B_3A_2}$, until all node pairs have been processed. For $\overline{A_2A_3}$, the interpolation is based on the quantified crack widths and slips at Points A_2 and A_3, which were obtained in Step 5.2 and their respective coordinates from Step 4.2.

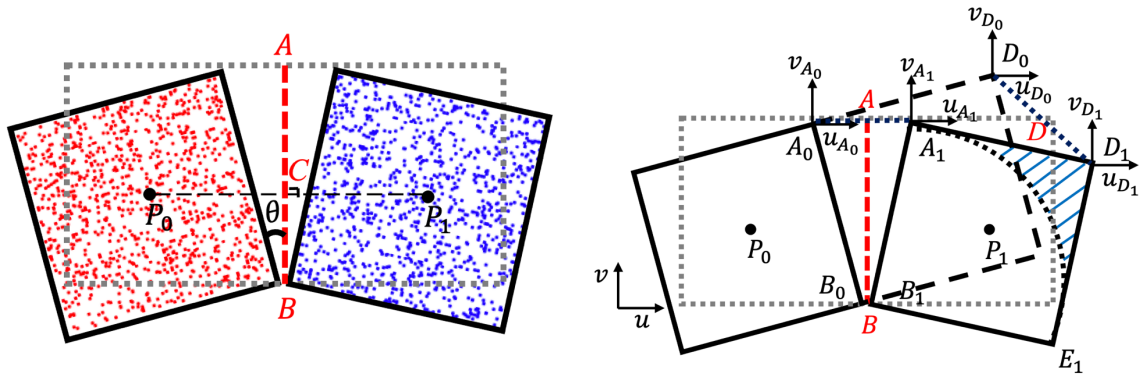
8.2.5.3. Crack measurements pruning

Once crack measurements are interpolated along the crack path, sections that extend beyond the boundaries of the structural components are removed, along with the associated crack widths and slips. In the above real-world example, the truncated crack path is shown in Figure 8.15e. Because the rolling windows extend beyond the boundary of the structural component, this step ensures that crack measurements are only conducted inside the physical boundaries of the component. Specifically, the crack width and slip at Location A_3 are determined within the rolling window depicted in Figure 8.15c in Step 5.2. This particular point coincides with a window opening and is actually outside the structural component. Therefore, the crack width at this point is not meaningful. On the other hand, the crack width and slip determined at Point B_3 are relevant. However, to prevent conflicts with cracks identified and measured in adjacent structural components, the section between $\overline{B_1B_1'}$ is also removed.

8.3. Minimum detectable crack width

The minimum detectable crack width establishes the smallest width that the proposed PC-Cr method can reliably detect and measure. It primarily depends on the detected dominant motion and the initial clustering from `Rigid_Model_Filter`.

To illustrate the concept, consider an idealised cracking event shown in Figure 8.16a, where a crack $\overline{AB}$ is formed as a result of two unit rigid blocks centred at Point P_0 and P_1 (referred to as Rigid Block 0 and Rigid Block 1, respectively) rotating around Point B by a small angle θ in opposite directions. Assume that feature points are evenly distributed across the rigid blocks and that their centroids coincide with the centroid of the respective rigid block. For the sake of simplicity, it is also assumed at this stage that displacements of feature points from feature matching do not contain any noise.



(a) (b)

Figure 8.16; (a) Schematic of an idealised cracking event where a crack, represented by $\overline{AB}$, forms due to two unit rigid blocks rotating around Point B by a small angle θ in opposite directions. Red and blue points denote simulated feature points in Rigid Block 0 and Rigid Block 1, respectively. P_0 and P_1 are the centroids of Rigid Block 0 and Rigid Block 1, respectively. The grey dashed boundary outlines the rolling window. (b) Schematic illustrating the crack clustering process and outlier determination. u_{A_0}, v_{A_0} and u_{D_0}, v_{D_0} represent the predicted displacements of Points A and D, based on the motion of Rigid Block 0. Their predicted locations are A_0 and D_0, respectively. u_{A_1}, v_{A_1} and u_{D_1}, v_{D_1} are the actual displacements of Points A and D in Rigid Block 1, with actual locations A_1 and D_1, respectively. The blue shaded area indicates the region where the difference between predicted and actual displacements exceeds the crack width at Point A.

Suppose that `Rigid_Model_Filter` accurately detects the motion of Rigid Block 0. As depicted in Figure 8.16b, using this motion, the model predicts that Point A has moved to Point A_0, with the displacements being u_{A_0} and v_{A_0}. As shown in Figure 8.16a-b, due to the cracking, Point A has actually moved to Point A_1 in Rigid Block 1, with corresponding displacements u_{A_1} and v_{A_1}. The difference between the predicted and actual displacements of Point A is the absolute difference between u_{A_0} and u_{A_1}. In this particular example, this absolute difference is the crack width at Point A.

The point with the maximum difference between predicted and actual displacements in Rigid Block 1 is Point *D*. The distance between the predicted location of Point *D* (Point D_0) and its actual location (Point D_1) is approximately 1.41 times the crack width at Point *A*. If the threshold for `Rigid_Model_Filter` is set equal to this crack width (crack width at Point *A*), points located in the blue shaded area in Figure 8.16b will be treated as 'outliers' based on the prediction using the detected motion of Rigid Block 0. This accounts for about 21.5% of all points in Rigid Block 1.

As the threshold for `Rigid_Model_Filter` decreases, more points in Rigid Block 1 will be treated as 'outliers' during the initial round of clustering. This allows them to subsequently form a separate cluster. As the size of this cluster grows, it becomes more representative of the behaviour of the rigid block, leading to more accurate crack detection and measurement. However, as discussed in Section 8.2.3.1, the threshold for `Rigid_Model_Filter` is set in relation to the re-sampling voxel size and cannot be reduced beyond the size of the voxel used for re-sampling. However, reducing the point density is necessary to help decrease the minimum detectable crack size.

In the scenario described above, setting the threshold of `Rigid_Model_Filter` to be equal to the crack width at Point *A* initially gave the impression that the remaining feature points were unlikely to yield satisfactory crack identification. This is because the centroid of the shaded area remains considerably distant from the actual centroid, P_1. However, it is apparent that, in reality, the displacements of feature points within the rigid blocks are subject not only to rigid motion but also to random noise attributable to point density. If the random noise is assumed to be bound by a value equal to the crack width at Point *A* (as the threshold for `Rigid_Model_Filter` is related to the re-sampling voxel size), a significantly larger number of feature points—beyond those depicted in the blue shaded region in Figure 8.16b —will be classified as 'outliers'. This will enable them to form a

more representative cluster in subsequent iterations. It is worth noting that, in the case of small cracks, the dominant motion detected by `Rigid_Model_Filter` in the first iteration is likely to be a compromised motion in order to maximise the number of inliers. This explains why feature points from two clusters spanning the crack are shown in Figure 8.11a when the crack is relatively small. Due to these behaviours, as a rule of thumb, the proposed method can be expected to identify and measure crack segments with a crack width greater than the re-sampling voxel size.

8.4. Application to the large-scale building settlement test

8.4.1. Overview

The proposed PC-Cr method was applied to all piers and spandrels of 3O-RF-W3 and 3O-JF-W1. In the case of 3O-JF-W1, cracks were also observed on two additional elements; these elements were included for completeness. The detected cracks and measured crack widths were validated through post-test laser scan point clouds, digital images, and DIC measurements in the context of each test.

3O-RF-W1 was excluded because the only crack observed had a maximum width of 1.02 mm, which was well below the re-sampling voxel size used for that structural component (2.2 mm for Spandrel 2 in 3O-RF-W1). Another test, 50O-RF-W1, was also excluded due to its low point density in the pre- and post-test point clouds. The re-sampling voxels used for most structural components in 50O-RF-W1 exceeded 4 mm, thereby hindering the proposed method's ability to detect cracks smaller than that size.

In applying the proposed PC-Cr method to 3O-RF-W3 and 3O-JF-W1, the exact same segmentations and feature correspondences used in Chapter 7 were reused. For this reason, Step 1 (point cloud preprocessing) and Step 2 (feature calculation) will not be repeated in this section.

All applications and analyses were conducted on a 2019 MacBook Pro equipped with a 2.4 GHz Quad-Core Intel Core i5 processor and 8GB RAM.

8.4.2. Rolling window initialisation and displacements filtering

The number of rolling windows used in the application is summarised in Table 8.1. The divisions specified in Table 8.1 indicate that the width and height of each rolling window ranged from 300 mm to 400 mm, regardless of the type of structural component. These dimensions remained constant for each structural component.

Table 8.1; Summary of parameters used in determining the number of rolling windows for different types of structural components, as part of the PC-Cr processes, for applications to the large-scale building settlement test.

Structural component type	Number of rolling windows along vertical direction	Number of rolling windows along horizontal direction
Slender pier	5	1
Stocky pier	5	8
Spandrel	1	3

The parameters used for displacement filters in this application largely remained consistent with those used in conventional filters for PC-EFA (see Chapter 7). The only difference lies in the boundary filter: the corner points of each rolling window were used instead of the corner points of each structural component.

Table 8.2; Parameters used in displacement filters as part of the PC-Cr processes, applied to the large-scale building settlement test.

Boundary filter	Feature quality filter (Number of standard deviation)	Feature quality filter (Selecting on log scale)	Distance threshold (mm)	Normal threshold
Corner points of each rolling window	0.1	Yes	150	0.8

8.4.3. Feature clustering and crack identification

As discussed in Section 8.2, the maximum number of clusters for each rolling window is limited to two. This constraint was implemented by setting the maximum number of iterations for feature clustering and crack identification to two. Consequently, only the first two most dominant motions were used to determine the crack location in case of cracking.

If interconnected cracks are of particular concern, the termination criteria for feature clustering and crack identification could be set based on the parameters outlined in Table 8.4, referred to as 'cracking test parameters'. The process would then continue until the most recently identified cluster no longer satisfies the cracking tests when compared with any of the previously identified clusters. In such cases, the 'minimum centroid distance threshold' specified in Table 8.4 would need to be set dynamically, based on the number and relative position of already identified clusters. While this capacity offers an intriguing avenue for more nuanced crack detection, such nuances are beyond the scope of the current study and will not be elaborated further.

In the feature clustering, parameters used in `Rigid_Model_Filter` and `Rigid_Model_Clustering` functions are summarised in Table 8.3.

Table 8.3; Summary of parameters employed in the `Rigid_Model_Filter` and `Rigid_Model_Clustering` functions as part of the PC-Cr processes for applications to the large building settlement test.

Process	Outlier Threshold	Sample drawing method	Number of samples in each draw	Maximum iterations	Minimum percentage
Rigid model filter	1.2 × re-sampling voxel size	Random	2	20,000	-
Rigid model clustering	1 × re-sampling voxel size	Random	2	20,000	50%

In both functions, the outlier thresholds were set in relation to the re-sampling voxel size used for each structural component. Variations in point density across each structural component were considered negligible due to their relatively small size. The `Rigid_Model_Filter` employed a slightly larger threshold than that used in `Rigid_Model_Clustering` to account for feature points also subjected to legitimate secondary motions, such as bending and shearing. In each iteration for both functions, two samples were drawn randomly. The maximum number of iterations was conservatively set to 20,000, allowing both functions to handle an inlier rate as low as 2.2%. Lastly, the minimum percentage parameter in `Rigid_Model_Clustering`, which governs the

minimum size of an eligible cluster, was set at 50% of the number of feature points that passed the `Rigid_Model_Filter`.

Table 8.4; Summary of parameters employed in crack identification as part of the PC-Cr processes for applications to the large building settlement test.

Process	Minimum centroid distance threshold (mm)	Difference of centroid displacement threshold
Crack identification	125	0.75 × re-sampling voxel size

Parameters used in crack identification are summarised in Table 8.4. These two parameters were applied consistently across different tests for each structural component.

Since this application considered only two clusters in any given rolling window, the minimum centroid distance threshold was set at a fixed value, less than half of the smallest dimension of the rolling window. The difference of centroid displacement threshold was set at 0.75 times the re-sampling voxel size of the structural component under study. The proposed algorithm is relatively insensitive to this threshold; when set between 0.5 and 1, the algorithm returned the exact same set of identified cracks.

8.4.4. Crack measurement

Since this application considers only two clusters in any given rolling window, the crack measurement process is deterministic, given the intersection points on the rolling window and the optimal motions of the clusters. The process does not require any additional parameters.

8.4.5. Post-processing

The sole parameter used in the post-processing step is the maximum node distance threshold, set at a fixed value of 400 mm (the maximum rolling window size). When multiple cracks are present in a single structural component, this threshold ensures that the branch-and-bound search does not incorrectly connect different, non-connecting cracks that are separated by more than the size of a rolling window. It is worth noting that if two non-

connecting cracks have nodes with distances less than the threshold, the branch-and-bound search may attempt to connect them, leading to an erroneous crack path. In such cases, more advanced clustering methods are required for grouping crack segments before attempting to connect them.

8.5. Results and discussion

In the following section, the results of applying the proposed PC-Cr method to each structural component of 3O-RF-W3 and 3O-JF-W1 are presented as follows. First, the overall damage state of the masonry façade at the end of each test is described. Then, for each structural component where a crack was detected by the proposed method, the detection and measurement details are presented and discussed in conjunction with observed damage and virtual LVDT measurements (referred to as vLVDT) from the DIC. As introduced in Chapter 3, virtual LVDTs were established within the DIC along each observed crack. These vLVDT utilised the relative displacements of adjacent DIC targets, positioned perpendicular to the crack's orientation, to measure the crack widths (see Figure 3.3). Finally, a review of all other structural components is provided, followed by a summary of the performance of the proposed method for each test.

8.5.1. 3O-RF-W3

At an induced beam tip settlement of 35 mm, six cracks were observed in the test at the ground storey of the façade, as depicted in Figure 8.17. Among them, three were horizontal cracks (labelled as Cracks 1, 5, and 6 in Figure 8.17) located at the slender external piers; these correspond to the 'severe', 'moderate' and 'slight' categories, based on their maximum crack width from the DIC and in accordance with damage correlation in Table 3.6. Two 'moderate' diagonal cracks (labelled as Cracks 2 and 4 in Figure 8.17) were observed on the

stockier internal piers. Additionally, a ‘slight’ vertical crack (labelled as Crack 3 in Figure 8.17) was observed on the middle spandrel of the ground storey.

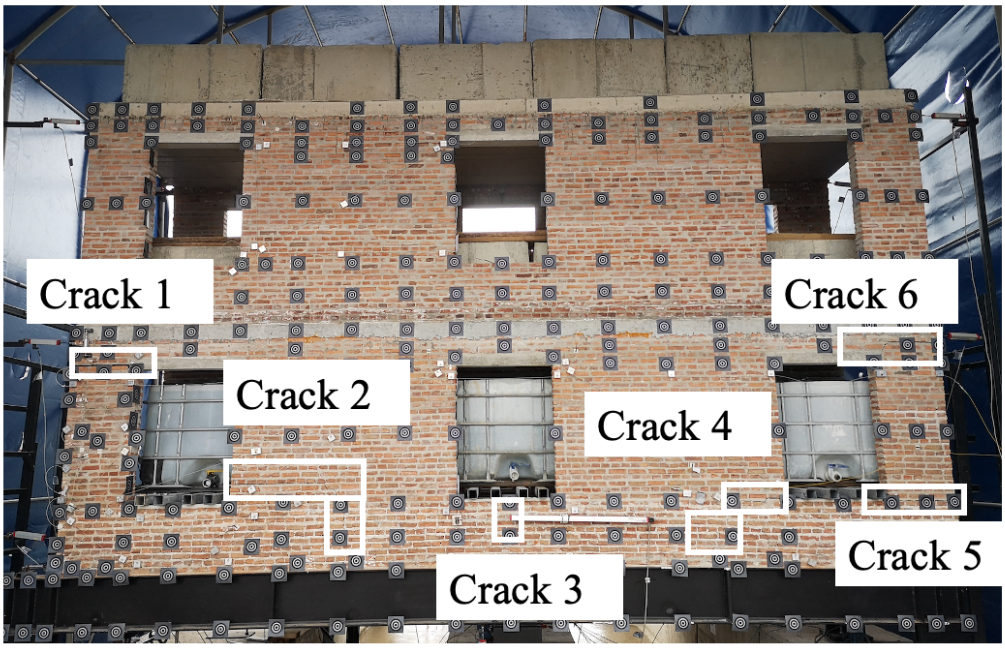
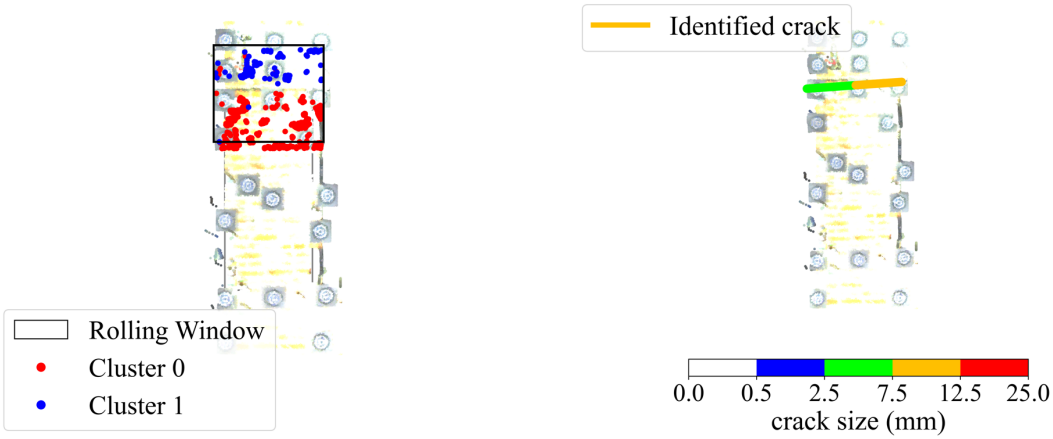


Figure 8.17; Image taken post-test for 3O-RF-W3, annotated to show observed cracks on the front wall façade. Original photos courtesy of Korhan Dalgic and Burcu Gulen.

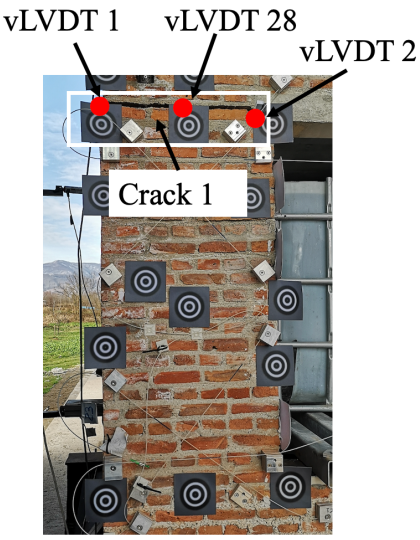
8.5.1.1. Crack 1

Pier 8 has a re-sampling voxel size of 3.6mm. Crack 1 on Pier 8 was detected by the proposed method in one of its rolling windows, as shown in Figure 8.18a. In the figure, feature points are almost entirely separated into two clusters along the observed crack. The number of feature points in Cluster 0 (the red cluster in Figure 8.18a) and Cluster 1 (the blue cluster in Figure 8.18a) are 481 and 131, respectively. Figure 8.18b shows that the detected crack path almost overlaps with the crack trajectory observed on the post-test point cloud. The maximum measured crack width of Crack 1, according to the proposed method, was 7.83mm, compared to 8.03mm according to virtual LVDT results (vLVDT 1) from the DIC. The physical appearance of the observed crack is also shown in Figure 8.18c in a digital image taken after the test. This crack formed as a result of the split of the pier from the remainder of the façade. It is worth noting that the determined crack path in Figure 8.18b is at a slight angle as opposed to almost horizontal (as shown in Figure 8.18c). This discrepancy was due

to congestion of FBG clamps in the region, resulting in considerably uneven feature point distribution. If precise location and orientation are concerns, this issue may be addressed by re-sampling the feature points in each cluster.



(a) (b)



(c)

Figure 8.18; (a) Feature clustering results from Rolling Window 4 as part of the PC-Cr processes applied to Pier 8 in 3O-RF-W3. Clustered feature points are shown in different colours, in accordance with the legend. Results are presented overlaid on the post-test point cloud of Pier 8 in 3O-RF-W3; (b) Output of the PC-Cr processes applied to Pier 8 in 3O-RF-W3. The determined crack path is drawn overlaid on the post-test point cloud of Pier 8 in 3O-RF-W3. The colour of the crack path reflects the crack width, in accordance with the colour bar; (c) Annotated image of Pier 8 in 3O-RF-W3 taken post-test, showing the physical appearance of the identified crack and the points (in red dots) where virtual LVDTs from DIC intersect the observed crack. Original photo showing the crack, courtesy of Korhan Dalgic and Burcu Gulen.

The uneven distribution of points also slightly affected the crack width measurements. Based on the proposed method, the left end of Crack 1, as shown in Figure 8.18b, was measured at 7.1 mm and fell into the ‘moderate’ category. This is in contrast to a measurement of 8.03

mm from vLVDT 1 (location indicated in Figure 8.18c) at the same point. At the right end of Crack 1, the crack width was measured at 7.9 mm based on the proposed method and is categorised as 'severe' in Figure 8.18b. This contrasts with a measurement of 7.0 mm from vLVDT 2 (location indicated in Figure 8.18c) at the same point. Despite these discrepancies primarily stemming from uneven feature point distribution, the difference in measured crack width between the proposed method and DIC is relatively small.

8.5.1.2. Crack 2

Pier 6 has a re-sampling voxel size of 3mm. Crack 2 on Pier 6 was detected by the proposed method in two of its rolling windows, as shown in Figure 8.19a-b. In these figures, feature points in both rolling windows are less distinctly separated compared to Crack 1, but they still reflect the crack's location. Compared to Figure 8.19a, the clusters in Figure 8.19b have more points spanning across the crack. In Figure 8.19a, Cluster 0 and Cluster 1 contain 283 and 227 feature points, respectively. In Figure 8.19b, the numbers are 388 and 375, respectively. Figure 8.19c shows that the detected crack path generally follows the horizontal section of the observed crack trajectory, albeit with some noticeable offset. This offset was due to concentrations of feature points around some DIC targets located above the observed crack (see Figure 8.19a-b).

The maximum measured crack width for Crack 2, according to the proposed method, was 5.14mm. This compares to a 4.24mm width measured by virtual LVDT (vLVDT 3) from the DIC. Both methods reported the maximum crack width at the same point, where vLVDT 3 intersects the crack (as shown in Figure 8.19d). The crack width reported by vLVDT 4 was 1.01mm, as opposed to the 1.5mm width reported at the right end of the identified crack path by the proposed method (see Figure 8.19c). The width reported at vLVDT 7 was

1.54mm, which was well below the minimum detectable crack limit (3mm), explaining why the diagonal section of the crack trajectory was not detected by the proposed method.

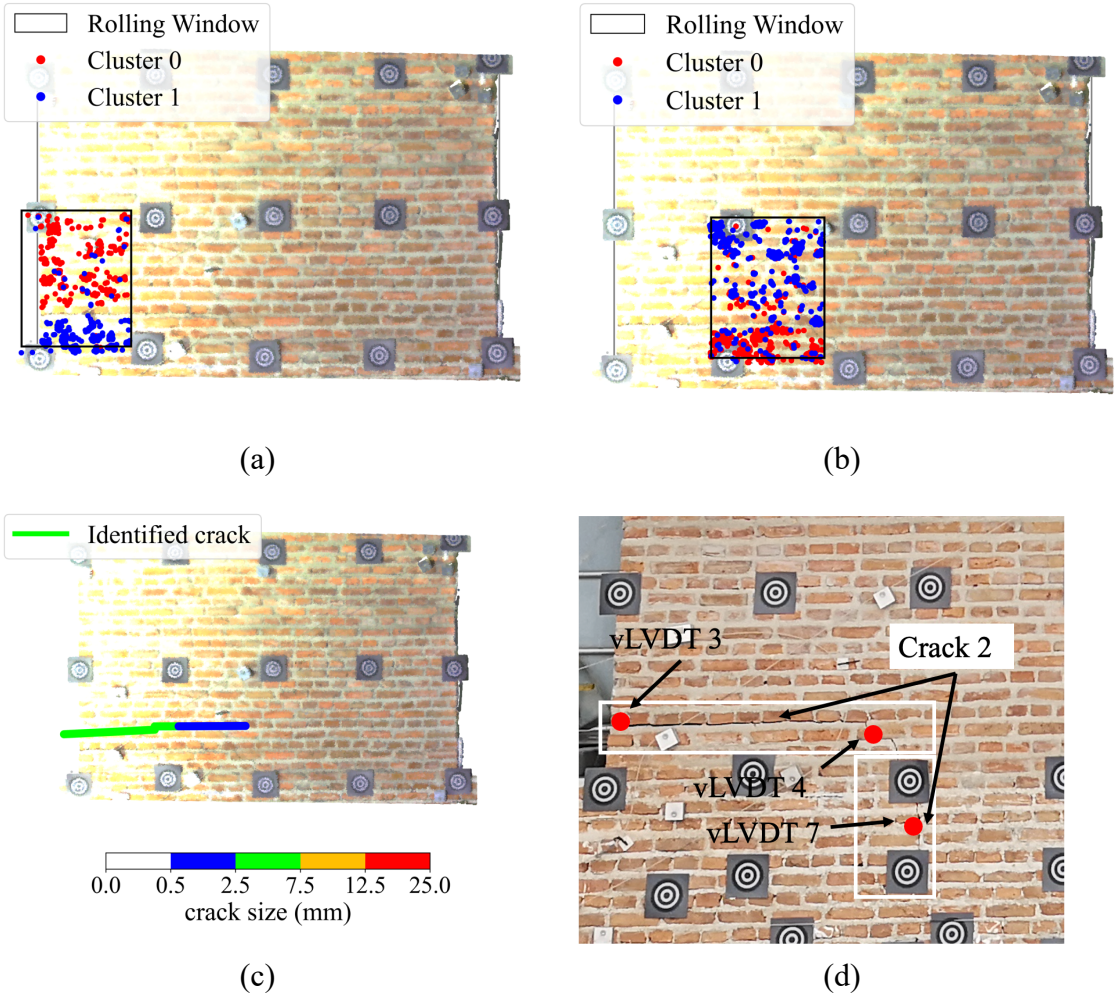


Figure 8.19; (a)(b) Feature clustering results from Rolling Window 1 and 11 as part of the PC-Cr processes applied to Pier 6 in 3O-RF-W3. Clustered feature points are shown in different colours, in accordance with the legend. Results are presented overlaid on the post-test point cloud of Pier 6 in 3O-RF-W3; (c) Output of the PC-Cr processes applied to Pier 6 in 3O-RF-W3. The determined crack path is drawn overlaid on the post-test point cloud of Pier 6 in 3O-RF-W3. The colour of the crack path reflects the crack width, in accordance with the colour bar; (d) Annotated image of Pier 6 in 3O-RF-W3 taken post-test, showing the physical appearance of the identified crack and the points (red dot) where virtual LVDTs from DIC intersect the observed crack. Original photo showing the crack, courtesy of Korhan Dalgic and Burcu Gulen.

8.5.1.3. Crack 4

Pier 4 has a re-sampling voxel size of 3.1mm. Crack 4 on Pier 4 was detected by the proposed method in one of its rolling windows, as shown in Figure 8.20a. Similar to Crack 2, feature points in the rolling window in Figure 8.20a are less distinctly separated but still largely reflect the crack's location. Unlike Crack 2, the distribution of feature points is more even.

In Figure 8.20a, Cluster 0 and Cluster 1 contain 317 and 211 feature points, respectively. A comparison of Figure 8.20b-c shows that the detected crack path closely aligns with the horizontal portion of the observed crack trajectory.

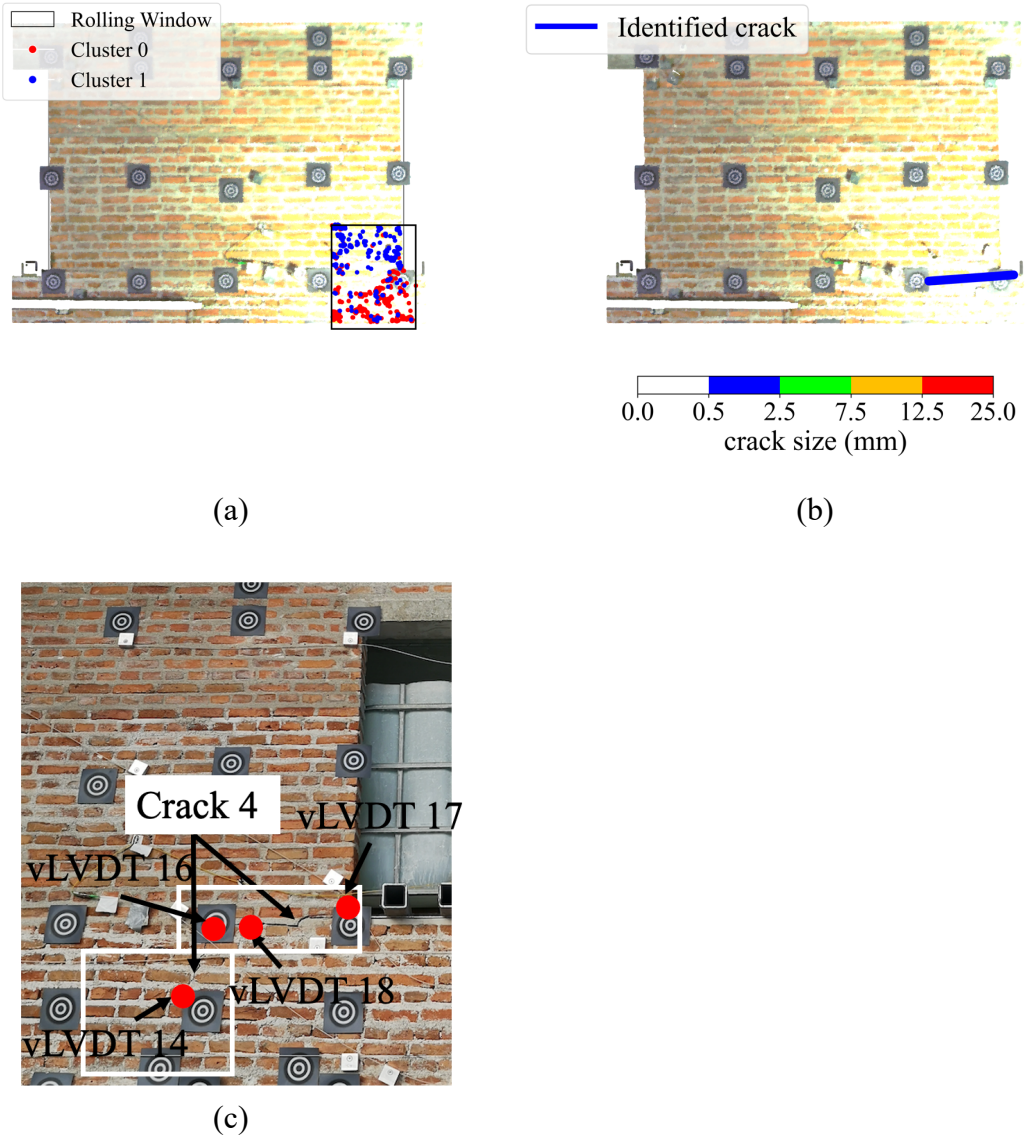


Figure 8.20; (a) Feature clustering results from Rolling Window 35 as part of the PC-Cr processes applied to Pier 4 in 3O-RF-W3. Clustered feature points are shown in different colours, in accordance with the legend. Results are presented overlaid on the post-test point cloud of Pier 4 in 3O-RF-W3; (b) Output of the PC-Cr processes applied to Pier 4 in 3O-RF-W3. The determined crack path is drawn overlaid on the post-test point cloud of Pier 4 in 3O-RF-W3. The colour of the crack path reflects the crack width, in accordance with the colour bar; (c) Annotated image of Pier 4 in 3O-RF-W3 taken post-test, showing the physical appearance of the identified crack and the points where virtual LVDTs from DIC intersect the observed crack. Original photo showing the crack, courtesy of Korhan Dalgic and Burcu Gulen.

The maximum measured crack width for Crack 4, according to the proposed method, was 2.47mm. This compares to a 3.79mm width measured by virtual LVDT (vLVDT 17) from the DIC. Both methods reported the maximum crack width at the same point, where vLVDT

17 intersects the right end of the crack (as shown in Figure 8.20c). The crack width reported by vLVDT 16 was 1.44mm, in contrast to the 1.58mm width reported at the end of the identified crack path by the proposed method (see Figure 8.20b). The width reported by vLVDT 14 was 1.49mm, which falls below the detectable crack limit of 3.1mm. This explains why the diagonal section of the crack trajectory was not detected by the proposed method.

8.5.1.4. Crack 5

Pier 2 has a re-sampling voxel size of 3.7mm. Crack 5 on Pier 2 was detected by the proposed method in one of its rolling windows, as shown in Figure 8.21a. Similar to Crack 1, feature points in the rolling window shown in Figure 8.21a are distinctly separated along the observed crack trajectory. In Figure 8.21a, Cluster 0 and Cluster 1 contain 542 and 194 feature points, respectively. A comparison of Figure 8.21b-c shows that the detected crack path closely aligns with the observed crack trajectory.

The maximum measured crack width for Crack 5, according to the proposed PC-Cr method, was 6.31mm. This compares to a width of 6.55mm measured by virtual LVDT (vLVDT 22, located at the right end of the crack, as shown in Figure 8.21c) from the DIC. It is worth noting that the point where PC-Cr reported the largest crack width was at the left end of the crack (near vLVDT 21 in Figure 8.21c). At vLVDT 21, the crack width reported by the DIC was 5.8mm, as opposed to 6.31mm as reported by the proposed PC-Cr method.

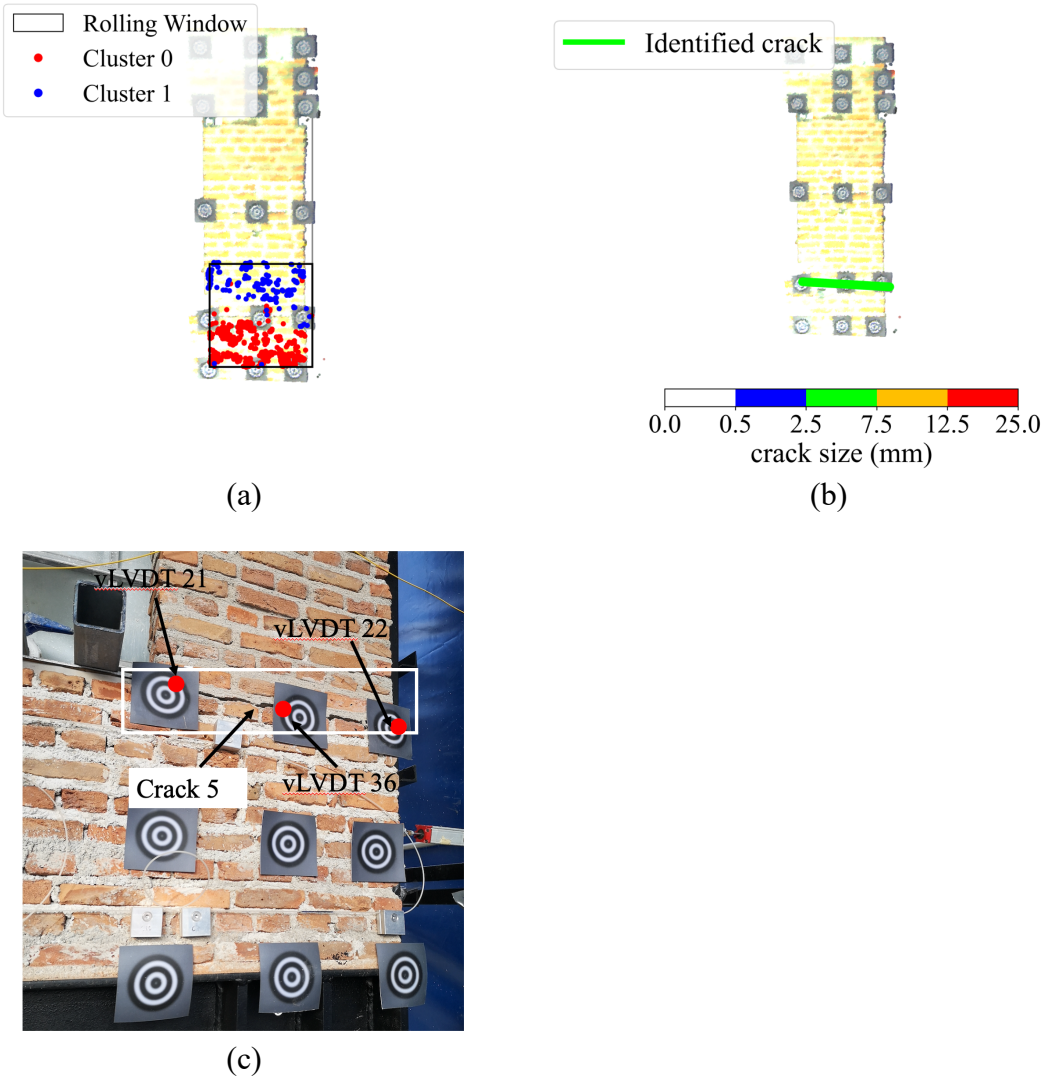
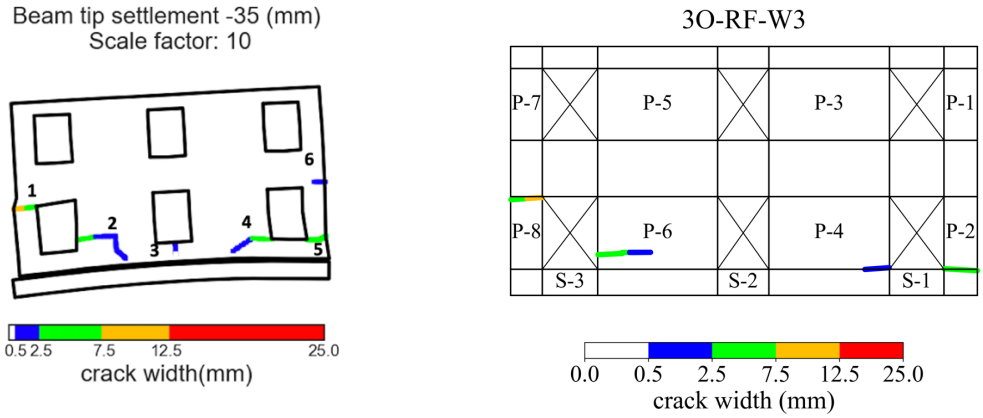


Figure 8.21; (a) Feature clustering results from Rolling Window 0 as part of the PC-Cr processes applied to Pier 2 in 3O-RF-W3. Clustered feature points are shown in different colours, in accordance with the legend. Results are presented overlaid on the post-test point cloud of Pier 2 in 3O-RF-W3; (b) Output of the PC-Cr processes applied to Pier 2 in 3O-RF-W3. The determined crack path is drawn overlaid on the post-test point cloud of Pier 2 in 3O-RF-W3. The colour of the crack path reflects the crack width, in accordance with the colour bar; (c) Annotated image of Pier 2 in 3O-RF-W3 taken post-test, showing the physical appearance of the identified crack and the points (in red dots) where virtual LVDTs from DIC intersect the observed crack. Original photo showing the crack, courtesy of Korhan Dalgic and Burcu Gulen.

8.5.1.5. Summary

Overall, as shown in Figure 8.22a-b, the proposed PC-Cr method detected the majority of the observed cracks on 3O-RF-W3. The only two cracks that were not detected—Cracks 3 and 6—both had maximum widths well below the minimum detectable crack width, which is defined by the re-sampling voxel size used for the structural component to which a crack belongs. There were also segments of Cracks 2 and 4 that went undetected, but this was due

to their small sizes relative to the point density. Contrasting Figure 8.22a and Figure 8.22b, the proposed method also demonstrated a high degree of accuracy in pinpointing crack locations. There were no false positives, where the proposed method indicated the presence of an unobserved crack on any structural components they were run on. As summarised in Table 8.5, considering the relatively coarse point density of 3O-RF-W3, the proposed method is deemed to have performed remarkably well. They were not only effective in detecting and locating cracks but also provided quantifiable crack measurements that are almost comparable to the DIC results.



(a) (b)

Figure 8.22; (a) Deformed shape of the front façade of 3O-RF-W3 with a beam tip settlement of 35mm, showing crack locations and sizes as indicated by the colour bar.(b) Cracks detected and measured by the proposed PC-Cr methods on the front façade of 3O-RF-W3 using pre- and post-test point clouds (corresponding to 35mm beam tip settlement) of each structural component. The widths of the presented cracks are indicated by the colour bar. Piers and spandrels are abbreviated and labelled in the figure for ease of reference: 'P-1' for Pier 1, 'S-1' for Spandrel 1, and so on.

Table 8.5; Comparison of maximum crack widths determined by virtual LVDT of DIC and the proposed PC-Cr method for 3O-RF-W3. Voxel sizes used in the proposed method to re-sample the pre- and post-test point clouds of respective structural components are also provided.

	Maximum crack width – DIC (mm)	Maximum crack width – PC-Cr (mm)	Re-sampling voxel size/ structural component
Crack 1	8.03	7.83	3.6mm/ Pier 8
Crack 2	4.24	5.14	3mm /Pier 6
Crack 3	0.64	Not detected	2.9mm /Spandrel 2
Crack 4	3.79	2.47	3.1mm /Pier 4
Crack 5	6.55	6.31	3.7mm /Pier 2
Crack 6	1.22	Not detected	3.7mm/ Pier 2

8.5.2. 3O-JF-W1

In 3O-JF-W1, at a beam tip settlement of 32 mm, two ‘very severe’ vertical cracks (Cracks 1 and 2, as shown in Figure 8.23) suddenly appeared. These initial cracks led to the development of a ‘severe–very severe’ crack (Crack 3) and a ‘moderate–slight’ crack (Crack 4) at lower levels. The ‘very severe’ damage caused by Cracks 1 and 2 resulted in a partial collapse of the central lintel at the top.

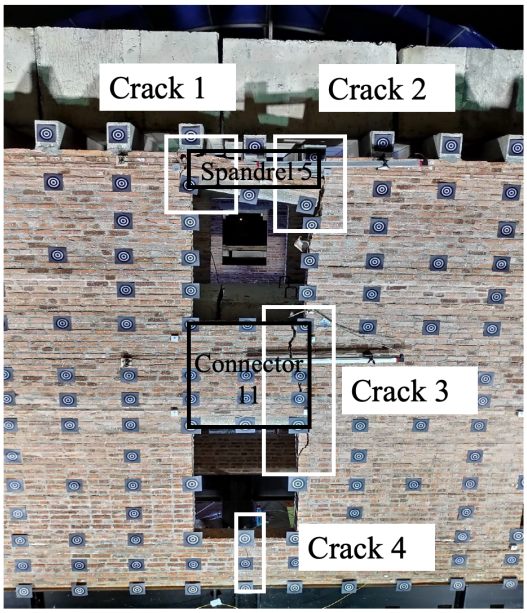


Figure 8.23; Image taken post-test for 3O-JF-W1, annotated to show observed cracks and additional connector elements (Spandrel 5 and Connector 11) on the front wall façade. Original photo courtesy of Korhan Dalgic and Burcu Gulen.

As illustrated in Figure 8.23, Crack 1 does not belong to any discretised piers or spandrels. Crack 2 partially affects an adjacent, stocky pier (Pier 3). Most of Cracks 1 and 2 are located on the masonry unit above the top lintel (referred to as Spandrel 5), as illustrated in Figure 8.23 with black boundary lines. While Crack 3 runs through the top left corner of Pier 4, the majority of its trajectory is located on a connector element (referred to as Connector 11, as illustrated in Figure 8.23 with black boundary lines) between windows on the ground and first storey. To capture all developed cracks, the proposed method was additionally run on the elements of Spandrel 5 and Connector 11. Spandrel 5 and connector 11 both have a concrete lintel at their base, but locally rigid behaviour on a smaller scale is considered valid.

Consistent with other spandrels, Spandrel 5 was divided into three rolling windows. Connector 11, on the other hand, was divided into nine rolling windows, arranged in a 3×3 fashion, giving each window a size roughly equivalent to those elsewhere.

8.5.2.1. Crack 1 and Crack 2

Crack 1 and Crack 2 are discussed together in this section, as the majority of their trajectories belong to a single element, Spandrel 5, which has a re-sampling voxel size of 1.9mm. When applying the proposed PC-Cr method to this element, Cracks 1 and 2 were detected by two separate rolling windows, as shown in Figure 8.24a-b. Unlike previous examples, feature points are sparsely located in both windows. This is believed to be related to the close proximity of the scanner to the wall, resulting in the element being at a sharp angle to the scanner. As shown in Figure 8.24a-b-c, this sharp angle caused the top section of the element to not be fully captured. In Figure 8.24a, Cluster 0 and Cluster 1 contain 72 and 65 points, respectively. In Figure 8.24b, these numbers are 45 and 38, respectively. Despite the sparsity of feature points in both cases, the clusters are fully separated along the observed cracks. Comparing Figure 8.24c-e, the identified cracks approximately align with the observed crack planes, albeit some offsets are observed. These offsets are influenced by the sparsity of the available feature points.

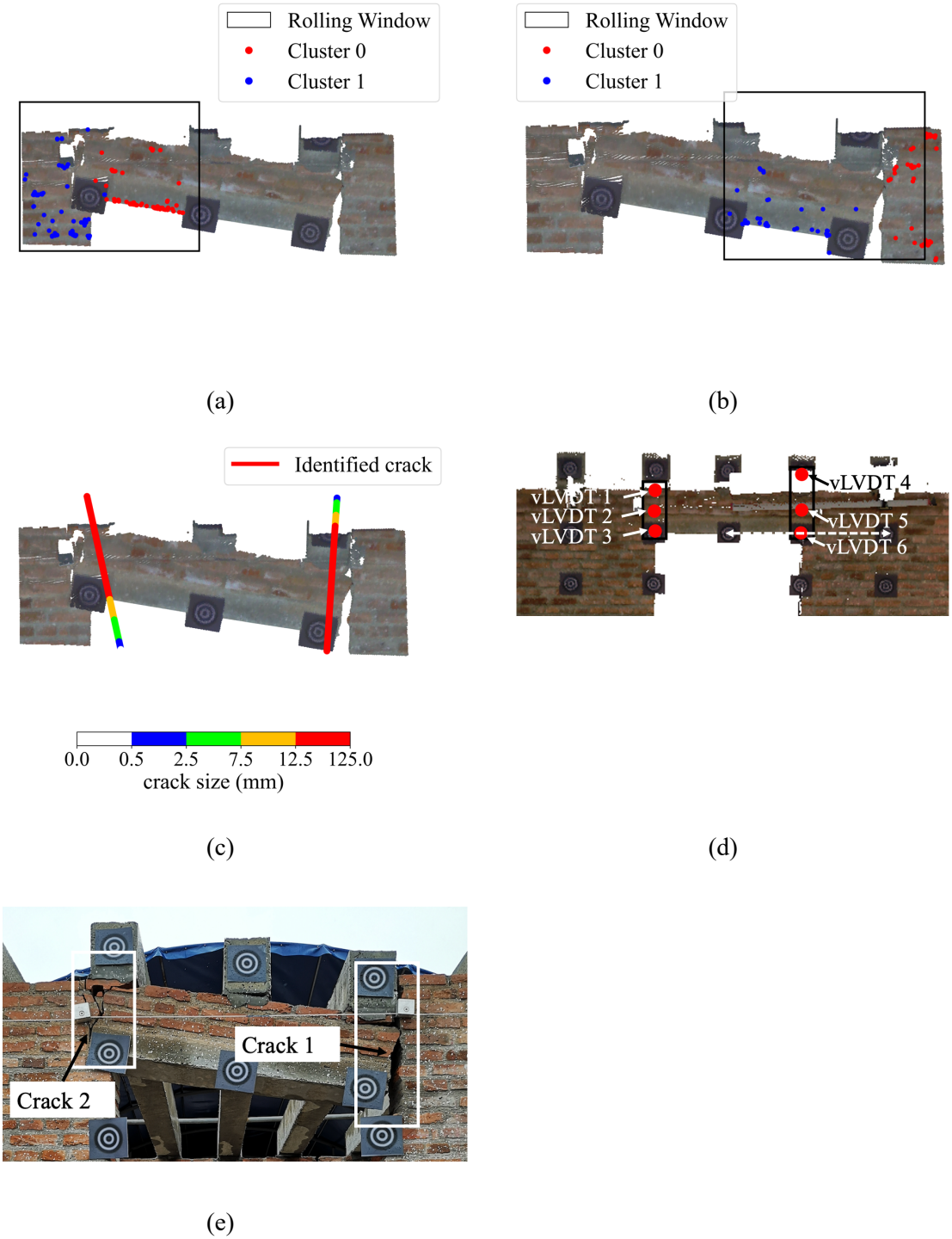


Figure 8.24; (a)(b) Feature clustering results from Rolling Window 0 and Rolling Window 2 as part of the PC-Cr processes applied to Spandrel 5 in 3O-JF-W1. Clustered feature points are shown in different colours, in accordance with the legend. Results are presented overlaid on the post-test point cloud of Spandrel 5 in 3O-JF-W1; (c) Output of the PC-Cr processes applied to Spandrel 5 in 3O-JF-W1. The determined crack path is drawn overlaid on the post-test point cloud of Spandrel 5 in 3O-JF-W1. The colour of the crack path reflects the crack width, in accordance with the colour bar; (d) Points (in red dots) where virtual LVDTs from DIC intersect the anticipated cracks, overlaid on the post-test point cloud of Spandrel 5 in 3O-JF-W1; (e) Annotated image of Spandrel 5 in 3O-JF-W1 taken post-test, showing the physical appearance of the identified crack. Original photo showing the cracks, courtesy of Korhan Dalgic and Burcu Gulen.

Due to the severity of the damage, the top lintel (and its supporting masonry unit) was subjected to unusually large movement. As a result, the points where virtual LVDTs intersect the crack cannot be displayed in the same manner as in previous examples. Instead, those points are shown in Figure 8.24d on the pre-test point cloud, in relation to the anticipated crack location.

The maximum measured crack width for Crack 1, according to the proposed method, was 42.48mm. This compares to a width of 40.40mm measured by virtual LVDT (vLVDT 5, as shown in Figure 8.24d) from the DIC. On the other hand, the maximum crack width for Crack 2, measured by the proposed method, was 36.80mm, as opposed to 31.22mm measured by virtual LVDT (vLVDT 1, as shown in Figure 8.24d) from the DIC. Both the proposed method and virtual LVDT reported the maximum crack width at the same location.

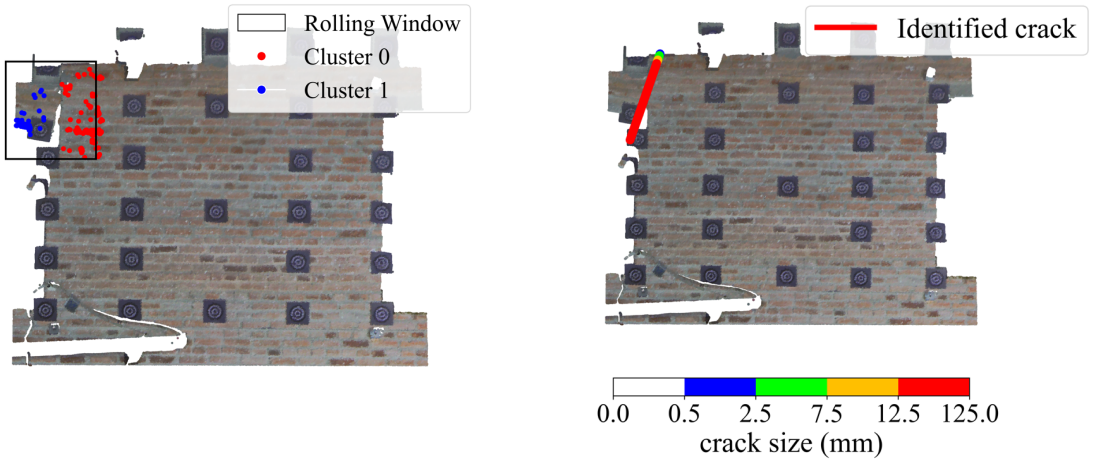


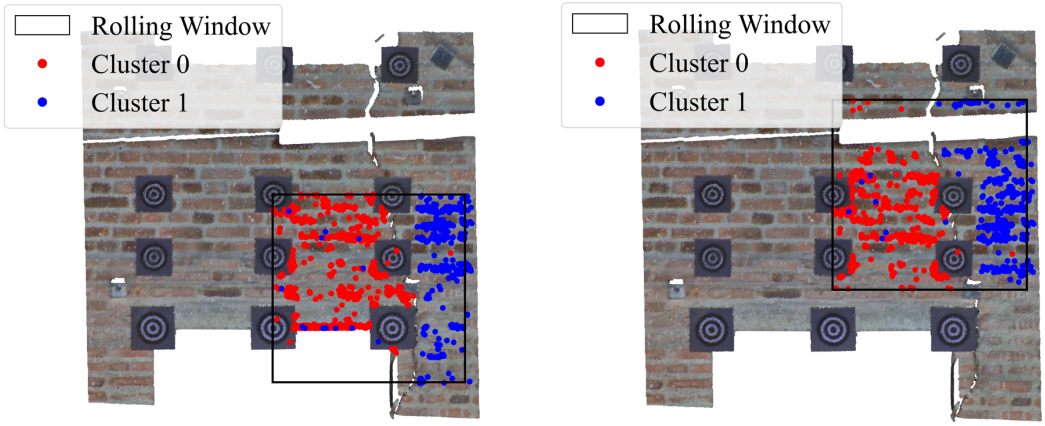
Figure 8.25; (a) Feature clustering results from Rolling Window 4 as part of the PC-Cr processes applied to Pier 3 in 3O-JF-W1. Clustered feature points are shown in different colours, in accordance with the legend. Results are presented overlaid on the post-test point cloud of Pier 3 in 3O-JF-W1; (b) Output of the PC-Cr processes applied to Pier 3 in 3O-JF-W1. The determined crack path is drawn overlaid on the post-test point cloud of Pier 3 in 3O-JF-W1. The colour of the crack path reflects the crack width, in accordance with the colour bar.

In addition, a section of Crack 1 also extended into Pier 3. Despite a small influence area, this extension was also detected by one of the rolling windows used in the proposed method when applied to Pier 3. Due to the large crack width, feature points in the rolling window, as shown in Figure 8.25a, are distinctly separated along the observed crack planes. In Figure

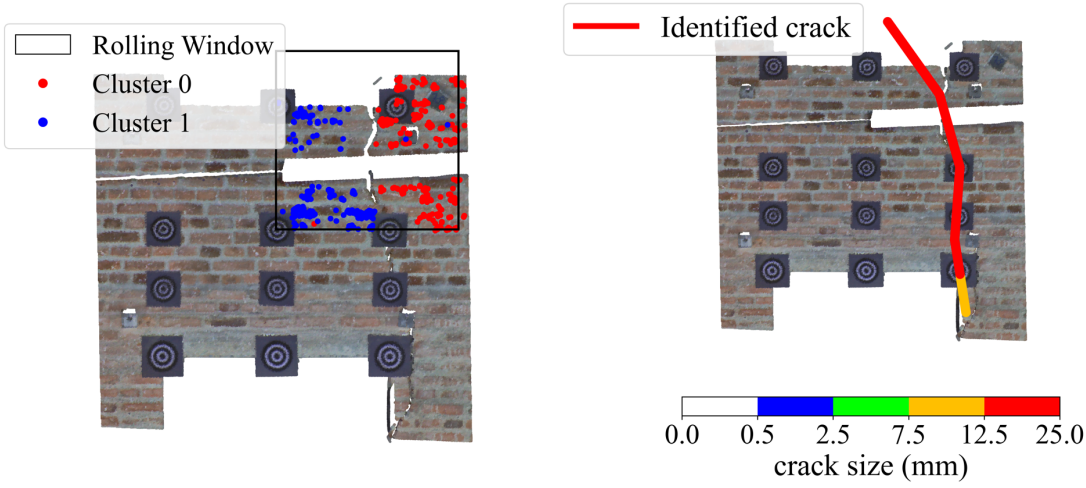
8.25a, Cluster 0 and Cluster 1 contain 135 and 77 feature points, respectively. As evident from Figure 8.25b, the detected crack path closely aligns with one of the observed crack planes.

8.5.2.2. Crack 3

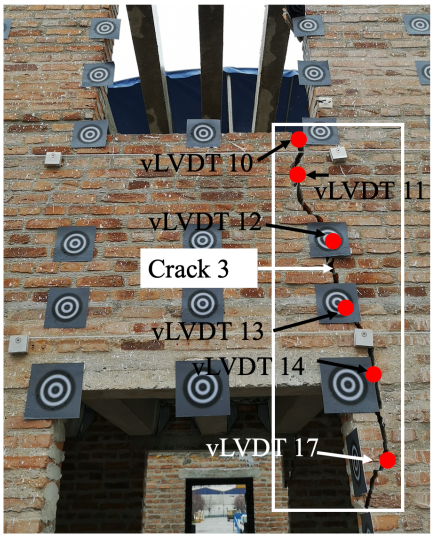
When the proposed PC-Cr method was applied to Connector 11, Crack 3 was detected by three of the rolling windows, as shown in Figure 8.26a-b-c. In these figures, feature points in the rolling windows are distinctly separated along the observed crack trajectory. In Figure 8.26a, Cluster 0 and Cluster 1 contain 973 and 447 feature points, respectively. These numbers are 648 and 445 in Figure 8.26b, and 295 and 255 in Figure 8.26c, respectively. A comparison of Figure 8.26d-e shows that the detected crack path closely follows the observed crack trajectory until the last segment at the top, where the predicted and observed paths diverge. This divergence is caused by the asymmetric spatial distribution of feature points in the clusters in that region.



(a) (b)



(c) (d)



(e)

Figure 8.26; (a)(b)(c) Feature clustering results from Rolling Window 6, Rolling Window 7 and Rolling Window 8 as part of the PC-Cr processes applied to Connector 11 in 3O-JF-W1. Clustered feature points are shown in different colours, in accordance with the legend. Results are presented overlaid on the post-test point cloud of Connector 11 in 3O-JF-W1; (d) Output of the PC-Cr processes applied to Connector 11 in 3O-JF-W1. The determined crack path is drawn overlaid on the post-test point cloud of Connector 11 in 3O-JF-W1. The colour of the crack path reflects the crack width, in accordance with the colour bar; (e) Annotated image of Connector 11 in 3O-JF-W1 taken post-test, showing the physical appearance of the identified crack and the points (in red dots) where virtual LVDTs from DIC intersect the observed crack. Original photo showing the crack, courtesy of Korhan Dalgic and Burcu Gulen.

The maximum measured crack width for Crack 3, according to the proposed method, was 18.32mm. This compares to a width of 19.18mm measured by virtual LVDT (vLVDT 10, located at the top end of the crack, as shown in Figure 8.26e) from the DIC. Both methods reported the maximum crack width at the same location. The virtual LVDT results suggest

that the smallest crack width of Crack 3 on Spandrel 5 was 12.5mm at vLVDT 14. At this point, the crack width reported by PC-Cr was 12.76mm, indicating crack measurements from PC-Cr are consistently reliable.

In addition, a section of Crack 3 also extended into Pier 4. This extension was detected by one of the rolling windows of the proposed method when applied to Pier 4. Due to the large crack width, feature points in the rolling window are distinctly separated along the observed crack trajectory, as shown in Figure 8.27a. In this figure, Cluster 0 and Cluster 1 contain 348 and 198 feature points, respectively. As evident from Figure 8.27b, the detected crack path roughly aligns with the observed trajectory. According to the proposed method, the maximum measured crack width for Crack 3 in Pier 4 was 9.23mm.

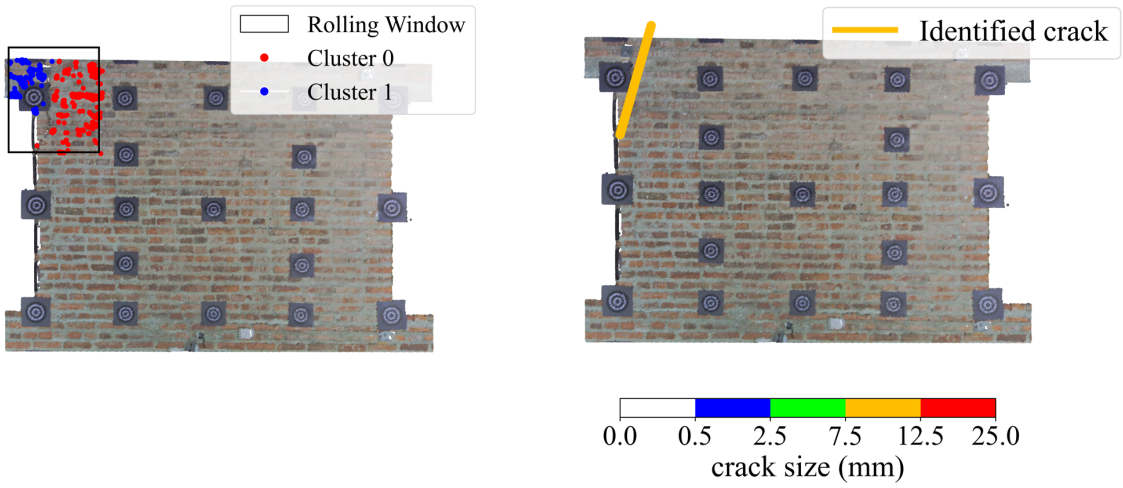


Figure 8.27; (a) Feature clustering results from Rolling Window 4 as part of the PC-Cr processes applied to Pier 4 in 3O-JF-W1. Clustered feature points are shown in different colours, in accordance with the legend. Results are presented overlaid on the post-test point cloud of Pier 4 in 3O-JF-W1; (b) Output of the PC-Cr processes applied to Pier 4 in 3O-JF-W1. The determined crack path is drawn overlaid on the post-test point cloud of Pier 4 in 3O-JF-W1. The colour of the crack path reflects the crack width, in accordance with the colour bar.

8.5.2.3. Crack 4

Spandrel 2 has a re-sampling voxel size of 1.5mm. When the proposed method was applied to Spandrel 2, Crack 4 was detected by one of the rolling windows, as illustrated in Figure 8.28a. Unlike cases involving larger cracks, feature points in the rolling window shown in

Figure 8.28a are less distinctly separated along the observed crack trajectory. In Figure 8.28a, Cluster 0 and Cluster 1 contain 1036 and 764 feature points, respectively. A comparison of Figure 8.28b-c reveals that despite the less distinct separation of clusters, the detected crack path aligns closely with the observed crack trajectory.

The maximum measured crack width for Crack 4, according to the proposed method, was 3.77mm. This is comparable to a width of 4.18mm measured by virtual LVDT (vLVDT 18, located at the top end of the crack, as shown in Figure 8.28c) obtained from the DIC. At vLVDT 20, the DIC reported a maximum crack width of 2.21mm, in contrast to 2.5mm as reported by the proposed method. These results further demonstrate the consistent reliability of crack size measurements from the proposed method.

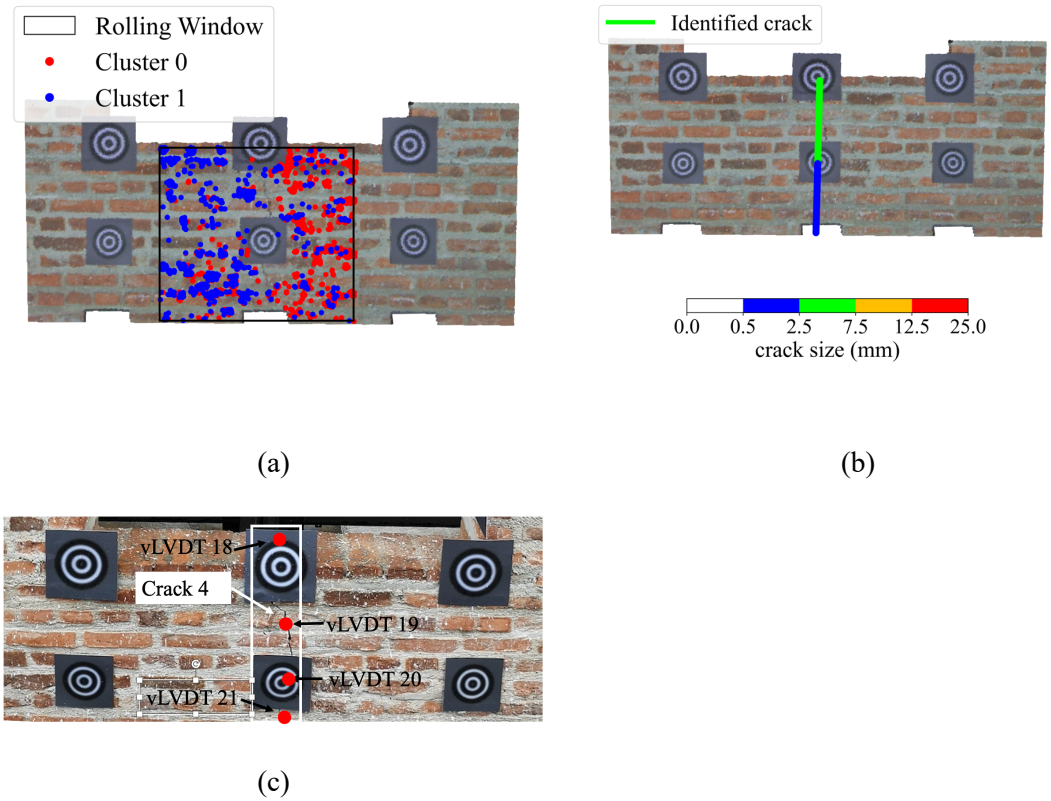


Figure 8.28; (a) Feature clustering results from Rolling Window 2 as part of the PC-Cr processes applied to Spandrel 2 in 3O-JF-W1. Clustered feature points are shown in different colours, in accordance with the legend. Results are presented overlaid on the post-test point cloud of Spandrel 2 in 3O-JF-W1; (b) Output of the PC-Cr processes applied to Spandrel 2 in 3O-JF-W1. The determined crack path is drawn overlaid on the post-test point cloud of Spandrel 2 in 3O-JF-W1. The colour of the crack path reflects the crack width, in accordance with the colour bar; (c) Annotated image of Spandrel 2 in 3O-JF-W1 taken post-test, showing the physical appearance of the identified crack and the points (in red dots) where virtual LVDTs from DIC intersect the observed crack. Original photo showing the crack, courtesy of Korhan Dalgic and Burcu Gulen.

8.5.2.4. Summary

Overall, as illustrated in Figure 8.29a-b, the proposed PC-Cr method successfully detected all observed cracks in 3O-JF-W1. A comparison of these figures shows that the proposed method also demonstrated a high degree of accuracy in pinpointing crack locations. Similar to the findings for 3O-RF-W3, there were no false positives; that is, the proposed method did not indicate the presence of any unobserved cracks on any of the structural components to which they were applied.

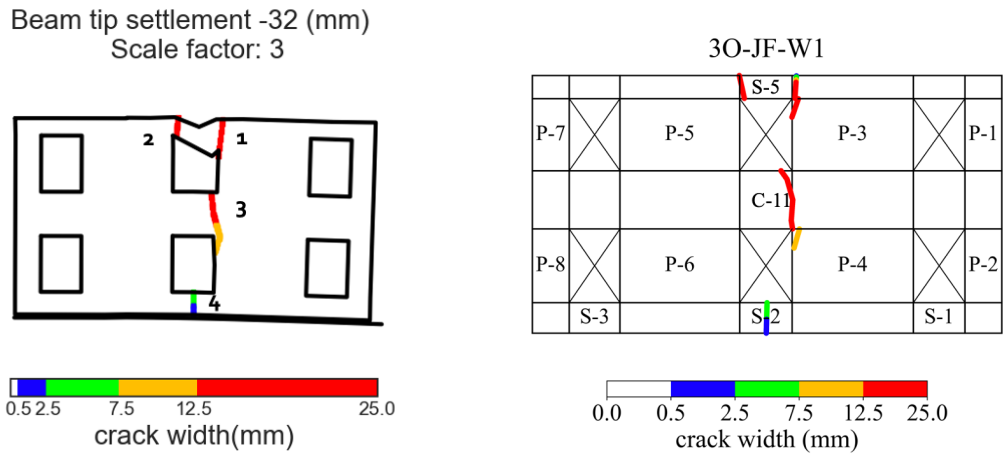


Figure 8.29; (a) Deformed shape of the front façade of 3O-JF-W1 with a beam tip settlement of 32mm, showing crack locations and sizes as indicated by the colour bar.(b) Cracks detected and measured by the proposed PC-Cr methods on the front façade of 3O-JF-W1 using pre- and post-test point clouds (corresponding to 32mm beam tip settlement) of each structural component. The widths of the presented cracks are indicated by the colour bar. Piers and spandrels are abbreviated and labelled in the figure for ease of reference: 'P-1' for Pier 1, 'S-1' for Spandrel 1, and so on. Element Connector 11 is abbreviated and labelled as 'C-11'.

As summarised in Table 8.6, the proposed method has proven its capability to provide maximum crack width measurements comparable to those obtained using the DIC method, even though it operates in a more relaxed monitoring environment.

Upon detailed examination of each crack, the proposed method further demonstrated its reliability and accuracy in measuring crack width along the identified crack paths. This is evidenced by the close agreement with measurements obtained from the DIC. These discrepancies are typically on the sub-millimetre level and can be further improved by increasing the point cloud density.

Table 8.6; Comparison of maximum crack widths determined by virtual LVDT of DIC and the proposed PC-Cr method for 3O-JF-W1. Voxel sizes used in the proposed method to re-sample the pre- and post-test point clouds of respective structural components are also provided.

	Maximum crack width – DIC (mm)	Maximum crack width – PC-Cr (mm)	Re-sampling voxel size/ Structural component
Crack 1	40.40	42.48	1.9mm/ Spandrel 5; 2.4mm/ Pier 3
Crack 2	31.22	36.80	1.9mm/ Spandrel 5;
Crack 3	19.19	18.32	1.6mm /Connector 11; 2mm/ Pier 4
Crack 4	4.18	3.77	1.5mm /Spandrel 2

8.6. Conclusion

This chapter first introduces a novel crack detector and crack quantifier, termed PC-Cr, designed for monitoring buildings subjected to settlement using point cloud data. The proposed method employs a newly formulated crack model, referred to as the segmented rigid-body crack model, to detect and quantify cracks from a kinematic perspective. In this model, cracking is characterised by multiple distinct rigid-body motions, inferred from matched feature points and their respective positions before and after a deformation event (i.e. settlement). Cracks are located based on the clustering of feature points that possess different kinematic properties. Crack measurements are then derived based on the inferred kinematic motions.

Compared to PC-EFA, the proposed PC-Cr method has considerably wider applicability. This is because the basic kinematic assumption of rigid-body motion, embedded in the segmented rigid-body crack model, is almost universally applicable to all common building materials, particularly on a smaller, local scale. For this reason, the PC-Cr method is implemented in small rolling windows traversing the regions of interest. Additionally, the success rate of feature point clustering and model parameter estimation is established using probability theory and the observed error distribution of displacements from feature matching. Nearly all parameters used in the proposed PC-Cr methods are determined based on physical evidence and do not require experimentation or tuning.

Following the introduction of the detailed methodology, the minimum detectable crack width is established from a theoretical perspective. The study indicates that the proposed method is capable of detecting crack segments with maximum widths greater than the point cloud density.

Lastly, applications of the proposed PC-Cr method to large-scale building settlement tests are presented. The detection and measurement details of the proposed method were compared and discussed in conjunction with observed crack trajectories and DIC crack measurements along the identified crack paths. The results showed that the proposed method was robust against displacement noise from feature matching and occlusions in the point clouds. Despite operating under relaxed monitoring conditions, the proposed method detected all cracks with widths greater than the established minimum detectable crack width. The method also did not indicate the presence of any unobserved cracks on any of the structural components to which they were applied, further demonstrating its reliability in crack identification. The crack measurement results were largely consistent with those of virtual LDVTs from the DIC along the identified crack paths. Discrepancies were generally at the sub-millimetre level and could be further improved with denser point cloud data.

It is worth noting that, although the proposed method was primarily applied to piers and spandrels in large-scale building settlement tests for consistency with other methods presented in this thesis, they are, in fact, robust enough to be applied to any area of interest on masonry surfaces. This versatility was demonstrated through additional tests on two elements (Spandrel 5 and Connector 11), where complex interactions between the reinforced concrete lintel and masonry exist. From an application perspective, the proposed method can complement PC-EFA by providing assurance for its strain-based crack interpretations and by pinpointing crack locations. Alternatively, they can also function as a stand-alone method to scan larger areas of interest, such as an entire façade.

9. Conclusions and future research

9.1. Conclusions

Monitoring surface buildings during underground construction is essential to ensuring the safe and smooth progression of such projects and to preventing damage to third-party assets. Masonry buildings, many of which hold significant cultural and historical value, are particularly susceptible to settlement induced by underground works due to their inherent low tensile strength. However, in practice, comprehensive monitoring activities on buildings are often constrained due to their intrusive and labour-intensive nature, especially the direct monitoring of damage, such as cracks. The prevailing damage assessment protocol predominantly relies on equivalent beam models and discrete, often inadequate, displacement monitoring data. However, despite the wide application of the equivalent beam models, they have yet to be fully validated in data-rich environments on a realistic scale. Alternatively, the challenges arising from the direct monitoring of strain and cracks on buildings could potentially be mitigated by employing non-contact and full-field displacement measurement tools.

The primary objectives of this research are to develop innovative and versatile applications that employ computer vision techniques to assist the industry in assessing damage to masonry buildings subjected to underground-induced settlement. To this end, a large-scale masonry building settlement test campaign, consisting of three half-scale building models with varying setups, was commissioned through a collaborative project. In these tests, building displacements and damage across the entire façade were monitored by Digital Image Correlation (DIC) cameras, with laser scans performed before and after each test. These unique and invaluable datasets have bridged a longstanding gap in suitable data on

the detailed responses of representative building models to settlement. They have paved the way for a series of research activities aimed at addressing the limitations of current practices.

Specifically, Chapter 4 of this research initially explores the efficacy of the widely-used equivalent beam models in detecting damage in masonry buildings subjected to settlement. The DIC data collected from the building settlement test campaign offers a valuable direct comparison between the actual observed damage and the damage categories predicted by equivalent beam models. Such a comparison has not been previously attempted at this scale and level of detail. The findings indicate that the use of equivalent beam models, including the Deep Beam Model, Sandwich Beam Model, and Bay Beam Model, along with standard damage-crack width-tensile strain relationships for estimating damage based on displacement measurements, often yields low-fidelity results. All three versions of the equivalent beam models tend to underestimate the severity of building damage, especially in the case of severe damage. Additionally, the results suggest that none of the equivalent beams are adept at precisely locating damage. A major reason for this discrepancy is the mismatch between the kinematic assumptions inherent in the equivalent beam models and the actual deformations observed in the buildings.

In light of these findings, an Equivalent Frame Approach (EFA) was proposed in Chapter 5. This approach idealises the building façade as an equivalent frame and employs beam approximation at the level of individual structural components, such as piers and spandrels. Displacement field functions from beam theory are directly fitted to the measured displacement data in a least squares sense. Partial derivatives of the displacement fields are then used to obtain the strain fields and estimate the maximum tensile strain in the structural component. Subsequently, based on the estimated maximum tensile strain, a damage class is assigned to each structural component using a strain-damage correlation. Numerical validation demonstrated that this level of discretisation can accurately reflect the underlying

kinematics, not only in the linear range but also in the nonlinear range, from the onset of cracks up to the 'moderate' damage category. When applied to large-scale settlement tests, using DIC displacement measurements at discrete target locations, the EFA approach provided high-fidelity results, offering an excellent indication of both damage intensity and location. The damage categories assigned through EFA are largely consistent with those determined through measured crack width, and the areas of high strain concentration indicated by EFA generally align with observed damage locations.

Additionally, Chapter 5 reveals that the standard correlations between tensile strain and crack damage no longer hold when tensile strains are derived at the structural component's level. This finding has implications not only for monitoring data processing but also for predicting damage categories prior to underground construction. If alternative assessment procedures are used in which a higher fidelity structural analysis (such as a finite element model or an equivalent frame model) is selected, then the adoption of the standard tensile crack width – tensile strain correlation could lead to over-conservative damage assessments.

The adoption of higher fidelity methods for damage assessment, such as the EFA, would require a larger number of displacement measurement points than currently adopted in practice. To overcome this limitation, Chapter 6 introduced a novel method called Point Cloud-based Equivalent Frame Approach (PC-EFA). This method leverages core EFA principles and uses point clouds of the building under investigation before and after a deformation event, such as settlement, as input data. Compared to traditional monitoring approaches, collecting point clouds is a swift and non-intrusive process with minimal prerequisites. In the proposed PC-EFA, initial displacements are obtained through a local region-based feature match algorithm. Leveraging domain knowledge on expected maximum settlement, this feature matching employs a less computational 3-dimensional local neighbour search to narrow the search space for the more computationally intensive

high-dimensional feature search. Moreover, two kinematic-based filters—namely, the rigid model filter and the beam model filter—are integrated to exclude feature points inconsistent with predominant kinematic motions. Considering the inherent noise related to point density, an Iterative Sampling and Fitting-based Strain Interpretation (ISFSI) method is proposed to reliably estimate model parameters and derive strains. The ISFSI method has demonstrated robustness in managing non-biased point density-related displacement errors. Compared to displacement results, the derived strains offer a more tangible indication of the structural component's response and can act as damage indicators through strain-damage correlations.

In both numerical simulations and their applications to large-scale settlement tests presented in Chapters 6 and 7, PC-EFA provided comparable results in strain interpretation and damage classification to EFA methods using DIC data. These findings suggest PC-EFA can be effectively used to provide early warning to potential damage as well as give indications of certain types of cracks, whose kinematics can be approximated by beam theory. In the applications of PC-EFA in Chapter 7, the proposed PC-EFA has also exhibited robustness against challenges arising from varying point densities. Moreover, nearly all parameters used in the proposed PC-EFA are determined based on physical evidence and do not require experimentation or tuning.

However, the continuum model (i.e. the beam model) employed in PC-EFA can only approximate the kinematic behaviour post-cracking up to 'moderate' damage. Inevitably, some cracks, whose kinematics are not adequately represented by the continuum model, may go undetected by PC-EFA. To overcome these limitations, a novel crack detector and quantifier, termed PC-Cr, was proposed. This method employs a newly formulated crack model, known as the segmented rigid-body crack model, to detect and quantify cracks from a kinematic perspective. Compared to PC-EFA, the proposed PC-Cr method has considerably wider applicability. This is because the basic kinematic assumption of rigid-

body motion, embedded in the segmented rigid-body crack model, is almost universally applicable to all common building materials, particularly on a smaller, local scale. In applications of the proposed PC-Cr method to large-scale building settlement tests, all cracks with widths greater than the established minimum detectable crack width were detected without any false positives. The crack measurement results were largely consistent with those obtained from virtual LDVTs using DIC along the identified crack paths.

Regarding the limitations, the PC-EFA and PC-Cr methodologies intrinsically depend on the quality of surface feature matching to establish correspondences and derive the initial displacement field. Findings from the current test campaign show that variations in common masonry surfaces can reliably establish correspondences using conventional feature descriptors, such as FPFH. However, it is crucial to recognise that the accuracy and resolution of both methods are significantly influenced by the density of the point cloud. The tests have confirmed that both methodologies can operate effectively with point cloud densities as low as 3mm, yielding reliable outcomes. With ongoing advancements in scanning technology, the impact of point cloud density on these methods is expected to diminish.

The methods presented in this thesis adhere to a critical principle that is frequently overlooked in the assessment of building damage using computer vision techniques: the selection of an adequate model capable of capturing kinematics at the appropriate scale. By integrating this domain knowledge into the methods, the solution space is refined, enabling more effective handling of noisy displacement data. Rather than treating challenges like crack detection as purely computer vision problems, this hybrid approach delivers robust and satisfactory answers to the complex research question.

9.2. Future research

9.2.1. Additional field applications and validations

The proposed PC-EFA and PC-Cr methods, along with their implementations, have been applied to point cloud data collected from the large-settlement test campaign. They were rigorously validated using the EFA method with DIC displacement data, as well as with crack measurements from virtual LDVTs in DIC. The software packages developed for these methods are currently in an application-ready state; nevertheless, it might be advantageous to further test the limits of these methods through additional field applications.

In the case of PC-EFA, given that full-field strain measurements are extremely challenging to implement on-site, the validation for future field applications will likely involve the EFA method using discrete displacement measurements from geodetic surveys. This process might necessitate the installation of a relatively dense grid of prisms on the structural components under study. Additionally, the utilisation of LVDT could prove beneficial in validating the strain component derived from PC-EFA along specific axes.

To ascertain the abilities of both PC-EFA and PC-Cr in damage indication and quantification, a systematic manual crack measurement scheme will be essential. This scheme is anticipated to incorporate frequent crack inspections, supplemented by the extensive use of tell-tales and crack rulers.

Given the demanding monitoring scheme required for further field validation, the identification of a suitable project with cooperative contractors will likely be a key element in successful implementation.

9.2.2. Process optimisation for PC-EFA and PC-Cr

In the preprocessing stage (Step 1) of both the PC-EFA and PC-Cr methods, Faro Scene is utilised to execute a target-based bundle registration of pre- and post-test point clouds to the reference coordinate system. The use of Faro Scene and checkerboard targets in the large settlement test was to minimise registration error, enabling a more accurate analysis of the point cloud displacement profile by comparing it with interpolated DIC results. Beyond this, from an application standpoint, the strain interpretation and damage screening offered by PC-EFA, and the crack identification and quantification by PC-Cr, require only a rough initial registration to aid their local feature correspondence search, as rigid registration errors do not induce additional distortion. When artificial targets are unavailable, geometric properties of the point cloud, such as the Fast Point Feature Histogram (FPFH), can be employed. For the sake of process optimisation, consideration could be given to integrating the initial registration with the rest of the implementation on a single platform. Assessing the performance of the proposed methods without using artificial targets for initial registration is also a worthwhile consideration for a future testing programme.

Additionally, in the preprocessing stage (Step 1), the point cloud segmentation step necessitates human visual perception and cognition to discern individual structural components and implement segmentation by specifying a bounding box. While such intervention demands minimal effort, implementing semantic segmentation could be considered for process optimisation in large-scale applications.

9.2.3. Extension of building material adaptivity for PC-EFA and PC-Cr

While the proposed methods—PC-EFA and PC-Cr—were primarily developed for monitoring masonry buildings subjected to settlement, they could, in theory, be adapted to other types of buildings, such as those made of stone or concrete, as long as there are

adequate geometric features to establish unbiased correspondences before and after a deformation event. This adaptability could potentially expand the applicability of the proposed methods during underground construction. Elements like mouldings, textures, and patterns on these buildings can act as geometric surface features; however, it is anticipated that their FPFH features may be less distinct and unique compared to masonry surfaces. Importantly, both PC-EFA and PC-Cr offer the flexibility to incorporate different point feature descriptors. More descriptive geometric features, like SHOT (Signature of Histograms of Orientations) (Salti et al., 2014), may potentially be effective, albeit being more computationally intensive. Furthermore, if SHOT features turn out to be unreliable, the exploration of higher-level features, which combine variations in local geometry, colour, and laser intensity, could be a viable alternative.

9.2.4. Enhancement in handling complex cracking with PC-Cr

The post-processing capabilities of the proposed PC-Cr method could potentially benefit from further development and testing, especially in cases involving complex, multiple interconnecting cracks. One inherent challenge is effectively clustering crack segments that are part of different cracks and/or branches. Managing the computational complexity introduced by the crack path optimisation, due to the intricate geometry of multiple interconnecting cracks, presents another substantial challenge. It is anticipated that conducting such development and validation in a laboratory environment, accompanied by full-field DIC monitoring, would be most effective, as manual measurements of multiple interconnecting cracks are both laborious and error-prone. For this purpose, mechanical testing of masonry frames under various loading conditions to induce different crack patterns may be considered.

10. References

Acikgoz, S., DeJong, M.J., Soga, K., 2018. Sensing dynamic displacements in masonry rail bridges using 2D digital image correlation. Struct. Control Heal. Monit. 25, 1–24.

Acikgoz, S., Luciano, A., Dewhirst, M., Dejong, M.J., Mair, R., 2022. Innovative monitoring of the response of a heritage masonry building to nearby tunnelling in London Clay. Geotechnique 72, 200–215.

Acikgoz, S., Soga, K., Woodhams, J., 2017. Evaluation of the response of a vaulted masonry structure to differential settlements using point cloud data and limit analyses. Constr. Build. Mater. 150, 916–931.

Alhaddad, M., 2016. Photogrammetric monitoring of cast-iron tunnels and applicabilty of empirical methods for damage assessment. PhD Thesis, University of Cambridge.

Amberg, B., Romdhani, S., Vetter, T., 2007. Optimal Step Nonrigid ICP Algorithms for Surface Registration. In: 2007 IEEE Conference on Computer Vision and Pattern Recognition. IEEE, pp. 1–8.

Azhari, F., 2022. Automated Crack Detection and Characterisation from 3D Point Clouds of Unstructured Surfaces. PhD Thesis, Queensland University of Technology.

Barrias, A., Casas, J.R., Villalba, S., 2016. A review of distributed optical fiber sensors for civil engineering applications. Sensors (Switzerland) 16, 748.

Berrocal, C.G., Fernandez, I., Rempling, R., 2020. Crack monitoring in reinforced concrete beams by distributed optical fiber sensors. Struct. Infrastruct. Eng. 0, 1–16.

Bomarito, G.F., Hochhalter, J.D., Ruggles, T.J., Cannon, A.H., 2017. Increasing accuracy and precision of digital image correlation through pattern optimization. Opt. Lasers Eng. 91, 73–85.

Boscardin, M.D., Cording, E.J., 1989. Building Response to Excavation-Induced Settlement. J. Geotech. Eng. 115, 1–21.

Brackenbury, D., 2022. Automated image-based inspection of masonry arch bridges. PhD Thesis, University of Cambridge.

BRE, 1989. Simple measuring and monitoring of movement in low-rise buildings. Part 1: cracks. BRE Digest 343, London.

British Tunnelling Society, 2004. Tunnel lining design guide. Thomas Telford Ltd, London.

Burhouse, P., 1969. Composite action between brick panel walls and their supporting beams. Proc. Inst. Civ. Eng. 43, 175–194.

Burland, J.B., Broms, B.B., De Mello, V.F.B., 1977. Behavior of foundations and structures. In: Proc., 9th Int. Conf. on Soil Mechanics and Foundation Engineering. Tokyo, pp. 495– 546.

Burland, J.B., Standing, J.R., Jardine, F.M., 2001. Building response to tunnelling: Case studies from construction of the Jubilee Line Extension, London Volume 2, Case studies. Thomas Telford, London.

Burland, J.B., Wroth, C.P., 1974. Settlement of buildings and associated damage. In: Settlement of Structures, Proceedings of the Conference of the British Geotechnical Society. pp. 611–654.

Caudal, P., Grenon, M., Turmel, D., Locat, J., 2017. Analysis of a Large Rock Slope Failure on the East Wall of the LAB Chrysotile Mine in Canada: LiDAR Monitoring and Displacement Analyses. Rock Mech. Rock Eng. 50, 807–824.

Chen, J., Liu, B., Zhang, H., 2011. Review of fiber Bragg grating sensor technology. Front. Optoelectron. China 4, 204–212.

Cook, D., 1994. Studies of Settlement and Crack Damage in Old and New Facades. In: Proceedings of 3rd International Masonry Conference. British Masonry Society, London, pp. 203–211.

Crossrail Limited, 2008. Crossrail Information Paper D12 – Ground Settlement [WWW Document]. URL http://74f85f59f39b887b696f-ab656259048fb93837ecc0ecbcf0c557.r23.cf3.rackcdn.com/assets/library/document/d/original/d12groundsettlement.pdf (accessed 7.28.20).

Dais, D., Bal, İ.E., Smyrou, E., Sarhosis, V., 2021. Automatic crack classification and segmentation on masonry surfaces using convolutional neural networks and transfer learning. Autom. Constr. 125,

103606.

Dalgic, K.D., Gulen, B., Liu, Y., Acikgoz, S., Burd, H.J., Marasli, M., Ilki, A., 2023. Masonry buildings subjected to settlements: Half-scale testing, detailed measurements, and insights into behaviour. Eng. Struct. 278, 115233.

Dalgic, K.D., Gulen, D.B., Acikgoz, S., Burd, H.J., Hendriks, M.A.N., Giardina, G., Ilki, A., 2021. Large Scale Experimental Settlement Tests to Evaluate Structural Models for Tunnelling-Induced Damage Analysis. In: Barla, M., Di Donna, A., Sterpi, D. (Eds.), Challenges and Innovations in Geomechanics. Springer International Publishing, Cham, pp. 164–171.

Department for Communities and Local Government, 2010. English Housing Survey: Housing stock report 2008 [WWW Document]. English Hous. Surv. URL https://assets.publishing.service.gov.uk/government/uploads/system/uploads/attachment_data/file/6703/1750754.pdf

Devriendt, M., 2012. Trigger levels for displacement monitoring. Geotech. News 23–25.

Erdélyi, J., Kopáčik, A., Kyrinovič, P., 2020. Spatial data analysis for deformation monitoring of bridge structures. Appl. Sci. 10, 1–14.

Fan, Z., Li, C., Chen, Y., Mascio, P. Di, Chen, X., Zhu, G., Loprencipe, G., 2020. Ensemble of Deep Convolutional Neural Networks for Automatic Pavement Crack Detection and Measurement. Coatings 10, 152.

FARO Technologies Inc, 2023. The Scene Classic User Documentation User Manual [WWW Document]. URL https://downloads.faro.com/index.php/s/CJpAZrodftrR4q5?dir=undefined&openfile=155165

Feng, D., Feng, M.Q., 2018. Computer vision for SHM of civil infrastructure: From dynamic response measurement to damage detection – A review. Eng. Struct. 156, 105–117.

Finno, R.J., Voss, F.T., Rossow, E., Blackburn, J.T., 2005. Evaluating Damage Potential in Buildings Affected by Excavations. J. Geotech. Geoenvironmental Eng. 131, 1199–1210.

Fischler, M. a, Bolles, R.C., 1981. Random sample consensus: A paradigm for model fitting with apphcatlons to image analysis and automated cartography. Commun. ACM 24, 381–395.

Fryskowska, A., 2019. An improvement in the identification of the centres of checkerboard targets in point clouds using terrestrial laser scanning. Sensors (Switzerland) 19, 1–22.

Gawronek, P., Makuch, M., Mitka, B., Gargula, T., 2019. Measurements of the Vertical Displacements of a Railway Bridge Using TLS Technology in the Context of the Upgrade of the Polish Railway Transport. Sensors 19, 4275.

Ghorbani, R., Matta, F., Sutton, M.A., 2015. Full-Field Deformation Measurement and Crack Mapping on Confined Masonry Walls Using Digital Image Correlation. Exp. Mech. 55, 227–243.

Giardina, G., Marini, A., Hendriks, M.A.N., Rots, J.G., Rizzardini, F., Giuriani, E., 2012. Experimental analysis of a masonry façade subject to tunnelling-induced settlement. Eng. Struct. 45, 421–434.

Giardina, G., Milillo, P., DeJong, M.J., Perissin, D., Milillo, G., 2019. Evaluation of InSAR monitoring data for post-tunnelling settlement damage assessment. Struct. Control Heal. Monit. 26, 1–19.

Glisic, B., Inaudi, D., 2012. Development of method for in-service crack detection based on distributed fiber optic sensors. Struct. Heal. Monit. 11, 161–171.

Habel, W.R., Krebber, K., 2011. Fiber-optic sensor applications in civil and geotechnical engineering. Photonic Sensors 1, 268–280.

Harris, C.R., Millman, K.J., van der Walt, S.J., Gommers, R., Virtanen, P., Cournapeau, D., Wieser, E., Taylor, J., Berg, S., Smith, N.J., Kern, R., Picus, M., Hoyer, S., van Kerkwijk, M.H., Brett, M., Haldane, A., del Río, J.F., Wiebe, M., Peterson, P., Gérard-Marchant, P., Sheppard, K., Reddy, T., Weckesser, W., Abbasi, H., Gohlke, C., Oliphant, T.E., 2020. Array programming with NumPy. Nature 585, 357–362.

High Speed Two Limited, 2017. High Speed Two Phase One C3 : Ground Settlement [WWW Document]. URL https://assets.publishing.service.gov.uk/government/uploads/system/uploads/attachment_data/file/672194/C3_-_Ground_Settlement__v1.pdf (accessed 7.28.20).

Howlader, M.K., Masia, M.J., Griffith, M.C., 2021. Digital image correlation for the analysis of in-plane tested

unreinforced masonry walls. Structures 29, 427–445.

Hu, F., van Leijen, F.J., Chang, L., Wu, J., Hanssen, R.F., 2019. Monitoring deformation along railway systems combining Multi-temporal InSAR and LiDAR data. Remote Sens. 11, 1–19.

Hua, T., Xie, H., Wang, S., Hu, Z., Chen, P., Zhang, Q., 2011. Evaluation of the quality of a speckle pattern in the digital image correlation method by mean subset fluctuation. Opt. Laser Technol. 43, 9–13.

Hunter, J.D., 2007. Matplotlib: A 2D graphics environment. Comput. Sci. Eng. 9, 90–95.

ITA-AITES, 2019. Tunnel Market Survey 2019 [WWW Document]. URL https://nff.no/wp-content/uploads/sites/2/2021/01/Market-Survey-2019.pdf (accessed 9.23.23).

Jafari, B., Khaloo, A., Lattanzi, D., 2017. Deformation Tracking in 3D Point Clouds Via Statistical Sampling of Direct Cloud-to-Cloud Distances. J. Nondestruct. Eval. 36, 1–10.

Jovančević, I., Pham, H.H., Orteu, J.J., Gilblas, R., Harvent, J., Maurice, X., Brèthes, L., 2017. 3D Point Cloud Analysis for Detection and Characterization of Defects on Airplane Exterior Surface. J. Nondestruct. Eval. 36, 74.

Laefer, D.F., Hong, L.T., Erkal, A., Long, J.H., Cording, E.J., 2011. Manufacturing, assembly, and testing of scaled, historic masonry for one-gravity, pseudo-static, soil-structure experiments. Constr. Build. Mater. 25, 4362–4373.

Laefer, D.F., Truong-Hong, L., Carr, H., Singh, M., 2014. Crack detection limits in unit based masonry with terrestrial laser scanning. NDT E Int. 62, 66–76.

Lagomarsino, S., Penna, A., Galasco, A., Cattari, S., 2013. TREMURI program: An equivalent frame model for the nonlinear seismic analysis of masonry buildings. Eng. Struct. 56, 1787–1799.

Lague, D., Brodu, N., Leroux, J., 2013. Accurate 3D comparison of complex topography with terrestrial laser scanner: Application to the Rangitikei canyon (N-Z). ISPRS J. Photogramm. Remote Sens. 82, 10–26.

Lava, P., Cooreman, S., Debruyne, D., 2010. Study of systematic errors in strain fields obtained via DIC using heterogeneous deformation generated by plastic FEA. Opt. Lasers Eng. 48, 457–468.

Lazarus, D., Jung, H. Il, 2018. Damage assessment and monitoring for buildings on the Elizabeth line. Struct. Eng. 96, 14–24.

Li, H., Wang, W., Wang, M., Li, L., Vimlund, V., 2022. A review of deep learning methods for pixel-level crack detection. J. Traffic Transp. Eng. (English Ed. 9, 945–968.

Lionello, G., Cristofolini, L., 2014. A practical approach to optimizing the preparation of speckle patterns for digital-image correlation. Meas. Sci. Technol. 25, p.107001.

Liu, Y., Acikgoz, S., Burd, H.J., 2022a. Terrestrial Laser Scanning based deformation monitoring for masonry buildings subjected to settlement induced by underground construction. In: García-Asenjo, L., Lerma, J.L. (Eds.), Proceedings of the 5th Joint International Symposium on Deformation Monitoring - JISDM 2022. Editorial Universitat Politècnica de València, Valencia, pp. 375–382.

Liu, Y., Gulen, B., Acikgoz, S., Burd, H.J., Gilson, B., Ilki, A., Dalgic, K.D., 2022b. A critical evaluation of proxy measures used to quantify excavation-induced damage in masonry buildings. In: Lancellotta, R., Viggiani, C., Flora, A., de Silva, F., Mele, L. (Eds.), Geotechnical Engineering for the Preservation of Monuments and Historic Sites III. CRC Press, pp. 1015–1025.

Loverdos, D., Sarhosis, V., 2022. Automatic image-based brick segmentation and crack detection of masonry walls using machine learning. Autom. Constr. 140, 104389.

Madrigal, C.A., Branch, J.W., Restrepo, A., Mery, D., 2017. A method for automatic surface inspection using a model-based 3D descriptor. Sensors (Switzerland) 17, 2262.

Mair, R.J., 1998. Recent experiences of tunneling and deep excavations in London SOA-7. In: 1998-Fourth International Conference on Case Histories in Geotechnical Engineering. pp. 1193–1206.

Mair, R.J., Taylor, R.N., Burland, J.B., 1996. Prediction of ground movements and assessment of risk of building damage due to bored tunnelling. Geotech. Asp. Undergr. Constr. Soft Gr. 713–718.

Maneewongvatana, S., Mount, D.M., 1999. Analysis of approximate nearest neighbor searching with clustered point sets. arXiv Prepr. 9901013.

Marti, J.G., Nevard, S., Sanchez, J., 2017. The use of InSAR (Interferometric Synthetic Aperture Radar) to

complement control of construction and protect third party assets [WWW Document]. Crossrail Learn. Leg. URL https://learninglegacy.crossrail.co.uk/documents/use-insar-interferometric-synthetic-aperture-radar-complement-control-construction-protect-third-party-assets/ (accessed 7.23.20).

Mehdi Mirzazadeh, M., Green, M.F., 2018. Fiber Optic Sensors and Digital Image Correlation for Measuring Deformations in Reinforced Concrete Beams. J. Bridg. Eng. 23, 1–15.

Mohan, A., Poobal, S., 2018. Crack detection using image processing: A critical review and analysis. Alexandria Eng. J. 57, 787–798.

Mojsilović, N., Salmanpour, A.H., 2016. Masonry walls subjected to in-plane cyclic loading: Application of digital image correlation for deformation field measurement. Int. J. Mason. Res. Innov. 1, 165–187.

Mugnai, F., Lombardi, L., Tucci, G., Nocentini, M., Gigli, G., Fanti, R., 2019. Geomatics in bridge structural health monitoring, integrating terrestrial laser scanning techniques and geotechnical inspections on a high value cultural heritage. ISPRS Ann. Photogramm. Remote Sens. Spat. Inf. Sci. 42, 895–900.

Mukupa, W., Roberts, G.W., Hancock, C.M., Al-Manasir, K., 2017. A review of the use of terrestrial laser scanning application for change detection and deformation monitoring of structures. Surv. Rev. 49, 99–116.

Neuner, H., Holst, C., Kuhlmann, H., 2016. Overview on current modelling strategies of point clouds for deformation analysis. AVN Allg. Vermessungs-Nachrichten 123, 328–339.

Pan, B., 2018. Digital image correlation for surface deformation measurement: Historical developments, recent advances and future goals. Meas. Sci. Technol. 29, 082001.

Pan, B., Qian, K., Xie, H., Asundi, A., 2009. Two-dimensional digital image correlation for in-plane displacement and strain measurement: A review. Meas. Sci. Technol. 20, 062001.

Rajaram, S., Vanniamparambil, P.A., Khan, F., Bolhassani, M., Koutras, A., Bartoli, I., Moon, F., Hamid, A., Benson Shing, P., Tyson, J., Kontsos, A., 2017. Full-field deformation measurements during seismic loading of masonry buildings. Struct. Control Heal. Monit. 24, 1–14.

Ritter, S., Giardina, G., Franza, A., DeJong, M.J., 2020. Building Deformation Caused by Tunneling: Centrifuge Modeling. J. Geotech. Geoenvironmental Eng. 146, 04020017.

Rodríguez, G., Casas, J.R., Villaba, S., 2015. Cracking assessment in concrete structures by distributed optical fiber. Smart Mater. Struct. 24, 035005.

Rots, J.G., 1991. Smeared and discrete representations of localized fracture. Int. J. Fract. 51, 45–59.

Rusu, R.B., Blodow, N., Beetz, M., 2009. Fast Point Feature Histograms (FPFH) for 3D registration 3212–3217.

Rusu, R.B., Blodow, N., Marton, Z.C., Beetz, M., 2008. Aligning point cloud views using persistent feature histograms. 2008 IEEE/RSJ Int. Conf. Intell. Robot. Syst. IROS 3384–3391.

Salti, S., Tombari, F., Di Stefano, L., 2014. SHOT: Unique signatures of histograms for surface and texture description. Comput. Vis. Image Underst. 125, 251–264.

Shi, Y., Cui, L., Qi, Z., Meng, F., Chen, Z., 2016. Automatic road crack detection using random structured forests. IEEE Trans. Intell. Transp. Syst. 17, 3434–3445.

Skempton, A.W., MacDonald, D.H., 1956. The allowable settlements of buildings. In: Proceedings of the Institution of Civil Engineers. pp. 727–768.

Son, M., Cording, E.J., 2005. Estimation of Building Damage Due to Excavation-Induced Ground Movements. J. Geotech. Geoenvironmental Eng. 131, 162–177.

Stałowska, P., Suchocki, C., Rutkowska, M., 2022. Crack detection in building walls based on geometric and radiometric point cloud information. Autom. Constr. 134, 104065.

Standing, J., Selman, R., 2001. Building response to Tunnelling - Case studies from construction of the Jubilee Line Extension, London, Ciria. Thomas Telford, London.

Sun, Y., Pang, J.H.L., 2007. Study of optimal subset size in digital image correlation of speckle pattern images. Opt. Lasers Eng. 45, 967–974.

Sutton, M.A., Yan, J.H., Tiwari, V., Schreier, H.W., Orteu, J.J., 2008. The effect of out-of-plane motion on 2D and 3D digital image correlation measurements. Opt. Lasers Eng. 46, 746–757.

Teza, G., Galgaro, A., Zaltron, N., Genevois, R., 2007. Terrestrial laser scanner to detect landslide displacement fields: A new approach. Int. J. Remote Sens. 28, 3425–3446.

The Pandas development team, 2023. pandas-dev/pandas: Pandas (v1.5.3) [WWW Document]. URL https://doi.org/10.5281/zenodo.7549438

Tian, L., Pan, B., 2016. Remote bridge deflection measurement using an advanced video deflectometer and actively illuminated LED targets. Sensors (Switzerland) 16, 1–13.

VINCI Construction, 2014. Crossrail C510 - Overview Crossrail C510 [WWW Document]. URL http://www.aftes.asso.fr/contenus/upload/File/Publications/Autres/2015-03-26/9-VGP - Crossrail-.pdf (accessed 7.9.20).

Virtanen, P., Gommers, R., Oliphant, T.E., Haberland, M., Reddy, T., Cournapeau, D., Burovski, E., Peterson, P., Weckesser, W., Bright, J., van der Walt, S.J., Brett, M., Wilson, J., Millman, K.J., Mayorov, N., Nelson, A.R.J., Jones, E., Kern, R., Larson, E., Carey, C.J., Polat, İ., Feng, Y., Moore, E.W., VanderPlas, J., Laxalde, D., Perktold, J., Cimrman, R., Henriksen, I., Quintero, E.A., Harris, C.R., Archibald, A.M., Ribeiro, A.H., Pedregosa, F., van Mulbregt, P., Vijaykumar, A., Bardelli, A. Pietro, Rothberg, A., Hilboll, A., Kloeckner, A., Scopatz, A., Lee, A., Rokem, A., Woods, C.N., Fulton, C., Masson, C., Häggström, C., Fitzgerald, C., Nicholson, D.A., Hagen, D.R., Pasechnik, D. V., Olivetti, E., Martin, E., Wieser, E., Silva, F., Lenders, F., Wilhelm, F., Young, G., Price, G.A., Ingold, G.L., Allen, G.E., Lee, G.R., Audren, H., Probst, I., Dietrich, J.P., Silterra, J., Webber, J.T., Slavič, J., Nothman, J., Buchner, J., Kulick, J., Schönberger, J.L., de Miranda Cardoso, J.V., Reimer, J., Harrington, J., Rodríguez, J.L.C., Nunez-Iglesias, J., Kuczynski, J., Tritz, K., Thoma, M., Newville, M., Kümmerer, M., Bolingbroke, M., Tartre, M., Pak, M., Smith, N.J., Nowaczyk, N., Shebanov, N., Pavlyk, O., Brodtkorb, P.A., Lee, P., McGibbon, R.T., Feldbauer, R., Lewis, S., Tygier, S., Sievert, S., Vigna, S., Peterson, S., More, S., Pudlik, T., Oshima, T., Pingel, T.J., Robitaille, T.P., Spura, T., Jones, T.R., Cera, T., Leslie, T., Zito, T., Krauss, T., Upadhyay, U., Halchenko, Y.O., Vázquez-Baeza, Y., 2020. SciPy 1.0: fundamental algorithms for scientific computing in Python. Nat. Methods 17, 261–272.

Wang, Q., Kim, M.K., 2019. Applications of 3D point cloud data in the construction industry: A fifteen-year review from 2004 to 2018. Adv. Eng. Informatics 39, 306–319.

Winston, P.H., 1984. Artificial Intelligence (2nd Ed.). Addison-Wesley Longman Publishing Co., Inc., USA.

Wu, C., 2011. VisualSFM: A Visual Structure from Motion System [WWW Document]. URL http://ccwu.me/vsfm/ (accessed 8.15.20).

Xu, X., Yang, H., 2019. Intelligent crack extraction and analysis for tunnel structures with terrestrial laser scanning measurement. Adv. Mech. Eng. 11, 1–7.

Ye, X.W., Su, Y.H., Han, J.P., 2014. Structural Health Monitoring of Civil Infrastructure Using Optical Fiber Sensing Technology: A Comprehensive Review. Sci. World J. 2014, 1–11.

Yiu, W.N., Burd, H.J., Martin, C.M., 2017. Finite-element modelling for the assessment of tunnel-induced damage to a masonry building. Geotechnique 67, 780–794.

Yoneyama, S., 2016. Basic principle of digital image correlation for in-plane displacement and strain measurement. Adv. Compos. Mater. 25, 105–123.

Zhong, M., Sui, L., Wang, Z., Hu, D., 2020. Pavement crack detection from mobile laser scanning point clouds using a time grid. Sensors (Switzerland) 20, 1–20.

Zhou, Q.-Y., Park, J., Koltun, V., 2018. Open3D: A Modern Library for 3D Data Processing. arXiv Prepr. 1801.09847.

Zou, Q., Zhang, Z., Li, Q., Qi, X., Wang, Q., Wang, S., 2019. DeepCrack: Learning hierarchical convolutional features for crack detection. IEEE Trans. Image Process. 28, 1498–1512.